Development and Analysis of Apatite-Mullite Glass-Ceramic Scaffolds; Towards Tissue Engineering of the Vertebral Endplate

Niki Gosling

Doctor of Philosophy

University of York
Department of Biology

March 2014

Abstract

Calcification of the vertebral endplate (EP) is a key factor relating to the onset of degenerative disc disease, a primary influencer of lower back pain which carries substantial social and economic burden. The aim of the current project was to investigate the feasibility of using apatite-mullite glass ceramic (AM-GC) to provide a bioactive scaffold for tissue engineering applications in the region of the vertebral EP. Consequently this material was fully characterised with regard to the natural tissues from a number of functional perspectives, mechanical, compositional, biological and those factors relating to the *in vivo* mass transfer of nutrients. Scaffolds were manufactured via a novel particle sintering approach to provide a range of porous substrates. Insight into the potential for tissue engineering the complex structures of the EP were provided using primary human mesenchymal stem/stromal cells (MSCs) due to their capacity to differentiate into both the osteogenic and chondrogenic lineages that constitute the natural EP structure.

The results identified a novel heating regime able to produce AM-GC scaffolds mechanically suitable for EP application displaying mean pore size characteristics able to promote osteointergration with natural bone. Though identified as a bulk nucleating system substantial influence on surface composition was attributed to particle size fractions, with the 45-90 µm range deemed most suitable for bone applications. The differentiation capacity of MSCs on scaffolds utilising this particle size range exhibited excellent *in vitro* biocompatibility characteristics. Demonstrating a clear osteoconductive capacity along with the ability to support chondrogenic micro-mass culture, inferring potential for future development of *in vitro* AM-GC based EP constructs. To facilitate this future goal a permeability testing methodology was developed to replicate the *in vivo* nutrient mass transfer environment of the natural tissue. Initial testing proved this system fit for purpose allowing future *in vitro* engineered constructs to be comparatively analysed against natural EP mass transfer characteristics. Ensuring that future tissue engineering efforts in the region of the vertebral EP provide the necessary nutrient supply functionality essential for successful clinical application.

Contents

Figures

Tables

Acknowledgements

I would like to express my deepest gratitude to those who have helped and guided me throughout this PhD study.

First, and foremost I would like to thank my supervisors Dr. Paul Genever, Prof. David Wood and Prof. Richard Hall whose guidance has provided invaluable knowledge and insight into the vastly differing and complex areas of this interdisciplinary PhD project.

Many people at both the University of York and University of Leeds especially the technicians for providing their time and expertise in assisting me with the many different experimental techniques. Particularly Mr Mark Bentley for his consistent effort and input into the experimental testing equipment design and development. I would also like to extend my highest gratitude to Dr Nigel Bubb, Dr William Vickers and Dr Scott Finlay for their technical support while getting to grips with the testing equipment and material production processes used throughout this thesis.

I would like to thank all the members of the Biological Tissue Research Group at the University of York for their continual support and patience when helping a Yorkshire born and bred engineer develop the skills and biological competence required to succeed in such a diverse area of research. Without them this work would not have been possible.

Thanks to my close friends and colleagues who helped keep me sane throughout the tough times. Special thanks to both Dr Adam Liddle and Dr Simon Taylor who I met on my first day as an undergraduate and have been a constant source of friendship and support ever since.

Finally I send my thanks to my family for their unending support which provided me with the ability to persevere. Most importantly to me I need to thank my wife Lucy, who has been everything I could not during this time, my achievements pale in comparison to her strength and sacrifice throughout this PhD.

Declaration

The author would like to confirm that all work submitted within this thesis is his own and has not been submitted for examination at this or any other institution for another award. Throughout the thesis appropriate credit has been given where reference has been made to the work of others.

The following oral and poster presentations were made over the period of PhD study and contained information from within the thesis:

Oral Publications

1. Niki Gosling, Richard M. Hall, David J. Wood & Paul G. Genever: **Novel Porous Glass-Ceramics as Suitable Vertebral Endplate Constructs.** Biomaterials and Tissue Engineering Group (BITEG) conference, The University of Leeds, 17/12/2010.

2. Niki Gosling, Richard M. Hall, David J. Wood & Paul G. Genever: **Development and Optimisation of a Functional Vertebral Endplate Constructs.** Doctoral Training Centre Joint Conference, The University of Leeds, 08/07/2011.

3. Niki Gosling, Richard M. Hall, David J. Wood & Paul G. Genever: **Development and Optimisation of a Functional Vertebral Endplate Constructs.** Tissue and Cell Engineering Society (TCES) conference, The University of Leeds, 21/07/2011.

4. Niki Gosling, Richard M. Hall, David J. Wood & Paul G. Genever: **Novel MSC Supportive Glass-Ceramic Scaffolds for Bone Tissue Engineering.** Leeds Dental Institute Research Day, The University of Leeds, 2012.

<u>Poster Publications</u>

1. Niki Gosling, Richard M. Hall, David J. Wood & Paul G. Genever**: Development and Optimisation of an Apatite-Mullite Glass-Ceramic for Functional Vertebral Endplate Constructs.** The 5TH UK Mesenchymal Stem Cell (MSC) Meeting, Aston University, Birmingham, 01/07/2011.

2. Liddle, A.M., **Gosling, N**., McLure, S.W.D., Taylor, S.D., Oakland, R.J., Kapur, N., Hall, R.M. **Regional Variations in the Vertebral Endplate Properties within Animal Models.** Ninth Annual Global Symposium on Motion Preservation Technology, Spine Arthroplasty Society, London, UK, 2009

3. Niki Gosling, Richard M. Hall, David J. Wood & Paul G. Genever**: Apatite-Mullite Glass-Ceramic as a Suitable Scaffold Material for Bone Tissue Engineering.** American Society for Bone and Mineral Research (ASBMR) Annual Meeting, Minneapolis, USA, 12-15th October 2012.

4. Niki Gosling, Richard M. Hall, David J. Wood & Paul G. Genever**: Development and Optimisation of an Apatite-Mullite Glass-Ceramic for Functional Vertebral Endplate Constructs.** Leeds University Industry Research Day, Weetwood Hall, Leeds, 12/07/12.

Chapter 1: Introduction

1.1 *Spinal Anatomy & Tissue Structure*

1.1.1   Spinal Column

The normal spinal column consists of 33 individual vertebra which are split into five anatomical regions. The seven most superior vertebra constitute the cervical region, the following twelve the thoracic region and the remaining five the lumbar region. Directly inferior to the lumbar region in the adult spine are a further nine fused vertebra, the first five of which form the sacrum and the final four the coccyx (Figure 1.1) [1].
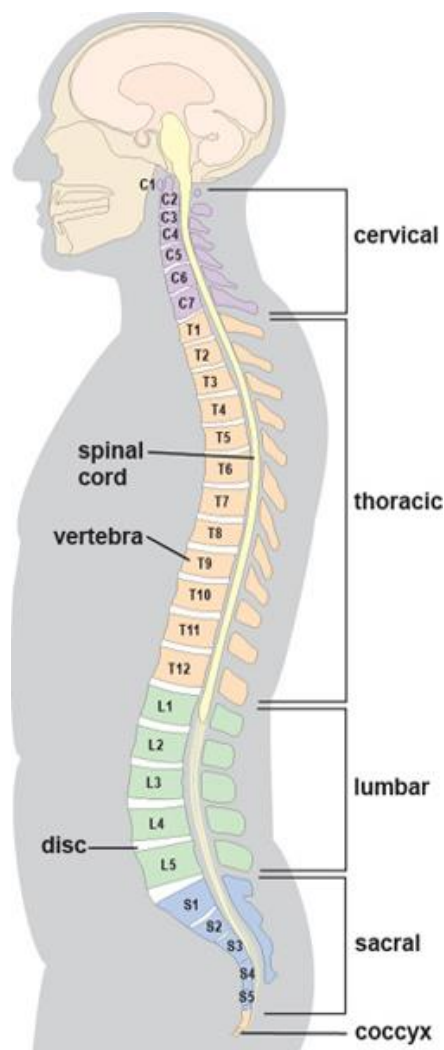
Figure 1.1: The anatomy of the normal adult spine indicating the five regions, the individual vertebral bodies, the intervertebral disc and spinal cord location [2].

The vertebral column functions to provide stability by supporting the weight of the head and trunk. It encapsulates the spinal cord, therefore, providing protection to the central nervous system, whilst simultaneously aiding in the mobility of the torso and both upper and lower limbs [1]. The individual vertebra themselves are composed of an outer layer of dense cortical bone which surrounds an inner cancellous bone structure.
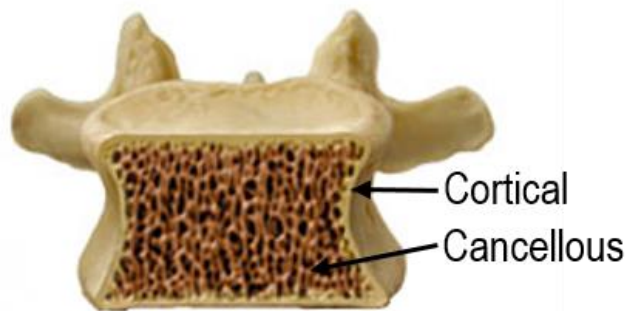
Figure 1.2: Section through the frontal plain of a vertebral body indicating the location of both cortical and cancellous bone structures within, after [3]

1.1.2 Bone Structure

Although morphologically the structures of both cortical and cancellous bone differ substantially from one another, their compositional structures are very similar. Essentially bone is a calcified tissue retaining both organic and inorganic phase constituents. The inorganic phase is composed of a carbonate hydroxyapatite (HA) approximated by the formula $(CaX)_{10}(PO_4HPO_4CO_3)_6(OHY)_2$ in which X represents cations such as, Mg^{2+}, Na^+ or Sr^{2+}, that can substitute for Ca^{2+} ions and Y represents anions, Cl- and F- which can substitute for the hydroxyl group [4]. This is often idealised to calcium HA, of composition $Ca_{10}(PO_4)_6(OH)_2$. This mineral phase accounts for approximately 75% of bone composition by weight and 65% by volume [4]. The crystalline HA is present as irregularly-shaped crystals with widths of between 30 to 45 nm and thickness of approximately 5 nm. These crystals are arranged parallel to each other along the collagen fibrils of the organic phase matrix [5]. Within natural bone the Ca:P molar ratio can be both below or above 1.67 (the stoichiometric value for pure HA), dependent on factors such as age, species and bone type [4]. The organic phase of bone is primarily composed of type I collagen (approximately 90%) though there are a total of 15 different types of collagens present in mature bone as well as a range of non-collagenous proteins and glycosaminoglycans (GAGs) [6, 7]. The HA crystals bond to the collagen fibres via interactions with the polar groups of the protein molecules and the CaP structure [8].

Above the level of the individual collagen and mineral components bone exists in two distinct forms, woven/primary bone and lamellar/mature bone. Within woven bone the collagen fibres are orientated randomly, while in lamellar bone the collagen is highly organised into parallel sheets. Woven bone is laid down rapidly during foetal development and during fracture repair, it has a low level of mineral content in comparison to the mature bone, with which it is eventually replaced. Macroscopically bone is considered as being either densely packed cortical bone or more porous trabecular bone. Cortical bone, sometimes referred to as compact bone is approximately 30% porous and accounts for around 80% of the skeleton. It is found at the outer walls of the tissue encapsulating the cancellous bone which has a porosity of approximately 70% and makes up the remainder of the skeleton [9]. Pore size within cortical bone ranges from 1µm to 100µm while that within the cancellous structure ranges from 200µm to 400µm. These varied pore size distributions and the inherent degree of interconnectivity in natural bone structures are critical factors affecting aspects such as nutrient diffusion, cell attachment, repair and regeneration [4].

The basic structural unit of cortical bone is the osteon, a cylinder of bone composed of a large number of concentric lamellae surrounding a central Haversian canal. This central canal contains the blood vessels and some nerve tissue, while the space between individual osteons is filled with interstitial lamellae with circumferential lamellae at the periphery. Between the sheets of individual lamellae are small lacunae, containing osteocytes, the differentiated progeny of bone-forming osteoblasts (1.2.2) [10]. The lacunae are connected to one another by canaliculi and have a part to play in the stress/strain related remodelling of natural bone tissue [11]. At its outermost edge, cortical bone is covered by a thin layer of fibrous tissue called the periosteum, which is present in all regions except at the articulating joint surfaces where articular cartilage is found. In contrast to the cortical bone structure, cancellous bone is composed of a large network of interconnected plates or struts termed trabeculi. The trabecular osteons, also referred to as packets are saucer shaped stacks of lamellae. The space between the cancellous bone structure is occupied by bone marrow and is the site of haematopoiesis. Like the periosteum on the outer surface of bone, the internal surfaces are covered in a membranous sheath called the endosteum [9, 10].

1.1.3   The Intervertebral Disc

The intervertebral disc (IVD) is situated between adjacent vertebrae of the spinal column, giving rise to the interbody joints from the level of the 2nd cervical vertebrae to the sacrum. The IVD has two main biomechanical functions within the spinal column: firstly, to both allow and restrict motion at the interbody joint and secondly, to support the transmission of loads between

subsequent vertebra [1]. The IVD essentially consists of two distinct components, a central nucleus pulposus (NP) which is itself encapsulated circumferentially by the annulus fibrosus (AF). Both the NP and AF are covered inferiorly and superiorly by a third component, the vertebral endplates (Figure 1.3). The endplates, therefore, lie between the disc and the adjacent vertebra and it is still debatable as to which component they actually belong [12].
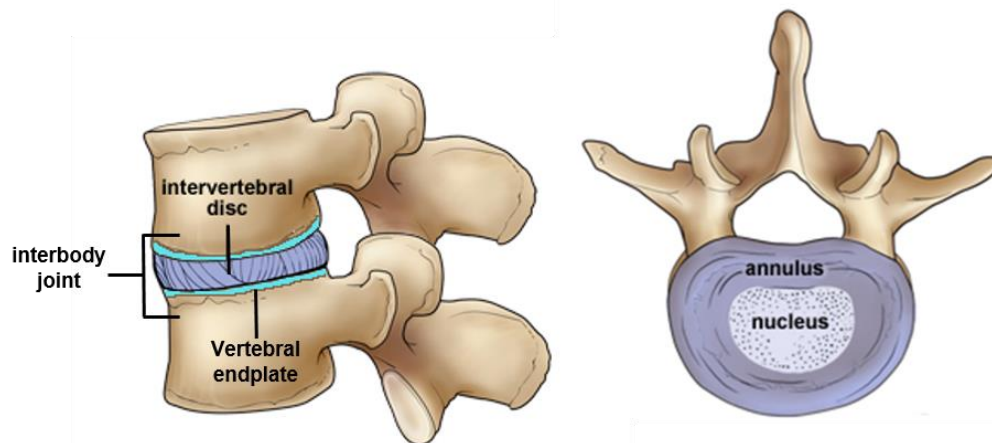
Figure 1.3: Illustration of the anatomical location of the interbody joint, indicating both the IVD and vertebral endplate regions. The right hand image shows a transverse section through the intervertebral disk indicating both the annulus and nucleus regions within, after [2]

1.1.3.1 Nucleus Pulposus Structure

The NP is composed of a gel like proteoglycan-water rich matrix containing a network of randomly orientated collagen fibres. The proteoglycan (PG) contents of the NP accounts for approximately 65% of its dry weight [12]. The principal PG unit present in the IVD is aggrecan, composed of mostly sulphated GAGs covalently bonded to a central protein core. The most prominent GAGs are chondroitin sulphate and keratin sulphate, the fixed negative charge densities of which greatly increase the water-binding capacity of the tissues [1, 12, 13]. Approximately 25% of the aggrecan within the NP binds to hyaluronic acid to form large aggregates in the adult IVD [12]. Complex three-dimensional (3D) molecules are formed *in vivo* from entangled PG units and aggregates. These molecules due to their size, shape and fixed charge density retain water in the tissue, providing the NP with the osmotic pressure needed to maintain its fluid content and resilience to compressive loading [1, 12, 13].

Collagen accounts for approximately 20% of the NP dry weight and is predominantly type II collagen at approximately 80%, but small amounts of types III, VI, IX and XI collagen are also

present [12-15]. The collagen molecules are randomly orientated throughout the tissue and function to hold the complex PG structures together and to restrain their swelling pressure. Elastin is also present within the NP although to a much lesser extent than either collagen or PG, only accounting for approximately 5% of the dry weight of the entire IVD. The NP elastic fibres are radially orientated and thought to provide resistance to tensile forces and aid in tissue recovery after loading [16].

1.1.3.2 Annulus Fibrosus Structure

The AF is composed of a series of between 15-25 loosely connected concentric lamellae with highly organised collagen fibre networks. Individual lamellae are not continuous around its entire circumference, instead at any region approximately 48% of the lamellae are incomplete [17]. The collagen fibres within each lamellae lie parallel to each other at approximately 65° to the vertical axis of the spine with consecutive layers arranged at right angles to one another [18]. Although it is commonly depicted, there is no clear boundary between the inner AF and the NP *in vivo*, rather, a gradual transition takes place between the two tissues.

The collagen of the AF accounts for around 60% of the tissue dry weight and is predominantly type I collage [1, 19]. However, type II collagen is also present in the inner AF region as the transition into the NP occurs [19, 20]. Much smaller amounts of collagen types III, V, VI, IX and XI have also been isolated from the tissue [14, 20]. PG's are present to a lesser extent within the AF accounting for about 20% of the tissue dry weight. However, a greater proportion is in the aggregated form, approximately 55%, compared to 25% reported in the NP. The PG's occupy space between tightly packed collagen fibres and lamellae, functioning to bond the components together whilst also imbibing water into the structure. The anterior AF has the highest PG content and overall there is a gradual increase towards the inner region [1, 12, 20]. Recently an elaborate network of elastin fibres has been demonstrated in the AF. In the outer annulus, fibres are densely packed between lamellae but run parallel to collagen fibres within them. However, the inner AF fibre network forms a dense crisscross pattern between lamella. The lamella fibres run parallel to each other but form angles of approximately 60° or 120° to those of adjacent lamella [16, 21].

1.1.3.3 Vertebral Endplate Structure

The vertebral endplates cover both the cranial and caudal surfaces of the IVD, separating it from the underlying cancellous bone of the adjacent vertebra. Each endplate (EP) consists of both a cartilage component and an osseous layer of calcified cartilage. The cartilage component of the EP has a thickness in the range 0.3-0.9 mm and covers the whole surface of the NP and the inner two thirds of the AF [22, 23]. The cartilage periphery is surrounded by a ring apophysis which fuses with the adjacent vertebral body to form a raised bony rim to the EP (Figure 1.4) [1, 24]. The collagen fibres of the NP and inner AF turn through angles of approximately 90° and 120° respectfully to become continuous in the cartilage EP. The collagen fibres of the EP run parallel and horizontally and are always completely separate from those of the underlying bone. However, intimate contact between the IVD and the adjacent vertebra is achieved through fibres in the outer third of the AF [22, 23, 25]. The osseous layer of calcified cartilage sits between the cartilage EP and cancellous bone of the adjacent vertebra. It is most prominent in the peripheral regions where, histologically, a tidemark is visible between the cartilage EP and the calcified layer. The thickness of the calcified layer and prominence of the tide mark both decrease in the more central regions of the EP becoming thinnest in that of the NP [23, 24].
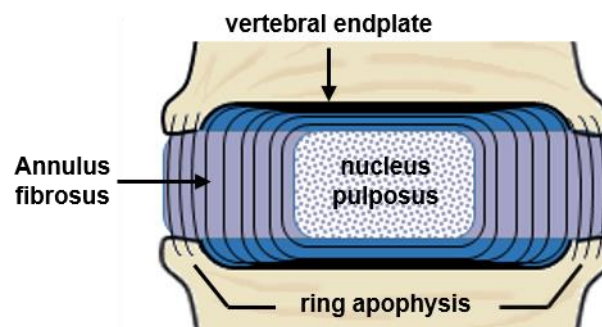
Figure 1.4: Frontal plane schematic representation of the vertebral EP location and structure within the interbody joint. The EP cartilage (blue) covers the inner two thirds of the AF and all of the NP. The ring apophysis creates a rased rim around the cartilage EP component.

Collagen makes up approximately 10% of the EP tissue dry weight and is practically all collagen type II [26]. Other collagens ,types IX, VI, III, have also been detected in small amounts [14], however, collagen type X is the most prominent. Type X collagen is found predominantly at the bone-cartilage border in the adult EP and is a calcium-binding collagen thought to be involved in calcification [27]. The PG content of the EP varies both horizontally and vertically across the

structure. Horizontally, PG content increases towards the centre of the EP and vertically the PG content decreases away from the NP and towards the calcified cartilage layer [23]. Furthermore, all the tissues of the IVD contain small amounts of the PGs decorin and biglycan which contain the GAG chain dermatan sulphate. However, in the EP these PG's are substituted for CS which provides a higher water binding capacity to the tissue [28, 29].

1.2 Cellular Mechanisms of Bone

1.2.1   Bone Formation

Within the developing skeleton, bones are formed from mesenchymal cell condensations; the location and timing of these condensations is determined by complex patterning events. The source of the condensing cell population varies in relation to the skeletal regions. Craniofacial regions are derived from cells of the neural crest, while the paraxial and lateral plate mesoderm give rise to the bones of the axial skeleton and limbs respectively [30]. These events are primarily governed by regulatory transcription factors and signalling pathways such as the Wingless-related integration site (Wnt), Notch, fibroblast growth factors (FGFs) and retinoic acids [30, 31]. Though it is important to be aware of these complex patterning events that govern mesenchymal condensation prior to bone formation, the detailed processes are extremely complex and as such out of scope for the current work.

Progression from a mesenchymal condensation to a fully developed bone proceeds naturally through one of two mechanisms:

1. *Intramembranous Ossification;* bone synthesised in the absence of a preliminary cartilage phase. This direct differentiation of the condensed mesenchymal cells into osteoblasts occurs in areas such as the calvaria of the skull, the maxilla, the mandible and the subperiosteal bone forming layer of the long bones [31, 32].

2. *Endochondral Ossification;* bones form following chondrogenic differentiation of the condensed mesenchymal cells. Endochondral ossification involves the mineralisation of a cartilage scaffold synthesised by the chondrogenic cells in the developing organs, most notably in the long bone [30].

Sry-related HMG box 9 (Sox9) and Runt-related transcription factor 2 (Runx2) have been identified as the master transcription factors governing chondrogenic and osteogenic differentiation, respectively, from the osteochondral progenitors within the mesenchymal condensations [33, 34]. Whilst both Sox9 and Runx2 are co-expressed in the osteochondral progenitor cell population, the subsequent termination of the respective gene occurs rapidly on either chondrogenic or osteogenic differentiation [30]. Therefore, the mechanism controlling this expression segregation is key to our understanding of both the intramembranous and endochondral ossification processes.

Though there are a myriad of complex signalling pathways involved in bone formation, the canonical Wnt signalling pathway has been identified as one that is key with regard to the ossification mechanism undertaken [35]. The binding of Wnt proteins to the transmembrane Frizzled receptor and Lrp 5/6 co-receptors stimulates intracellular destruction complex inhibition. This in turn prevents the proteolytic degradation of β-catenin within the cell cytoplasm. β-catenin can then subsequently translocate to the nucleus and influence the expression of downstream target genes via transcription factor mediated activation [36]. Specifically in areas of intramembranous ossification, Wnt signalling enhances bone formation through the up-regulation of Runx2 expression and subsequent inhibition of Sox9, promoting osteogenesis [30, 37].

In the case of endochondral ossification, initial Wnt signalling activity is low leading to higher expression of Sox9 and inhibition of osteogenesis. Therefore, only chondrogenic differentiation progresses and the cells switch from production of collagens I and III to the cartilage-specific collagens II, IX, and XI and aggrecan [38]. This cartilage region is then able to grow by interstitial and appositional growth to resemble the final geometry. At the later stages of endochondral ossification Wnt signalling is upregulated in the central region leading to increased levels of β-catenin. These central chondrocytes subsequently stop proliferating and become hypertrophic, characterised by the abundant expression of collagen X. In the same instance up regulation of Wnt signalling in the perichondral region leads to osteogenesis and the formation of a bone collar surrounding the central hypertrophic region. In order to ensure blood supply to the developing bones during endochondral ossification, vascular ingrowth is facilitated by the expression of high levels of Runx2 by the hypertrophic chondrocytes, leading to the up regulation of the pro-angiogenic factors, vascular endothelial growth factor A and connective tissue growth factor. These factors also promote the invasion of osteoblastic progenitor cells and cartilage/bone resorbing cells from the perichondrium to facilitate the formation of a primary ossification centre

leading to the resorption of the hypertrophic cartilage and deposition of cancellous bone and bone marrow [31, 39].

In the case of endochondral ossification, Indian hedgehog (Ihh) signalling is also required to promote osteoblast differentiation through the activation of Runx2 [40, 41]. However, in the case of intramembranous ossification it is still not clear what controls the apparent Ihh independent Runx2 mediated differentiation, though it is believed that sonic hedgehog may be a contributor to this process, compensating for the lack of Ihh. Although much less defined with respect to both the Wnt and Hedgehog signalling pathways, the role of both the bone morphogenic proteins (BMPs) and FGF ligands and receptors is considerable in relation to the osteoblastic and chondrogenic differentiation of mesenchymal cell populations. However, their specific roles in the natural processes of intramembranous or endochondral ossification are poorly understood [30, 31].

1.2.2 Bone Remodelling

During life bone remodelling is carried out by a collective functional unit of cells commonly referred to as the basic multicellular unit [42]. This process requires the coordinated action of four component cells of bone; bone lining cells, osteocytes, osteoclasts and osteoblasts. Remodelling takes place over the four distinct phases outlined below.

1.2.2.1 Activation

In this first stage of the remodelling cycle, mononuclear cells of the monocyte/macrophage lineage differentiate to form osteoclasts via the action of two key factors: the monocyte/macrophage colony-stimulating factor (M-CSF) and the receptor activator of nuclear factor κβ (NF- κβ) ligand (RANKL) [43]. It is proposed that in response to mechanical loading or micro damage in old bone, local osteocytes signal to recruit pre-osteoclasts from bone marrow or circulation to the specific site, though the signalling mechanisms for this process are not yet known [44]. Once at the resorption site the pre-osteoclasts infiltrate the bone lining cell layer and fuse to form multinucleated cells. These cells then attach to the bone via membrane integrin receptors binding to arginine-glycine-aspartic acid motifs within the bone matrix. This creates an annular sealing zone between the cell and bone matrix. The pre-osteoclasts are then terminally differentiated to form mature osteoclasts due to elevated concentrations of M-CSF and RANKL [9, 43].

1.2.2.2 Resorption

Within the annular sealing zone created between the osteoclast and bone matrix, termed the resorbing compartment, an acidic environment is created by proton pumps on the osteoclast membrane, the pH has be found to drop as low as 4.0 within the compartment [45]. Simultaneously a number of enzymes are also secreted into the compartment such as, tartrate resistant acid phosphate, cathepsin K and the matrix metalloproteinases (MMPs) collagenase (MMP13) and gelatinase (MMP9) [46]. This effectively dissolves both the organic and mineral phases of bone, leaving behind resorption pits within bone referred to as Howship's lacunae on the surface of trabecular bone and cylindrical tunnels within cortical regions. This phase of the resorption process is concluded with the apoptotic cell death of the local osteoclast population [9].

1.2.2.3 Reversal

In this phase the lacunae are populated by a number of residual mononuclear cells that have been liberated from the previously resorbed bone matrix, primarily monocytes and osteocytes [9]. It is during this phase that a signalling mechanism commonly referred to as coupling is suspected to occur, the term stems from the assumption that a coupling must exist between resorption and bone formation and was first reported in 1964 [47]. To date, the exact process by which coupling takes place is unclear; however without it there would be net loss in bone mass [42]. One possible hypothesis for the coupling mechanism is that the liberation of growth factors from the bone matrix during the resorption phase acts as a chemo-attractant for osteo-precursors and also aids in stimulating proliferation and differentiation to mature osteoblasts. There are a number of likely growth factors within bone that could theoretically provide this function, such as, transforming growth factor beta (TGF-β), BMPs and FGF family members.

1.2.2.4 Formation

The mature osteoblasts which originate from mesenchymal stem/stromal cells (MSCs) are present at the bone surface in clusters which function to lay down new bone matrix. This process can be considered in two stages, the first being the production and maturation of an osteoid layer, through the rapid production of type I collagen rich matrix [39, 42]. In the second step, following the osteoid matrix deposition the osteoblasts trigger mineralisation of the tissue via release of matrix vesicles. These vesicles function to concentrate calcium and phosphate ions to trigger apatite formation whilst also providing enzymes to degrade local inhibitors of mineralisation such as, pyrophosphate, adenosine triphosphate (ATP) and PG within the matrix [48].

During the formation of new bone matrix, some osteoblasts become embedded within the progressive structure and form osteocytes. The osteocytes are highly branched and maintain contact with one another through the canaliculae, providing a network able to transmit information relating to mechanical stimuli to cells of the bone surface to initiate or regulate bone remodelling [11, 49], thus completing the remodelling cycle from activation through to formation (Figure 1.5). From the total osteoblast cell population involved in the formation phase only approximately 15% differentiate to form the osteocyte network [42]. Some cells remain on the surface to form bone lining cells while the remainder, between 50%-70%, die via apoptosis [9].
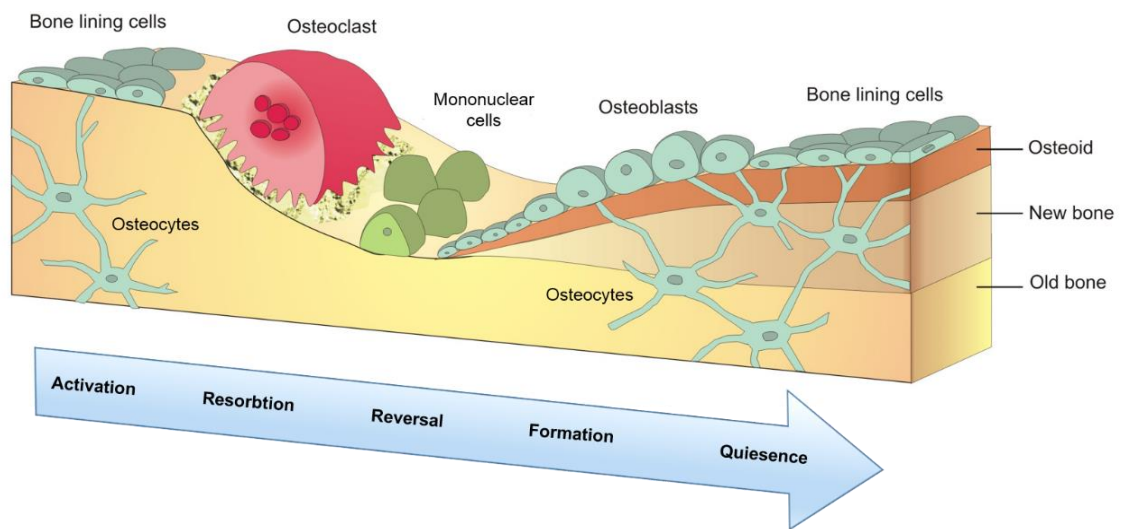
Figure 1.5: Progressive illustration of the four main phases of the remodelling process and the cells which make up the basic multicellular unit, after [50]

1.3 *Intervertebral Disc Degeneration and the Vertebral Endplates*

Lower back pain (LBP) is a major cause of disability affecting all cultures and ethnicities in similar proportions, with between 49% and 80% of the population suffering from LBP at some point during their lifetime [15, 51, 52]. Not only does LBP affect the quality of life for the individuals but it also carries large economic burdens. Previous estimates of the direct costs to health care in the UK have been as high as £1.6 billion [53]. However, this pales in comparison to the estimated cost due to lost production days, disability benefits and insurance claims which has been reported at over £12 billion [15].

Degenerative disease of the IVD is thought to be one of the primary factors influencing LBP, with disc tissues examined in relation to LBP showing signs of degeneration in almost every case [54, 55]. These degenerative changes are closely linked to age and can start to occur as early as the

second decade of life [13, 56]. However, substantial variations between individual degenerative states are also seen, with young people exhibiting discs similar to those seen in the elderly and visa versa. Hence, the pathology of IVD degeneration is undoubtedly complex and still far from fully understood, with many factors thought to contribute to its progression, such as nutritional, mechanical, biomechanical, and genetic aspects.

1.3.1   Intervertebral Disc Nutrition and Degeneration

The adult IVD is the largest avascular structure within the body, with the cells reported in some cases as being up to 8 mm away from the nearest blood supply [57, 58]. Disc tissue is reliant on regions beneath the EP and in the outer AF for both the supply and disposal of metabolites and metabolic waste products respectively [59]. The outer AF obtains metabolites from its own constituent blood vessels, however, the NP and inner AF are dependent on metabolite diffusion through the cartilage EPs [60, 61]. This diffusion can occur from two apparent sources; capillary bed vessels present beneath the cartilage EP or marrow cavities of the underlying cancellous bone (Figure 1.6). Both components are abutting directly onto the cartilage EP and have been demonstrated through histological studies and simple injection techniques coupled with radiographs [23, 62]. The capillary bed density is greatest in the central region adjacent to the NP diminishing towards the periphery, with around 36% of the EP area providing vascular nutrient transfer in the adult IVD. However, the marrow cavities account for approximately 20% of the contact area at the bone cartilage interface over the entire EP surface [23, 63].
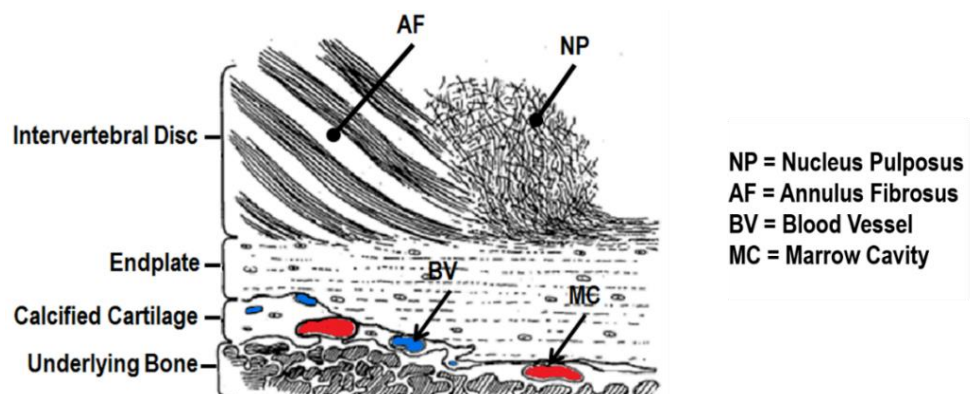
Figure 1.6: Schematic representation of the EP/IVD interface region illustrating the presence of both blood vessels and marrow cavities responsible for nutrient supply, adapted from [23].

The solute diffusivity of the cartilage EP is dependent largely on the tissue composition. decreased hydration and/or increased concentrations of either PG or collagen restricts solute

diffusion. Small uncharged molecules such as oxygen, amino acids and water are able to diffuse readily into the IVD tissue. However, Due to the fixed negative charge density of EP cartilage anions such as sulphate or chloride are to a degree excluded. There is also a steric exclusion of larger molecules from the EP cartilage, the degree of which increases with molecular weight [23, 63]. Even glucose, the cell's main energy source, with a molecular weight of 180 is excluded to some extent from the IVD tissue [63]. Steep gradients of nutrient concentration are, therefore, present throughout the IVD as a consequence of its avascularity, selective permeability and steric exclusion. The disc interior then suffers from low oxygen tension and pH, both of which decrease with distance from the EP [64].

The thickness of the cartilaginous component of the vertebral EP can decrease with advancing age undergoing calcification by unknown mechanisms. Gradual mineralisation of the EP cartilage takes place in the young adult, followed by resorption of the tissue and replacement with real bone throughout middle to old age. This process leaving only a thin layer of calcified cartilage or bone between the disc and adjacent vertebra [65]. *In vitro* testing of dye diffusion through the EP and underlying bone indicated a progressive barrier to solute permeability with increasing age [66]. The EP calcification undoubtedly restricts the nutrient supply to the IVD giving rise to increased acidity and low oxygen tension within the extracellular environment, consequently reducing cell viability and PG synthesis rates [56, 67]. Degenerative changes in the IVD have been observed to occur as early as the second decade of life, originating in the NP [56, 68]. With increasing age disc degeneration progresses, loss of PG content and, hence, hydration occurs; due to aggrecan molecule degradation smaller fragments are able to leave the disc reducing the osmotic swelling pressures. The lamellae structure begins to appears more irregular and both the collagen and elastin networks become progressively more disorganised (Figure 1.7) [69].
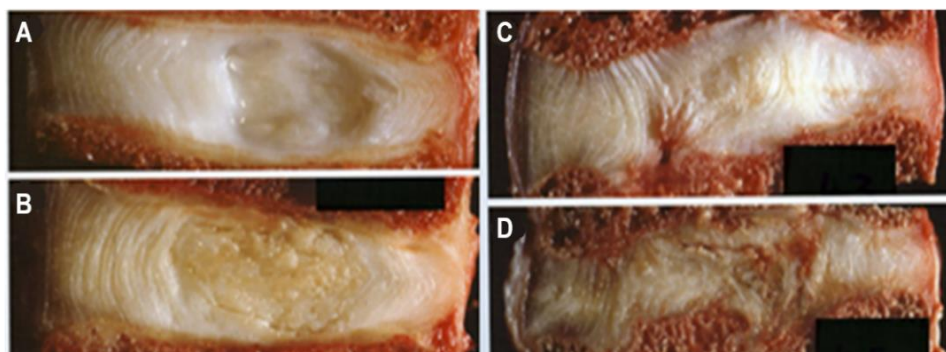
Figure 1.7: Image representing the progression from a healthy IVD and EP tissue (A) towards that of one displaying a significantly degenerated state (D) [12].

Attempts at the classification of age related changes in the lumbar IVD have proposed that EP changes proceed those seen in the NP. This and positive correlations reported between the degree of EP calcification and the degenerative state of the IVD has led to the view in some cases that degeneration of the IVD is first initiated by calcification of the cartilage EP [56, 70]. However, there are many other factors which may impair nutrient supply and aid in the progression of the degenerative state such as genetics, trauma and biomechanical factors to name but a few.

As degradation of the IVD increases there is often traumatic damage to the EP with the invasion of blood vessels and nerve fibres into the inner AF and even the NP in the later stages, suggesting that the body's own attempts at tissue repair in the EP may be associated with the presence of back pain [25]. IVD degeneration has also been associated with other spinal defects such as herniated or prolapsed discs. Reduced IVD heights due to loss of hydration could also lead to abnormal spinal loading which may affect surrounding muscles and ligaments contributing to conditions such as spinal stenosis [69].

1.3.2 Current Treatments for IVD Degeneration

IVD degeneration causing pain is thought to be one of the primary factors influencing LBP, with disc tissues examined in relation to LBP showing signs of degeneration in almost every case [54, 55]. Between 49% to 80% of the population suffer from LBP at some point during their lifetime and to date there is no optimal treatment for the persistent symptoms [51, 52]. At present the most commonly prescribed surgical treatments are interbody fusion, total disc replacement (TDR) and NP replacement (NPR) [13]. Interbody fusion entails the removal of the IVD at the respective level and subsequent replacement with bone graft material and possibly additional supporting structures [71]. This fusion methodology removes the IVD and associated motion to successfully alleviate pain, however, follow up studies have indicated disc degeneration at adjacent levels thought to have occurred from altered spinal biomechanics [72]. TDR and NPR devices, therefore, attempt to preserve the motion at the level of the IVD to reduce any adjacent level effects. Although TDR devices and interbody fusion have produced satisfactory clinical outcomes they require more invasive surgery than the NPR devices [13]. The NPR devices place emphasis back on the native AF tissue to support the hydrostatic loading of the implant, as is the case *in vivo*. However, there are complications that still arise for all the current methodologies such as subsidence of devices and bone graft materials into the adjacent vertebra and also extrusion of the NPR devices [73, 74].

1.3.3 Tissue Engineering of the IVD and EP

The complications associated with IVD degeneration treatment modalities have led to increased focus on biological and regenerative approaches. Transplantation of both allogeneic and autogenic IVD discs have had previous success in animal studies and recently allogeneic discs have been used in human trials [75, 76]. The human transplant tissues were able to maintain cell viability after deep freezing and once implanted showed no significant immune response. However, subsequent disc degeneration appeared unavoidable within the transplant tissues. This coupled with the limited tissue availability and potential for disease transmission restricts transplant application, supporting the need for cell based therapy approaches [75, 77]. Tissue engineering strategies aim to repair or replace the degenerative tissues using either *in situ* regenerative techniques or functional *in vitro* developed replacements. In the case of the IVD its functional properties are the consequence of the complex extra-cellular matrix (ECM) composition, therefore, it is this matrix that needs to be replenished and subsequently maintained following disc degeneration.

Culture of IVD cells has proven to be complex, hindering the progression of tissue engineering research into the area [13, 78]. The cells of the NP are particularly difficult to culture with low cell yields from IVD tissue and poor *in vitro* proliferation [13]. Techniques for the co-culture of IVD cells have aided in overcoming this problem, enhancing the matrix production and accelerating the proliferation of cells [79]. Co-culture of AF and NP cells in both animal and human studies have been observed to stimulate the proliferation of each cell type. Furthermore, reinsertion of the co-cultured cells into the disc has been found to delay the onset of degeneration [79-82]. This delayed degeneration effect has been reported to increase when NP cells are co-cultured with MSCs in rabbit degenerative models [83]. However, a study of human MSCs co-cultured with NP and AF cells found a significant increase in PG and GAG synthesis for AF cells when cultured with MSCs but no difference was seen in NP matrix synthesis [84].

Even though the reinsertion of co-cultured IVD cells have shown promising results the technique does not address the calcification of the cartilage EP. The tissues of the IVD are still void of nutrition from the underlying capillary bed and marrow contacts, hence, this approach can only ever delay the degeneration process unless this issue is addressed. An approach to restore the cartilage EP would most likely require the use of a construct able to replace both the cartilaginous and bony regions of the natural tissue. Also, in replacing the vertebral EP there is a greater need for a scaffold component in order to satisfy the mechanical requirements during any *in vivo* based

attempt to restore natural EP function. In light of this point one study aimed to determine if NP tissue could be cultured *in vitro* on the surface of a calcium polyphosphate (CPP) substitute material. Following 6 weeks culture a continuous layer of tissue, approximately 1.8 mm thick, formed across the CPP surface with an *in vitro* GAG content equivalent to the *in vivo* tissue. The compressive mechanical properties of the NP tissue measured in terms of both equilibrium stress and modulus were also found not to differ significantly at weeks 4 and 6 when compared to those of the natural bovine tissue [77].

The same group in a later study attempted to add a cartilage EP component to the construct between the NP and CPP layers. In order to create this EP layer bovine chondrocytes were seeded on the CPP substrate. The construct was then maintained for 2 weeks in culture, NP cells were then seeded onto this surface and cultured for a further 6 weeks. The NP cells formed a second continuous layer which fused with the first [85]. The incorporation of the cartilage layer was found to be beneficial to the construct by improving the tissue attachment to the CPP substrate, demonstrated by increased peak load and energy required for failure during interfacial shear strength testing when compared to the previous biphasic constructs composed of NP cells on the CPP substrate alone. Although it was shown that addition of a cartilage like layer improved CPP interface characteristics, the shear strength values for *ex vivo* bovine tissue samples were found to be at least ten fold greater than that of the *in vitro* generated samples.

1.3.4   Summary

IVD degeneration can be a debilitating disease where the current gold standard treatment is a highly invasive fusion procedure. This has led to an increased focus on biological and regenerative approaches, such as replacement bone scaffolds. Although CaP based scaffolds have shown promising results in the development of bioactive constructs, the resorbable nature of the material could have a negative impact on the stability of the structure over time and the mechanical properties it maintains. Also, the inherent low strength and brittle nature of mono-phase bioactive glass materials, such as the commonly used HA and tri-calcium phosphate, may not be ideally suited to vertebral EP applications, where load bearing is a primary function. A potential alternative material family would be that of glass ceramics, where mechanical strength can be enhanced through thermal processing whilst still providing a bioactive substrate for bone bonding and osteointergration.

1.4 *Glass-Ceramics*

In order to develop a glass-ceramic based approach to potential bone replacement scaffolds, it is important to understand both the structural and compositional factors governing the production process and subsequent phase formations. Glass-ceramics are a natural progression from standard glass materials because of their improved inherent structural properties in relation to bone scaffold applications. The key factors are discussed in the next section.

1.4.1 *Definition of Glass*

The use of glass in the application of science began in thirteenth century Italy and then sixteenth century Netherlands with the development of eye glasses and telescope lenses respectively. However, is was not until the 1920s that systematic characterisation of glasses started to occur through the pioneering work of Turner in The Department of Glass Technology at the University of Sheffield. This work when considered alongside that of Tammann, who in the 1930s was the first to investigate glass as a particular state of aggregated matter, referred to as *the vitreous state* provides the groundwork which led to the modern generalised definition of glass as an amorphous or non-crystalline material [86]. One of the most widely accepted current definitions of a glass was proposed by the American Society for Testing and Materials and is as follows:

"*Glass is an inorganic product of fusion which has cooled from a liquid to a rigid condition without crystallising*" [87]

This definition by no means covers the whole scope of the term 'glass' from a strict materials science perspective, as organic substances can be cooled to possess amorphous and rigid characteristics. Also, this definition is only applicable to those glasses formed by the traditional melt cooling techniques when alternative methods do exist. As such it should be noted that more complete scientific definitions of a glass have been given in literature [88]. However, in the current work we are solely concerned with glasses produced via thermal fusion of inorganic components which subsequently undergo rapid cooling. Therefore, the current definition will not only suffice but provide focus for the reader in a highly diversified field of materials science.

1.4.2   Theories of Glass Structure

Stereotypically solid materials are defined as having either a crystalline (ordered) or amorphous (non-crystalline, vitreous) structure. Therefore, in a given material the fundamental units of structure in the amorphous glass are the same as those in the crystalline structure, but in the glass they are not arranged in any regular order. Preferentially when cooled below their melting temperatures solid materials would take up the crystalline form, providing an equilibrium state. This is due to the fact that the ordered crystalline form is associated with the least free energy and is thermodynamically the preferred choice of the system. However, in the case of glass formation the mobility of the compositional elements is significantly restricted upon cooling to the degree where solidification occurs in the absence of crystallisation to give an amorphous structure. The amorphous or glass state is, therefore, characterised by an inherent random distribution of bond angles and distances which generates a non-equilibrium state within the material (Figure 1.8) [89]. Materials in the glassy state are said to be metastable, relating to the fact that they have a greater free energy than that of the corresponding crystalline solid.
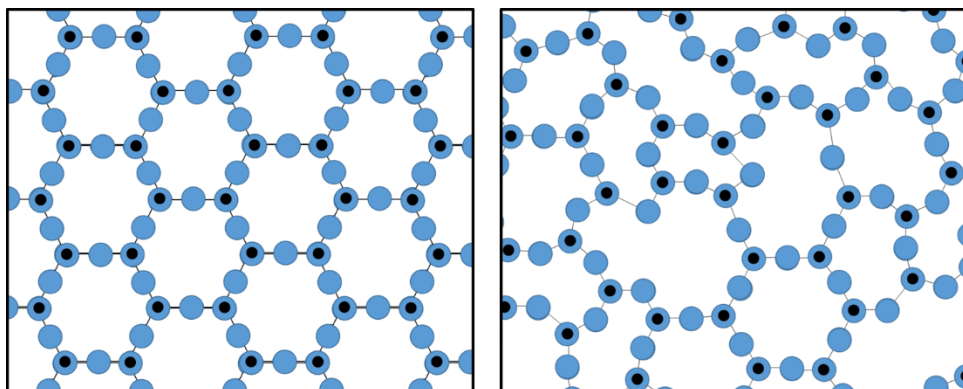
Figure 1.8: Schematic compairing crystalline (left) and non-crystalline (right) material structures. The lack of order in the non-crystalline material structure is due to the restricted mobility of the compositional elements upon cooling.

Generally when a melt containing the compositional elements of a system is cooled, provided nuclei are present, then solidification will occur at a given temperature, termed the freezing point (T_f). This solidification proceeds through the formation of an ordered crystal lattice throughout the material's microstructure. The solidification of a material at T_f can be commonly identified by a discontinuous volume change attributed to the crystallisation process. However, it is possible in some materials to continue cooling a melt below T_f without crystallisation occurring. If a melt is able to be cooled below T_f without solidification, then no discontinuous volume change is observed and the liquid is said to be supercooled. Following supercooling there exists a point at

which the gradient of the specific volume-temperature curve reduces significantly to become equal to that of the corresponding crystalline material. This is termed the glass transition temperature (T_g) and represents the point at which the transformation from a supercooled liquid to a glass occurs (Figure 1.9) [90]. The cooling rate is, therefore, a critical factor in glass formation, if this is not high enough there may be enough time for crystallisation to occur within the melt. However, if performed rapidly using methods such as quenching, which is utilised in the current study, then it is possible for the melt to solidify without any trace of crystallisation throughout the microstructure.
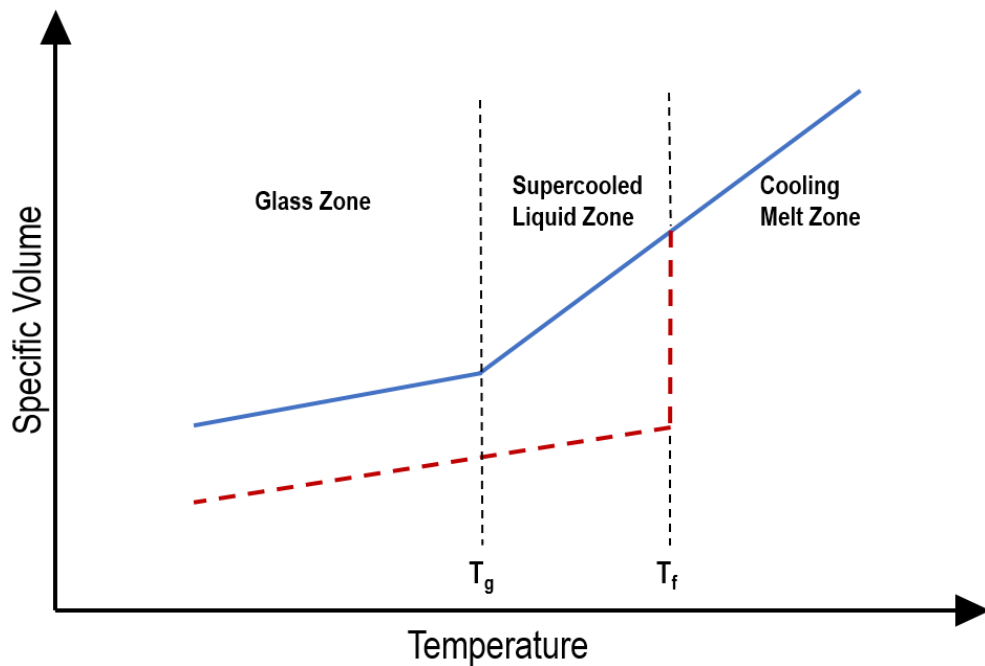
Figure 1.9: Plot illustrating the change in specific volume with temperature in the formation of a crystaline (red line) and non-crystalline (blue line) solid. Both the T_f and T_g points are indicated for the crystalline and non-crystalline traces, respectively.

1.4.2.1 The SiO₄ Tetrahedron

The materials studied in the current research stem from ionomer glass compositions traditionally used in dental applications [91]. These materials can be described as fluoro-alumino-calcium-silicates, therefore, the principal building block of an anionic silicate compound is perhaps the best place to start in understanding their complex structures. Silicates are the most abundant minerals in the earth's crust and are primarily composed of oxides. Conventionally, it is thought better to describe the structure of silicates in terms of their basic structural unit, the SiO_4 tetrahedron, rather than the unit cell approach. This basic building block is composed of a central

silicon atom which is bonded to 4 oxygen atoms, situated at each corner of the tetrahedron (Figure 1.10). Since we are considering this as the basic unit each oxygen carries a negative charge, hence, it being referred to as an anionic compound SiO_4^{4-}.
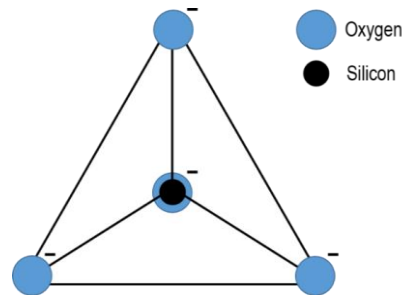
Figure 1.10: Schematic representation of the SiO_4^{4-} tetrahedron structure, the central silicon atom is bonded to four oxygen atoms situated in each corner of the tetrahedral structure.

Whilst there are detailed descriptions in literature relating to the physio-chemical aspects of the tetrahedral structure, a brief summary of the key factors is given below:

- The bond angle between two oxygen atoms is 109° 28´.
- Si-O bond distance is 1.6Å.
- The edge length of a SiO_4^{4-} tetrahedron is 2.62Å.

Since each of the 4 oxygen atoms requires an extra electron to achieve stability, numerous silicate structures arise from the differing ways in which the SiO_4^{4-} tetrahedral units can be combined in either one, two and 3D formations. These structures are typically characterised based on the number of bridging oxygen's or degree of polymerisation between respective tetrahedral units, Table 1.1 gives an overview of these classifications [89].

Type of Silicate	Name	Anion Complex	Bridging Oxygens	Si:O Ratio
Island	Nesosilicates	$[SiO_4]^{4-}$	0	1:4
Group	Sorosilicates	$[Si_2O_7]^{6-}$	1	1:3.5
Ring	Cyclosilicates	$[SiO_3]^{2-}$	2	1:3
Chain	Inosilicates	$[SiO_4]^{2-}$	2	1:3
Layer	Phyllosilicates	$[Si_2O_5]^{2-}$	3	1:2.5
Network	Tectosilicates	$[SiO_2]$	4	1:2

Table 1.1: Summary of silicate crystal structures arising from the different ways in which the tetrahedral units can be combined.

From Table 1.1 it can be seen that silicon dioxide, or silica (SiO_2) represents a 3D network silicate (4 bridging oxygen's, 1:2 Si:O ratio), in which each corner oxygen atom of the SiO_4 tetrahedra is shared with an adjacent tetrahedral unit. Therefore, the material network formed is electrically neutral and stable; this stable network forms the basic model for which we can expand our knowledge and understanding of glass structure theory.

1.4.2.2 Basic Principals of Glass Formation

Goldschmidt's Criterion

One of the earliest contributions to the current understanding of glass formation was made by Goldschmidt in 1926. Goldschmidt's Criterion represented one of the first attempts to identify characteristics common to glass forming oxides. His criterion relates the unit cell co-ordination number (the number of anions immediately surrounding the cation) of a given crystal structure to the relative size ratio between the cation and anion radii. Hence, the criterion states that for a cation to have a co-ordination number of 4 the ratio of the cation radius (r_c) to the anion radius (r_a) must be between 0.225 and 0.414. The fulfilment of this criterion maintains that the oxygens take up positions at the corners of the tetrahedral structure surrounding the cation. This is demonstrated in SiO_2 for which $r_a : r_c = 0.28$, hence, allowing the formation of the SiO_4 tetrahedron network (Figure 1.10). Goldschmidt observed this tetrahedral crystalline formation for a number of glass forming oxides, including P_2O_5 which is utilised in the glass composition of the current study. This criterion was, therefore, proposed to be a prerequisite by Goldschmidt for glass forming ability.

Zachariasen network theory

Following from the work of Goldschmidt came one of the most recognised theories of glass formation used to date, the Zachariasen network theory. This theory proposed by Zachariasen in 1932 was built upon the observation that though a good indication of glass forming ability could be attributed to Goldschmidt's criterion, it was not an absolute method, as some basic oxides did not conform to the rules [92]. For example BeO, though having a radius ratio permitting of the tetrahedral structure, cannot be obtained in the glassy state [93]. Zachariasen postulated that the interatomic forces within a glass must be similar to those in the equivalent crystalline material and that as a consequence the atoms of the glass structure must also be connected in a 3D network, although it is clear from a thermodynamic perspective there must exist an energy difference between the glassy and crystalline state, with the glass system possessing a higher free energy. This energy difference must be small as a substantial difference would act as a driving force to

convert the amorphous network into the organised crystalline form. This led Zachariasen to the conclusion that the co-ordination number of the cations in the glass system must be the same as that in the crystalline form. Given that XRD data has demonstrated that the network within glass is not periodic in nature, it is believed that there is sufficient distortion of the bond angles to represent a random network structure, however, the individual units of this structure are proposed to be practically identical to that of the regular crystal lattice (Figure 1.8) [94].

Based on these principals Zachariasen proposed a set of criteria further to those of Goldschmidt's that basic oxides must satisfy in order to form a glass network, i.e. glasses formed from simple binary compounds, such as, SiO_2 and P_2O_5:

1. An oxygen anion should not be bonded to more than two cations.
2. The number of oxygen anions around a given cation will be small.
3. The polyhedral elements must only share corners and not faces or edges.
4. At least three corners of each oxygen polyhedral element should be shared.

Therefore, should any basic oxide meet the criteria listed above they are capable of forming a glass network when cooled from a melt and are as such referred to as 'network forming oxides' and the oxygen's that link the cations are known as 'bridging oxygen's'. The more bridging oxygen's present, the greater the crosslink density of the glass. Though this represented a great leap forward in our understanding of an oxide's ability to form a glass the basic nature of the oxides to which it relates is far removed from the complex glass systems commonly examined. For example the parent glass studied in the current work contains the network forming oxides SiO_2 and P_2O_5 but it also includes compounds such as Al_2O_3, CaO and CaF_2. Therefore, Zachariasen defines two further forms of oxide and their influence and function within the random network structure. These are the network modifying oxides and the intermediate oxides.

The modifying oxides, such as CaO utilised in the current study, act to disrupt the glass network by introducing non-bridging oxygen's as the Si-O-Si bonds are broken. This occurs due to the oxygen anions introduced to the network by the modifying oxide taking up a position within a tetrahedral structure that would have previously been the link between two adjacent tetrahedral cations. These oxygen ions carry a partial negative charge and are connected to the glass network at one end only. The resulting network is looser and by decreasing the connectivity a larger flexibility of the structure is obtained. This as consequence leads to lower values for both T_g, T_f and the viscosity of the glass which get less as the cross linking density is reduced [94].

The modifying oxide cations take up positions within the interstices of the random network, as illustrated in the example relating to the addition of CaO to the SiO_4 tetrahedral network (Figure 1.11).
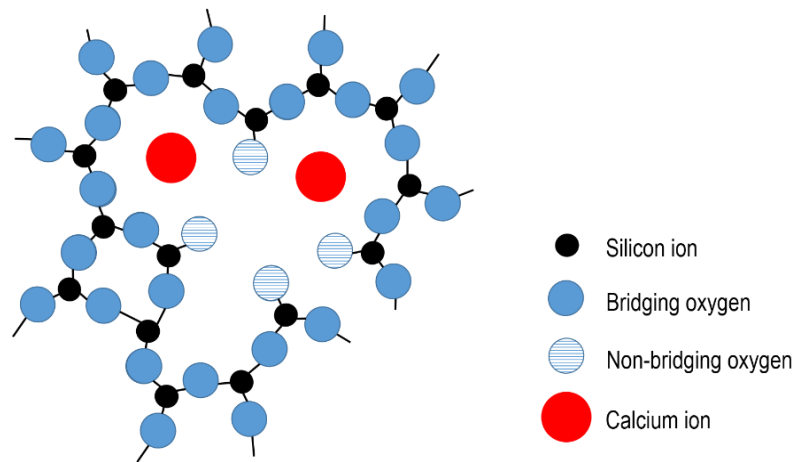
Figure 1.11: Illustration of a modifying oxide effect on a continuous glass network structure. Si-O-Si bonds are broken by the addition of oxygen anions to the glass network, the modifying oxide cations then take up positions within the interstices of the random network.

In the case of intermediate oxides, this is an oxide that would not be deemed able to form a glass network independently, however, it is capable of taking up a position within another network. In this instance Al_2O_3 used in the current system provides a good example. The Al^{3+} cation is capable of taking up either a six or four fold co-ordination number with oxygen, therefore, in a SiO_4 tetrahedral network the Al^{3+} cation can be substituted in for a Si^{4+} cation. This being the case an additional unit positive charge is also required to maintain electro-neutrality of the network. This can be provided by divalent or univalent cations present in the interstices of the glass network at a ratio of 1:1 or 2:1 with AlO_4 respectively. An example of an Al_2O_3 intermediate oxide in an SiO_4 network is illustrated below (Figure 1.12).
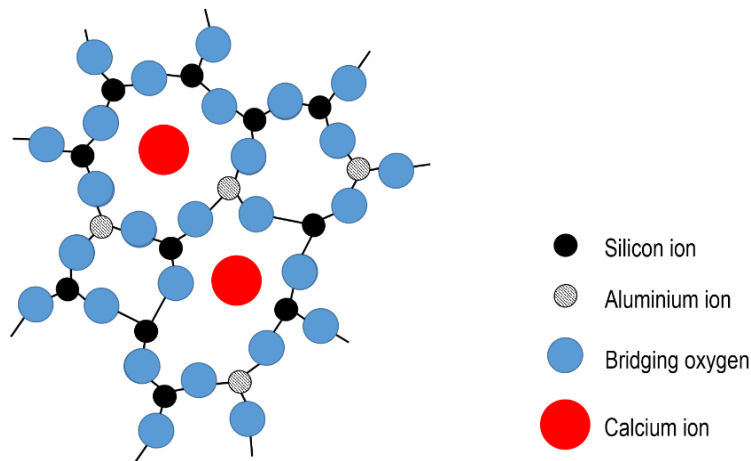
Figure 1.12: Illustration of an intermediate oxide effect on a continuous glass network structure. The Al^{3+} cation is capable of taking up four fold co-ordination with oxygen, replacing a Si ion within the structure. This leaves an additional unit of positive charge which is balanced by the cations present in the interstices.

1.4.3 Definition of Glass-Ceramics

Glass-ceramic materials possess a fine-grained polycrystalline structure which is formed through the heat treatment of a suitable amorphous parent glass composition to undergo controlled nucleation and crystal growth. This is in contrast to a traditional ceramic in which the crystal structure comes from the preparation of a starting composition and further processing to induce solid state reactions [95]. Although, glass-ceramics are able to reach high degrees of crystallinity between 50-90%, varying amounts of a residual glassy phase remain present within the structures. However, due to the precipitation of the crystal phase/phases within the material and subsequent ion depletion, the residual glass composition can differ vastly from that of the original parent glass [94]. It is as a consequence of the inherent highly viscous nature of glass that the atomic rearrangements which facilitate crystal growth take place relatively slowly upon heating. This considered along with the fact that viscosity increases rapidly on cooling lends to the high degree of control that can be achieved over the crystallisation present in a glass-ceramic via heat treatment profile selection. Hence, glass-ceramics are distinguished from glasses by the presence of major amounts of crystalline phases as glasses are by definition amorphous and non-crystalline.

1.4.4   Evolution of Glass-Ceramics

Although the ability to crystallise or devitrify a glass composition when treated at a sufficient temperature for a given time period has long been known, the practical application of this process is relatively recent from a materials science perspective. The discovery and some early work on glass-ceramics is attributed to a French chemist, Réaumur in 1739, who showed that glass bottles when packed in a mixture of sand and gypsum produced opaque porcelain like materials following heating for several days. However, due to the lack of control able to be achieved over the heat treatment regime at the time the components suffered low mechanical strength and high geometric distortions. It was not until the 1950's that S. D. Stookey of the Corning Glass Works developed, through controlled heat treatment, a material regarded as the first true glass-ceramic [93]. These materials had significantly greater mechanical strength than the parent glass and suffered no geometric distortion with only minor dimensional changes during processing. These superior mechanical properties of glass-ceramics evolve due to the apparent fully dense nature of the final components, with a lack of porous voids (defects). The presence of many small crystals throughout the structure also acts as a mechanism to prevent crack growth as it is arrested at grain boundaries. Today the range of glass-ceramics and their applications are extremely broad as the only prerequisite to their formation is the ability to form a glass and control its crystallisation [96, 97].

1.4.5   The Glass-Ceramic Production Process

The glass ceramic production process first requires the development of a homogeneous parent glass component of the desired geometry. This component then undergoes ceramming via subjection to a controlled heat treatment process, traditional two stage glass-ceramic heating regimes are carried out as follows:

1. Nucleation phase; the component temperature is raised to that at which crystal nuclei form within the glass structure.

2. Crystal growth phase; the temperature is raised further to allow for ion mobility and subsequent crystal growth upon the nuclei.

The rate at which the temperature is raised can lead to temperature gradients resulting in fracture, however, it is far less significant in powders and small particle sintering where rates of

between 10 to 20 °C/min are typically used. Once the material reaches the dwell temperature for the crystal growth phase, termed the upper crystallisation temperature, rapid crystal growth can occur in the absence of any deformation due to softening of the residual glass phase. Slow cooling of the material is also preferred as this allows for viscous flow of the residual glass and subsequent stress relaxation, a typical glass-ceramic heating regime is shown below (Figure 1.13).
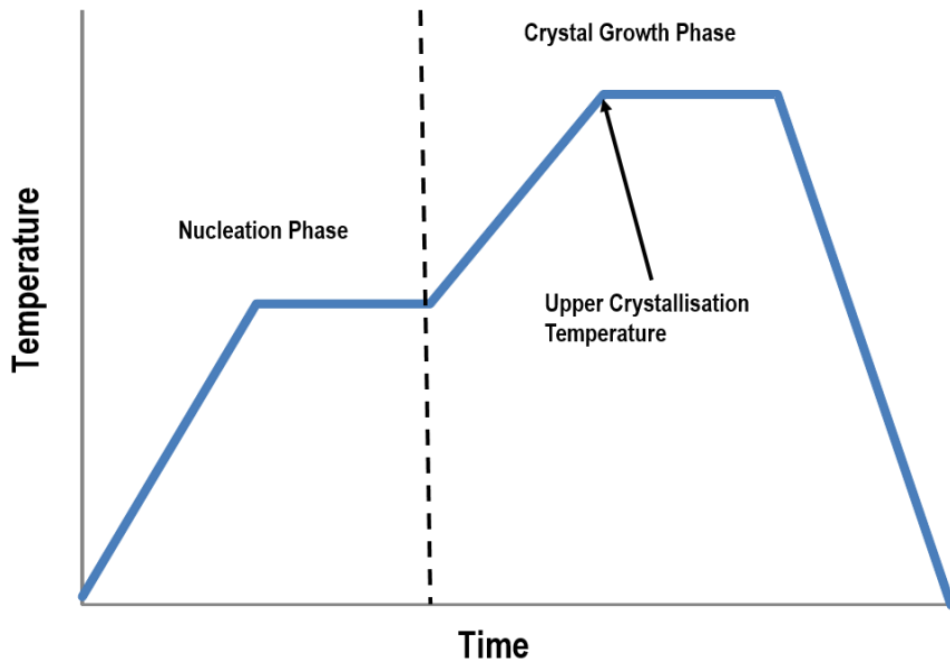
Figure 1.13: Typical two stage heating regime for glass-ceramic components. The two platous represent both the nucleation phase and crystal growth phase respectively.

1.4.6   Nucleation and Crystallisation of Glasses

The glass-ceramic production process relies equally upon both the nucleation and crystallisation phases as a function of the parent glass heat treatment regime. It is, therefore, important to have a basic understanding of the theory governing each of these processes phases. Particularly as they themselves are inter-related, given that crystallisation is governed by both nucleation density and crystal growth. There are two ways in which a glass can nucleate and subsequently crystallise; via either homogeneous nucleation or heterogeneous nucleation, each of which will be covered in basic detail below.

1.4.6.1 Homogeneous Nucleation

For true homogeneous nucleation to occur the melt must be free of all foreign material with the potential to act as sites that would preferentially lead to heterogeneous nucleation (e.g. dust particles), though this is extremely difficult to achieve or prove [93, 98]. Hence, homogeneous nucleation represents a condition in which the nuclei are formed from constituent ions of the parent glass phase.

The drive to form nuclei and subsequently crystallise is provided by the associated reduction in the free energy (G) of the crystalline phase in comparison to that of the melt. This free energy change (ΔG) occurs due to the higher degree of order, entropy, associated with the crystalline phase. At the equilibrium T_f both the crystalline and melt phases have equal G, therefore, no phase change will occur. However, as the melt cools ΔG increases as the free energy per unit volume of the solid phase (G_{vs}) falls below that of the liquid phase. Therefore, the ΔG associated with the ordering of the amorphous phase during the nucleation process can be given by Equation 1.1 when a spherical shape is assumed for the nucleating particle. Where r is the radius of the nucleus.

$$\Delta G = -\frac{4}{3}\pi r^3 \Delta G_{vs}$$

Equation 1.1

However, in opposition to this drive towards a lower G state is the positive energy required to overcome the surface tension of the surrounding environment within the melt. Therefore, the ΔG associated with an enlarged spherical crystalline nucleus against the surface tension of the surrounding environment is given in Equation 1.2. Where σ is the surface tension and r the radius of the nucleus.

$$\Delta G = 4\pi r^2 \sigma$$

Equation 1.2

Therefore, the total ΔG associated with the nucleation of a crystalline phase may be given as the sum of the two energy terms previously determined, Equation 1.3 .

$$\Delta G = -\frac{4}{3}\pi r^3 \Delta G_{vs} + 4\pi r^2 \sigma$$

Equation 1.3

If we then plot the free energy of nucleation as a function of the nuclei radius we can observer the maxima point of the curve, which relates to critical values for both free energy and nuclei radius, denoted ΔG^* and r^* respectively (Figure 1.14). If the nuclei radius is below r^* then it is unstable and liable to re-enter solution, however, if it is equal to or greater than r^* then it is regarded as stable. These nuclei will cause an associated reduction in ΔG on propagation, maintaining that growth is favourable.
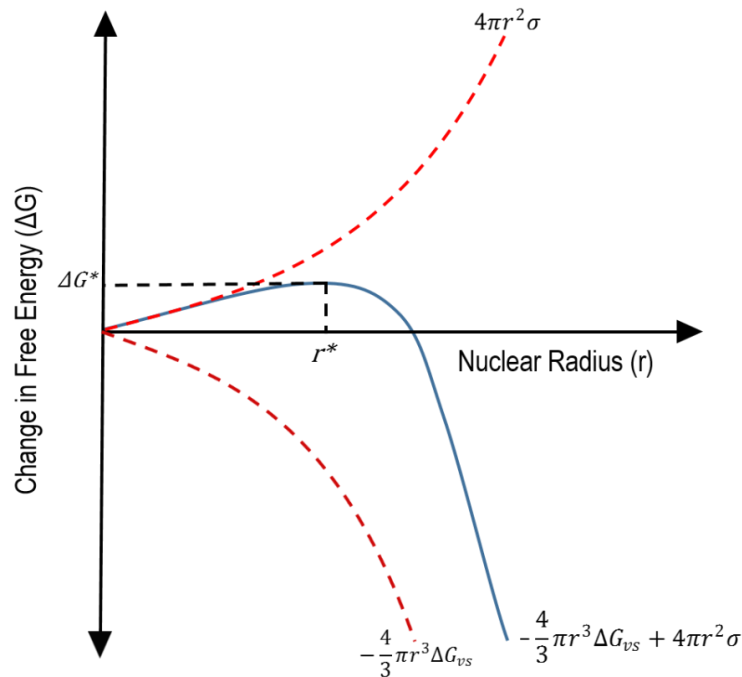
Figure 1.14: Plot of free energy against nucleus radius, indicating the maxima at which the critical radius (r*) and associated free energy (ΔG*) are observed.

However, it is important to note that ΔG^* is itself a function of the degree of undercooling (ΔT) of the melt. Hence, as the temperature (T) approaches the melting temperature (T$_m$) for a given composition the degree of $\Delta T \rightarrow 0$, Therefore, ΔG^* and r^* become infinitely large and no nucleation will occur. Also, it is important to consider that for a viscous liquid, such as the undercooled melt, as ΔT increases there is an ever increasing activation energy to overcome in facilitating the diffusion of component building blocks of the nucleus from within the homogeneous melt to the site of nucleation, termed the enthalpy of activation (ΔG_D). This being the case, statistical techniques have been employed to predict I, the rate of homogeneous nucleation (Equation 1.4). Where, A is a constant, ΔG^* is the free energy of nucleation, k is Boltzmann's constant and T is absolute temperature.

$$I = A \exp \left[\frac{-\Delta G^* + \Delta G_D}{kT} \right]$$ **Equation 1.4**

Therefore, for a low level of undercooling there is little change in the volume free energy term, G_{vs}, leading to a significantly large ΔG^* and a subsequently low rate of nucleation. With increasing amounts of undercooling G_{vs} increases and so ΔG^* becomes similar to ΔG_D in magnitude; this leads to the regions for which the greatest nucleation rates are observed. As the supercooling progresses the viscosity increases rapidly and ΔG^* becomes insignificantly small in comparison to ΔG_D and the nucleation rate subsequently diminishes. Therefore, as crystallisation proceeds within the supercooled liquid it is governed by the rate of nucleation (I) and crystal growth as a function of temperature. In order to generate the largest number of crystals within the material, nucleation should then be carried out as close as possible to the temperature at which the maximum I occurs [93, 94, 98].

In the nucleation of supercooled liquids there also exists a region known as the metastable zone. This zone represents the temperature range within which the melting temperatures for the exceptionally small nuclei are considerably below that of the bulk material. Hence, the nuclei are unable to be sustained within the material and fall back into solution. However, crystallisation can still occur within the metastable zone provided the melt is seeded (heterogeneous nucleation). Figure 1.15 below demonstrates graphically a typical relationship between both nucleation rate (**I**), the rate of crystal growth (**U**) and decreasing temperature.
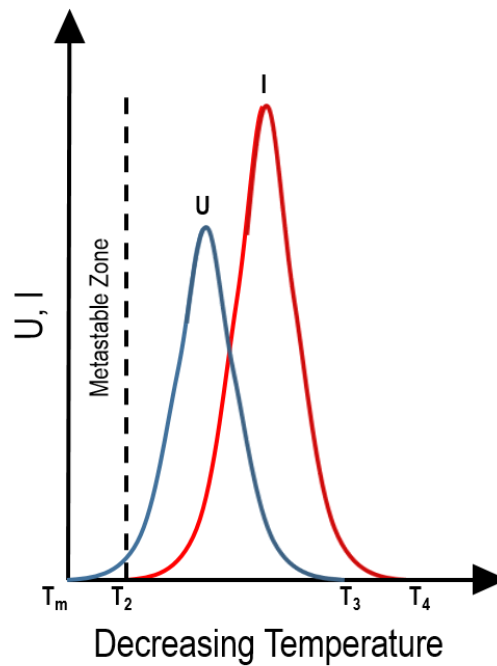
Figure 1.15: Nucleation (I) and crystal growth rate (U) as a function of decreasing temperature. Note that the critical region for crystal growth lies between T_2 and T_3 and the metastable zone exists between T_m and T_2.

1.4.6.2 Heterogeneous Nucleation

Heterogeneous nucleation refers fundamentally to nucleation of a phase within a material that is catalysed by the presence of a pre-existing / foreign surface (e.g. container surface, added particles, dust). The heterogeneous nucleation mechanism was first proposed and subsequently demonstrated by Turnbull in the 1950s. He observed that when a material was separated into many small droplets the maximum degree of undercooling achievable was significantly increased, however, there were always some droplets that nucleated before reaching that maximum point [99]. This is explained by the fact that the maximum degree of undercooling reached was in fact representative of the true limit set by the purely homogeneous mechanism; however, those droplets that nucleated prior to this contained foreign bodies that act as catalysts to reduce the energy barriers to nucleation and allowed the process to advance at a lesser degree of undercooling. We should also consider that had the material been treated as a bulk and not as droplets then the degree of undercooling would be limited by the heterogeneous nucleation mechanism, as only one nucleation event is required to crystallise the entire melt.

The way in which the heterogeneous nucleation mechanism proceeds can be explained if we consider first what we already know in relation to the homogeneous mechanism, in that there exists a critical radius which must occur before the nucleus becomes stable and crystal growth can proceed, and that this is itself governed by the degree of undercooling present. However, the forming nucleus (embryo) does not need to be a complete sphere; a hemispherical nucleus on a surface can reduce the free energy for heterogeneous nucleation to occur. Heterogeneous nucleation will proceed given that there is a strong enough interfacial bond strength between the substrate in question and the nucleating melt. This can be determined scientifically by measuring the contact angle of a forming crystal nucleus on a foreign substrate (Figure 1.16). Hence, for $\theta <$ 180° heterogeneous nucleation will occur but will not for $\theta = 180°$ [94].
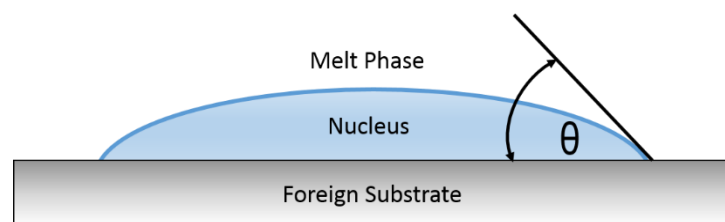
Figure 1.16: Schematic of early stage heterogeneous nucleation with contact angle identified. This is representative of a nucleus forming on a foreign substrait, if the contact angle is less than 180° then hetrogeneous nucleation can occur.

1.4.7   *Summary*

It is clear from the theory controlling glass and glass-ceramic material formation that there are key parameters to consider in the heat treatment and production process. These are:-

- The relationship between oxides within the parent glass structure and the subsequent crystalline material composition;
- The determination of optimal processing parameters, such as nucleation time and temperature;
- The identification of the principle parent glass composition required to produce the necessary crystallisation and enhanced structural properties through defined heating regimes.

1.5 *Aims and Objectives*

A review of the literature has demonstrated a clear clinical driver for an effective tissue engineered approach in the treatment of degenerative disc disease. The vertebral EP represents the principle nutrient pathway into the IVD tissues from adjacent vertebrae. Therefore, this biological function in any scaffold developed should be regarded of equal importance to that of the bioactive material characteristics and the subsequent cellular response it promotes.

1.5.1 *Study Aim*

To develop a bioactive construct that facilitates the natural function of the vertebral EP tissue interface, using a novel glass-ceramic substrate, capable of sustaining osteogenesis of primary human MSCs.

1.5.2 *Objectives*

1. Reproducibly manufacture a glass-ceramic material suitable for further development and characterisation towards providing a substrate scaffold for tissue engineering applications.

2. Characterise the glass-ceramic material further to demonstrate the full range of both compositional and mechanical properties obtainable in relation to proposed function.

3. Demonstrate the osteogenic differentiation capacity of primary human MSCs on the glass-ceramic substrate to determine potential for bone replacement application.

4. Develop a comparative test methodology to assess the biological function of natural EP tissue against that of *in vitro* tissue engineered constructs.

Chapter 2: General Methods

This chapter is dedicated to outlining those methods which are common across multiple sections of this thesis. Due to the highly interdisciplinary nature of the overall investigation, the more specific methods are presented in their corresponding chapters.

2.1 *General Material Manufacture & Analysis*

2.1.1 *Glass Powder Batch Production*

The apatite-mullite parent glass was produced in 500g batches, based on the $4.5SiO_2 \cdot 3Al_2O_3 \cdot 1.6P_2O_5 \cdot 3CaO \cdot 2CaF_2$ (molar ratio) castable glass system, LDIG105. To calculate the required mass of each reagent the molar ratios were multiplied by the respective molar masses, this was then multiplied by the scaling factor 0.443 to give the required mass (Table 2.1). The scaling factor was determined by dividing 500g batch mass required by the sum of the total masses of each reagent, 1127.744g.

Reagent	Molar Ratio	Molar Mass (g)	Total Mass (g)	Required Mass (g)
SiO_2	4.5	60.08	270.36	119.9
Al_2O_3	3	101.96	305.88	135.6
P_2O_5	1.6	141.94	227.104	100.7
CaO	3	56.08	168.24	74.6
CaF_2	2	78.08	156.16	69.2

Table 2.1: Masses of glass reagents needed to calculate the required mass of each for production of a 500g batch of LDIG105.

The only reagent not provided in the specified form was CaO, instead this was obtained by the thermal decomposition of $CaCO_3$ during the heating process. The equation for carbonate decomposition is shown below (Equation 2.1):

$$CaCO_3 \xrightarrow{heat} CaO + O_2$$

Equation 2.1

In order to account for the carbonate decomposition the starting mass of $CaCO_3$ was calculated to maintain the correct ratio of CaO in the final glass composition. This was obtained by dividing the required mass of CaO by its molar mass to give the moles of CaO needed, 1.33. This was then multiplied by 100.1, the molar mass of $CaCO_3$. Therefore, the starting mass of $CaCO_3$ required is

133.1g and the total reagents required to produce a 500g batch of LDIG105 are determined (Table 2.2).

Reagent	SiO_2	Al_2O_3	P_2O_5	$CaCO_2$	CaF_2
Required Mass (g)	119.9	135.6	100.7	133.1	69.2

Table 2.2: Required masses of each reagent for the production of a 500g batch of LDIG105

Reagents were weighed out on a digital balance (Sartorius Roughing balance, PT3100) and added to a clean plastic container with an agitating iron bar inside. The container was then placed onto a rolling machine for 1 hour to homogenise the reagents. The mixture was then transferred to an alumina crucible which itself was placed into a larger mullite crucible with lid. The reagents were then transferred to the furnace (1600°C, I Temp 15/16, Pyrotherm) at 800°C. The temperature was then raised at 15°C/min to 1450°C and held for 2hrs. Following heating the glass melt was shock quenched by slow pouring into a cold water tank to produce a glass frit (Figure 2.1). The frit was then collected using a suction pump and sieve, and allowed to dry for 24 hours in a drying cabinet to remove all moisture.

Figure 2.1: Quenching of the melt in water following heating to 1450°C to produce glass frit.

The frit was subsequently ground using a Gy-Ro Rotary Mill, 50g batches of frit were ground sequentially for 120 seconds each using a 250ml puck and mill. Finally the ground particles were separated into 0-45µm, 45-90µm, 90-125µm, 125µm-1mm and > 1mm fractions using a sieve stack and shaker (Octagon Digital) for 100 minutes. Six batches were independently produced in this manner prior to further analysis.

2.1.2   Post Processing & Sintering

In all instances scaffolds were sintered in graphite moulds which were filled with parent glass particles under minimal agitation and no compaction. In all cases lids were also added to minimise any variation in the local surface atmosphere during the heat treatment process. With the exception of chapter 3 all subsequent chapter scaffold components were sintered in a programmable furnace (UAF 15/5 furnace, Lenton Thermal Designs Ltd; Eurotherm 818 controller-programmer). The glass particle filled moulds were placed straight into the pre-heated furnace at 1200°C and held for 1 hour, after which the scaffolds were allowed to cool at the natural rate of the furnace (Figure 2.2). This regime is referred to throughout the thesis as heating regime A (hrA).
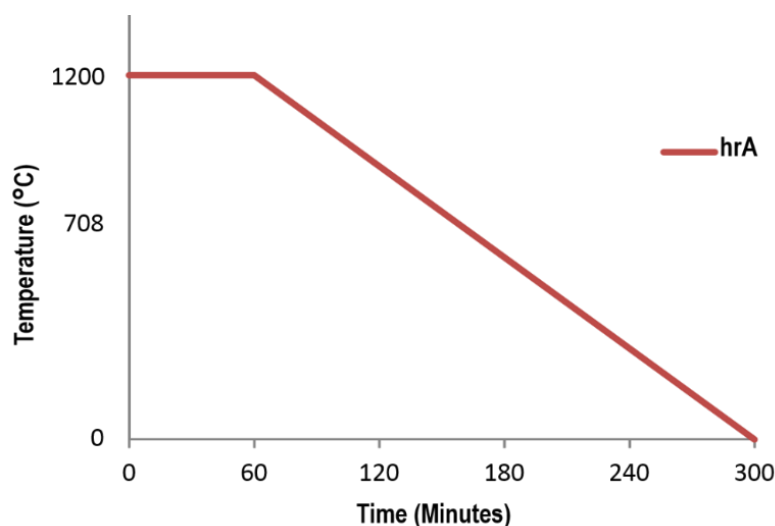
Figure 2.2: Graph illustrating the heating regime, hrA used to sinter the scaffold components in all chapters with the exception of chapter 3.

2.1.3   Differential Thermal Analysis

All differential thermal analysis (DTA) was performed using a modified Stanton Redcroft 673-4 to determine Tg, and peak crystallisation temperature (Tp) data. Platinum-rhodium alloy crucibles were used to hold approximately 0.15g of the glass sample and Al_2O_3 reference material respectively. Experiments were carried out at an initial heating rate of 15°C/min up to 400°C at which point the heating rate was reduced to 10°C/min to a final temperature of 1200°C. Data was only logged from 400°C to 1200°C, between which all significant heating events were assumed to have occurred.

2.1.4   X-ray Diffraction

Unless otherwise stated X-ray diffraction (XRD) tests were carried out using a D8 powder diffractometer (Bruker) with a copper anode producing an X-ray wave length of 1.5406Å. Samples were ground in a pestle and mortar and the powder examined using a 0.02° step size between 10° and 70° with a step time of 9.4 seconds. The resulting trace was then cross referenced with standards from the International Centre for Diffraction Data (ICDD), using crystallographica Search-Match V2 software in the Leeds Dental Institute.

2.2 General Imaging

2.2.1   Scanning Electron Microscopy

In preparation for scanning electron microscopy (SEM) in cases where scaffolds were seeded with a cellular component, the constructs were first fixed in 2.5% glutaraldehyde in 100mM phosphate buffer at 4°C overnight. Following fixation, samples were then dehydrated via a graded ethanol series composed of 30 minutes in 20, 50, 70, 90 and 100% ethanol. Finally, samples were subjected to 2 X 30 minute steps in 100% ultra-pure ethanol and one in hexamethyldisilazane (HMDS). Samples were then left sealed overnight in HMDS to dry in a desiccator.

Unless otherwise stated SEM of all samples was carried out under the following conditions. Samples were first sputter coated with gold-palladium at 15mA for 60 seconds in an argon atmosphere (Polaron range, SC7640), following which they were imaged on a Joel scanning electron microscope (JSM 6490LV) using secondary electron imaging.

2.3 General Cell Culture

2.3.1 Isolation and Culture of Human MSCs

The human MSCs used in the present study were isolated from the bone marrow of femoral heads (Harrogate District Hospital, Harrogate, UK) or knee condyles (Clifton Park Treatment Centre, York, UK) obtained with informed consent following routine joint replacement surgery. In the case of femoral heads the mononuclear cell fraction was isolated via density gradient centrifugation (Ficoll-Paque PLUS, GE Healthcare), this fraction was then seeded onto the surface of a T75 tissue culture plastic (TCP) flask in basal media (Dubecco's Modified Eagle Medium [DMEM] containing 10% foetal bovine serum, 100U/ml penicillin and 100µg/ml streptomycin). For MSCs isolation from knee condyles, samples were broken into bone fragments and placed into TCP treated Petri dishes in basal medium for up to 14 days, after which the adherent cell populations were also seeded into a T75 flask in basal medium. In both cases cells were allowed to settle for 4 days and then medium was changed every 3 days thereafter.

Passaging was carried out at 70% confluence and cells were detached using 0.05% trypsin and 0.02% ethlenediminetetraacetic acid (EDTA). Following the first passage, cells were seeded into T175 flasks at 1000 cells/cm^2. Cell culture was carried out at 37°C in a humidified atmosphere of 5% CO_2 and 95% air. All knee samples were shown to be positive for CD29, CD44, CD73, CD90, CD105, CD29, CD73 and negative for CD34 and CD45 by flow cytometry.

2.3.2 Osteogenic Differentiation Media

For osteogenic differentiation of MSCs basal medium was further supplemented with 50µg/ml L-ascorbic acid-2-phosphate, 5mM β-glcerophosphate and 10nM dexamethasone. This supplemented media was changed every 3 days throughout the culture time of the sample.

2.3.3 Chondrogenic Differentiation Media

MSCs under chondrogenic culture conditions were cultured in serum free DMEM supplemented with the addition of 100U/ml penicillin, 100µg/ml streptomycin, 50µg/ml L-Ascorbic acid-2-phosphate, 100nM Dexamethasone, 40µg/ml L-Proline (which is added fresh prior to each media change), 20ng/ml recombinant human transforming growth factor β3 (TGF- β3, NIBSC, cat no: 98/608) and 1% serum substitute ITS$^+$ premix (BD Biosciences, Cat no: 354352). This supplemented media was changed every 3 days throughout the culture time of the sample.

2.3.4   Osteochondral Media Supplementation

Samples consisting of multiple MSC elements having separately undergone osteogenic and chondrogenic pre-differentiation an requiring subsequent co-culture were treated with a cocktail medium designed to maintain both osteogenic and chondrogenic lineages. This osteochondral medium consisted of DMEM supplemented with 2% FBS, 50µg/ml L-Ascorbic acid-2-phosphate, 100nM Dexamethasone, 40µg/ml L-Proline (which is added fresh prior to each media change), 1% serum substitute ITS+ premix and 5mM β-glcerophosphate. This supplemented media was changed every 3 days throughout the culture time of the sample.

2.4 General Molecular Techniques

2.4.1   TRIzol Extraction of RNA

Samples were washed twice in phosphate buffered saline (PBS) and placed in a 5ml bijoux to which 1ml of TRIzol (Ambion, RNA) was added. Samples were then incubated for 5 minutes, 2 of which were spent under sonication on ice (Sonoplus HD 2070; Bandelin). The sample lysates were then transferred to 1.5ml micro-centrifuge tubes and stored at -80°C prior to any further analysis.

Following defrosting for 5 minutes at room temperature 0.2ml of chloroform was added to each sample and vortexed vigorously for 15 seconds. Following a further 5 minutes incubation at room temperature samples were centrifuged at 12000g and 4°C for 20 minutes (Eppendorf, 5415R). The RNA containing upper aqueous phase of the lysate was then transferred to a new centrifuge tube being careful not to disturb the interface. Once transferred 0.5ml of 100% isopropanol was added to each sample and vortexed briefly. Samples were then incubated for 30 minutes at 4°C in order to precipitate out the RNA from solution, which was then pelleted by centrifugation for 15 minutes at 12000g and 4°C. The isopropanol was then carefully removed and 1ml of 70% ethanol added to wash the pellet, followed by another centrifugation at 12000g for 5 minutes at 4°C. The ethanol was then removed and the pellet allowed to air dry for 3 to 5 minutes after which the pellet was re-suspended in 12µl of RNase/DNase-free H$_2$O.

2.4.2   Genomic DNA Digestion

DNAse digestion (DNA-free, Ambion; AM1906) was performed to eliminate any genomic DNA left in the samples. Firstly 1.2µl of DNAse I buffer and 1µl of DNAse I were added to each sample

and incubated for 30 minutes at 37°C. Next 1.4µl of DNAse inactivation reagent was added to each sample followed by a further 2 minutes incubation at room temperature. The samples were then centrifuged at maximum speed for 1 minute to pellet the inactivation reagent and the DNAse treated RNA transferred to a fresh tube. RNA concentration was subsequently quantified using a Nanodrop spectrophotometer (Nano Drop, ND-1000).

2.4.3   cDNA Synthesis

For cDNA synthesis a mixture containing 0.5µg of total RNA, 1µl Oligo dt primer and 1µl of 10mM deoxyribonucleotide triphosphates was made up to 12µl for each sample with DNAse/RNAse free H_2O. This was performed in duplicate for each sample so that one mixture could be used in a no reverse transcriptase (RT) controls for genomic DNA contamination. Following mixing samples were incubated for 5 minutes at 65°C then chilled on ice for a further 2 minutes. Separately a master mix was prepared containing 4µl of 1st standard buffer, 2µl of 0.1M DTT and 1µl of H_2O per sample. From the master mix 7µl was added to each sample, after which they were incubated for a further 2 minutes at 42°C prior to adding 1µl of SuperScript II RT to the relevant samples and 1µl of H_2O to the no-RT controls. The cDNA synthesis was then carried out by incubating the samples for 1 hour at 42°C, followed by a further 15 minutes at 70°C to inactivate the RT. Final cDNA concentrations were then quantified by Nano Drop and samples stored at -20°C prior to further use.

2.4.4   Relative Quantification

The SYBR green (Power SYBR Green, Applied Biosystems) fluorescence detection method was used to perform the real-time polymerised chain reaction (PCR) relative quantification analysis. Six osteogenic gene markers were investigated, alkaline phosphatase (ALP), Runx2, collagen alpha I (Col αI), osteocalcin (OC), osteonectin (ON), osteopontin (OP) and the housekeeping gene ribosomal protein subunit 27A (RPS27A) (Table 2.3). All primers have been previously optimised by absolute quantification for use in this manner and published in a peer reviewed journal [100]. For the analysis 5µl of 10ng/µl cDNA was added to a well containing 12.5µl of 2 X SYBR green master mix, 5.5µl DNAse/RNAse free H_2O and 2µl of the relevant primer pair mix (10µM each for both forward and reverse primers). The expression was analysed using the ABI 7000 system software (Applied Biosystems) with thermal cycling carried out at 95°C for 10 minutes followed by 40 cycles of 95°C for 15 seconds and finally 60°C for 1 minute. All samples were analysed in triplicate for three primary MSC lines, with gene expression levels calculated

using the $2^{-\Delta\Delta Ct}$ method. Briefly, the Ct value for each target gene was normalized to the Ct value of the housekeeping gene RSP27A at each time point, which was then normalized to the 24 hour sample expression levels in basal TCP conditions. The threshold levels were constant over all samples to allow for comparisons to be made.

Gene	Primer Sequence (5'-3')	Product Size (bp)	Accession Number
ALP	Forward GGGAACGAGGTCACCTCCAT Reverse TGGTCACAATGCCCACAGAT	67	NM_000478
Runx2	Forward AGTGATTTAGGGCGCATTCCT Reverse GGAGGGCGGCGTGGGTTCT	69	NM_001024630
Col αI	Forward CCTGCGTGTACCCCACTCA Reverse ACCAGACATGCCTCTTGTCCTT	84	NM_000088
Osteocalcin	Forward AGCAAAGGTGCAGCCTTTGT Reverse GCGCCTGGGTCTCTTCACT	63	NM_199173
Osteonectin	Forward CCTGGATCTTCTTTCTCCTTTGC Reverse ATCAGGCAGGGCTTCTTGCT	71	BC008011
Osteopontin	Forward ACCTGAACGCGCCTTCTG Reverse CATCCAGCTGACTCGTTTCATAA	66	BC022844
RPS27A	Forward TGGATGAGAATGGCAAAATTAGTC Reverse CACCCCAGCACCACATTCA	68	BC066293

Table 2.3: Osteogenic primer sequences used for real-time PCR analysis.

2.5 *Construct Histological Slide Preparation*

2.5.1 *Construct Fixation & Resin Embedding*

Following fixation in 2.5% glutaraldehyde in 100mM phosphate buffer at 4°C overnight samples were fixed in 100% ethanol. Samples were then resin embedded with Technovit 7200 VLC resin (Exakt Technologies, Cat No:5100) using the following series made up with 100% ethanol. Samples were first placed into 30% Technovit solution for 7 hours then transferred to 50% solution overnight. The following morning samples were transferred to 70% Technovit solution for 5 hours, followed by 100% for 2 hours. Finally samples were placed into a specialised container of 100% Technovit and placed under vacuum (Exakt 510, Dehydration and Infiltration System) overnight. In all instances where Technovit was used samples were incubated in the dark to prevent the resin from curing.

2.5.2 Construct Sectioning

Dehydrated and embedded constructs were placed into an embedding mould, three samples per mould, positioned on their sides. Technovit 7200 VLC resin was then poured into the mould until the samples were fully immersed. The mould was then positioned into a light polymerisation unit (Exakt 520, Light Polymerization Unit) and cured for 8 hours on a timer (Figure 2.3).
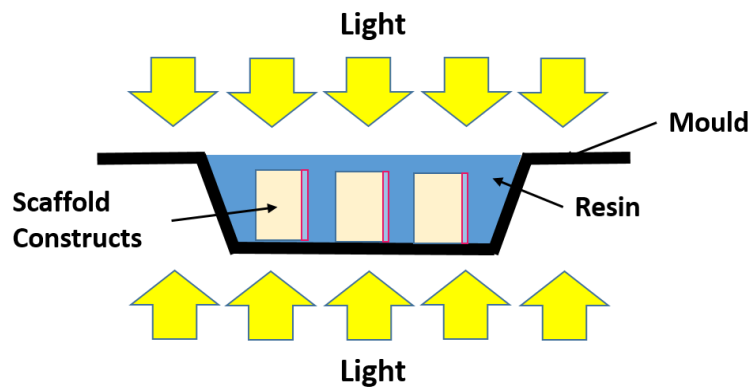
Figure 2.3: Light polymerisation of constructs submerged in Technovit resin.

Next the resin block was taken from the mould and any excess resin removed from the sample which was then placed into a second light curing box (Exakt 530, Re-infiltration Unit) overnight. Now completely cured the resin block was attached to the surface of a polymer slide, the slide surface was first roughened using a strip of coarse grinding paper and cleaned with 100% methanol. The resin block itself was also roughened with coarse grinding paper on the surface not previously in contact with the mould and cleaned with 100% methanol. Technovit 4000 cement (Exakt Technologies, Cat No:51090) was then made up in the fume cupboard as per the manufacturer's instructions. The cement was added to the roughened surface of the resin block and the resin block itself put into a precision press system (Exakt 402, Precision Adhesive Press), already containing the polymer slide, held by a vacuum to the top press surface. The top surface of the press was then brought down onto the cement toped resin block and locked in place for 10 minutes to produce an adhered slide resin block assembly (Figure 2.4, A). Once set the sample was removed from the press and placed into the exact bone saw system (Exakt 310, Band Cutting System). The sample was sectioned 1.7mm from the surface of the resin block in order to expose the central region of the scaffold constructs. This surface was then ground (Exakt 400, Micro Grinding System) and measuring control equipment used (Exakt AW 110) to ensure a level surface in relation the cement adhered slide (Figure 2.4, B). Next a second polymer slide was

adhered to the sectioned surface using Technovit 7210 VLC glue (Exact Technologies, Cat No:51100) by applying the glue to the sectioned surface and lowering the polymer slide into position within the precision press system. Once positioned the sample was held for 10 minutes under blue light in order to cure the glue (Figure 2.4, C). The sample was then transferred back to the bone saw and sectioned to provide a 400µm thick sample from the polymer slide surface. This sample was then placed back into the micro grinding and measurement control system and subjected to a series of grinding cycles starting from a low grit (600) and finally finishing with a high grit (4000) polished section with a thickness of approximately 40µm (Figure 2.4 D).
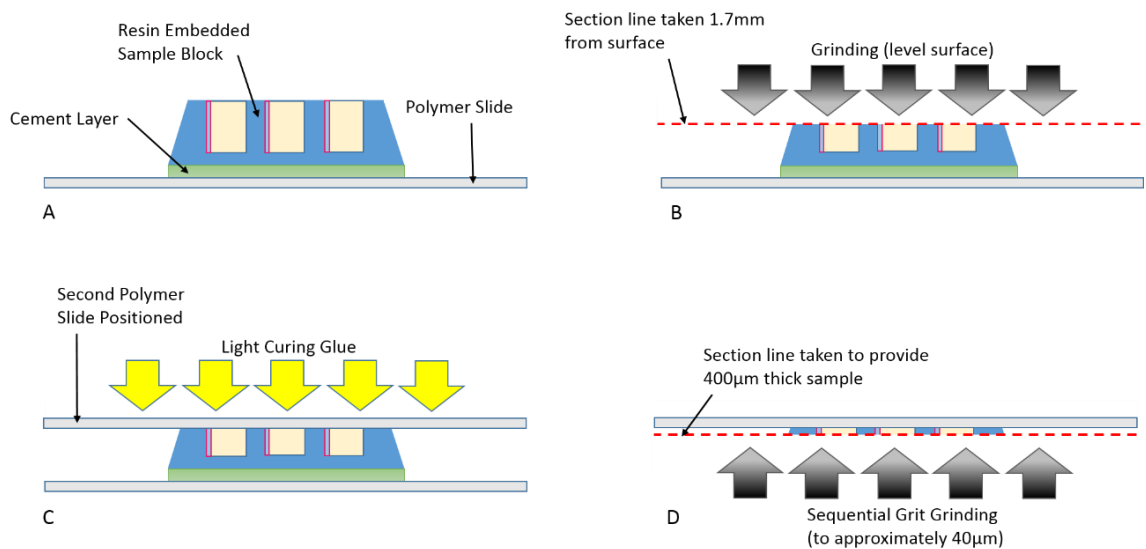
Figure 2.4: schematic representation of the process used to prepare resin embedded scaffolds for histological analysis.

Chapter 3: Bioceramic Scaffold Production

3.1 *Introduction*

Bioceramics are of great importance for bone replacement applications acting to alleviate pain and restore natural function to the body, which can be necessitated by multiple factors such as trauma, tumour or bone associated disease. These materials face extremely challenging prerequisites of being able to function within the corrosive environment of the body whilst undergoing continuous cyclic loading. This is particularly difficult in the case of ceramics as they are typically brittle by nature [101]. Bioceramics are generally characterised by their mode of interface with the host bone tissue, the four specific attachment types are summarised below (Table 3.1).

Implant Type	Mode of Attachment	Example
Nearly inert	Mechanical interlocking	Alumina, Zirconia
Porous	Porous ingrowth (biological fixation)	Hydroxyapatite, HA coated porous metals
Bioactive	Bonded interface (bioactive fixation)	HA, Bioactive glasses, Bioactive glass-ceramics
Resorbable	Natural tissue replacement	β-tricalcium phosphate

Table 3.1: The four traditional types of interfacial attachment seen between bioceramics and host tissues, with examples given in each instance.

No bioceramic should be considered totally inert, as all will elicit a non-specific immune system response due to initial tissue trauma [102]. On implantation of a nearly inert biomaterial, a non-adherent fibrous capsule develops around the component over time as the body attempts to isolate the perceived threat. Monolithic alumina is one example of a nearly inert bioceramic used widely in orthopaedic applications. In practice these components are commonly subjected to tight fits under compressive loading as any micro-motion at the site can cause thickening of the fibrous capsule leading to loosening and possible failure. To address the issues of micro-motion, porous ceramics were introduced to allow tissue ingrowth and greater interfacial areas, providing greater resistance to motion at the interface, termed biological fixation. Mineralised tissue replacement can also be achieved through the use of resorbable bioceramics, developed to dissolve over time following implantation and eventually be replaced with the host's natural tissue. Limitations surrounding this approach are that the compositions are only able to include those substances known to be metabolically stable, as not to cause chronic inflammation and/or pain for the patient.

Resorbable materials also pose the challenge of matching the resorption rate to that of new bone deposition, a factor that can vary greatly with patient factors such as age and health.

Current bioceramic research has placed substantial focus on materials of a bioactive nature, first defined by Hench and colleagues at the University of Florida in 1969 [103].

"A bioactive material is one that elicits a specific biological response at the interface of the material, which results in the formation of a bond between the tissues and the material."

The concept of bioactivity is classically thought of as an intermediate between the nearly inert and resorbable bioceramics. Initially glass compositions were coined as bioactive materials, 45S5 Bioglass® being the most notable and well characterised example. However, a lack of mechanical strength in clinical application of these materials led to the development of glass-ceramics through crystallisation of the parent glass compositions, as outlined earlier. This resulted in the introduction of many new materials, the most notable being the apatite wollastonite (AW) glass-ceramics developed by Kokubo *et al* in 1982, now commercially available as Cerabone® [104]. This material is composed of both apatite and wollastonite crystalline phases within a residual $CaO-SiO_2$ rich glass matrix. This structure provided a significant increase in the mechanical strength of the biomaterial, through the interlocking crystalline phases, whilst maintaining the ability to form a strong interfacial bond with natural bone. One other material developed for biomedical applications over the past 25 years is the apatite-mullite glass ceramic (AM-GC) under investigation in the current study. The AM materials were developed largely as a result of efforts to improve glass ionomer cements for restorative dental applications [105]. However, more recent efforts have identified compositions that crystallise to form both fluorapatite (FA) and mullite following heat treatment therefore illustrating a potential for a much broader scope of application, such as that of an EP substrate proposed in the current research.

3.1.1 *Apatite-Mullite Glass-Ceramic Development*

AM-GC was first developed as a consequence of research aimed at controlling the properties of ionomer glasses used for bone cement applications [91, 105]. It was demonstrated via studies on the $2SiO_2 \cdot Al_2O_3 \cdot CaO \cdot CaF_2$ glass system that fluorine loss during the melt process, through the formation of silicon tetrafluoride (SiF_4) and possibly aluminium triflouoride (AlF_3), led to the starting composition differing substantially from the final amorphous glass composition. However,

it was identified that the presence of the basic oxide, calcium oxide (CaO) as a substantial component eliminated the fluorine (F) loss [91].

In the first instance the AM-GC parent glass is considered a network of SiO_4 and AlO_4 tetrahedra with Ca^{2+} positioned in interstices throughout the network. Within this structure a Si^{4+} network forming cation is replaced with Al^{3+} giving the network a net negative charge. It is the presence of the Ca^{2+} network modifier that balances the charge and allows the structure to be maintained. With the addition of calcium fluoride (CaF_2) to the composition F^- takes up positions to form SiO_3F and AlO_3F producing non-bridging oxygens and fluorides throughout the network. This will act to reduce the overall cross linking density of the glass network and, hence, reduce Tg and possibly the Tp of the system. Also this addition causes the formation of the SiF_4 and AlF_3 responsible for fluorine loss during the melting process. It is important to balance the amounts of each of the components in order to minimise the release of fluoride, recognising that the calcium acts as both a source of positive charge to counteract the negative network charge induced by aluminium incorporation into the glass network and as a means of suppressing fluoride loss by charge balancing non-bridging fluorides in the glass network.

DTA of these glasses showed two crystallisation peaks, the first relating to Fluorite (CaF_2) and the second to anorthite ($CaAl_2Si_2O_8$). A further modification to the glass was then made by the addition of phosphate, this was due to reported increased bioactivity of ionomer cements containing high levels of phosphate [106]. Preliminary investigation into the glass compositions identified crystallisation of FA ($Ca_5(PO_4)_3F$) and mullite ($Al_6Si_2O_{13}$) phases following heat treatment. It was then thought that the addition of phosphate to the much more controlled glass systems mentioned previously would provide a suitable glass-ceramic for bone substitution as the presence of an appetite phase is highly desirable. The phosphate is believed to be incorporated into the network as a network forming ion. As phosphorus carries a plus five charge it can be charge compensated by alumina in the glass network, hence, P^{5+} is charge balanced by Al^{3+} taking up a four co-ordinate position in the network. It is this and the fact that the size of the $AlPO_7$ unit is similar to Si_2O_7 that lead to the belief that they may replace each other in the glass network [107].

These systems were found to crystallise as expected to FA and mullite following heat treatment. The apatite crystal structure, however, was found to differ from that identified in the commercial ionomer glass compositions. The new material apatite had a thin needle like structure with high

aspect ratio, similar to that found in bone and dentine as opposed to a squat hexagonal structure seen before [106]. Finally research was undertaken to determine the sole influence of fluorite content on the glass composition when the Ca:P ratio was maintained at 1.67, the stoichiometry of apatite. It was found that all glasses with fluorine content >2 for the $4.5SiO_2 \cdot 3Al_2O_3 \cdot 1.5P_2O_5 \cdot 3CaO \cdot 2CaF_2$ system exhibited a bulk nucleation via prior amorphous phase separation (APS) with no additional effect to the Tp's in the system, it was also found that for Ca:P ratios ≤ 1.5 surface nucleation would occur [108]. This considered all glass used in the present research is based on this system maintaining a fluorine content >2 and a Ca:P ratio of 1.56, greater than the 1.5 required in order for bulk nucleation to occur.

Recently, powdered AM-GC has been investigated for use in a selective laser sintering (SLS) production methods. In these studies 5% by mass of acrylic binder was used to produce a green part prior to sintering [109, 110]. Components with bend strengths of 6MPa were produced, however, these results were obtained using only 45-90µm glass particles and significant increases in bend strength up to 16.22MPa was subsequently achieved with the addition of varying percentages of <45µm particles.

3.1.2   Study Aim

In the current chapter the research aims to validate a suitable batch production process for the AM parent glass material, which on sintering provides both apatite and mullite crystalline phase constituents. In order to provide a consistent stock glass for use throughout the project, the combination of these batches must also be shown to be an acceptable approach. Though achieving this would infer that we have an AM-GC material it would not confirm that it is fit for application in terms of strength characteristics. Therefore, within this chapter the optimum heat treatment regime to providing a mechanical strength suitable for further development towards bone based biomaterial applications will also be examined.

3.2 Materials & Methods

3.2.1 Post Processing & Sintering

Graphite moulds were produced with the dimensions 30mm length, 4mm width and 3mm deep (Figure 3.1). Moulds were filled exclusively with 45-90μm particles of AW parent glass.
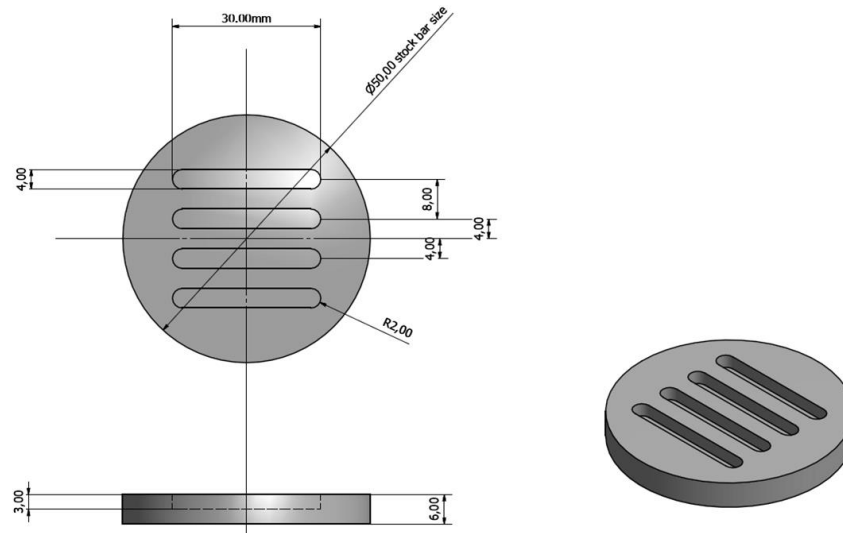
Figure 3.1: Graphite moulds designed for sintering of AM parent glass, 3mm thick lids were placed on moulds during sintering but are not depicted here.

Parts were then sintered in a programmable furnace (UAF 15/5 furnace, Lenton Thermal Designs Ltd; Eurotherm 818 controller-programmer) under two different heating regimes (Figure 3.2). The first heating regime required the parts be placed straight into the pre-heated furnace at 1200°C and held for 1 hour, after which the scaffolds were allowed to cool at the natural rate of the furnace (hrA). The second was a conventional two tier process determined by the optimum nucleation temperature (ONT) and time (ONt) analysis which involved heating the samples to 708°C at 10°C/min, holding at this temperature for 1 hour then raising to 1200°C at the same rate and holding for a further hour (hrB).
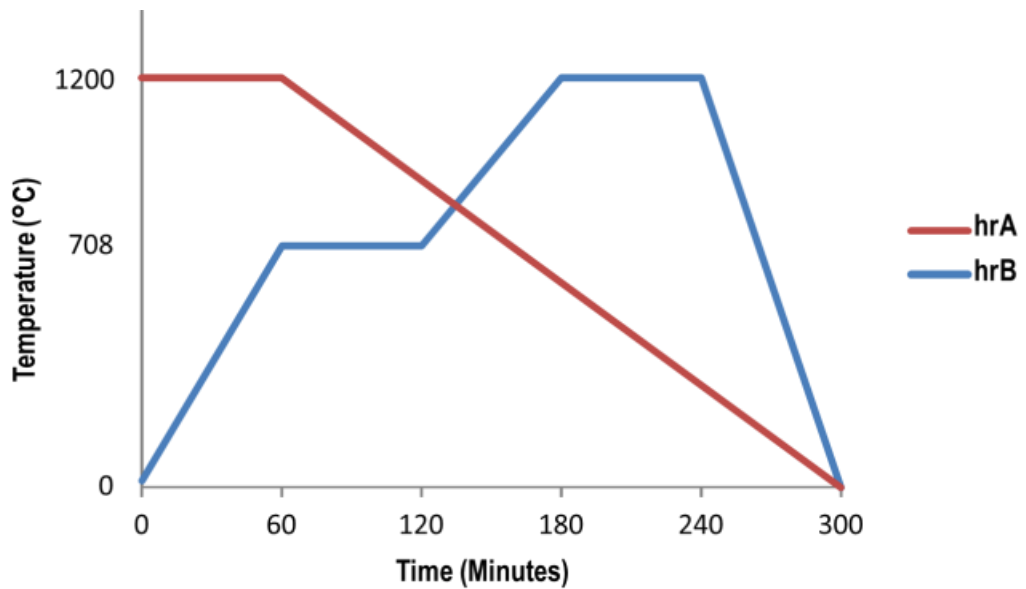
Figure 3.2: Graph illustrating the heating regimes, hrA and hrB, used to sinter the scaffold components.

3.2.2 Scanning Electron Microscopy of Scaffold Structure

Prior to SEM imaging scaffold samples were sectioned into 3mm long components using a diamond tipped precision cutting saw (Accutom-5, Struers) at 1500rpm and a feed rate of 0.05mm/s. Following which samples were prepared for standard analysis SEM as outlined previously (Section 2.2.1).

3.2.3 Flexural Strength Testing (Three-point Bending)

The mechanical characteristics were investigated by measuring the flexural strength of samples through a three point bend testing methodology using a UKAS accredited Lloyd Instrument (LR10K UTM) in accordance with the British standard for the mechanical testing of dental ceramics (BS EN ISO 6872:2008). Sintered scaffolds were supported by rollers with a 15mm span with a cross head situated in the centre above the sample (Figure 3.3).
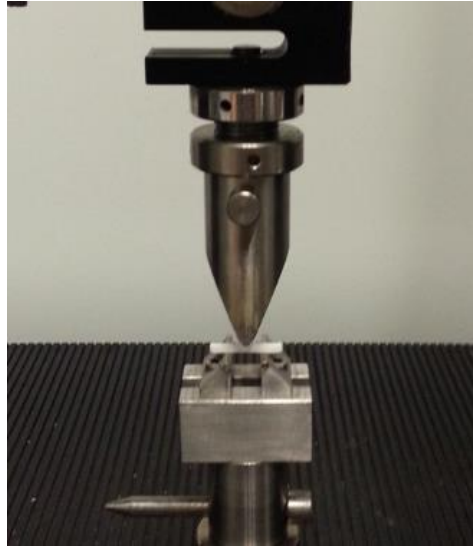
Figure 3.3: Image of flexural strength test rig with sintered AM-GC beam in position.

All the samples were tested with the cross head lowered at a feed rate of 1mm/min at room temperature. A 500N (± 5%) load cell was used to collect the load/displacement data for each sample with a sharp decrease in the recorded load identified as mechanical failure. The peak force was then used to calculate the flexural strength (σfs) from Equation 3.1. Where P is the loading force, l is the span of the roller supports, w is the sample width and b the sample thickness.

$$\sigma\text{fs} = \frac{3Pl}{2wb^2}$$

Equation 3.1

3.2.4 Optimum Nucleation Temperature and Time

The ONT was determined via the Marotta method [111] using a sequential nucleation hold technique. Isotherms were carried out during DTA analysis for one hour periods starting at Tg, then at 4 subsequent temperatures based on 20˚C increments. The ONt was obtained by carrying out sequential isotherms of varying time at the pre-determined ONT value. Isotherms were held for 15, 30 60, 120 and 240 minutes for subsequent samples during DTA analysis. A heating rate of 10˚C/min was used for all optimum nucleation data experiments.

3.3 Results

3.3.1 Batch Reproducibility

Out of a total six batches produced one batch was discarded prior to any further analysis, Batch 3, as its appearance differed notably from all other glass batches. This was perhaps due to human error during the production process. The remaining five batches were analysed to determine whether they could be considered equal and, hence, mixed to give a stock glass for the duration of the study.

3.3.1.1 Glass Transition and Crystalline Phase Evolution

In the first instance XRD was utilised to confirm that the glass powder batches produced (Section 2.1.4) were completely amorphous. The XRD pattern generated showed a large hump consistent with a high degree of scattering over a wide range of 2θ, characteristic of an amorphous structure (Figure 3.4).
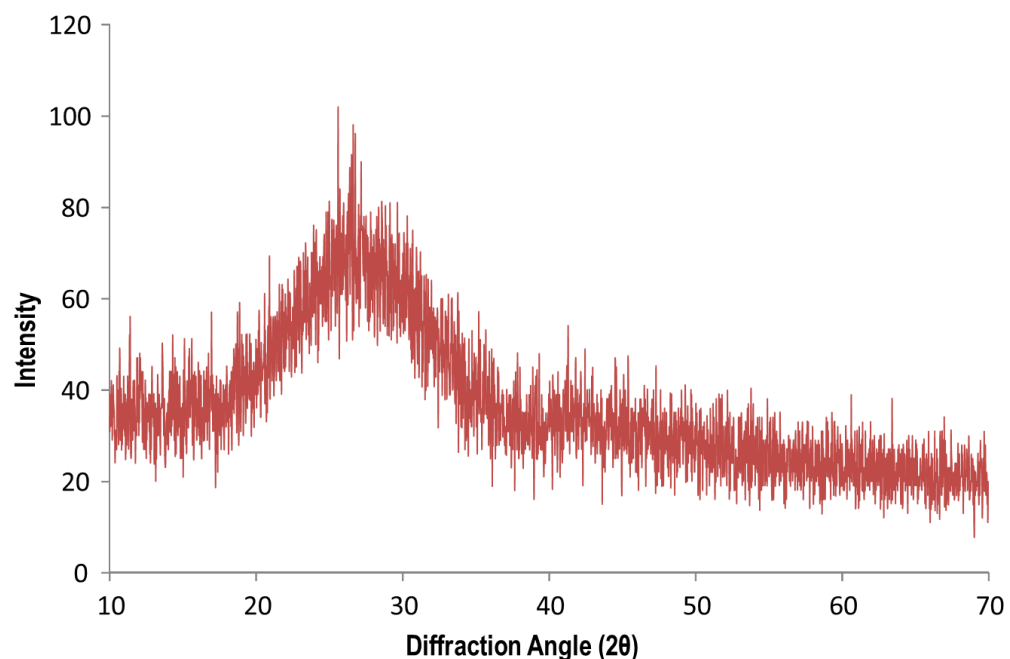
Figure 3.4: XRD trace for AM parent glass powder demonstrating amorphous hump region prior to any heat treatment.

The Tg's and subsequent crystallisation peak temperatures Tp1 and Tp2, believed to correspond to the evolution of apatite and mullite phases respectively were determined via DTA of each batch. A typical DTA plot is shown (Figure 3.5), with Table 3.2 displaying a summary of the glass

50

transition and crystallisation temperatures for each of the five batches examined. Between all five batches there was little variation observed in both the Tg and Tp2 temperatures with standard deviations of 1.2°C and 4.7°C respectively. The variation in Tp1 was notably higher with a standard deviation of 18.7°C. The current analysis yields mean values of 671°C for Tg, with Tp's at 782°C for Tp1 and 1012°C for Tp2. These values fall within a range comparable to previously characterised AM-GC compositions [112-114].
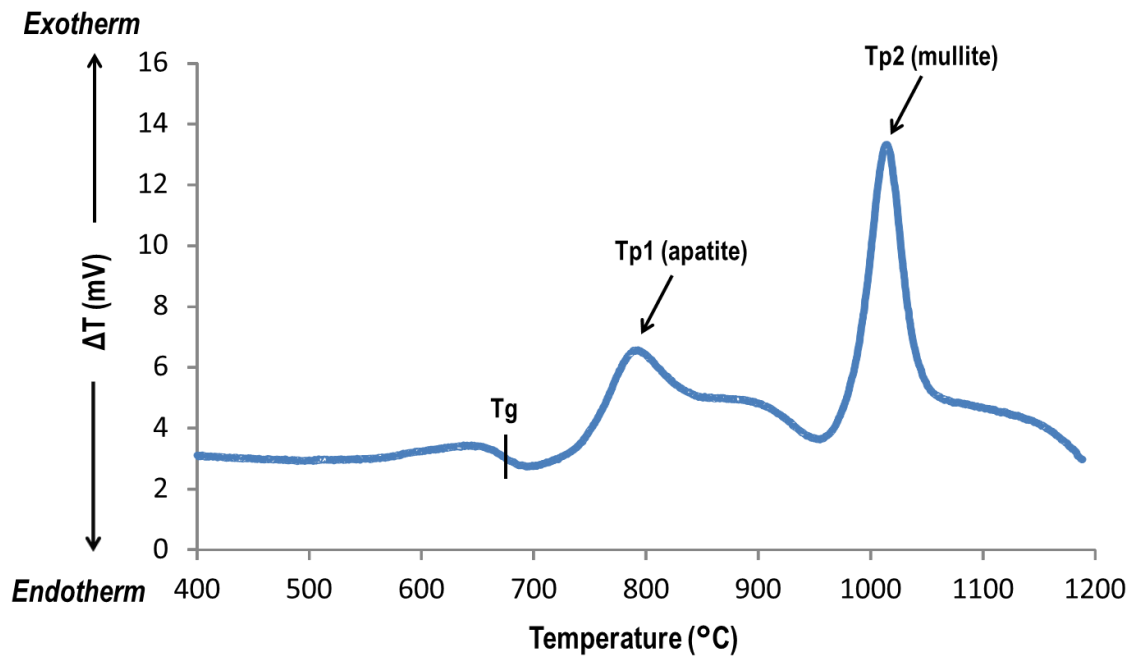
Figure 3.5: Typical DTA trace for a batch of AM parent glass carried out on the 45-90μm particle size range heated at 10°C/min.

Batch Number	Glass Transition (Tg)	Apatite (Tp1)	Mullite (Tp2)
1	669	762	1010
2	672	793	1015
4	671	777	1005
5	670	808	1013
6	672	769	1017
Mean	670.7	781.9	1012
Standard deviation	1.2	18.7	4.7

Table 3.2: Summary table of glass transition and crystallisation temperatures determined by DTA for all batches tested.

3.3.1.2 Sintering and Post Production

Each of the batches were sintered in the graphite moulds following hrA, the resulting microstructure of the sintered scaffold was then inspected by SEM. The scaffolds demonstrated a well sintered morphology with clear necking present between particles giving rise to a macro-porous scaffold structure (Figure 3.6, A-C). Upon closer inspection, the presence of crystalline phases was clear over the material surface with possible residual glass phases present (Figure 3.6, D). The material also demonstrated regions of micro-porosity distributed throughout the interlocking crystal structures (Figure 3.6, E).
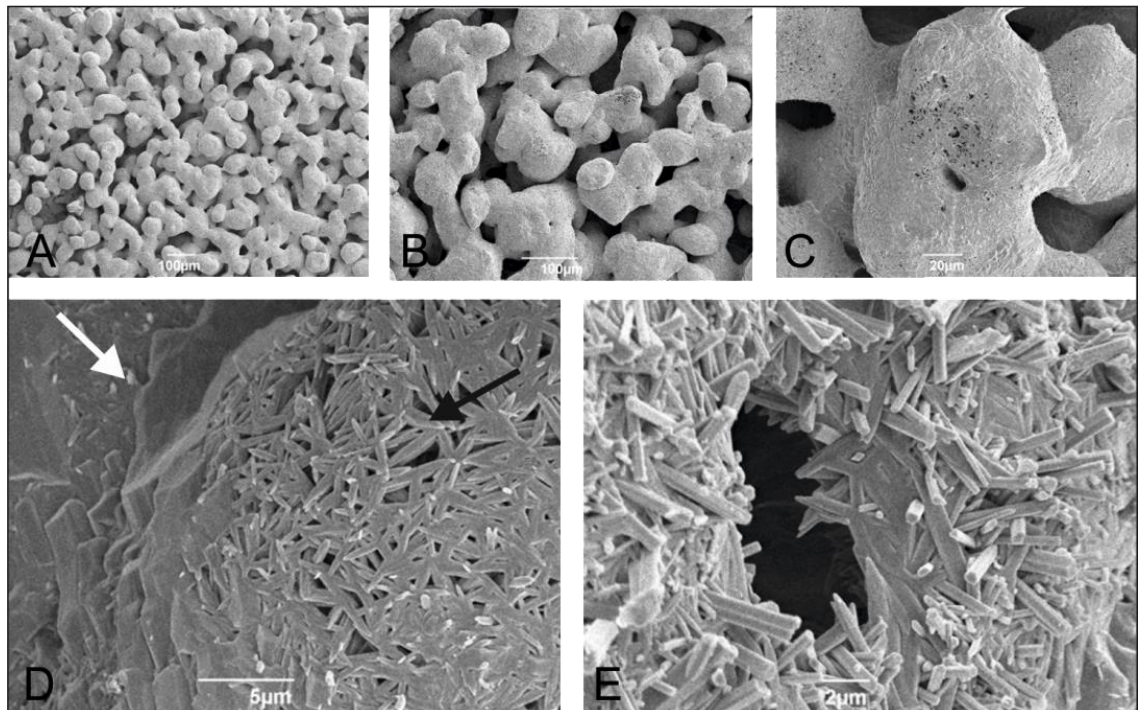
Figure 3.6: SEM imaging of sintered scaffold morphology illustrates the porous material structure and necking between particles (A-C). At High magnification crystalline phases are visible on the scaffold surface, indicated by arrows (D). Further magnification reveals micro-pores within the crystal phases (E).

XRD was carried out on each batch post sintering to identify the crystalline phases formed. The traces showed an excellent match for the presence of both fluorapatite ($Ca_5(PO_4)_3(F)$ – ICCD#15-0867) and mullite ($Al_6Si_2O_3$ – ICCD#15-0776) crystalline phases (Figure 3.7).
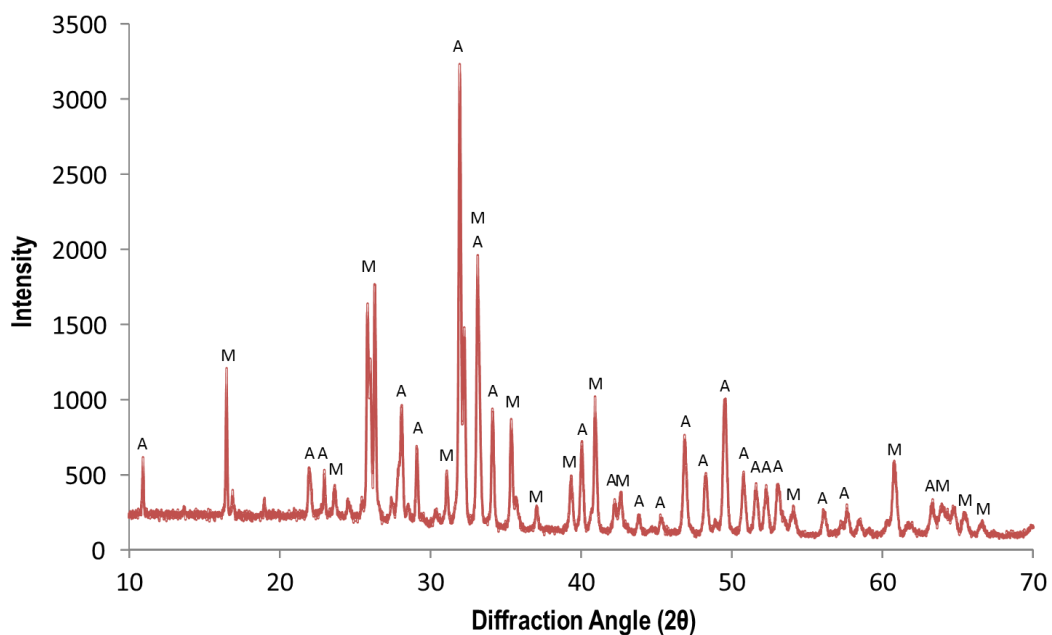
Figure 3.7: Representative XRD trace following sintering using hrA, where peaks labelled A represent fluorapatite and M is mullite.

The XRD traces for each batch were compared and appeared almost identical with regard to both peak position and magnitude (Figure 3.8). Also, the relative height between peaks within the individual traces are consistent and no notable peak broadening was seen in any batch. This indicates little chance of variation in crystal size and phase ratios between batches.
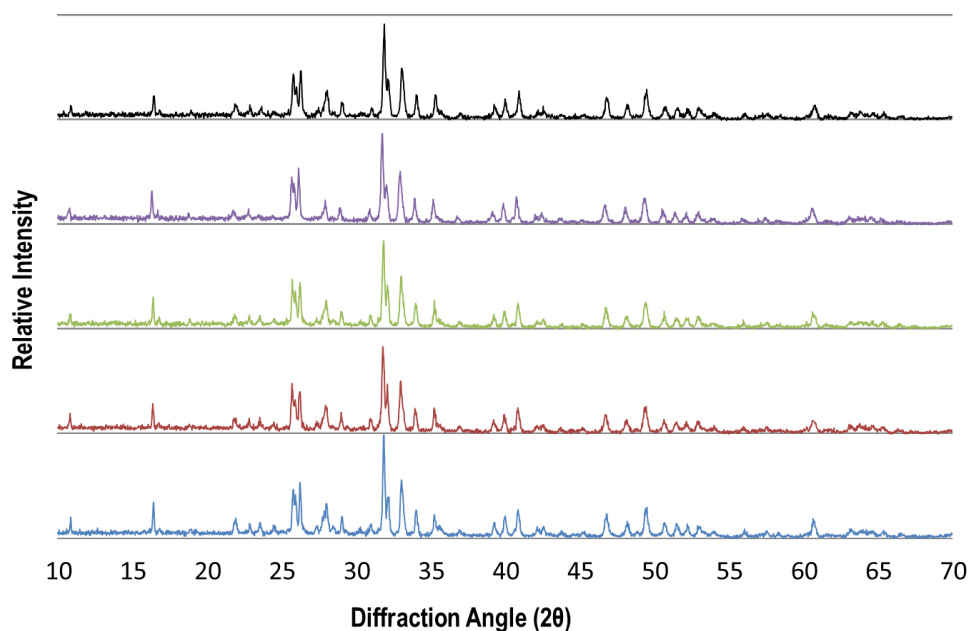
Figure 3.8: Comparison of post sintering XRD traces for all five batches produced, all traces appear almost identical in regart to both peak position and magnitude.

The flexural strength of each batch was assessed as described previously (3.2.3), with significant differences (P<0.05) between batches seen in most instances, although, batch 4 did not differ significantly from either batch 2 or 6. However, Batch 1 had a markedly higher flexural strength than did any other batch examined and also exhibited a greater range in the results (Figure 3.9). This being the case a quality control chart approach was also utilised to determine whether the batch production process could be considered in control from a manufacturing prospective. From the control chart it is seen that four successive points relating to batch 1 fall between 1-2 standard deviations away from the centre line (CL), which represents the mean value of all batches (Figure 3.10). This indicates a lack of control in the production process and given that the flexural strength of batch 1 also differed significantly from all other batches it was deemed unsuitable for mixing into the stock glass powders.
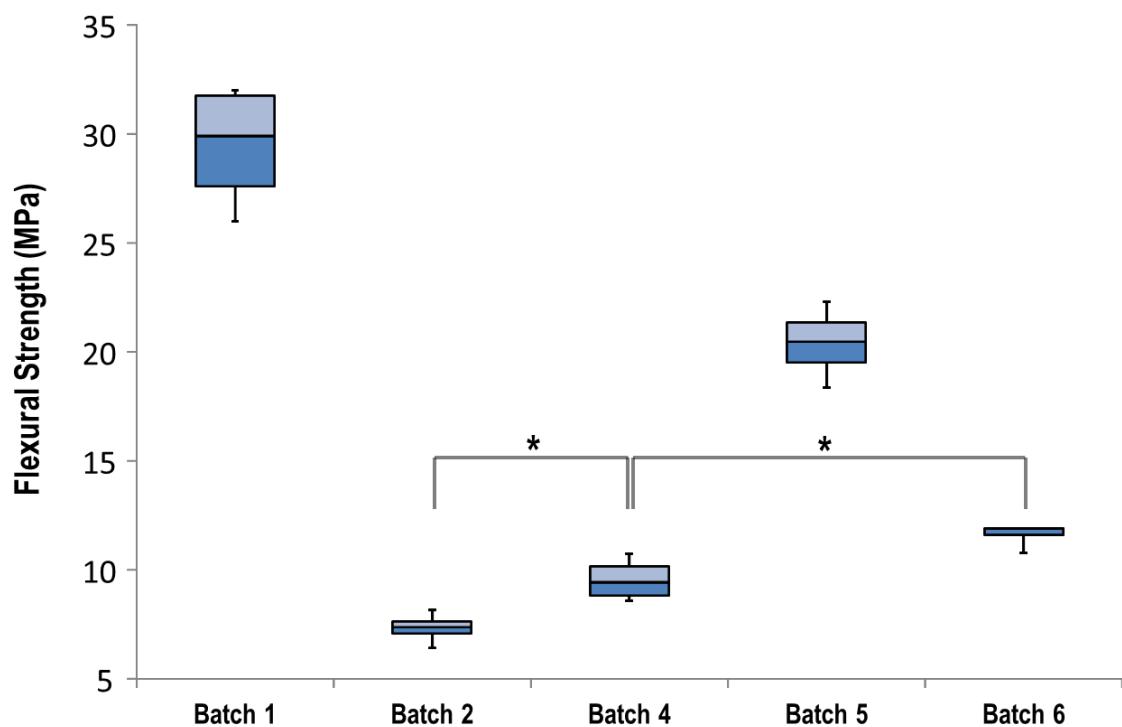
Figure 3.9: Box plots showing the post-processing flexural strength of each batch produced. All batches were sintered following hrA, with n=4 and * indicates no significant difference at *P<0.05*.
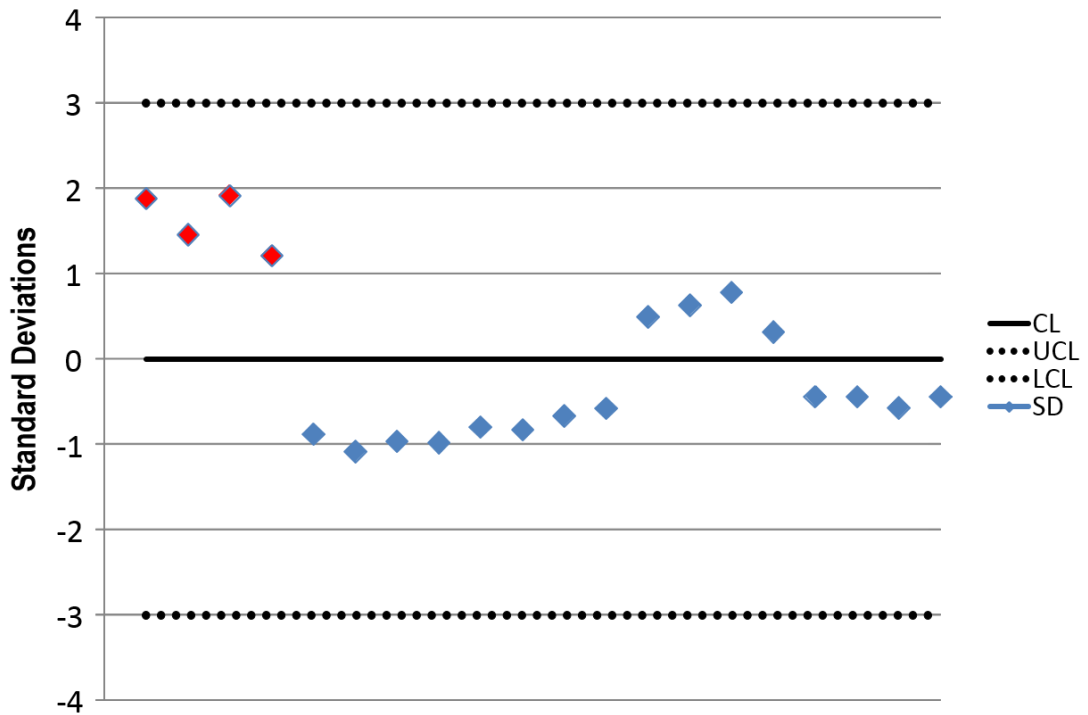
Figure 3.10: Control chart illustrating the number of standard deviations (SD) each sample fell away from the total mean, represented by the centre line (CL). The red points indicate the data associated with batch 1.

3.3.2   Optimum Heat Treatment

The optimum heat treatment regime is determined here following the mixing together of batches 2, 4, 5 and 6 in equal masses. Batch 1 was excluded from the stock glass due to the reasons stated previously (3.3.1.2). For the remainder of the thesis the glass examined will be the combined stock glass.

3.3.2.1 Optimum Nucleation Temperature

The ONT results, as determined via the Marotta method [111], for both the FA and mullite phases are presented in Table 3.3 and Table 3.4 respectively. In each case the hold temperatures are displayed along with the associated Tp's (Tp1 or Tp2) and their difference with regard to the temperature at which peak crystallisation occurred without a nucleation hold (Tp1' or Tp2').

	Hold Temperature	Tp1	Tp1' – Tp1
Apatite Phase (Tg = 668) (Tp1' = 781)	748	822	-41
	728	786	-5
	708	754	27
	688	759	22
	668	779	2

Table 3.3: Results of optimum nucleation temperature analysis for the apatite phase formation within the AM parent glass.

	Hold Temperature	Tp2	Tp2' – Tp2
Mullite Phase (Tg = 668) (Tp2' = 1012)	748	1010	2
	728	1009	3
	708	1012	0
	688	1015	-3
	668	1012	0

Table 3.4: Results of optimum nucleation temperature analysis for the formation of the mullite phase within the AM parent glass.

It can clearly be seen that the influence on Tp is much more pronounced on the apatite phase than on the mullite phase. When compared directly the influence on the mullite phase is barely notable (Figure 3.11). This considered the ONT was taken as 708°C as this represented the greatest reduction in Tp1 and corresponds to no variation seen in Tp2.
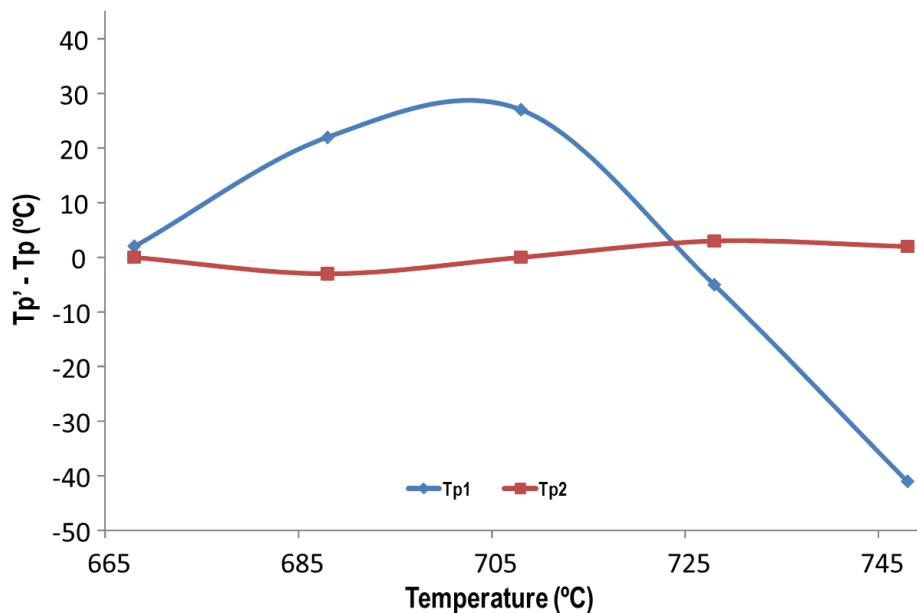
Figure 3.11: Optimum nucleation temperature plot for both the apatite (Tp1) and mullite (Tp2) phases of the AM parent glass.

3.3.2.2 Optimum Nucleation Time

The ONt was determined for both the FA and mullite phases, with data shown in Table 3.5 and Table 3.6, respectively. In each instance the hold times are displayed alongside the associated Tp's (Tp1 or Tp2) and their difference in relation to a straight run with no hold time (Tp1' or Tp2'). All isothermal holds in this data were carried out at 708°C, previously determined as the ONT (3.3.2.1). The data clearly shows the greater influence of hold time on the FA phase when compared to the mullite phase, which showed little influence of hold time on Tp2.

	Hold Time	Tp1	Tp1' – Tp1
Apatite Phase (Tg = 668) (Tp1' = 781)	15	765	16
	30	755	26
	60	749	32
	120	748	33
	240	752	29

Table 3.5: Results of optimum nucleation time analysis for the fluorapatite phase of AM parent glass.

	Hold Time	Tp2	Tp2' – Tp2
Mullite Phase (Tg = 668) (Tp2' = 1012)	15	1013	-1
	30	1011	1
	60	1014	-2
	120	1012	0
	240	1011	1

Table 3.6: Results of optimum nucleation time analysis for the mullite phase of AM parent glass.

Direct comparison highlights the negligible influence of hold time on Tp2 but also demonstrates that there is little if not no gain seen for Tp1 from prolonging the isotherm over 60 minutes, with holds over 120 minutes having a negative influence (Figure 3.12). This considered the ONt was chosen as 60 minutes rather than 120 minutes, reducing the time scale for scaffold heat treatment significantly. This is thought to be a desirable trade of for the 1°C reduction in Tp1.
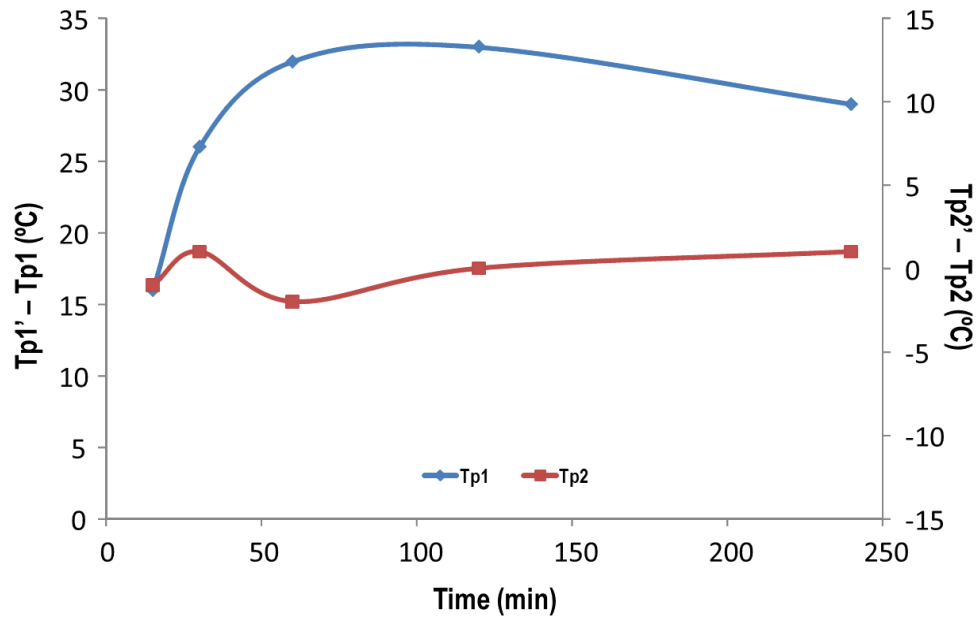
Figure 3.12: Optimum nucleation time plot for both the fluorapatite (Tp1) and mullite (Tp2) phases of the AM parent glass.

3.3.2.3 Flexural Strength

The effect of the optimum heat treatment on the post processed scaffolds was assessed by measuring the flexural strength of the samples (Section 3.2.3) produced under hrA, and that determined as optimum, hrB. The variables recorded and subsequent flexural strengths as calculated from Equation 3.1, along with the mean and standard deviation data are presented in Table 3.7 and Table 3.8 for hrA and hrB respectively.

Sample Number	Average Width (mm)	Average Thickness (mm)	Fracture Load (N)	Flexural Stress (MPa)
1	3.41	2.49	27.12	28.10
2	3.36	2.53	30.83	32.35
3	3.42	2.49	31.89	33.86
4	3.43	2.53	31.94	32.86
5	3.37	2.54	29.34	30.37
6	3.36	2.51	26.65	28.28
7	3.34	2.50	28.84	31.01
8	3.33	2.54	26.47	27.86
9	3.34	2.43	28.62	32.59
10	3.42	2.46	36.47	39.55
Mean	3.38	2.50	29.82	31.77
SD	0.04	0.03	3.08	3.42

Table 3.7: Flexural strength data for samples sintered under hrA.

Sample Number	Average Width (mm)	Average Thickness (mm)	Fracture Load (N)	Flexural Stress (MPa)
1	3.48	2.62	17.24	16.30
2	3.45	2.59	13.19	12.75
3	3.43	2.67	17.45	16.00
4	3.48	2.64	15.50	14.43
5	3.48	2.71	14.63	12.83
6	3.48	2.57	15.86	15.53
7	3.47	2.60	15.74	15.10
8	3.40	2.58	14.82	14.73
9	3.51	2.62	14.51	13.56
10	3.49	2.69	15.47	13.73
Mean	3.47	2.63	15.44	14.50
SD	0.03	0.05	1.27	1.26

Table 3.8: Flexural strength data for samples sintered under hrB.

The data shows a 17.27 MPa difference in flexural strength, representing a 54.4% reduction for samples processed using the optimum heat treatment, hrB, when compared to those processed using hrA. One way ANOVA found this difference to be statistically significant at the $P<0.05$ level. There was also a notable increase seen in the range of hrA when compared to hrB which can clearly be seen from boxplots of the data (Figure 3.13).
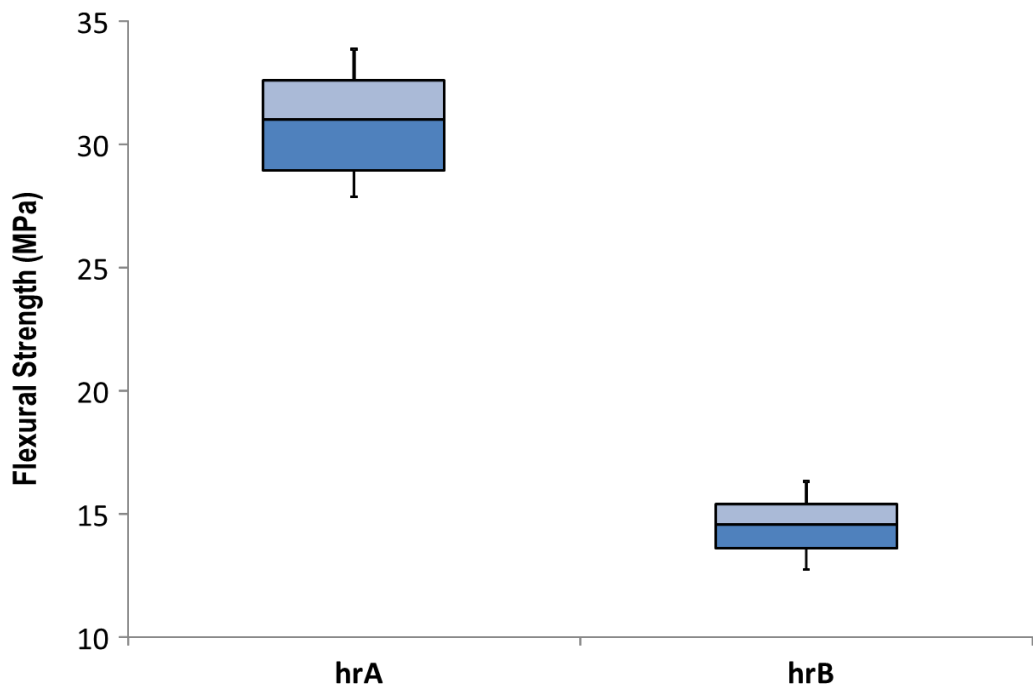
Figure 3.13: Box plots showing the flexural strength of the post-processed stock batch produced under either hrA or hrB. Samples differed significantly at the *P<0.05* level.

3.4 *Discussion*

The batch reproducibility analysis confirmed the composition used in the present study is crystallising from an amorphous structure to produce both FA and mullite phases following heat treatment. With the Tg, and Tp's (Tp1 and Tp2) observed in a range reported for similar compositions of AM containing glass-ceramics [112-115]. However, the specific values are slightly elevated when we consider the cross-link density (CLD) of the glass network under investigation. The CLD of a glass is a useful measure taken from the inorganic polymer approach to glass structure and allows for predictions to be made regarding the nature of a given glass composition [94]. The CLD of the current composition is 1.18, however, previous reports found both Tg and crystallisation temperatures to occur up to 50°C lower than those reported here [114, 115]. The higher values seen in the current study would normally be associated with an increase in the CLD, however this is not the case. The major contributor to the CLD of the glass in the current system is the fluorine (F) level, as divalent oxygen is replaced by univalent F atoms in the glass network [113]. While the initial F levels are still similar to other compositions examined, one explanation could be the loss of F through SiF_4 or AlF_3 formation during the melt phase of the production process.

The possibility of F loss may also help to explain the notably higher variability in Tp1 between batches (Table 3.2). During DTA previous studies have noted that loss of F produces a lower intensity and broader Tp1 in relation to Tp2 as was seen in the present analysis (Figure 3.5) [94, 113]. Thermo gravimetric analysis of weight loss during DTA previously reported substantial reductions around the region of Tp1 but only a small degree around that of the Tg believed to be due to SiF_4 [115], this may explain why Tg demonstrates a greater stability between batches as little F loss at this point may be inconsequential compared to that seen at Tp1. Substantial loss of F, however, would be expected to influence the amount of FA evolution during sintering and to promote the precipitation of other minor phases such as anorthite ($CaAl_2Si_2O_8$), which has already been identified in compositions lacking Fluorine [114]. From the DTA it is possible that following Tp1 an exotherm event was observed, which may be due to a minor phase formation (Figure 3.5). However, it is also possible that this event is due to an endotherm associated with a second glass transition due to prior amorphous APS as this has been noted previously [115]. Earlier research into ionomer glasses showed them to consist of both CaP rich and Al-Si rich regions indicative of glass-in-glass APS [116], also SEM studies have identified microstructures relating to both the spinodal decomposition and nucleation and growth mechanisms underlining

APS [105, 114, 115]. This may also help to explain the stability of the mullite phase formation (Tp2) between batches. If prior APS has taken place then the loss of F which is suspected to influence Tp1 may not influence Tp2, as it is evolved from a second glass phase independent of that responsible for Tp1 and less influenced by F content.

Initial XRD analysis provided an excellent match for the presence of both FA and mullite phases, therefore, substantial F must still be retained within the material following heat treatment. This is also supported by SEM showing the presence of an interlocking structure of high aspect ratio crystals, indicative of an apatite phase presence [113]. The flexural strength displayed a large range between batches (7.34 – 20.4 MPa) even following the removal of batch 1. This level of variation seen between batch flexural strength values further enforces the probability of F level instability, as increased F has been shown to influence the flexural strength of the samples significantly in AM-GC compositions [117]. Although a flow chart analysis was used in combination with ANOVA methods to determine that batch 1 should be excluded. It should be noted that the sequential 8 points falling below the CL would also indicate a lack of control (Figure 3.10). However, as the difference between these batches was not significant from an ANOVA perspective they were considered suitable for inclusion.

The ONT and ONt were determined due to their marked influence on Tp1 and subsequent lack of in regard to Tp2. This is possibly due to the previous explanation of glass-in-glass APS, hence, no nucleation is occurring in Tp2 as the glass phase responsible is perhaps uninfluenced in the temperature range used. One other explanation might be that a substantial degree of surface nucleation is occurring in the mullite phase and overwhelming the bulk nucleation effects. Although, this would not be expected in the current composition [94, 114].

Following the optimum heat treatment regime (hrB) the mixed stock glass samples were found to possess a statistically significant reduction in flexural strength compared to the initial sintering technique (hrA). This is perhaps due to the fact that under optimum conditions the larger number of nuclei forming during the hold period gives rise to a higher crystalline fraction in the material prior to raising the temperature for sintering to take place. During hrA samples are placed straight into the furnace at 1200°C. This may allow for substantial sintering to take place before the subsequent crystallisation of the material. However, the flexural strength values of 14.5 MPa achieved here for hrB still exceeded those reported previously for porous AM-GC structures and are comparable to scaffolds strengthened by subsequent addition of 50% <45μm particles.

Hence, those components processed via hrA far surpass the flexural strength levels achieved previously [109].

The tensile and compressive strength of natural bone tissue varies over a large range based on many factors such as porosity, bone mineral density and age to name but a few, making direct comparisons difficult. However, in depth reviews have reported tensile fracture stress ranges from 3 – 15 MPa for cancellous bone [118, 119]. The current samples generated a mean flexural strength of 31.77 ± 3.42 MPa and 14.5 ± 1.26 MPa for hrA and hrB respectively. However, it should be noted that flexural strength data will tend to generate higher values than those determined via tensile fracture stress [120]. This being the case, those samples treated under hrA would still be considered to surpass the tensile strength level required to function as a cancellous bone substitute and those treated under hrB would fall within it. In the current study hrA would be more desirable as this would push the tensile strength levels further towards those of cortical bone which are reported in the range 45 – 150 MPa [118, 121]. Although we do not reach the levels reported for cortical bone, the tissues of the vertebral EP on which the current study will later focus is considered to be a highly dense trabecular structure but not easily defined as either cancellous of cortical bone [122].

3.5 *Conclusion*

In the current chapter it has been demonstrated that the AM parent glass can be produced in a batch process, providing a stock glass for the remainder of the project. On sintering within carbon moulds the AM parent glass crystallises to provide both FA and mullite phases within its structure, generating an AM-GC material. Utilising hrA in this sintering process generated a mean flexural strength far surpassing those reported previously, indicating the suitability of the current material for further investigation towards bone replacement applications. Hence, the following chapters will utilise the stock glass presented here and all subsequent sintering processes will be carried out under hrA. Therefore, the work carried out has provided a consistent stock material, in which there is a high level of confidence going forward. Further work can now start turning towards other aspects of both material composition and structure that are more relevant to the proposed application as a functional EP construct.

Chapter 4: Apatite-Mullite Scaffold Analysis

4.1 *Introduction*

Current knowledge of the mechanisms underlying the bonding nature of bioactive ceramics and glass-ceramics has found there to be a common, time dependent, kinetic surface modification that occurs following implantation, whereby a biologically active hydroxyl-carbonate apatite (HCA) layer develops on the material surface. This layer is chemically and structurally equivalent to that of natural bone and is believed to promote osteoblast adherence to the surface and deposition of mineralised tissue, bonding the implant to the host bone, termed osseointegration.

4.1.1 Silica Containing Bioactive Materials

There are 11 steps to the mechanism proposed for the bonding of silica containing bioactive materials to bone [123]:

1. Formation of SiOH bonds due to rapid exchange of Na^+ and/or Ca^{2+} with H^+ or H_3O^+ from solution causing hydrolysis of silica groups.
2. Increasing HO^- within solution promotes attack on the silica glass network and soluble silica is lost in the form $Si(OH)_4$.
3. Condensation and re-polymerisation of SiO_2 on the material surface, now depleted of alkalis and alkali-earth cations.
4. Ca^{2+} and PO_4^{3-} groups migrate to the material surface through the SiO_2 rich layer, giving a $CaO-P_2O_5$ rich surface film. The film subsequently grows through incorporation of calcium and phosphates from solution.
5. Crystallisation of the amorphous $CaO-P_2O_5$ by incorporation of OH^- and CO_3^{2-} from solution forming the HCA layer.
6. Adsorption and desorption of growth factors in the HCA layer to influence stem cell differentiation.
7. Action of macrophages to remove debris from the site allowing cells to occupy the space.
8. Attachment of stem cells to the bioactive surface.
9. Differentiation of stem cells to form bone forming osteoblasts.
10. Deposition of extracellular matrix by osteoblasts.
11. Mineralisation of the matrix.

Note that following stage 6 all subsequent events are cell mediated (Figure 4.1).

Surface Reaction Stages	11	Mineralisation	Cellular events
	10	Matrix maturation	
	9	Differentiation of stem cells	
	8	Attachment of stem cells	
	7	Action of macrophages	
	6	Adsorption of biological moieties in HCA layer	Surface events
	5	Crystallisation of hydroxyl carbonate apatite (HCA)	
	4	Adsorption of amorphous Ca + PO_4 + CO_3	
	3	Polycondensation of SiOH + SiOH $\rightarrow$ Si-O-Si	
	1 & 2	Formation of SiOH Bonds	

Figure 4.1: The mechanistic steps proposed responsible for the bioactive nature of silica containing biomaterials. The surface reaction events are segregated into those imparted by the material (1-6) and by the cells (7-11).

Although the mechanism for bone bonding and osseointegration is well defined, the significant difference observed between the rate of bonding among bioactive materials indicates a substantial influence of other biochemical factors occurring at the interfaces. Therefore, bioactive materials are proposed to exists in two classes; Class A, those materials that elicit both an extracellular and intracellular response from the cells occupying the interface, and Class B, those materials that only elicit an extracellular response [124]. From a biological perspective, Class B bioceramics provide an osteoconductive environment, able to support an osteoprogenitor cell population and new bone deposition, whereas Class A materials may also possess an osteoinductive capacity deeming them capable of stimulating the differentiation of an osteoprogenitor cell towards a bone-forming osteoblastic phenotype [125].

The current study focuses on the use of AM-GC as proposed biomaterial for bone replacement application. Therefore, the material can be considered as a silica containing bioceramic consisting of both FA ($Ca_5(PO_4)_3F$) and mullite ($Al_6Si_2O_{13}$) crystalline phases within a proposed residual glassy matrix. However, one concern over the use of AM-GC is the use of Al_2O_3 in the glass, as the addition of alumina to AW glass-ceramic compositions has been shown previously to inhibit bone bonding [101]. This negative influence of alumina is believed to occur due to Al^{3+} causing an increased resistance to ion exchange at the biomaterial surface [126]. However, other multiphase silica rich ceramics containing phlogopite mica and apatite phases have demonstrated bone bonding despite containing Al_2O_3. This is believed to be attributed to the Al^{3+} being

incorporated in to the stable crystalline phase, avoiding any influence on the surface reaction kinetics [127]. This may also be the case for the current AM-GC with regard to the mullite phase being present.

Freeman *et al.* found that following 28 days implantation into the mid-shaft of rat femurs, monolithic AM-GC of similar compositions to those examined here showed good osseointegration and osteoconductive potential, while an un-sintered parent glass control showed a marked inflammatory response and evidence of fibrous tissue encapsulation [128]. Goodridge *et al.* also observed direct contact and new bone ingrowth on porous AM-GC produced by SLS techniques following 4 weeks implantation in rabbit tibiae. This study moreover addressed the possible cytotoxic effect of the material as leaching ions such as Al^{3+} would have toxic effects. Extract and direct contact assays found there to be no cytotoxic effect of porous AM-GC on either human dermal fibroblasts or MG-63 cells, an immortalised human osteoblastic cell line, at either 18 hours or 7 days culture [110]. However, simulated body fluid (SBF) studies have failed to identify HCA layer formation on AM-GC and other FA and aluminosilicate composites which also showed no detectable levels of Al^{3+} up to 108 days [110, 129]. This distinct lack of evidence for HCA layer formation is believed due to the inherently greater resistance of FA to dissolution when compared to materials such as HA. One recent study on the influence of HA and mullite nano composites on human foetal osteoblasts reported there to be no concern over either material's safety regarding implantation or the presence of mullite triggering apoptosis at a cellular level [130].

4.1.2 Study Aim

Given that the previous chapter provided a stock AM parent glass and valid production methods, it is now the aim of the current chapter to analyse the AM-GC with specific focus on the underlying material factors governing aspects such as, the nucleation mechanism and subsequent final crystalline and amorphous phase compositions. This will aid in our current understanding of how the material can be utilised in a clinical setting, furthering our current scientific understanding of the AM-GC behaviour under the given processing regime. This may also aid in understanding the resistance to HCA layer formation demonstrated by AM-GC materials. This chapter also aims to address material factor effects, such as particle size range, on the functional characteristics of the scaffold with a view to bone replacement applications, specifically in the region of the vertebral endplates.

4.2 Materials & Methods

4.2.1 Biaxial Flexural Strength

The maximum tensile strength of AM-GC discs was determined using the biaxial flexural strength (BFS) test methodology. This was performed in accordance with the British standard for the mechanical testing of dental ceramics (BS EN ISO 6872:2008). It should be noted that specimen dimensions used in the current analysis could not adhere directly to the standard due to particle size constraints on mould geometries. However, this will not inhibit the ability to produce meaningful results as the equations used in the analysis are dimensionally unconstrained. In order to perform the testing a custom mould was manufactured to generate AM-GC discs with diameter greater than 11 mm to allow for positioning in the test apparatus. Each scaffold was sintered according to the previously determined optimum heating regime, hrA (Section 3.2.1). Six samples each were tested for scaffolds composed solely of the following particle size ranges; 45-90 μm, 90-125 μm, 125-1000 μm and 1000-2000 μm.

Individual sample tests were carried out on a UKAS accredited Lloyd instrument (LR10K UTM). The dimensions of each test sample were recorded and the sample placed concentrically on the supporting balls of the testing fixture (Figure 4.2). Once positioned a 1.5 mm diameter hardened steel indenter is used to apply load to the centre of the component under a constant cross head speed of 1 mm/min, with load/displacement data collect throughout using a 500 N (± 5%) load cell. The observation of a sharp decrease in recorded load was then determined as mechanical failure. The peak force was subsequently used to calculate the BFS (σ_{bfs}) for each sample according to Equation 4.1.

$$\sigma bfs = - 0.238\ 7 P(\text{X-Y})/b^2$$

Equation 4.1

Where:

σ = the maximum centre tensile stress, in megapascals;

P = the peak load causing fracture, in Newtons;

$X = (1 + v) \ln(r_2 / r_3)^2 + [(1 - v) / 2](r_2 / r_3)^2$

$Y = (1 + v)[1 + \ln(r_1 / r_3)^2] + (1 - v)(r_1 / r_3)^2$

b = the sample thickness

In which:

v is Poisson's ratio (as the value for the AM-GC is not known, use *v* = 0.25);

r_1 is the radius the support circle, in millimetres;

r_2 is the radius of loaded area, in millimetres;

r_3 is the radius of the specimen, in millimetres;
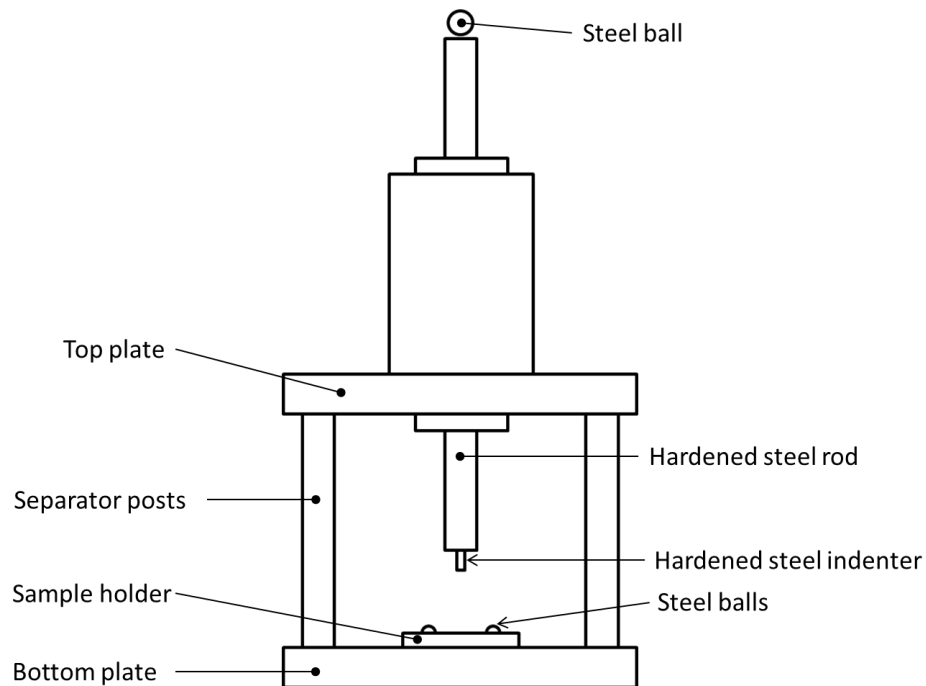
Figure 4.2: Biaxial flexural strength test fixture schematic in accordance with BS EN ISO 6872:2008.

4.2.2   Micro CT Analysis

All specimens underwent computated tomography (CT) assessment using a micro-CT scanner (µCT100, Scanco Medical AG, Bassersdorf, Switzerland). Scaffolds were secured in a 9 mm diameter scanning pot using packing foam ensuring that the bottom of the scaffold in the transverse plane was parallel to the base of the pot. Scanning ensued with a 5 µm voxel size which analysed the scaffold from just above to just beneath the top and bottom surfaces, respectively. In order to determine the threshold settings able to provide a true representation of scaffold geometric parameters and to maintain consistency between individual samples a 17.2 mm diameter fully dense AM-GC rod was utilised. The rod was scanned a distance of 5 mm along its shaft and a resulting transverse section image used to set the threshold limit. The threshold, determined in Hounsfield units (HU), was adjusted until the diameter on the scan matched that of the AM-GC rod (17.2 mm). In order to achieve this the upper and lower threshold limits were determined as 10000 HU and 3053 HU respectively.

For each scaffold analysed an individual volume of interest (VOI) was identified, taken as a cylinder just within the boundaries of the scaffolds natural geometry, illustrated in Figure 4.3. The spacing, porosity and connection density data was then calculated for each scaffold within this cylindrical VOI using the predetermined threshold levels.
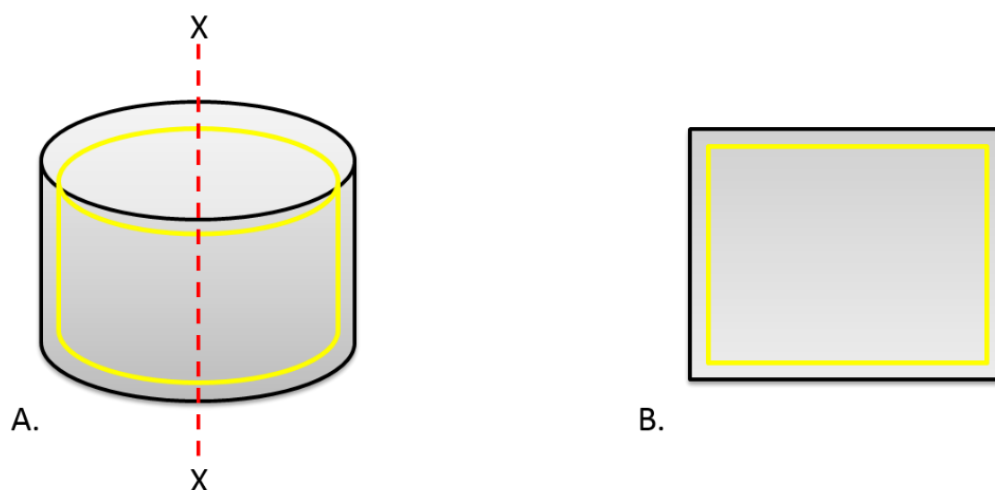
Figure 4.3: schematic illustrating the cylindrical VOI (yellow lines) taken within the 3D scaffold geometry (A), and a plain view of a section taken through X-X (B).

4.2.3 Thermal Analysis

The mechanism by which the AM parent glass undergoes nucleation was investigated by performing differential scanning calorimetry (DSC) (Pegasus DSC 404 F3, NETZSCH) on three particle size fractions, <45 µm, 45-90 µm and 1000-2000 µm. The testing was carried out in platinum-rhodium crucibles, under a protective nitrogen gas screen in an air atmosphere. Approximately 35 mg of parent glass was used in each test, preformed against a Al_2O_3 reference. Lids were placed on samples prior to testing and experiments carried out at a heating rate of 10°C/min up to a final temperature of 1200°C. For each of the particle fractions investigated the Tg and subsequent peak crystallisation temperatures Tp1 and Tp2 were determined using the NETZSCH system software (Proteus, thermal analysis, version 6.0). Peak positions were identified using an automatic peak search with a 15% threshold value and Tg identified as the midpoint of the respective endotherm or exotherm.

4.2.4 Rietveld Analysis

In order to quantify the crystalline phases present in the AM-GC scaffolds and any subsequent variation as a factor of particle size a Rietveld analysis method was performed. The analysis was carried out on XRD data for scaffolds composed solely of the following particle size fractions; <45 μm, 45-90 μm, 90-125 μm, 125-1000 μm and 1000-2000 μm. All scaffolds were sintered in 10 mm diameter moulds covered with a lid and processed under hrA (Section 2.1.2).

Scaffolds composed of a given size fraction were ground for 120 seconds using a puck and mill in a Gy-Ro Rotary system, following which 10 wt.% of corundum was then added to each AM-GC sample to act as an internal reference standard during analysis. AM-GC powders were then loaded into sample holders against an off axis quartz plate in order to minimise background effects. XRD was carried out using a Philips X'Pert run with 40 kV and 40 mA outputs, logged using the X'Pert Data Collector software. A 15x15 mm fixed incident beam mask was used and data was collected in the 2θ range between 10° and 70°, with a step size and time of 0.033° and 3.18 s, respectively. The diffraction patterns were refined via the Rietveld method using Xpert HighScore Plus (PANalytical) system software. The model data files for crystal structures used during the refinement were obtained from the ICDD database and are given in Table 4.1. The refinement took into account several background coefficients, a scale factor and specimen displacement with lattice constant parameters also considered for each phase. Peak profiles were modelled using a pseudo-Voigt function with one Gaussian and one Lorentzian coefficient. The half width parameters U and W were also included in the refinement to account for peak broadening effects. The refinement process was carried out on the individual material phases in the order they are presented.

Crystalline Material	ICDD N°
Corundum	04-007-1400
Fluorapatite	04-009-4021
Mullite	04-009-6556
Anorthite	04-011-2883

Table 4.1: Crystalline material data files obtained from the ICDD database, Rietveld refinement analysis was performed for materials in the order they are presented in the table.

Following the quantification of the individual phase fractions by Rietveld analysis the weight percentage of amorphous material present was calculated according to Equation 4.2. The weight percentage values determined for each crystalline phase were then rescaled in order to account for the amorphous content in the absence of corundum.

$$W_{\%A} = \frac{\left(1 - \frac{W_{\%S}}{W_{\%R}}\right)}{100 - W_{\%S}} \times 10^4 \qquad \text{Equation 4.2}$$

Where:

$W_{\%A} =$ Weight percentage of amorphous phase.

$W_{\%S} =$ Weight percentage of internal standard; weighed prior to analysis.

$W_{\%R} =$ Weight percentage of internal standard; as determined via Rietveld refinement analysis.

4.2.5 *Energy Dispersive X-Ray Spectroscopy*

Following BFS testing microstructural observations of samples were made via SEM, carried out on a Hitachi S-3400N fitted with an energy dispersive X-ray spectroscopy (EDX) attachment (Bruker Quantax, 129ev, SDD). Prior to imaging samples were sputter coated with gold at 20 mA for 40 s in an argon atmosphere (Agar Scientific) to give an approximate coating of 5 nm. Images were collected using the secondary electron detector at a fixed working distance of 10 mm. In order to collect EDX data an accelerating voltage of between 5-20 eV was used in combination with a probe current of between 50-60 µA.

4.3 Results

4.3.1 Mechanical and Structural Characterisation

4.3.1.1 Biaxial Flexural strength

For samples sintered under hrA using the BFS and subsequent max tensile strength values as determined from Equation 4.1, along with the mean and standard deviation data are presented in Table 4.2 to Table 4.5 for the respective particle size range components. The mean maximum tensile strength (MTS) was observed to drop in correlation with increasing particle fraction size from 116.37 ± 16.70 MPa to 16.18 ± 10.47 MPa for the 45-90 µm and 1000-2000 µm particle fractions, respectively. This represents an 86% reduction in mean MTS seen over the total particle size ranges.

Sample Number	Sample Radius (mm)	Sample Thickness (mm)	Fracture Load (N)	Max Tensile Stress (MPa)
1	5.70	2.10	52.07	129.06
2	5.70	2.15	57.50	135.97
3	5.72	2.15	52.57	124.22
4	5.70	2.15	38.64	91.37
5	5.75	2.15	48.10	113.60
6	5.75	2.15	44.04	103.99
		Mean	48.82	116.37
		SD	6.73	16.70

Table 4.2: Biaxial flexural strength of the 45-90 µm particle fraction.

Sample Number	Sample Radius (mm)	Sample Thickness (mm)	Fracture Load (N)	Max Tensile Stress (MPa)
1	5.95	2.20	33.37	74.83
2	5.95	2.20	35.70	80.05
3	5.95	2.20	34.17	76.62
4	5.95	2.20	32.30	72.43
5	5.95	2.20	23.99	53.79
6	5.95	2.20	28.38	63.64
		Mean	31.32	70.23
		SD	4.36	9.77

Table 4.3: Biaxial flexural strength of the 90-125 µm particle fraction.

Sample Number	Sample Radius (mm)	Sample Thickness (mm)	Fracture Load (N)	Max Tensile Stress (MPa)
1	6.10	2.45	14.27	25.70
2	6.15	2.45	40.86	73.50
3	6.10	2.45	27.79	50.05
4	6.15	2.40	15.15	28.40
5	6.20	2.45	18.23	32.75
6	6.10	2.45	27.11	48.83
		Mean	*23.90*	43.20
		SD	10.14	18.06

Table 4.4: Biaxial flexural strength of the 125-1000 µm particle fraction.

Sample Number	Sample Radius (mm)	Sample Thickness (mm)	Fracture Load (N)	Max Tensile Stress (MPa)
1	6.20	2.40	6.66	12.47
2	6.10	2.40	3.14	5.90
3	6.12	2.30	5.79	11.83
4	6.20	2.30	12.02	24.50
5	6.15	2.35	4.68	9.16
6	6.20	2.30	16.31	33.25
		Mean	8.10	16.18
		SD	5.02	10.47

Table 4.5: Biaxial flexural strength of the 1000-2000 µm particle fraction.

One way ANOVA found there to be a significant difference ($P<0.05$) in most instances in regard to the mean MTS as a function of particle size fraction. The only instances where no significant difference was observed was for the 125-1000 µm particle fraction in relation to either 90-125 µm or 1000-2000 µm components. This may in some part be due to the large range (25.7-73.5 MPa) demonstrated in the 125-1000 µm test samples (Figure 4.4).
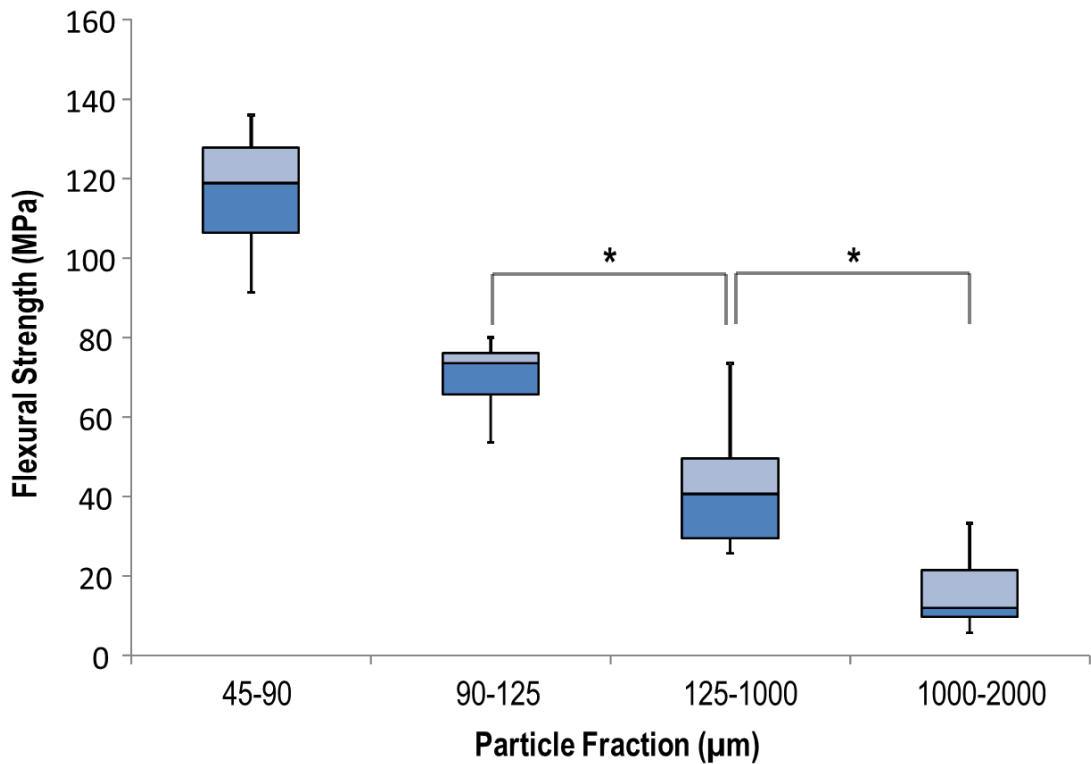
Figure 4.4: Box plot of biaxial flexural strength in relation to particle size fraction. Six samples were included in each test group (n=6) with * indicating no significant difference at P<0.05.

4.3.1.2 µCT Structural Analysis

Computational analysis of µCT scan data for all but the <45 µm particle fraction scaffolds provided 3D model representations of the pore space present throughout the structures (Figure 4.5). This data was threshold controlled against a 100% dense AM-GC bar to ensure a true representation of the porous fraction was provided. The imaging demonstrated a clear interconnectivity structure between the pore spacing in all instances. It can also be observed that there are a number of extremely small pores present in the 1000-2000 µm particle fraction (Figure 4.5, D) this is representative of pores present within the body of a single particle at this size range.
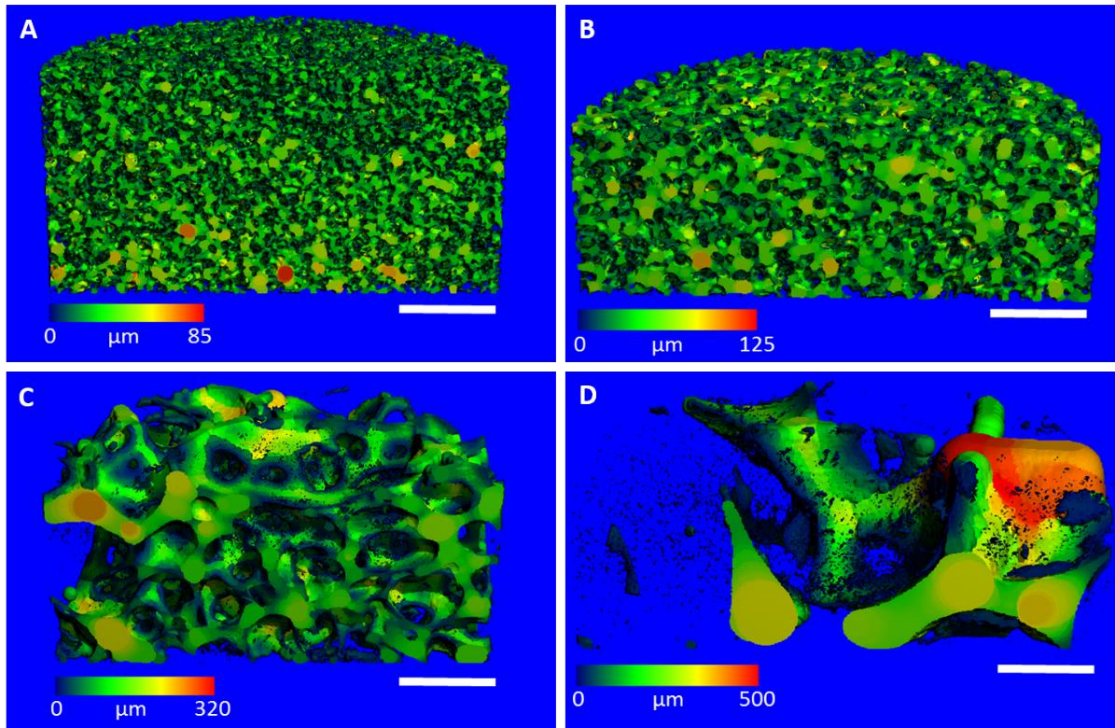
Figure 4.5: Sectioned image of pore space distribution throughout scaffolds composed of a given particle size range; 45-90 μm (A), 90-125 μm (B), 125-1000 μm (C) and 1000-2000 μm (D).

The mean spacing between the particles of a given size fraction are presented in Table 4.6, along with their respective standard deviations. It can be observed that the standard deviation increases notably with particle size, specifically as we move to the 1000-2000 μm fraction. This is due to the substantial increase in particle size and, hence, pore size in relation to the volume of interest taken during the scan which remained constant throughout. Therefore, a significantly lower number of pores were available to measure and a lower accuracy is observed in the mean. The spacing data showed a consistent increase in mean pore size with particle fraction.

	Particle Size (μm)			
	45-90	**90-125**	**125-1000**	**1000-2000**
Mean Spacing (μm)	29.9	44	125.4	265.2
SD	11.5	17.9	64.5	145.5

Table 4.6: Mean pore spacing within the scaffold structure for a given particle size fraction.

When examining the porosity of the components as a percentage of the total volume an initial increase is seen between the 45-90 µm and 90-125 µm particle size range, however, all subsequent particle size increases lead to a reduction in overall percentage porosity (Figure 4.6). The connection density of the solid scaffold component was observed to decrease substantially with increasing particle fraction until reaching the 125-1000 µm level, following which a small increase was seen for the 1000-2000 µm size range (Figure 4.6). Although we observe reduced total porosity as a function of particle size fraction form the 90-125 µm range onwards, the connection density, which is perhaps best thought of as a representative of the number of sintered particles per unit volume within the structure, drops significantly.
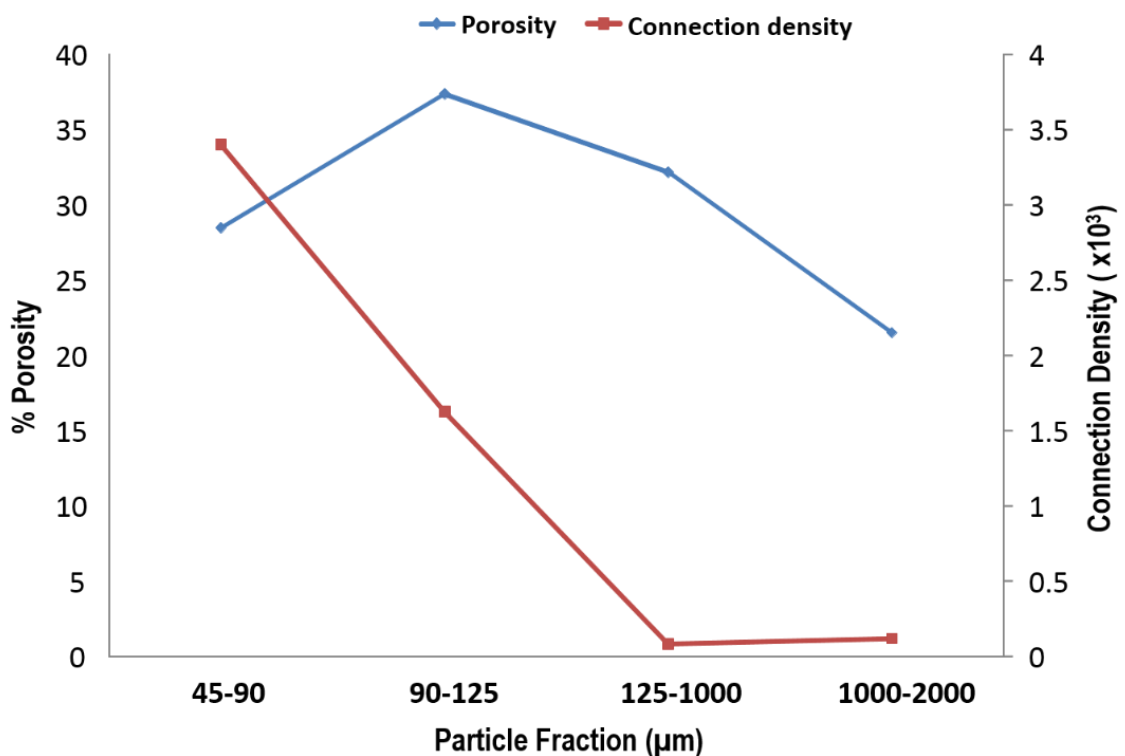
Figure 4.6: Volume percentage porosity and connection density for each of the particle size fractions investigated.

4.3.2   Nucleation and Crystallisation Behaviour

4.3.2.1 Nucleation Mechanism

In order to determine the nucleation mechanism of the current AM parent glass three particle size fractions (<45 µm, 45-90 µm, 1000-2000 µm) were analysed via DSC to examine their influence on the crystallisation temperatures Tp1 and Tp2, relating to FA and mullite phases respectively.

The DSC traces for each of the AM parent glass particle sizes appear to be largely independent of particle size fraction (Figure 4.7).
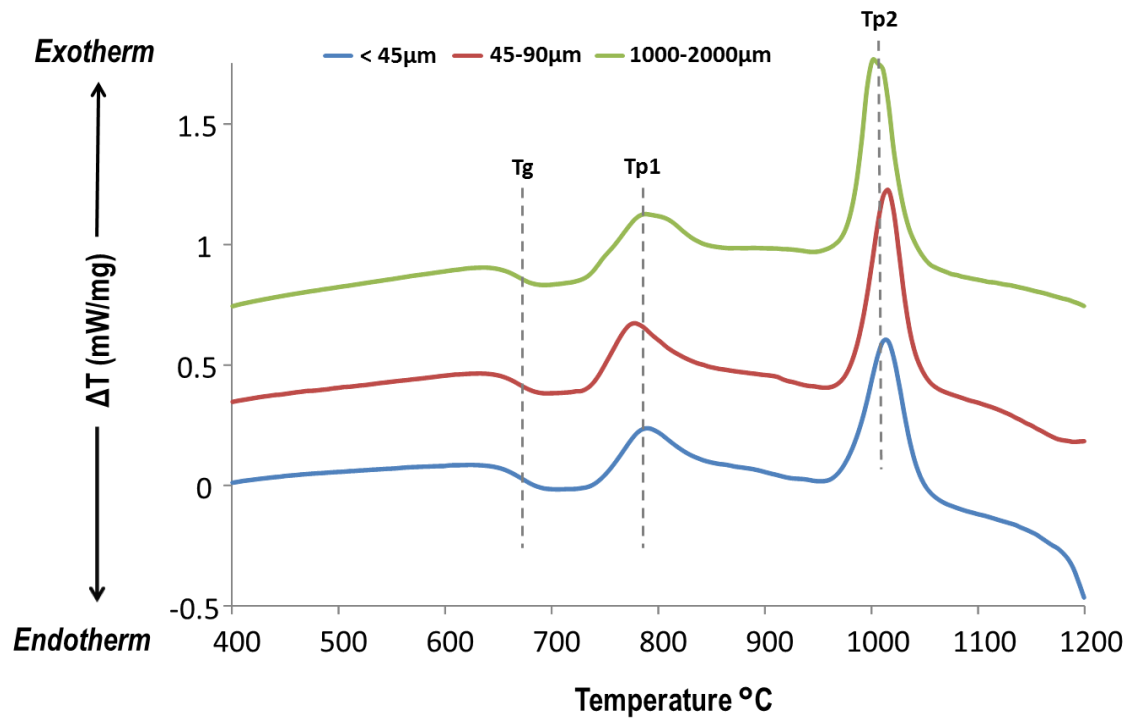
Figure 4.7: DSC traces for the three particle size fractions examined. Note the lack of fluctuation in peak positioning

The largest variation of 30°C was observed in the Tg values between the <45 μm and 45-90 μm size particle fraction. However, this had no notable influence on the crystallisation temperatures observed as a consequence, with the maximum difference observed for each of the crystallisation peaks being only as much as 12°C for both Tp1 and Tp2. The crystallisation peak and Tg values for each particle size fractions are summarised below in Table 4.7.

Particle Fraction (μm)	Tg	Tp1	Tp2
< 45	667	789	1013
45 - 90	637	777	1014
1000 - 2000	659	786	1002

Table 4.7: Glass transition and peak crystallisation temperature (°C) data for given AM parent glass particle size fractions as determined by DSC.

4.3.2.2 Rietveld Analysis

Quantitative analysis of the crystalline and amorphous phases present in each of the particle size fractions investigated was obtained via the Rietveld refinement method performed on powder XRD patterns. The model calculated pattern showed a good fit with the observed XRD trace data in each case, with the 45-90 µm particle trace fit shown as a representative example (Figure 4.8). The model parameters detailed previously (Section 4.2.4) were refined simultaneously using a least square methodology to generate the best agreement with measured data. The difference plot displayed in Figure 4.8 also shows there to be no significant deviations from the observed XRD profile. Table 4.8 presents the quantification data for each of the particle fractions investigated with the associated weighted profile R-factor (R_{wp}) values, which represent the percentage mean deviation between the observed and calculated data in the refinement.

	Particle Size (µm)				
	<45	45-90	90-125	125-1000	1000-2000
Fluorapatite	38%	33%	30%	29%	30%
Mullite	33%	24%	21%	24%	24%
Anorthite	11%	10%	9%	8%	7%
Glass	18%	33%	40%	39%	40%
R_{wp}	7.2	4.5	5.6	5.3	7.3

Table 4.8: Results of the quantitative Rietveld analysis for each of the particle size fractions analysed (wt. %).

The results indicate that all the particle size fractions achieved a high degree of crystalinity with between 18-40% of amorphous glass phase remaining. Although there was a sequential drop of 1% in anorthite content with increasing particle size this only amounts to a maximum 4% difference over the total range. FA was the major crystalline phase present in all size fractions investigated, though the mullite content was only fractionally lower in each case, with differences ranging between 5-9%. Overall the composition remains almost constant, however, in the case of the <45 µm particle fraction there is a more pronounced reduction in amorphous phase content with a concomitant increase observed in both FA and mullite phase fractions (Table 4.8).
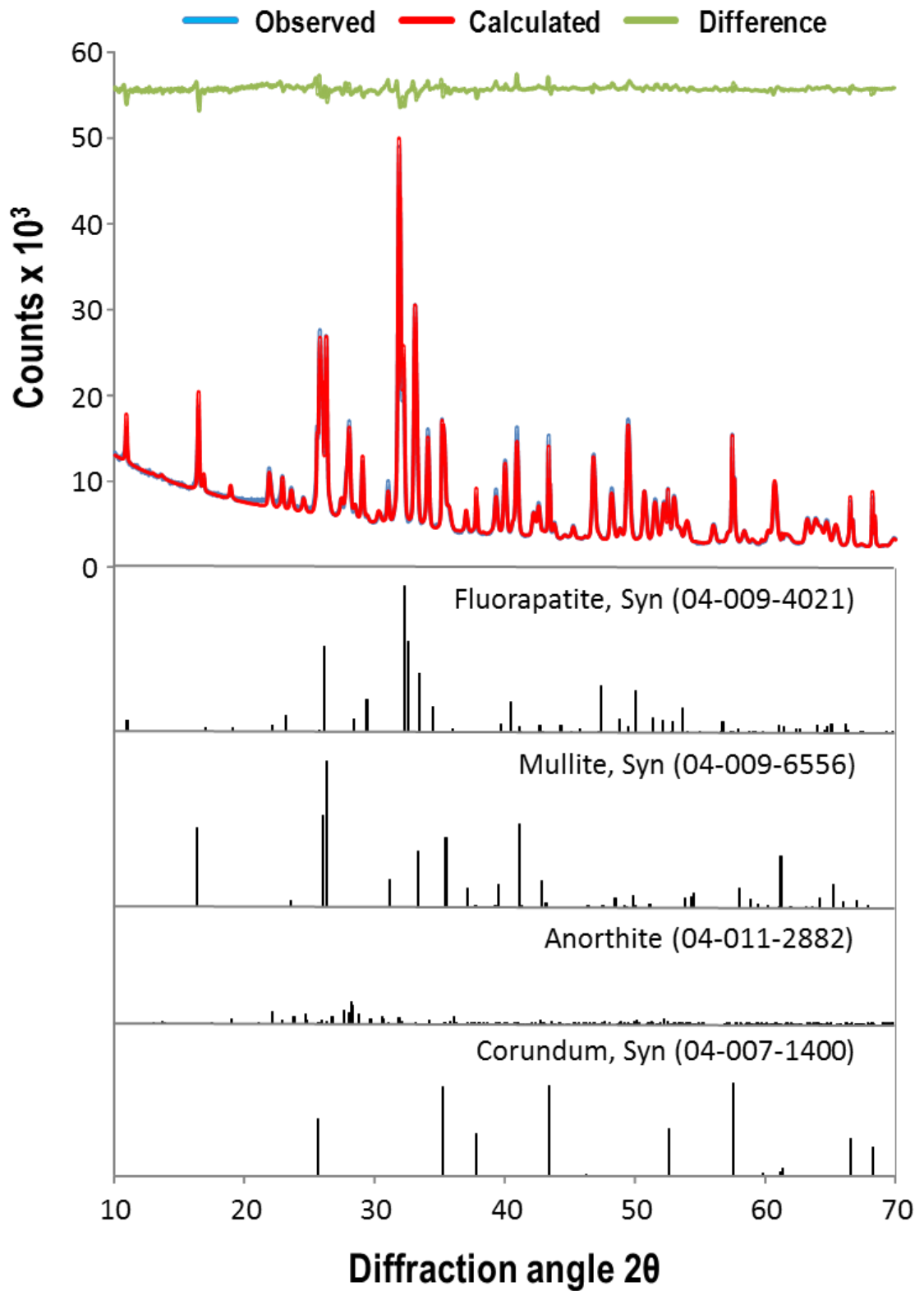
Figure 4.8: Observed, calculated and difference curves as determined by Rietveld refinement of the AM-GC 45-90 µm particle fraction. Markers representing the individual phase patterns for fluorapatite, mullite, anorthite and corundum are also indicated.

4.3.2.3 SEM & EDS

SEM imaging was carried out at both low (Figure 4.9) and high (Figure 4.10) magnification for the AM-GC fracture surfaces. The images revealed a consistent and highly crystalline matrix throughout the internal micro-structure of the material with minimal influence seen on crystallinity between the range of particle size fractions investigated.
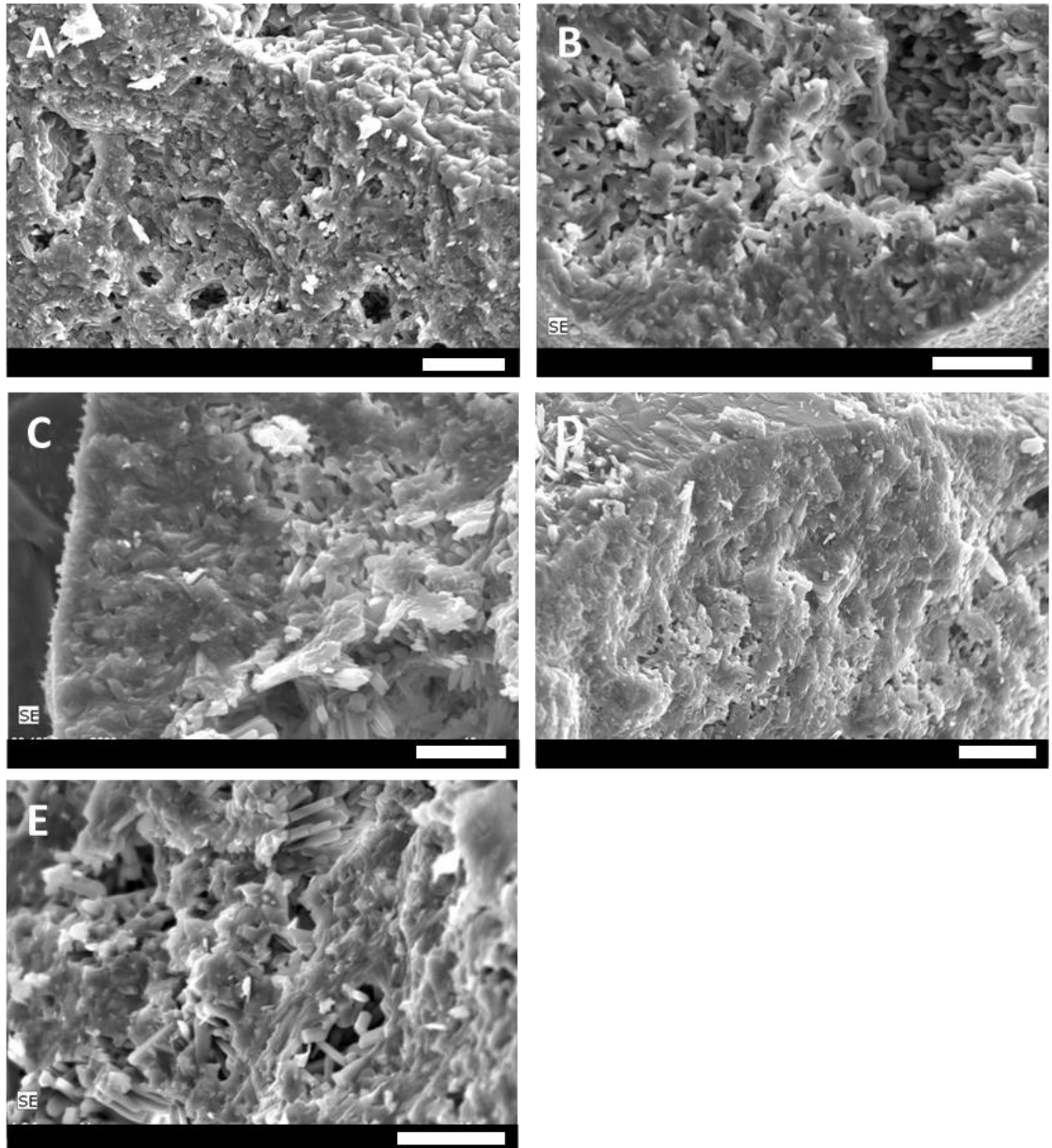
Figure 4.9: Low magnification imaging of the fracture surfaces for scaffolds composed of a given particle size range; <45 µm (A), 45-90 µm (B), 90-125 µm (C), 125-1000 µm (D), 1000-2000 µm (E). All scale bars are equal to 10 µm.
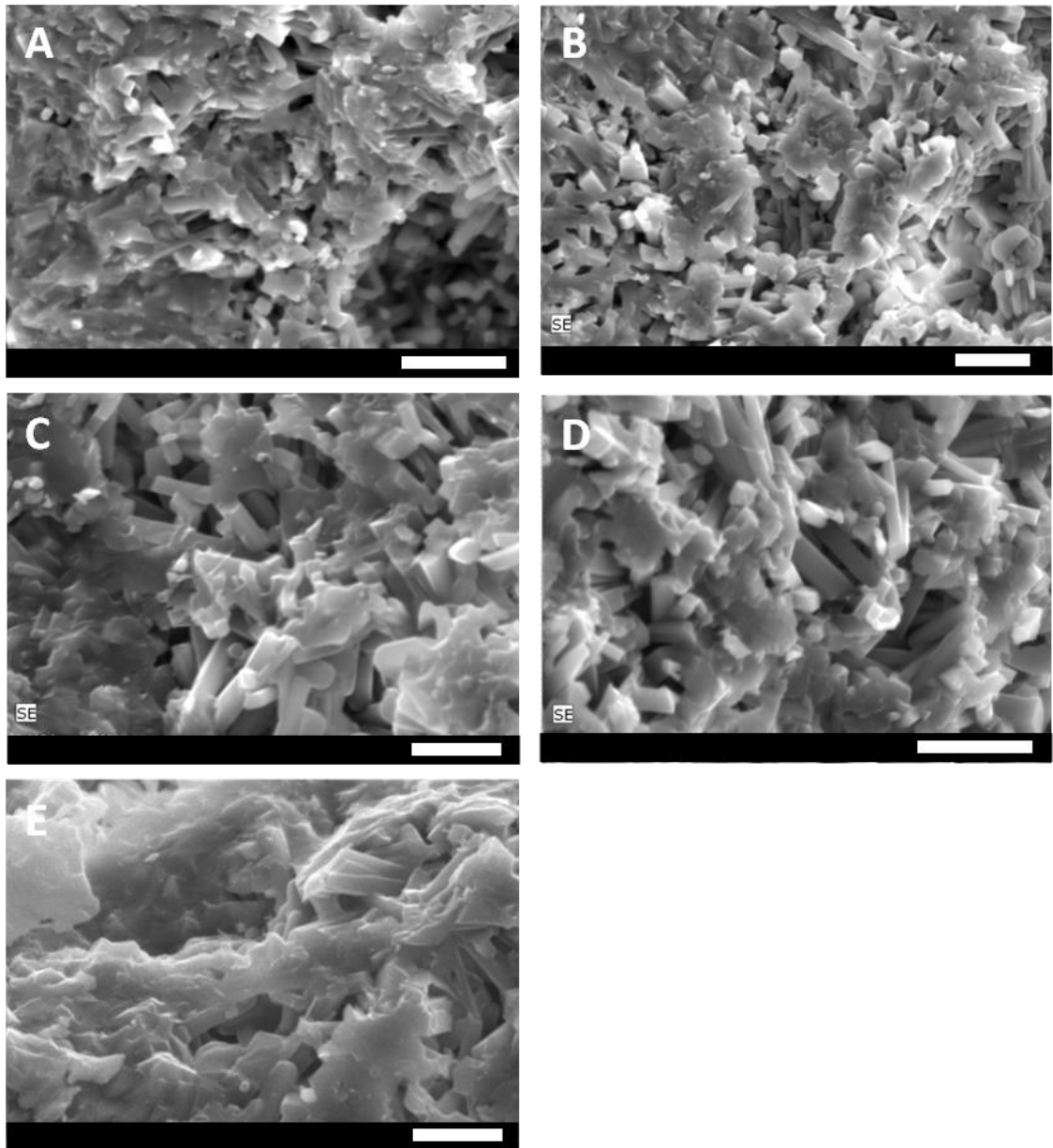
Figure 4.10: High magnification imaging of the fracture surfaces for scaffolds composed of a given particle size range; <45 µm (A), 45-90 µm (B), 90-125 µm (C), 125-1000 µm (D), 1000-2000 µm (E). All scale bars are equal to 5 µm.

EDX enhancement of the low (Figure 4.11) and high (Figure 4.12) magnification images demonstrated clearly a distinct Ca and P rich rod-like crystal phase interspersed among that demonstrating a less crystalline morphology with an Al heavy composition. The crystalline phase is a highly dense network of distinctly individual crystals having a random orientation throughout the structure. The crystals appear to have a consistently similar aspect ratio throughout the bulk material, independent of particle size, ranging between approximately 3-5 µm in length and 0.5-0.75 µm in width.
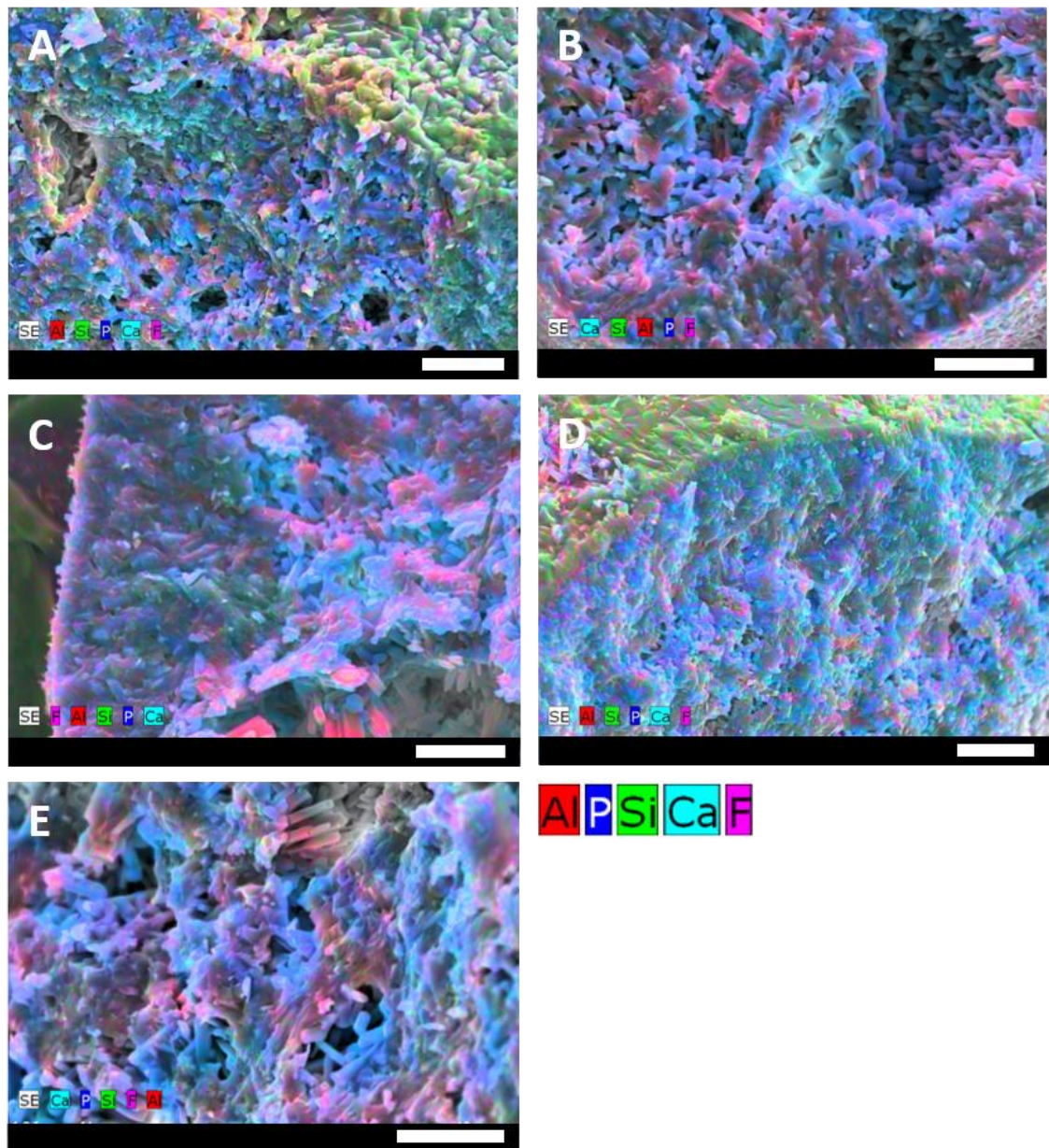
Figure 4.11: EDX enhanced low magnification imaging of the fracture surfaces for scaffolds composed of a given particle size range; <45 µm (A), 45-90 µm (B), 90-125 µm (C), 125-1000 µm (D), 1000-2000 µm (E). All scale bars are equal to 10 µm.

Except for a few indistinct regions the Al rich phase shows no appreciable crystalline structure throughout the bulk of the material fracture surfaces regardless of particle size. However, Rietveld analysis indicates the presence of between 21% to 33% mullite ($Al_6Si_2O_{12}$) in the bulk material, for which Al is a main constituent. Therefore, based on this and the apparent high density of the Ca and P rich crystal phase, it is perhaps possible that there is such a high nucleation density present within the material that the aluminosilicate crystals have neither the space or available elemental components to form the defined needle-like structures.
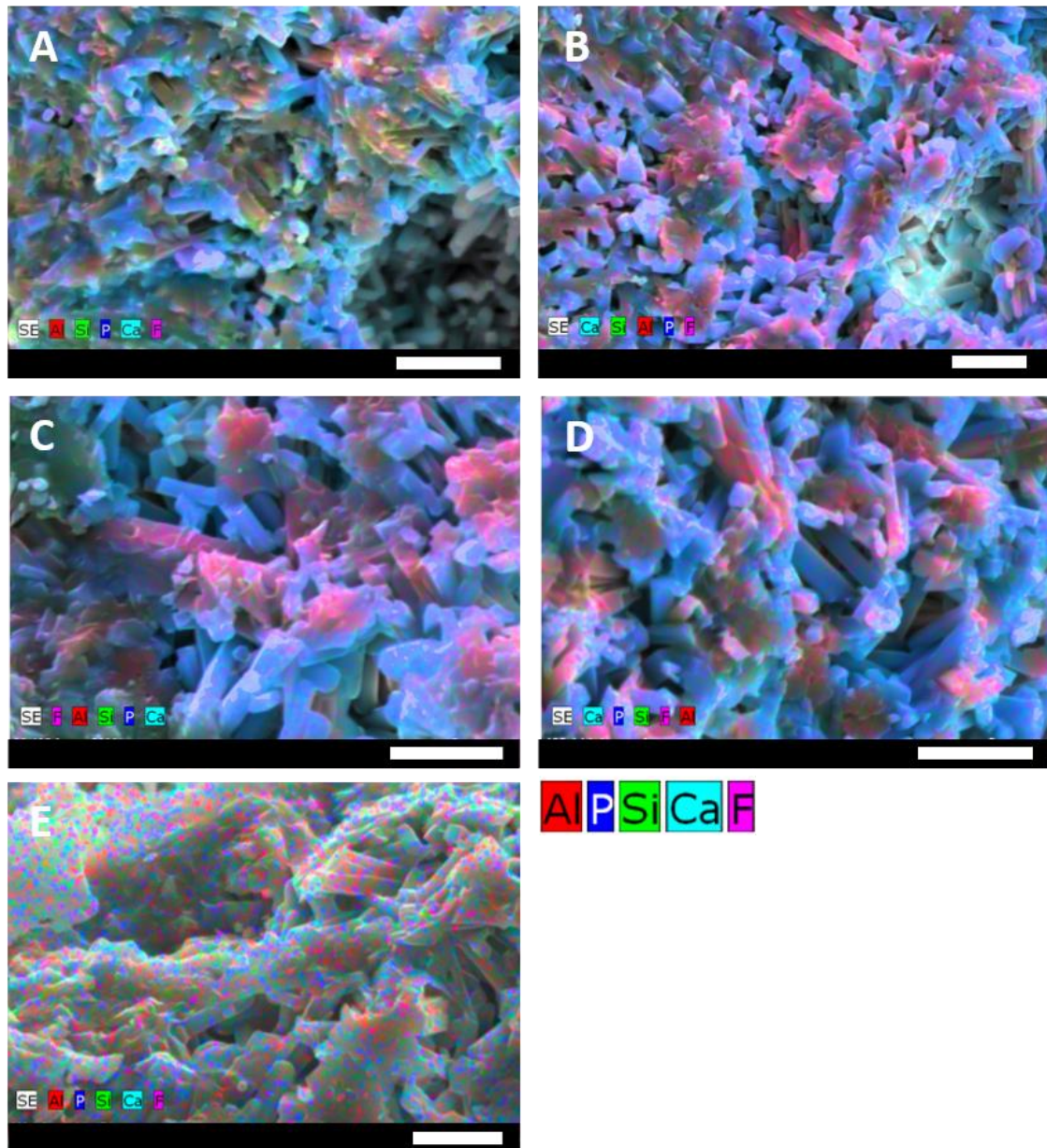
Figure 4.12: EDX enhanced high magnification imaging of the fracture surfaces for scaffolds composed of a given particle size range; <45 μm (A), 45-90 μm (B), 90-125 μm (C), 125-1000 μm (D), 1000-2000 μm (E). All scale bars are equal to 5 μm.

Well defined aluminosilicate crystals with significantly larger aspect ratios than those seen in the bulk fracture surfaces were able to be identified growing into pores present within the material. Point scan spectral analysis was performed in this region for the 45-90 μm fracture surface in order to better elucidate the phases present (Figure 4.13).
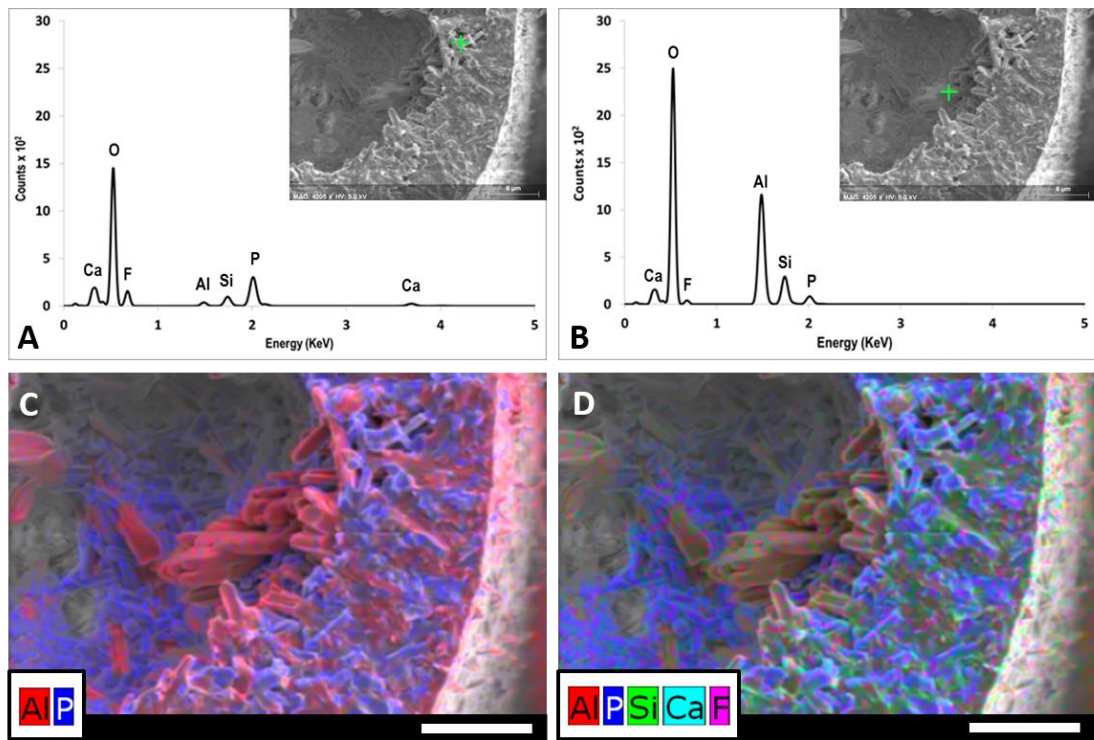
Figure 4.13: Spectral analysis of crystalline phases present within pore structures of 45-90 μm particle fraction fracture surface. The spectral traces for the apatite (A) and proposed mullite (B) phases are shown. EDX enhanced SEM images are also shown demonstrating both Al and P rich regions (C) and the presence of a residual glassy phase rich in Si throughout the bulk (D).

The spectra quantification was able to report a Ca:P and Ca:O ratio of 1.68 and 0.48, respectively. This is in very close agreement with the natural apatite ratios of 1.66 and 0.41, therefore, it is believed to confirm the presence of a significant apatite phase, previously predicted via the Rietveld refinement analysis. The Al rich phase demonstrated a composition with an Al:O ratio of 0.48, extremely close to that of mullite (0.46) but due to the complex nature of the material it was not possible to match any other ratios directly to the mullite composition. This is likely due to the fact that any residual glass or tertiary crystalline phase, such as anorthite, would also contain varying degrees of Al, Si and O making definitive identification via EDX extremely difficult. However, based on the Al:O ratio and previous research into the current system, the Al heavy crystalline phase is believed to be mullite [113, 114, 117]. It can also be observed from the EDX enhanced images that a Si rich (green) non-crystalline component throughout which crystalline phases are distributed is present, this is representative of the residual glassy phase within the material (Figure 4.13, D). The significantly defined aluminosilicate crystals present within the pore region is further evidence of the restraining nature of the apatite crystal phase on mullite crystal maturation in the bulk. This in combination with the distinct rod-shaped morphology of the apatite

phase may imply the reversal of a prior APS process in which crystallisation then occurs directly from a more homogeneous glass melt.

Though the bulk of the material at the fracture surface appears to share a common crystalline microstructure independent of particle size fraction, low (Figure 4.14) and high (Figure 4.15) magnification SEM imaging of the natural scaffold surfaces showed vastly differing characteristics throughout the range investigated. The <45µm particle scaffolds demonstrated no clear crystallinity over the surface region, although, under high magnification some evidence of a semi-crystalline structure with ill-defined faceted crystal growth morphology is present (Figure 4.15, A). In contrast the scaffold composed solely of the 45-90 µm particle fraction showed a fully crystalline surface of the rod-like morphology similar to those previously observed in the bulk material. At the 90-125 µm size range the scaffold surface was still seen to be fully crystalline, however, a fine interlocking needle-like structure was observed interspersed with larger monolithic crystalline phase regions. In the 125-1000 µm range the amount of monolithic crystalline region increased significantly with higher aspect ratio needle-like crystals observed to be distributed in distinct island regions throughout. Finally at the surface of the 1000-2000 µm particles the structure was observed to be again semi-crystalline with no apparent distinct structure, comparable to that observed at the <45 µm level.
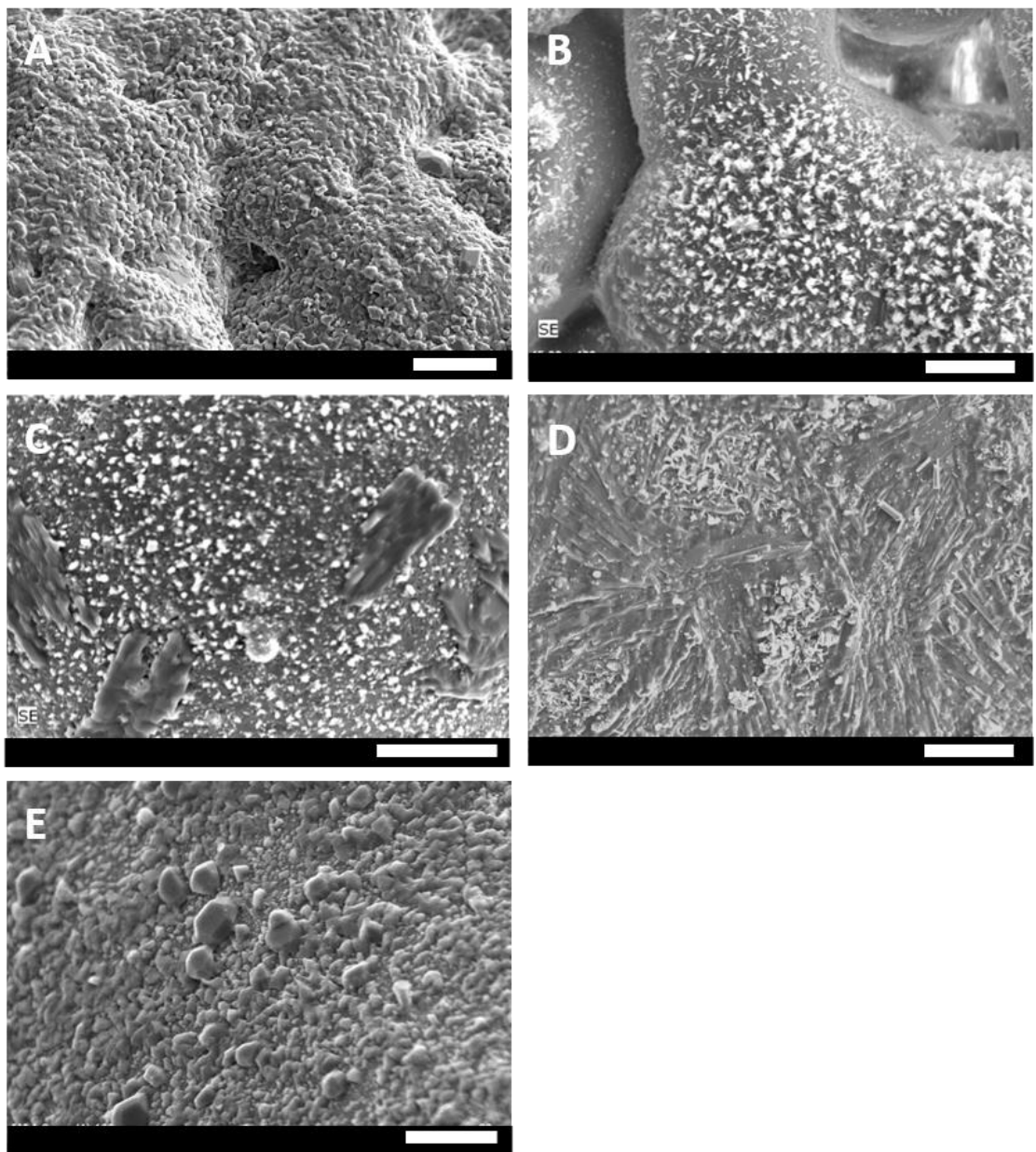
Figure 4.14: Low magnification imaging of the natural surfaces for scaffolds composed of a given particle size range; <45 μm (A), 45-90 μm (B), 90-125 μm (C), 125-1000 μm (D), 1000-2000 μm (E). All scale bars are equal to 20 μm.
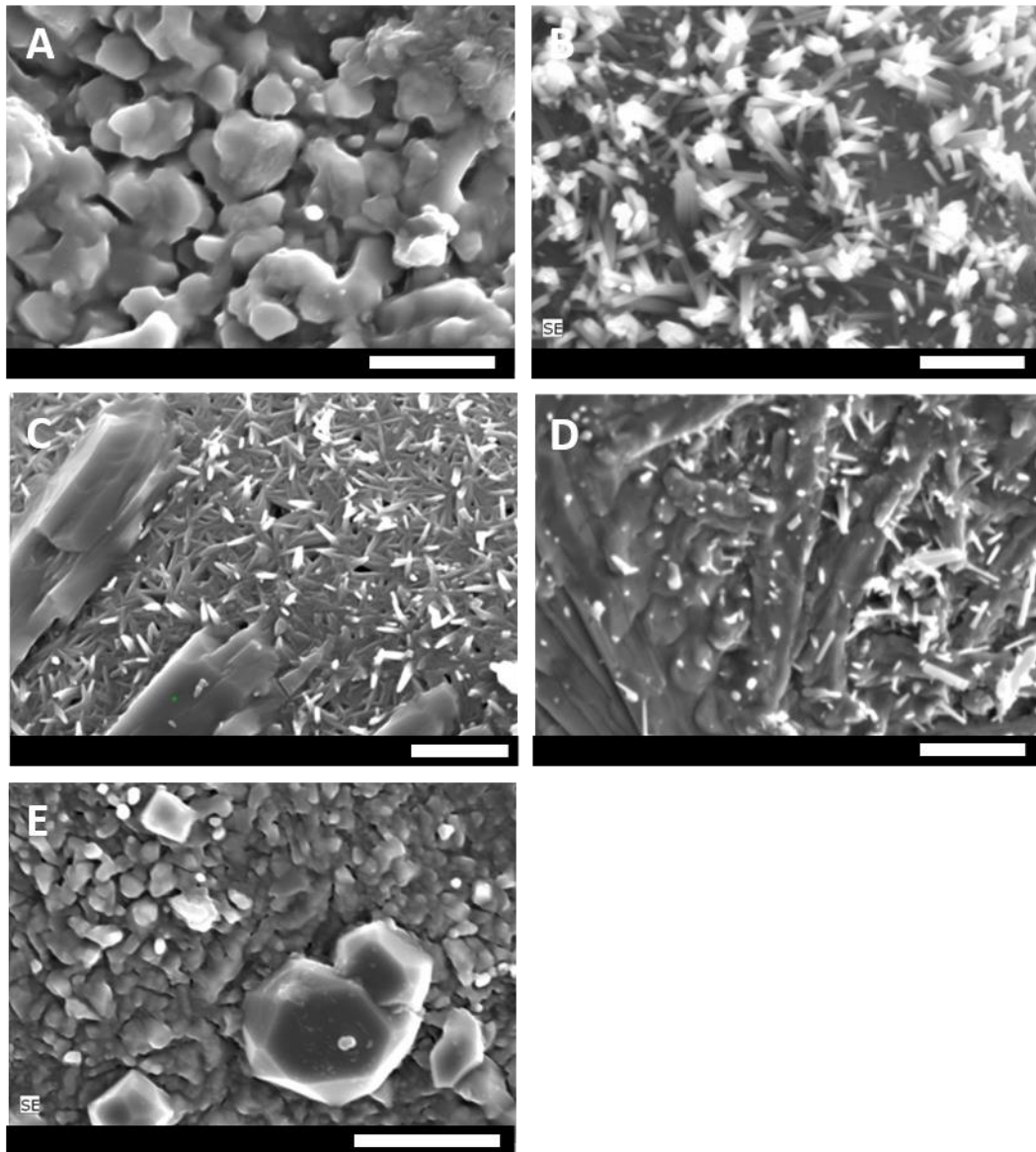
Figure 4.15: High magnification imaging of the natural surfaces for scaffolds composed of a given particle size range; <45 μm (A), 45-90 μm (B), 90-125 μm (C), 125-1000 μm (D), 1000-2000 μm (E). All scale bars are equal to 6 μm.

EDX enhancement of the low (Figure 4.16) and high (Figure 4.17) magnification natural surface images allowed the identification of distinct phases present throughout these regions.
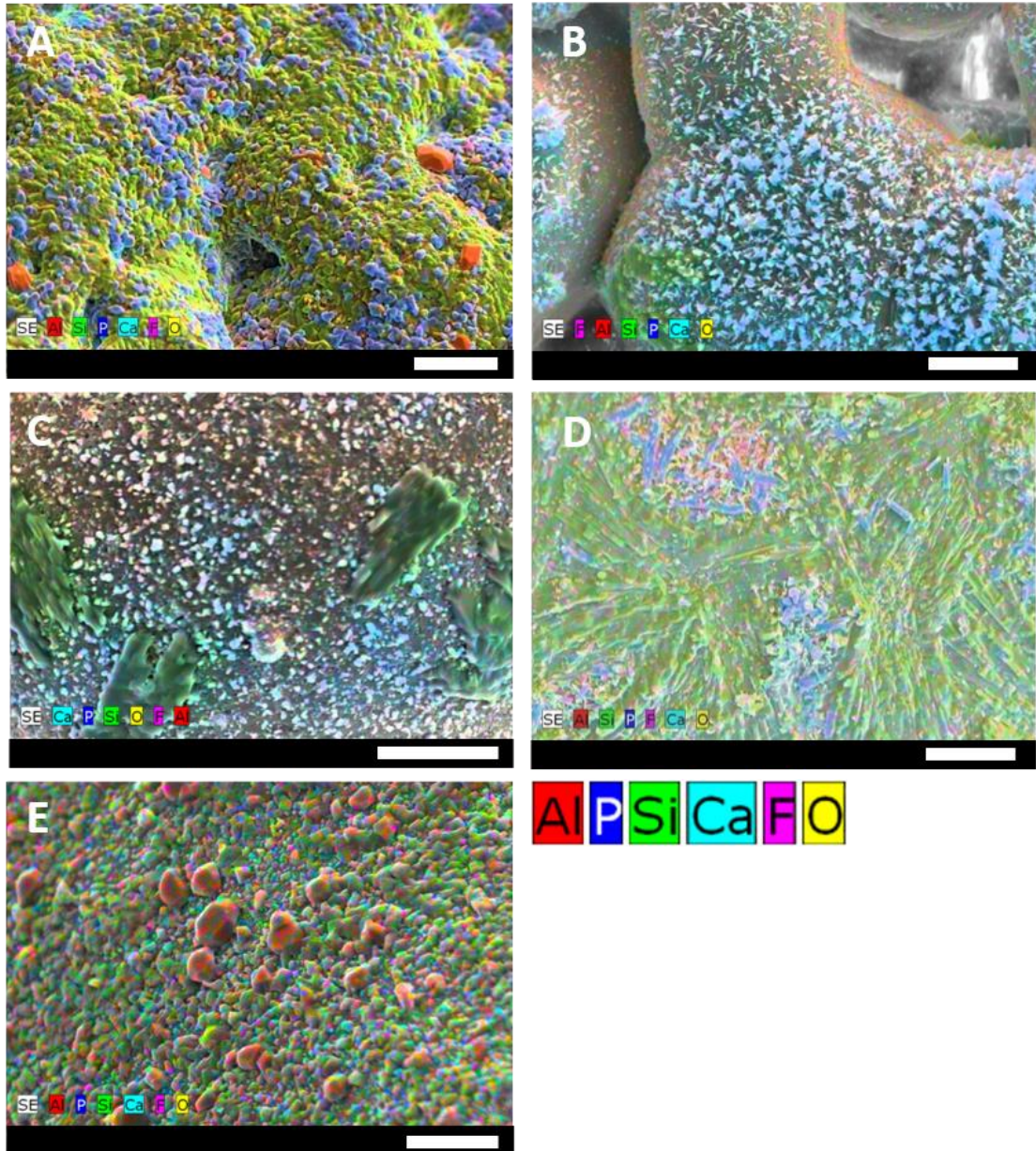
Figure 4.16: EDX enhanced low magnification imaging of the natural surfaces for scaffolds composed of a given particle size range; <45 µm (A), 45-90 µm (B), 90-125 µm (C), 125-1000 µm (D), 1000-2000 µm (E). All scale bars are equal to 20 µm.
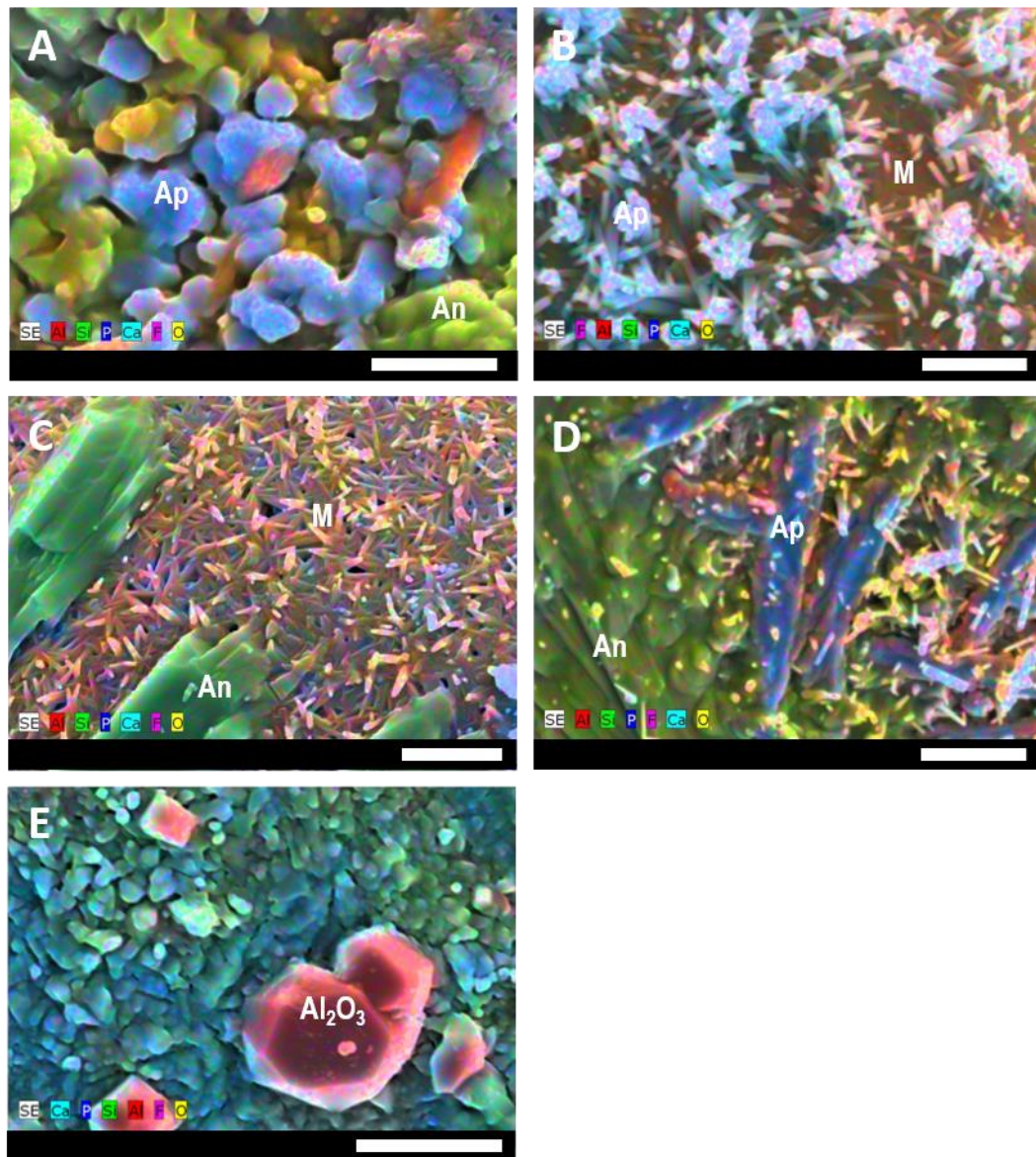
Figure 4.17: EDX enhanced high magnification imaging of the natural surfaces for scaffolds composed of a given particle size range; <45 μm (A), 45-90 μm (B), 90-125 μm (C), 125-1000 μm (D), 1000-2000 μm (E). All scale bars are equal to 6 μm.

Spectral analysis identified the presence of both apatite and anorthite phases at the natural surface of the <45 μm scaffolds (Figure 4.17, A). The rod-like crystalline phase at the 45-90 μm surface was Identified as the apatite phase due to the high Ca and P content, while the immediate substrate had a high Al content and is regarded as mullite. Though there is some indication of apatite at the surface of the 90-125 μm scaffolds the needle-like structure appears to be predominantly Al heavy (mullite), while the large monolithic regions have a compositional match to anorthite (Figure 4.16 and Figure 4.17, C). Anorthite was again identified at the 125-1000 μm surface, although in larger quantities, the needle-like regions dispersed throughout this

surface were observed to contain high levels of Ca and P and so were identified as apatite in the current analysis (Figure 4.16 and Figure 4.17, D).

At the 1000-2000 μm scaffold surface the composition was harder to define with no clear indication available, however, large Al heavy crystalline deposits were identified over the surface region that were also seen to a lesser degree on the <45 μm natural surfaces (Figure 4.16, A and E). Spectral analysis determined these regions to be alumina (Figure 4.18). In the first instance it was believed that this could be an artefact from the crucibles used to produce the parent glass melt, however, image and EDX analysis of the parent glass found it to be negative for any alumina contamination. Therefore it is considered that the alumina is a product of the sintering process at these particle size fractions.
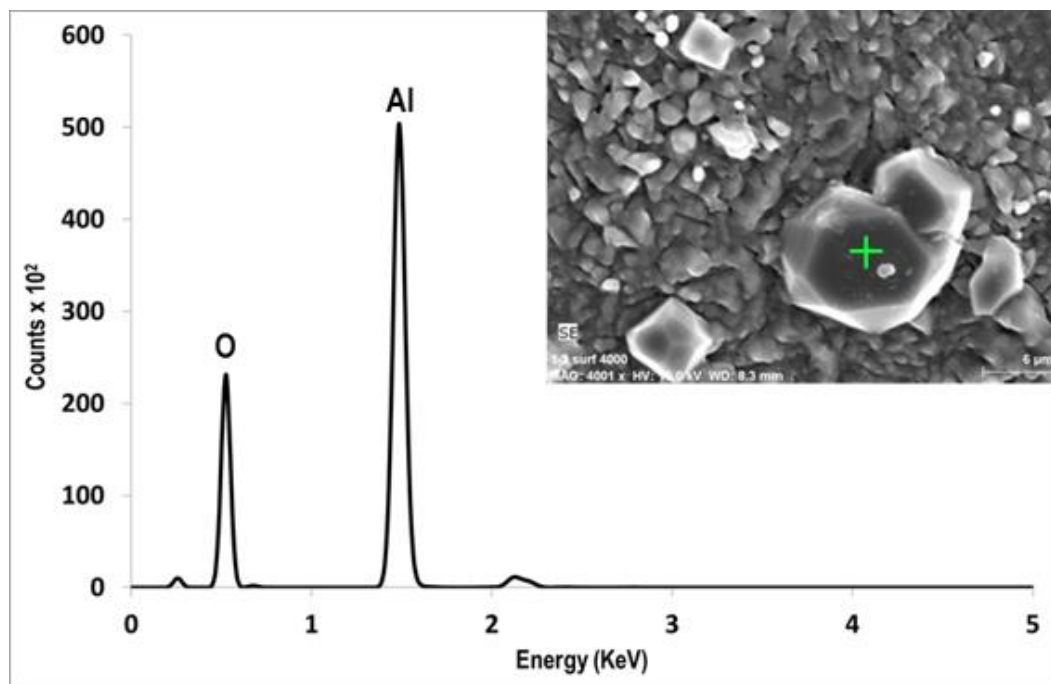
Figure 4.18: EDX spectrum of alumina at the surface of the 1000-2000 μm scaffold

4.4 *Discussion*

Previous studies have been undertaken to investigate the influence of factors such as the CaF_2 molar ratio and casting temperatures on the BFS of AM-GCs based on the $SiO_2 \cdot Al_2O_3 \cdot P_2O_5 \cdot CaO \cdot CaF_2$ glass system used in the present analysis [117, 131]. These studies reported optimum BFS values in the range 136.2 -152.8 MPa, while in the current study a max strength of 116.3 MPa was achieved. However, when we consider that the previous studies were performed on fully dense components, created through a lost wax casting process, the strength level achieved in the current porous components is quite substantial. The BFS testing allows for the determination of a brittle material's response to loading forces in terms of strength, defined as the ultimate stress that is needed to cause fracture and is strongly influenced by the size of flaws (pores in the scaffold structures) within the material. Though previously a three point bent test was used to determine material batch reproducibility and the optimum heat treatment regime, the BFS methodology is used in the current chapter in order to better evaluate its performance with respect to the intended application. This is due to the lower shear stress levels and edge effects experienced during the BFS testing methodology, giving a closer representation of pure bending [132].

With respect to the natural human EP tissue a number of studies have performed regional indentation tests reporting mean failure loads ranging from 100-259 N. However, independently the central region of the EP tended to undergo failure at loads between 50-100 N [133-135]. The current study reported mean failure loads ranging between 8.1-48.8 N over the four particle fractions investigated. Though these failure load levels are considerably below those reported in the natural EP it is important to note that due to the nature of testing, a comparison between BFS and natural EP strength would be more appropriate, as factors such as indenter geometry can vary in literature. However, accurate strength determined in relation to regional indentation studies could not be determined as in all cases a hemispherical indenter tip was used, although, an estimate considering a flat indenter tip of the same diameter generates a mean strength range of between 7.1-56.8 MPa, falling well within the current BFS range (16.2-116.4 MPa). This approximate strength range based on the assumption of flat indenters would be expected to give an under estimate of the natural EP failure strength. We also need to consider that the current BFS testing, carried out to BS EN ISO 6872:2008 standards, does not consist of an underlying substrate such as the trabecular bone of the natural EP which is believed to support approximately 40% of EP loading [136]. Therefore, the BFS values should be considered a

substantial underestimate of that achievable were the scaffolds to be integrated, as intended, with the supporting trabecular structure of the natural vertebral body.

There are a number of studies that determine EP failure strength under larger flat indenters designed to represent subsidence of intervertebral device components. Values for the EP strength are reported to range between 2.2-2.9 MPa [137, 138]. These values are reported corresponding to failure loads in the range of 500-3000 N, therefore, it is the authors opinion that significant edge effects will have contributed to the early EP failure due to the uneven conformity between the natural tissue and flat indenters of significantly large diameters. This notably lower strength could relate to the buckling of the underlying trabecular structure and not the EP failure itself. This can be supported by the noted observation of a hemispherical zone of failed trabeculi beneath large diameter indentation test sites [137]. Considering the strength capabilities of the natural EP and the porous AM-GC components created here and the fact that under normal daily loads the hydrostatic pressure of the disc is between 0.6 and 2 MPa [139, 140]. The scaffolds, regardless of size fraction, may be presumed at this point to have the strength levels required to support the daily loading under normal conditions.

Although there are conflicting views on whether the vertebral EP region is to be distinguished from that of a highly dense trabecular structure, the current functional comparison will consider the porosity of a highly dense trabecular region to that of the scaffolds. This is partly due to the scarcity of data regarding natural healthy EP tissue and the inherent interconnected structure produced by the sintered particles of the scaffolds. Dense trabecular bone is reported as having a porosity of approximately 40% [141]. In the current study, the maximum porosity achieved was 37.6%, obtained in the 90-125 μm particle range (Figure 4.6). Although there is only a 2.4% difference in the achievable porosity and that reported for dense trabecular regions, when considering the intended application as an osteointergrated scaffold we must also bear in mind the respective pore size, represented here by μCT spacing data (Table 4.6). Natural trabecular bone has a pore size range of between 200-600 μm. However, it is reported in literature that pores in the range 100-500 μm promote bone ingrowth and that pores must be > 100 μm in order for tissue to remain viable [142, 143]. This pore size limitation is imparted due to the need for blood supply of the ingrowing tissue, as vascular tissue does not appear in pores that measure < 100 μm [101]. Therefore, in order for the scaffolds to support viable tissue ingrowth based on the current production method only the 125-1000 μm or 1000-2000 μm particle fractions would provide the necessary pore size (Table 4.6), since there is no significant difference between the

BFS of the 90-125 μm and 125-1000 μm particle size fractions (Figure 4.4). In the current application, function would outweigh the need to mimic form in relation to scaffold geometry, as the near match in porosity observed in the 90-125 μm range scaffolds would be far outweighed by the potential ability of the 125-1000 μm scaffolds to provide vascular ingrowth and a more stable osseointegration. The use of this particle fraction would also still only represent a 7.8% difference in overall porosity in relation to dense trabecular bone.

In relation to the nucleation mechanism of the current composition, it was found that both Tp1 and Tp2, were independent of particle size. Therefore, in the current composition crystallisation proceeds via the bulk nucleation process. This is believed partly due to the high fluorine content of the composition but also due to the Ca:P ratio of 1.56, being close to the stoichiometry of natural apatite 1.67. It has been demonstrated previously for compositions based on the current glass system that for Ca:P ratios < 1.5, surface nucleation occurred and for Ca:P ratios > 1.67 crystallisation by bulk nucleation occurred [113, 114]. Hence, although the current composition undergoes bulk nucleation it sits on the compositional boundary at which surface nucleation may be expected. Quantitative Rietveld analysis further confirmed that the major crystalline phase present in all particle fractions investigated was FA, closely followed by Mullite. It was also identified that small percentages of anorthite were present within the structure, the degree of which reduced slightly in combination with increasing particle size fraction. The presence of anorthite is not surprising as it has previously been linked to the glass system under study, nor is it of major concern as it has itself been studied as a mineral component within FA based glass ceramics and proposed as a suitable inert biomaterial for use in bioceramic scaffold applications [114, 129].

The only sample to demonstrate any notable difference in relation to the phase composition is observed in the <45 μm particle fraction. This is in the form of a moderately higher FA and mullite content seen at the consequence of residual glassy phase content (Table 4.8). The maximum differences observed in FA and mullite content were 9% and 12%, respectively, though this is not an alarmingly high variation considering the number of variables present in the production process (e.g. heating/cooling rate, furnace positioning, mould geometry, grinding, weighing etc..) it is still worth noting. One possible explanation is attributed to the exceptionally larger surface area present in the <45 μm particles during heat treatment and the initial high temperatures at which this process is performed. Therefore, SiF_4 loss may occur, which has been eluded to in a previous chapter (Section 3.4), to a degree significant enough to influence the amount of

crystallisation, as reduced P_2O_5:CaF_2 ratios have been reported to increase FA content and reduce residual glass in other apatite based glass ceramics [114]. Aside from the discrepancy observed in the <45 μm fraction, particle size appears to have no notable influence on the bulk material phase compositions.

The DSC and Rietveld analysis data is also supported by SEM image analysis of the scaffold fracture surfaces which confirmed the presence of a highly crystalline internal micro-structure consistent over the range of particle sizes analysed (Figure 4.9 and Figure 4.10). Qualitative and quantitative EDS further identified distinct regions as crystalline apatite and a proposed Al rich mullite phase, all interspersed within a residual Si rich glassy matrix (Figure 4.13). The crystal density and random orientation of the apatite phase in particular is perhaps indicative of a high nucleation density, following which aspect ratio may be limited by impingement on neighbouring crystals, as larger aspect ratio apatite has be reported following traditional heat treatment regimens in the current AM-GC system [94]. However, when examining the apatite aspect ratio within an internal pore structures there is no notable increase seen but there is a significant increase in both the crystal definition and aspect ratio of the proposed mullite phase (Figure 4.13). This supports the theory that the apatite phase has formed directly from a droplet phase precipitated via prior APS.

The current glass system has previously been demonstrated as capable of APS through the nucleation and growth mechanism in which a Ca and P rich droplet phase is formed within an Al and Si rich matrix [115]. This current structure is a possible artefact of the rapid heating regime applied during the sintering process as has been previously proposed by Moisescu *et al.* [116]. They demonstrated the formation of rod shaped apatite within an alumina and silica rich matrix in the SiO_2-Al_2O_3-CO-P_2O_5-Na_2O-K_2O-F$^-$ glass system through rapid heating to 1200°C. Under typical heating regimes the apatite crystal phase formed via APS would have a greatly reduced aspect ratio as they are formed directly from the crystallisation of the Ca and P rich droplet phase. However, due to the rapid heating rate crystallisation cannot initially occur due to lack of time. This leads to the two phases formed via APS becoming more compositionally equal as they begin to melt, giving a subsequent reduction in the initial enrichment and size of the Ca and P droplets and, hence, the ability for crystal growth to occur as the Ca and P content of the matrix phase is much greater than would normally be the case. This generates the rod like appearance seen in the current analysis and also explains why the apatite crystals remain the same within the pore regions. In regard to the mullite phase it is perhaps the case that high nucleation density and

earlier formed apatite structure restricts mullite crystal growth. This is again evidenced by the apparent increased size and definition of mullite observed within the internal pores. This novel apatite structure may also account in some part for the relatively high strength levels observed in the porous scaffold components as the crystal interconnectivity is the prime contributor to the greatly increase strength characteristics of GC biomaterials [101].

In contrast to the bulk material composition SEM and EDS identified a vastly differing structure at the scaffold surface in relation to particle size fraction (Figure 4.15 and Figure 4.17). One possible theory as to why this occurs is again based on the degree of F lost through possible SiF_4 release as a function of available surface area [144]. The use of smaller particle sizes generates a greater surface areas over the scaffold component and the degree of F loss is proposed to increase, thereby leading to a surface composition which will have an associated nucleation density related to the heating regime used. On increasing the particle size the F loss is reduced and consequently the nucleation density is increased to such a degree that at the 1000-2000 µm particle size fraction there is little F left within the glassy phase to support notable crystal growth from the nuclei. This would support the observation of lower degrees of surface apatite crystal formation with increasing particle size. Also, the apatite crystals are seen to have a greater aspect ratio but be distributed in small island regions over the 125-1000 µm surface (Figure 4.16 and Figure 4.17, D), a growth characteristic associated with lower elemental resources in the surrounding matrix [94]. On reaching the largest particle size the lack of apatite formation may leave the glassy phase with excess Ca and P which in turn increased phase stability and hinders the mullite formation as Al is still charge balanced in the glass. This leads to the apparent lack of a crystalline apatite or mullite in the large particle scaffolds surface but also may account for the formation of alumina on the surface region as the glass is effectively super saturated with oxygen due to the lack of other phase formations. One obvious question that this theory raises is why a similar surface composition is observed between the <45 µm particle scaffolds and the 1000-2000 µm particle scaffolds. This is thought to be due to the <45 µm particles undergoing initial liquid phase sintering in the first instance, after which it acts as a pseudo solid component and, hence, it would be assumed to have a surface area in a range below even the 1000-2000 µm particle scaffolds.

4.5 *Conclusion*

It was clearly shown that an increase in particle size promoted a decrease in BFS, where the BFS range identified fell within that proposed as suitable for EP application. Another important factor to consider is mean pore size, as this will determine osteointegrative capacity of the material *in vivo*. Therefore, a particle size fraction between 125-1000 µm may be deemed more suitable at the bone-biomaterial interface. It was evident through DSC analysis that the material underwent bulk nucleation mechanism during thermal processing so phase composition was consistent across the differing particle fractions. However, the EDX assessment of the surface composition revealed a substantial difference in relation to particle size. Where there is high importance in generating a high bioactive response to the material, a particle range of 45-90 µm would also be highly applicable due to the greater appearance of surface apatite. This would naturally lend itself to a multi-layered approach, tailoring the construct with optimum regional morphology. The vertebral EP is deemed to be a dense surface layer and not a highly porous structure more suited to osseointegration. At this point, the biological response to the material was deemed to be a priority so a denser construct with a 45-90 µm particle fraction was carried forward for *in vitro* cell seeding and analysis.

Chapter 5: Characterisation of MSCs on AM-GC

5.1 *Introduction*

In order to assess the osteoconductive and/or osteoinductive capacity of the current AM-GC a suitable osteoprogenitor cell population is required. MSCs are progenitor cells able to differentiate into many different cell types, including the osteoblasts present in bone [126, 145]. Given the relative ease with which MSCs are able to be isolated and cultured they are a prime candidate to provide the osteoprogenitor cell population required and as such are utilised in the current study.

5.1.1 *Osteogenic Differentiation of MSCs*

Osteogenic differentiation of MSCs is influenced by a multitude of factors and their associated signal transduction cascades. In particular the canonical / non-canonical Wnt and transforming growth factor-β / BMP pathways are known to modulate osteogenisis in MSC populations [145]. The osteoblastic differentiation of MSCs can be split into several stages: lineage commitment (as osteoblasts and chondrocytes are thought to share a common osteo-chondrogenic precursor); proliferation; extracellular matrix deposition and maturation; and finally mineralization [146]. The osteoblastic differentiation process is characterised by temporal expression levels of a number of distinct osteoblastic markers, such as, ALP, Col αI, OP, ON and OC. Developmental studies have also identified Runx2 and Osterix as the key transcriptional activators of osteogenisis. With Runx2 known to be essential for endochondral bone development and regulation of the osteoblastic markers [147, 148].

Osteoblastic marker expression levels vary in relation to the specific stages of the differentiation process. The cells themselves are also characterised throughout this presumed linear differentiation sequence progressing from MSCs to osteo-chondrogenic precursors, pre-osteoblasts, osteoblasts, then lining cells or osteocytes [149]. Col αI the key framework provider for skeletal structure and subsequent matrix calcification is expressed in the early proliferative stages of osteogenesis then down regulated to low levels of expression throughout subsequent stages of differentiation. ALP is a cell surface glycoprotein involved with the mineralisation of tissues, genomic and enzymatic expression of ALP is upregulated following the subsidence of the proliferation stage but decreases once mineralisation is well progressed. Onset of mineralisation brings expression of other bone matrix markers, OP a sialoprotein constituents of the cement line involved with bone remodelling and ON a glycoprotein responsible for the

nucleation of HA within the matrix. Finally OC is a late marker of osteoblastogenesis upregulated in post proliferative mature osteoblasts and highly expressed in osteocytes, OC is the only gene not expressed in any other ECM producing cell types (Figure 5.1) [146, 148-151]. It should be noted, however, that these expression patterns are defined from a range of studies most of which differ with regard to aspects such as tissue source and cell preparation methods. Also, studies of this nature often utilise clonal cell lines to generate a greater accuracy when investigating temporal expression patterns of differentiation markers, however, it should be considered that the osteoblastic phenotype itself may present different levels of expression for given markers between donors [146]. It is therefore important when studying heterogeneous cell populations to use a range of markers in order to examine the *in vitro* osteogenesis of MSCs.
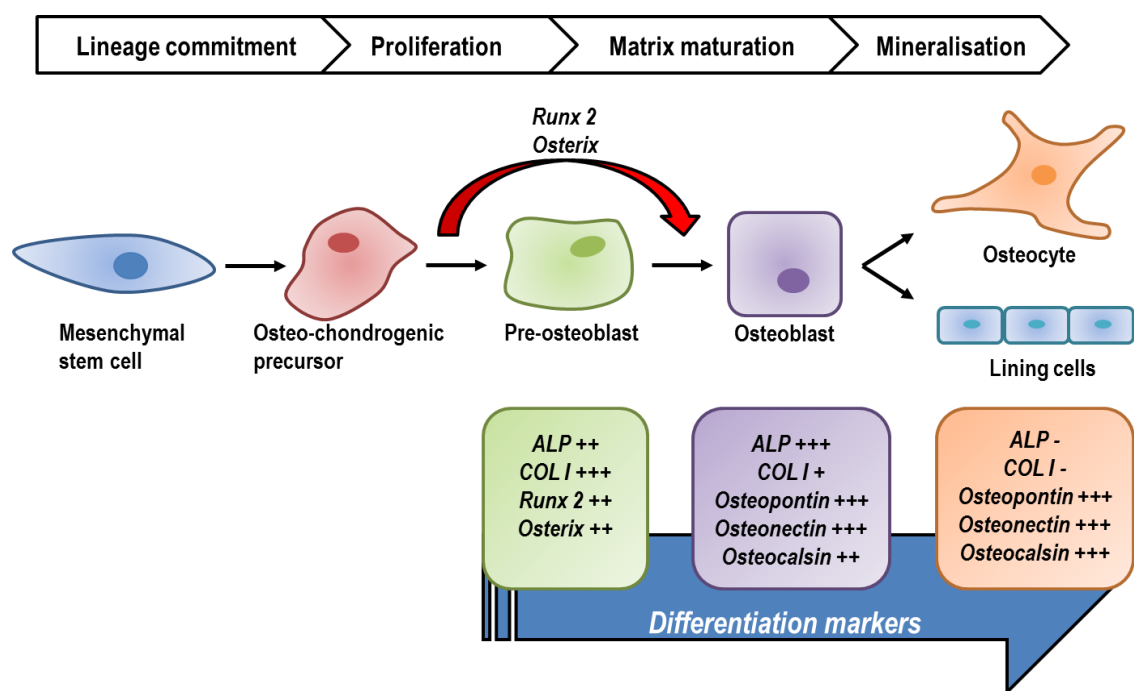
Figure 5.1: Schematic illustrating the stages of MSC differentiation in relation to both cell type and osteogenic differentiation marker expression.

The culture of osteoprogenitor and osteoblast like cell populations on FA based bioactive scaffolds has in many instances been reported to improve both the proliferative capacity and/or osteogenic differentiation potential of cells with respect to those cultured on more traditional HA based materials. This has been reported in most instances via aspects such as increased proliferation rates and enhanced ALP activity levels [152-154]. However, some studies have also examined the expression levels of differentiation markers. One study found that substitution of 40% FA into HA bioceramic generated higher levels of expression for osteoprotegrin, a protein

involved in bone metabolism, but also OP and ON matrix proteins [154]. The presence of OP mRNA has also been used to illustrate the process of new bone formation during *in vivo* analysis of fluoride substituted apatites [155]. It is the proposed fluorine release from the biomaterial compositions that is believed responsible for the enhanced osteogenic performance as fluorine is known to stimulate the proliferation and differentiation of bone cells [152]. However, the genomic up regulation of the osteogenic markers Col αI, Runx 2 and OC has also been demonstrated by HA/mullite compositions in the absence of fluoride highlighting the potential for the current AM-GC, having both FA and mullite phases present [130].

5.1.2 Osteoinductivity of Bioceramics

Osteoinduction refers to the ability of one tissue or material to induce a second undifferentiated tissue to differentiate into bone. The concept of bone induction was first proven in 1931 when the transitional epithelium of the urinary bladder was implanted into the abdominal wall muscle of dogs producing a ossification response [156]. However, it was not until a series of studies by Urist and Reddi on demineralised bone matrix identified BMPs as having more osteogenic potential than DBM alone [157-159]. Since there implication in the osteoinductive phenomenon the use of BMPs and other growth factors have been investigated for use in combination with many synthetic scaffold materials for bone tissue applications. Hence, it is now common place for BMPs to be used in combination with bioceramics for bone tissue repair in clinical application.

More recently research into the osteoinductive nature of bioceramics has identified many factors that can influence its capacity to induce osteogenesis, such as, surface topography, composition, particle size and porosity [142, 160]. It has also been demonstrated that bioceramics can induce ectopic bone formation even in the absence of exogenous growth factor addition [161]. However, it is believed that following implantation synthetic apatites facilitate protein adhesion from the circulating body fluids which may account for the marked influence of geometric and compositional factors on osteoinductivity [142, 160]. This being the case it is still unclear whether it is the biomaterial itself or an interaction between the biomaterial and relevant proteins that is primarily responsible for osteoinduction. One major factor to suggest a more significant role of the biomaterials is the fact that bone induced by bioceramics is always intramembranous while that induced by BMPs is mostly formed by endochondral pathways [162]. It is therefore the lack of current understanding of the exact mechanisms that lead to osteoinduction that blurs the boundaries between biomaterial and growth factor influence on osteogenesis.

5.1.3 Study Aim

To investigate cellular response to the AM-GC substrate previously developed in chapters 3 and 4, using MSC progenitor cell populations. This will include cell viability, proliferation and number before investigating further in to osteogenic differentiation aspects commonly desired for bone substitution applications.

5.2 Materials & Methods

5.2.1   Apatite-Mullite Custom Scaffold Production

Two mould geometries were used in the current chapter to address the specific cell culture application requirements. Both moulds were cylindrical and produced scaffolds with either a 10mm or 3.4mm diameter for use in 48 (AM_{48}) and 96 (AM_{96}) well plate studies respectively (Figure 5.2). The 45-90 µm stock glass particles were used exclusively to produce the scaffolds all of which were sterilized by autoclaving at 103 kPa for 15 minutes at a temperature of 121°C.
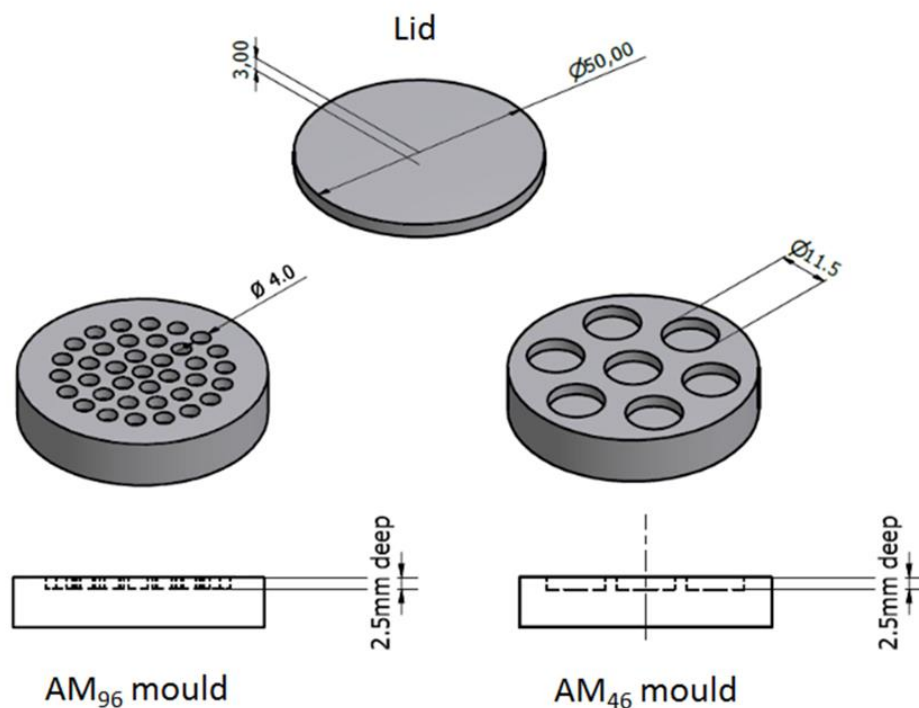
Figure 5.2: Carbon moulds for custom scaffolds produced for use with 96 well (left) and 46 well (right) cell culture assays.

5.2.2   Scaffold Seeding and Density Optimisation

Prior to cell seeding, all scaffolds were submerged in basal medium at 37°C for 30 minutes to allow for sufficient wetting out of the samples. In each case the required number of cells were suspended over the upper scaffold surface in 400 µl of basal medium. Scaffolds were then placed into the cell culture incubator at 37°C and 5% CO_2 for 1 hour after which the medium was re-suspended over the scaffold surface. Following a further 1 hour incubation, the scaffolds were

transferred to a new well with fresh media added and returned to cell culture prior to further analysis.

In order to determine optimum cell seeding numbers, AM$_{46}$ scaffolds were seeded with MSCs at 1×10^5 , 5×10^5 and 1×10^6 cells/scaffold. The level of cell confluence over the scaffold surface was then analysed using SEM 24 hours post seeding.

5.2.3 Scaffold Seeding and Construct Culture

AM-GC scaffolds were seeded with the optimum cell number to provide confluence at 24 hours in culture, determined as previously described (Section 5.2.2). Therefore, unless otherwise stated, 5×10^5 cells in 400 µl of basal medium were used for AM$_{46}$ scaffolds and 6×10^4 cells in 200 µl of basal medium for AM$_{96}$ scaffolds. In cases where osteogenic differentiation was induced, medium containing osteogenic supplements (Section 2.3.2) was added 24 hours after the seeding process.

5.2.4 Cell Viability Determination

To assess cell viability on the AM-GC scaffolds, MSCs were analysed using a live/dead fluorescence cell staining assay (Invitrogen, viability/cytotoxicity kit, L3224). 2 µl of the intracellular esterase stain, calcein AM (4 mM) and 4 µl of the nucleic acid stain, ethidium homodimer-1 (2 mM), were added to 1 ml of PBS to give an 8 µM solution. 250 µl of the solution was then added to the seeded AM$_{96}$ constructs in flat bottomed 96 well plates. The constructs were then incubated for 40 minutes in the dark at room temperature and subsequently washed in PBS then fixed in 4% glutaraldehyde in PBS for 15 minutes. Samples were imaged on the inverted confocal microscope (Zeiss, LSM 710 meta on an Axiovert 200M) at 488nm for green fluorescence and 543 nm for red fluorescence.

5.2.5 Click-iT Cell Proliferation Assay

Cell proliferation on the scaffold substrate was determined using a Click-iT EdU (5-ethynyl-2´-deoxyuridine) DNA incorporation assay (Invitrogen). AM$_{96}$ scaffolds were seeded subconfluently with 2×10^4 MSCs and cultured in basal medium for 48 hours, after which the Click-it EdU working solution was added to give a 50 nM concentration in basal medium. Scaffolds were then cultured for a further 24 hours prior to analysis. As a non-proliferative control, samples were cultured in medium containing 0.5% serum. Cells were fixed on the scaffold with 3.7% formaldehyde in PBS

and permeablised for 20 minutes in 0.5% Triton X-100 (Fisher chemical, BP151-500) in PBS. To label the EdU incorporating cell fraction, 0.5 ml of EdU detection reagent was added to each scaffold and incubated at room temperature for 30 minutes in the dark. Following EdU detection, cells were incubated in 5 μg/ml of Hoechst 33342 for 30 minutes at room temperature to provide a nucleic acid counterstain. Samples were imaged on the inverted confocal microscope (Zeiss, LSM 710 meta on an Axiovert 200M) at 405 nm for Hoechst fluorescence and 543 nm for EdU fluorescence.

5.2.6   Cell Number Determination

Cell number was analysed over a seven day period on both AM_{96} scaffolds and TCP control substrates using a colourimetric cell proliferation assay (Cell Counting Kit-8, Sigma-Aldrich). Six scaffolds and six wells of a 96 well plate were each seeded with $2x10^3$ cells suspended in 100 μl of basal medium. The assay was undertaken at the 24 hour, 3 and 7 day time points by adding 10 μl of Kit-8 reagent to 100 μl of basal medium and incubating for 1.5 hours at 37°C in a humidified atmosphere of 5% CO_2 with 95% air. Following incubation, medium was transferred to wells of a fresh 96 well plate and the absorbance analysed on a micro-plate reader (Dynex MRXII; Dynatech) at 450 nm. A cell number standard ranging from $2.5x10^4$ to $7.8 x10^2$ cells was also determined using MSCs seeded in 96 well plates in basal media, cell standards were left to attach for 6 hours before absorbance readings were determined. In all cases, 6 replicates were performed and average values used.

5.2.7   Alkaline Phosphatase & *von Kossa Staining*

AM_{96} scaffolds seeded with $6x10^4$ MSCs were investigated in triplicate at four time points, 24 hours, 7, 14 and 21 days and for two conditions, those cultured in basal media and those in osteogenic media (OM). ALP was identified by staining scaffolds for 2 minutes in 0.2 mg/ml naphtol AS-MX in 1% N, N-dimethylformamide diluted in 0.1 M Tris, pH 9.1 plus 1 mg/ml Fast Red TR. Following the ALP stain samples were washed in PBS, fixed in 4% paraformaldehyde then washed twice more, once in PBS then in dH_2O. The von Kossa stain was then performed, this consisted of 15 minutes in 1% silver nitrate in dH_2O on a light box followed by 2 washes in dH_2O and a final 5 minutes in 2.5% sodium thiosulfate. The stained scaffolds were then imaged on a stereo microscope (Zeizz, AxioCam MRc5).

5.2.8   Specific Alkaline Phosphatase Enzymatic Activity Determination

The level of ALP enzymatic activity was determined for MSCs seeded on AM_{96} scaffolds under both basal and osteogenic culture conditions, with TCP basal controls also included in the analysis. Samples were assayed at 24 hours, 7, 14 and 21 day time points via lysis in 250 μl of 0.1% Triton X-100 in 0.2 M carbonate buffer. Following lysis, samples were freeze-thawed from - 80˚C to 37˚C three times and 50 μl of solution was then moved to a fresh well. The ALP activity was determined using a p-Nitrophenyl Phosphate (pNPP) substrate (Sigma-Aldrich; P4744), 50 μl of the pNPP substrate working solution (0.3 mg/ml pNPP, 3.3 mM magnesium chloride in 0.2 M carbonate buffer) was added to the lysis solution and the level of activity determined against a p-Nitrophenyl standard (Sigma-Aldrich; N7660). Sample absorbance was then measured at 405 nm using a microplate reader (Dynex MRXII; Dynatech). ALP activity levels were normalised to sample DNA content using the fluorescent nucleic acid stain PicoGreen (Quant-iT; P7589, Molecular Probes). Briefly a further 50 μl of the cell lysate was removed from each sample and quantified using the PicoGreen assay which was carried out according to the manufacturer's instructions. Sample fluorescence was then measured on a micro-plate reader (BMG Labtech POLARstar OPTIMA) at 485 nm excitation and 520 nm emission.

5.2.9   Real-Time PCR

The expression level of a range of early and late stage osteogenic gene markers were investigated. ALP, Runx2, Col αl, OC, ON, OP and the housekeeping gene RPS27A were determined in MSCs cultured on AM_{46} scaffolds in the presence and absence of OM and on basal TCP controls. Scaffolds were seeded with 5×10^5 cells as described previously (Section 5.2.2) to give a confluent cell layer at 24 hours, following which OM was added to the relevant samples. In the case of the TCP controls 3×10^5 cells were seeded in T25 culture flasks, which also generated a confluent cell layer after 24 hours. Total RNA was isolated from the AM-GC and TCP samples at 0, 7, 14 and 21 day time points for a total of three individual donors in each case.

5.3 Results

5.3.1 MSC Attachment and Growth on AM-GC Scaffolds

5.3.1.1 Optimum Scaffold Seeding Density

AM_{46} scaffolds were seeded with MSCs at $1X10^5$, $5X10^5$ and $1X10^6$ cells/scaffold to determine a suitable seeding density. The results illustrated that a seeding density of $5X10^5$ cells/scaffold produced a confluent cell layer at 24 hours and was regarded as suitable for further analysis with respect to cell differentiation and viability (Figure 5.3, A-C). At higher magnifications, cells were observed to surround individual scaffold particles and also bridge gaps between the particles (Figure 5.3, D-E). The AM_{96} optimum seeding density was determined from the cells per unit area of scaffold used to obtain confluence on the AM_{46} samples. The AM_{96} scaffolds were, therefore, seeded at $6X10^4$ cells/scaffold. This generated a cell layer of comparable confluence to that seen on the AM_{46} scaffolds and hence, suitable for further analysis (Figure 5.3, F)
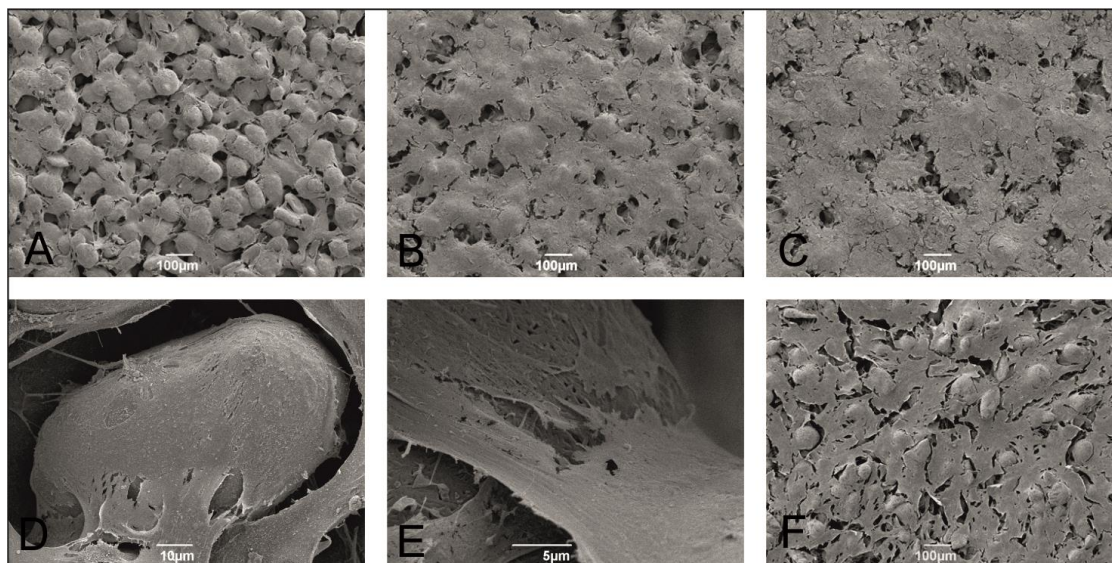
Figure 5.3: SEM imaging of cell seeded AM_{46} scaffolds. Low magnification images of scaffolds seeded with $1x10^5$ (A), $5x10^5$ (B) and $1x10^6$ (C) MSCs. Higher magnification identified cells surrounding individual scaffold particles (D) and bridging gaps between them (E). The AM_{96} scaffolds were seeded with $6x10^4$ MSCs to obtain confluence (F).

5.3.1.2 Cell Viability on AM-GC Substrate

AM$_{96}$ scaffolds were seeded with 6x10^4 MSCs in basal medium, the cell viability was assayed at 24 hours, 7, 14 and 21 days using the fluorescent live/dead cell stain. Confocal imaging demonstrated that the MSCs maintained viability up to 21 days, with a scarcity of dead cells present at any time point (Figure 5.4). The compromised cell fraction does not appear to noticeably increase over the 21 day assay period, with the viable fraction maintaining confluence throughout. A control sample is also shown as a comparator, in which cell death has been induced by addition of 70% ethanol for 5 minutes prior to the live/dead cell staining protocol. The images shown are 2D representations of a series of images taken at different focal planes throughout the respective sample. The results demonstrate that MSCs remain attached to the AM-GC substrate and maintain viability during culture up to 21 days.
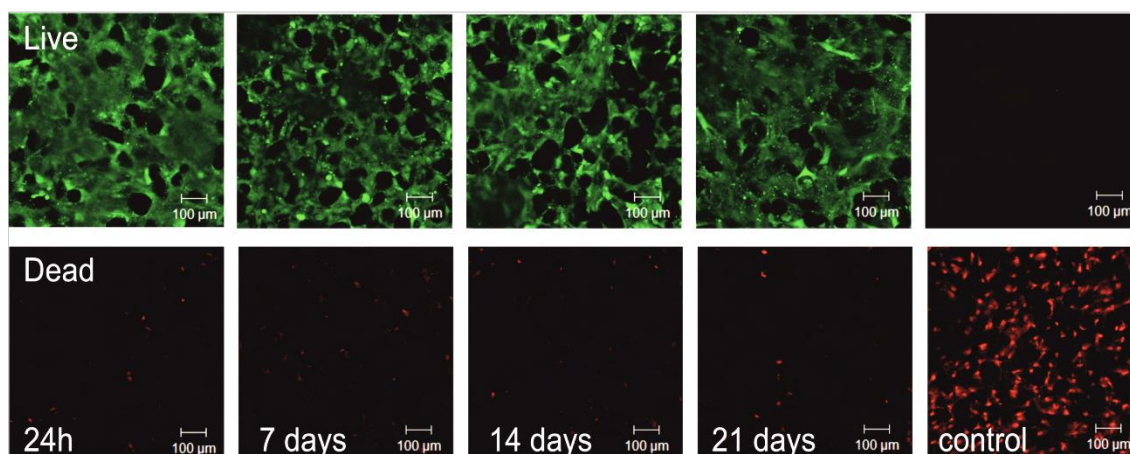
Figure 5.4: Cell viability over the AM$_{96}$ scaffold surface at 24 hours, 7, 14 and 21 days culture in basal medium. Fluorescent confocal imaging demonstrates the respective live (green) and dead (red) cell fractions. Right panel shows ethanol-treated positive dead cell control.

5.3.1.3 Cell Proliferation and Number on AM-GC Substrate

AM_{96} scaffolds seeded subconfluently with 2.5×10^4 MSCs were imaged using confocal microscopy to identify the incorporation of the EdU detection reagent following 24 hours exposure in culture. Cell counts determined that between 11.5% and 23.3% of MSCs proliferated over the 24 hour period. Samples cultured in 0.5% serum were also included as a non-proliferating control (Figure 5.5).
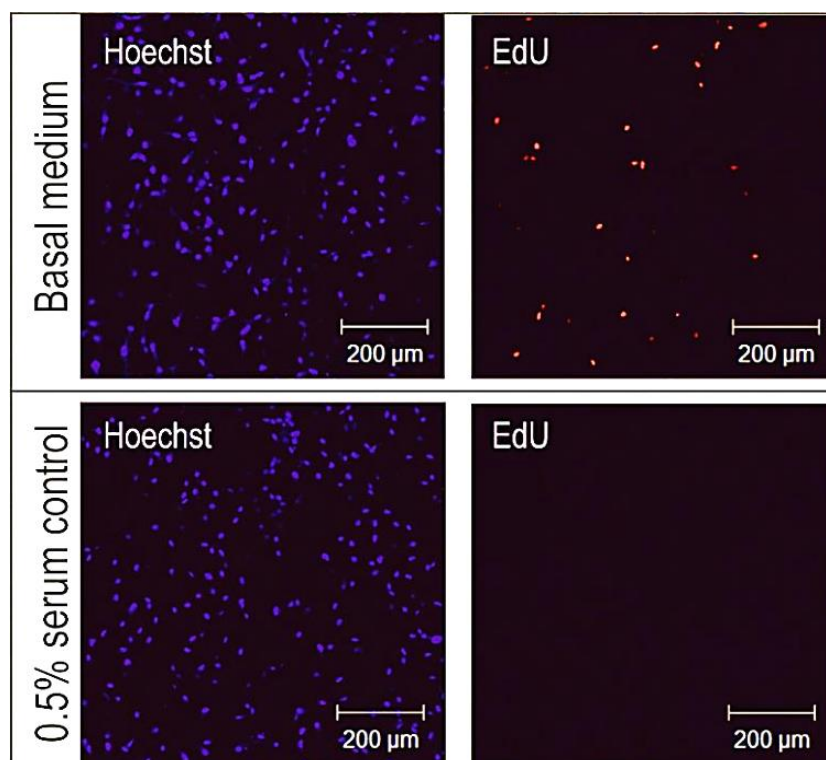
Figure 5.5: Confocal imaging of EdU incorporation into proliferating cell fraction on AM-GC scaffold surface. The 0.5% serum control provided a non-proliferating comparator.

Cell number was investigated on AM_{96} scaffolds and TCP controls initially seeded with 2×10^3 MSCs in basal media at 24 hours, 3 and 7 day time points using the cell counting Kit-8 assay (Figure 5.6, A-B). For both AM-GC scaffold and TCP substrates there was a significant increase in cell number seen between each time point ($p < 0.05$). The cell number observed on TCP controls was consistently higher than that on the AM-GC scaffolds due to the undoubted differences present in initial seeding efficiency. However, the population doubling times of 102 and 99 hours for the AM-GC and TCP substrates respectively only differed by $\approx 3\%$ suggesting the growth rate of MSCs on AM-GC scaffolds does not differ substantially to that on TCP.
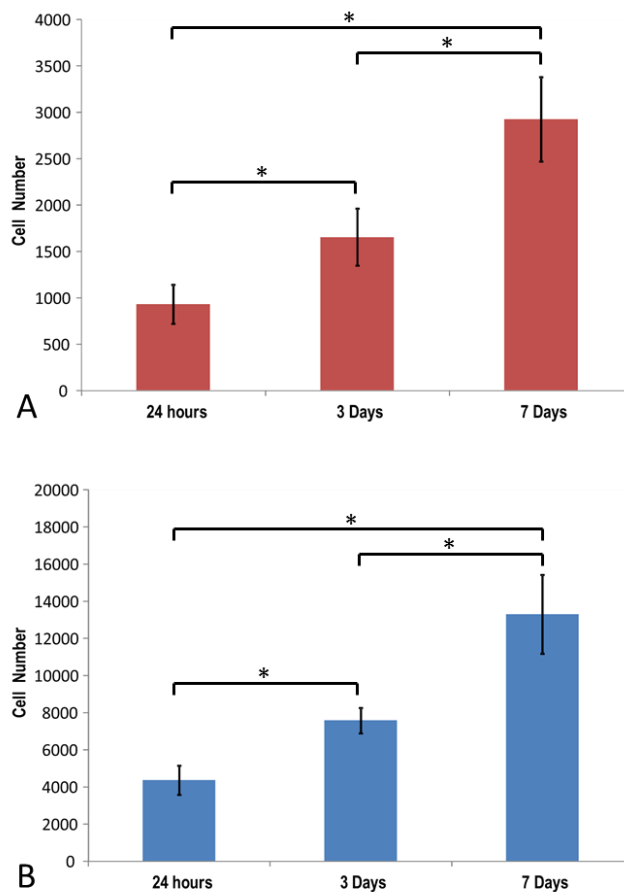
Figure 5.6: MSC number determination on both AM scaffold (A) and TCP (B) substrates. Both substrates were seeded with 2x10³ cells and assayed at 24 hours, 3 and 7 days culture in basal medium. Significance levels are indicated above bars. Data are displayed as mean values ±SD, n=6, *p < 0.05.

5.3.2 Osteogenic Differentiation on AM-GC Scaffolds

5.3.2.1 Alkaline Phosphatase Activity on AM-GC Substrate

AM-GC scaffolds were stained for ALP and von Kossa activity at 24 hours, 7, 14 and 21 days culture in both basal and osteogenic conditions. The ALP staining appears to show no discernible increase over the 21 day culture period when cultured in basal conditions (Figure 5.7). However, in the presence of OM supplements there is a small but present amount of ALP staining visible on the scaffold surface (Figure 5.8). This is most prominent at days 14 and 21 where the cells appear to have formed a more substantial cell/matrix layer over the scaffold surface which is evidenced by the fact that the natural scaffold contours were less visible under the stereo microscope. This change in the apparent surface texture is not seen in the 14 and 21 day basal samples. There was no evidence of von Kossa staining in any of the samples throughout the study possibly due to 3D nature of the stereo microscope imaging.

107
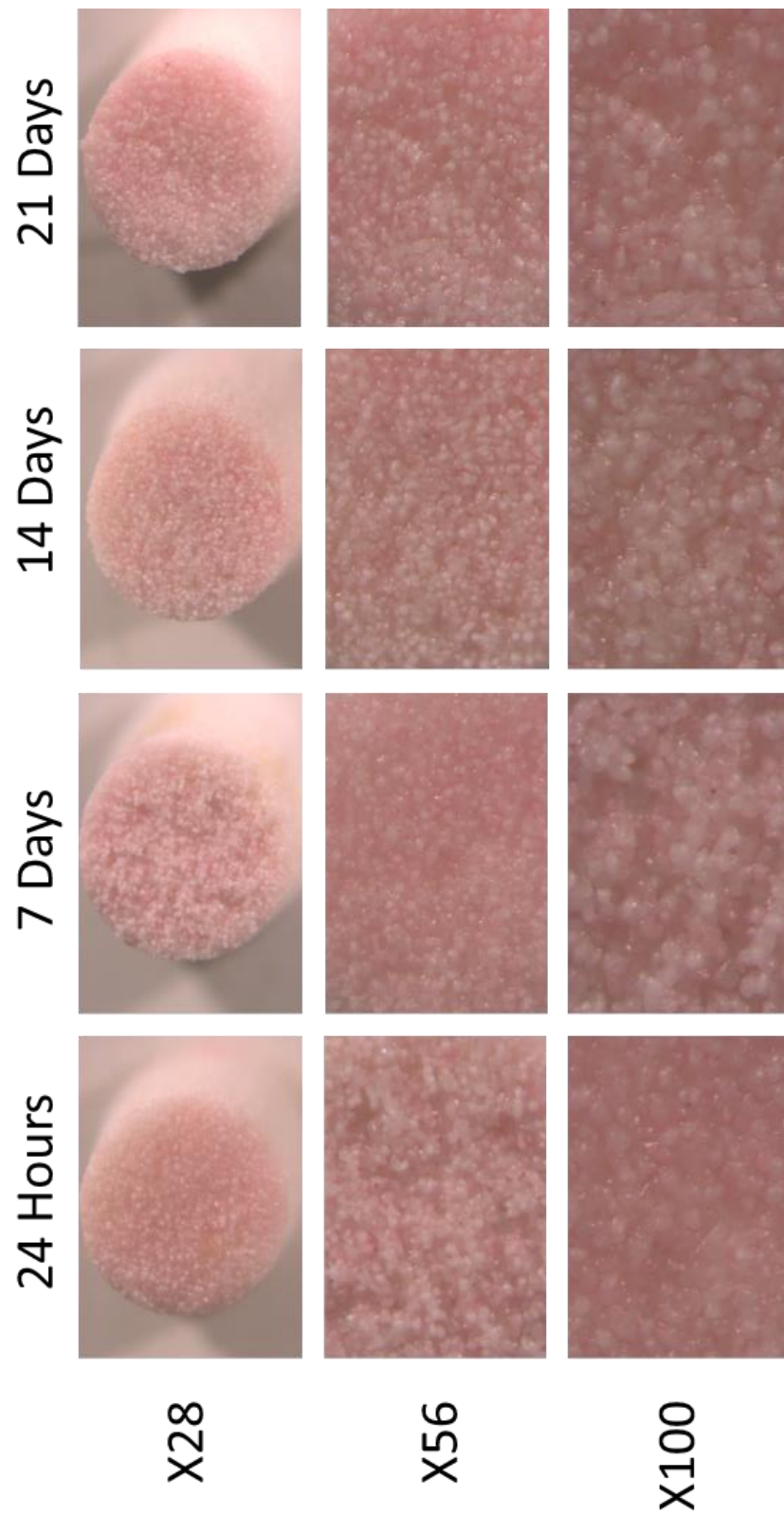
Figure 5.7: AM-GC scaffolds seeded with 6X104 MSCs in Basal medium and stained for ALP and von Kossa at 24 hours, 7,14 and 21 day time points.
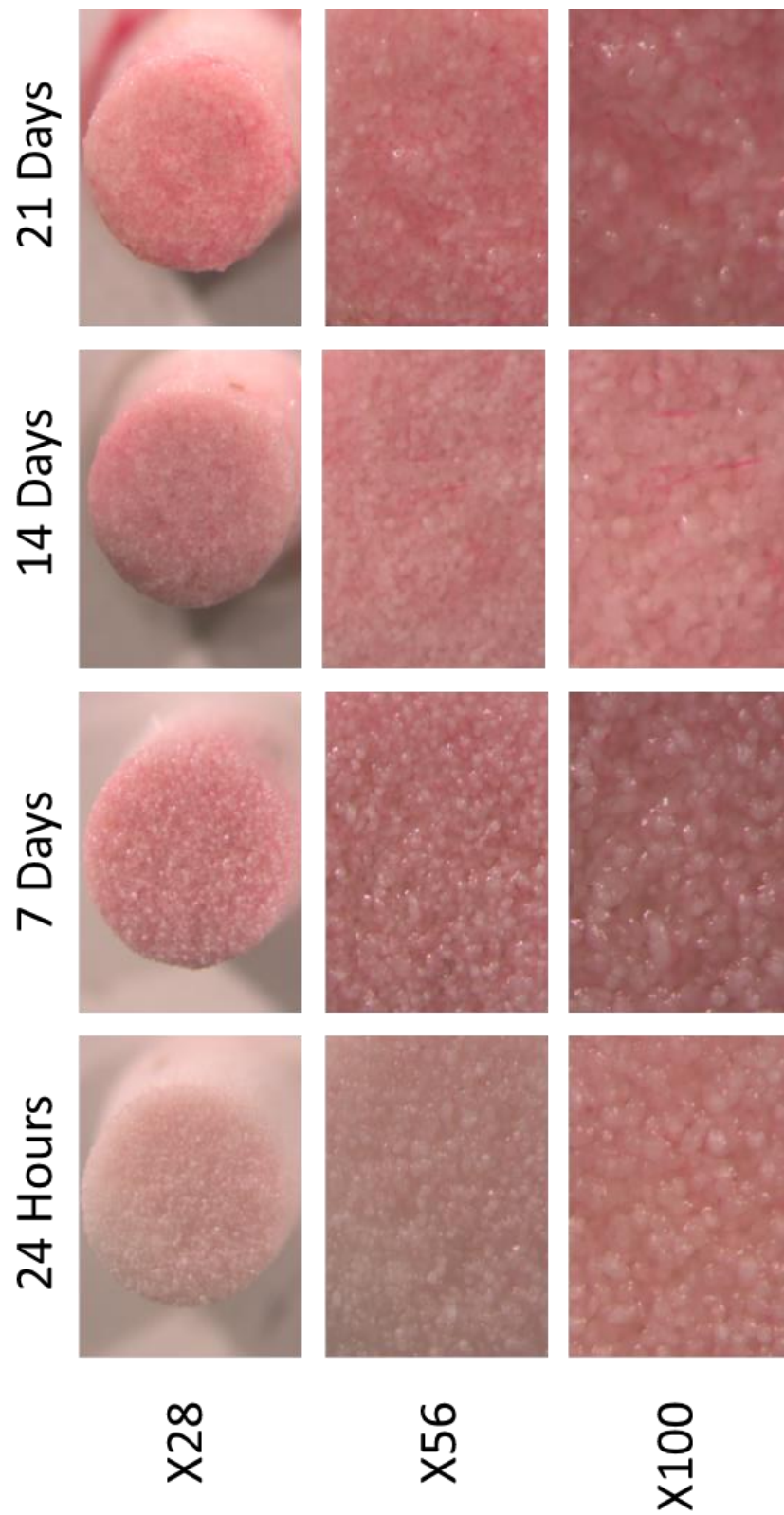
Figure 5.8: AM-GC scaffolds seeded with 6X10^4 MSCs in osteogenic medium and stained for ALP and von Kossa at 24 hours, 7, 14 and 21 day time points. Note the regions of red/pink seen at days 14 and 21 which indicate ALP activity

The specific enzymatic ALP activity was also assessed on AM-GC scaffolds for three independent primary MSC lines at 24 hours, 7, 14 and 21 days culture in both basal and osteogenic conditions, with TCP basal controls included at each respective time point (Figure 5.9).

For donor A (Figure 5.9, A) there was an initial drop in ALP activity from 24 hours to 7 days in all instances, however, between days 7 and 21 there was a subsequent increasing trend observed for all cases. Only at day 7 was the ALP expression significantly greater under AM-GC basal conditions when compared to TCP basal. Though ALP expression was significantly greater at both day 7 and 14 for AM-GC under osteogenic conditions, by 21 days the ALP expression under TCP basal conditions increased and no significant difference was observed.

In the case of donor B (Figure 5.9, B) ALP expression was observed to be significantly greater than that under TCP basal conditions at all instances of culture on AM-GC substrates. With the exception of between 24 hours and 7 day basal conditions, there was a notable increasing trend in ALP expression over time for AM-GC substrates. However, unlike for donor A, this increasing trend was not present in the TCP basal samples, which only displayed a notable increase at day 21. For donor B, ALP expression under AM-GC osteogenic conditions was greater than that of the basal comparator at both day 7 and day 14, however, by day 21 the expression was significantly greater in the AM-GC basal samples.

Donor C (Figure 5.9, C) demonstrated a notably different trend in ALP expression by maintaining levels throughout the culture period under osteogenic conditions on AM-GC, only showing a notable reduction at 14 days which was recovered again by day 21, with the ALP expression was significantly greater than that observed under any other conditions at each instance. In contrast The AM-GC basal comparator demonstrated a notable reduction in ALP expression from 24 hours to 14 days after which it remained constant. This expression level was, however, only significantly greater than that of the TCP basal samples at 24 hours and 7 days, after which there was no significant difference observed.
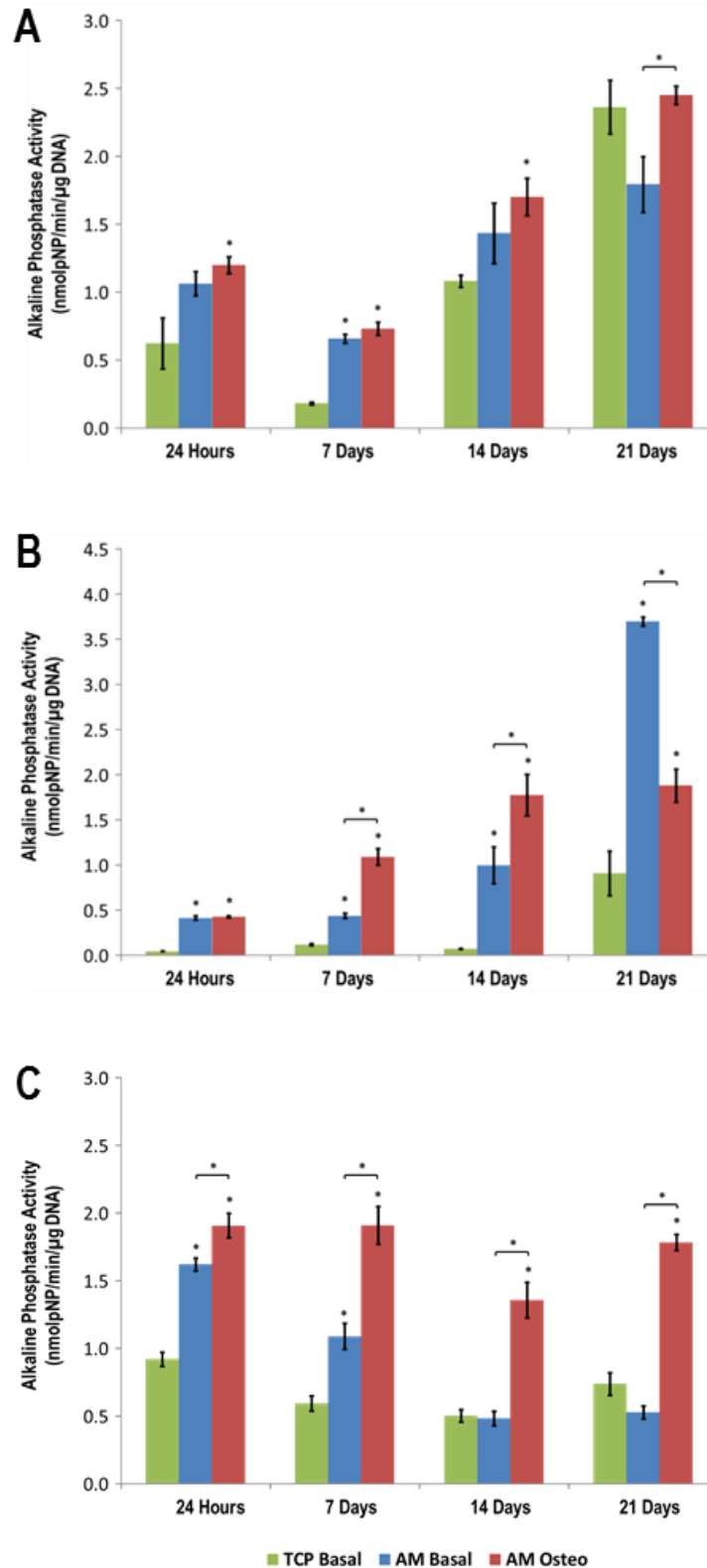
Figure 5.9: Specific ALP activity on AM-GC scaffolds and TCP basal controls at 24 hours, 7, 14 and 21 day time points for three independent donors, A, B and C. Indicators directly above bars relate to a significant difference with respect to TCP basal conditions at the same time point. With brackets indicating significant differences between AM-GC substrates in basal and OM conditions. Mean data are shown ± SEM (n=6) * p<0.05.

5.3.3   Real-time PCR

5.3.3.1 Between Donor Osteogenic Marker Expression Analysis

Because of the natural variation that is seen between donor cell response, it was necessary to split the three donors into separate datasets to allow for meaningful relationships to be extracted.

The expression levels of the six target genes, ALP, Runx2, Col αI, OC ON and OP were determined on AM-GC scaffold substrates in both basal and osteogenic culture conditions at 7, 14 and 21 day time points and compared to TCP basal controls. The analysis was carried out for three primary MSC donor cell lines with data shown as mean Log_{10} of $2^{-\Delta\Delta Ct}$ + the standard error of the mean.

When analysed over all three donors, MSCs cultured in basal conditions showed significantly ($p < 0.05$) greater ALP expression on AM-GC substrates when compared to TCP at two of the nine time points and showed significantly lower expression at three points. In the presence of OM instances of significantly greater ALP expression on AM-GC was increased to five out of nine time points, with three points still significantly lower. With regard to ALP expression donor C showed a notable difference in trend with all time points indicating significantly lower expression on AM-GC substrates in OM compared to TCP basal conditions, whereas donors A and B both show significant increases in all but one instance and no significant reductions (Figure 5.10).

The expression of Runx 2 was significantly ($p < 0.05$) greater at four out of the nine time points when cultured in basal media on AM-GC substrates compared to TCP and significantly lower at three time points. The inclusion of OM to AM-GC culture conditions caused a subsequent reduction in the number of times significantly greater Runx 2 expression was indicated to three instances and an increase in the number of times significantly lower expression was determined to five instances (Figure 5.11).

At three out of the nine time points expression of Col αI is significantly greater for MSCs cultured on AM-GC substrates compared to TCP in basal conditions, no significant reductions were indicated at any other time point. The inclusion of OM to AM-GC samples again decreased the number of significantly greater Col αI expression levels to two but also increased the number of significantly lower expression instances to two (Figure 5.12).
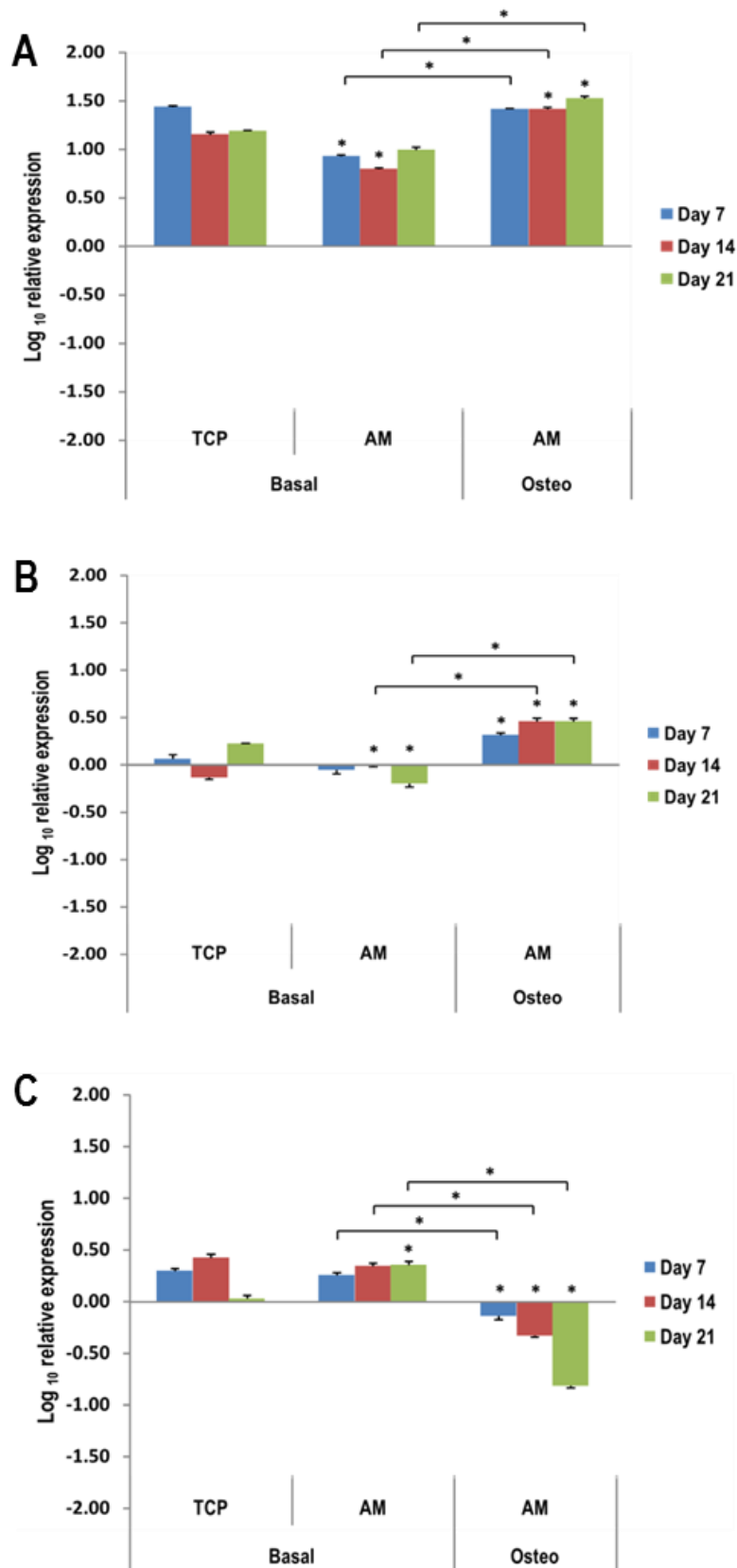
Figure 5.10: Real-time PCR analysis of alkaline phosphatase gene expression on AM-GC substrates in both basal and osteogenic conditions and also for basal TCP control samples at 7, 14 and 21 days. Three independent donors were analysed A, B and C and expression level normalised to that at day 0. Mean data are shown + SEM (n=3) * p<0.05.
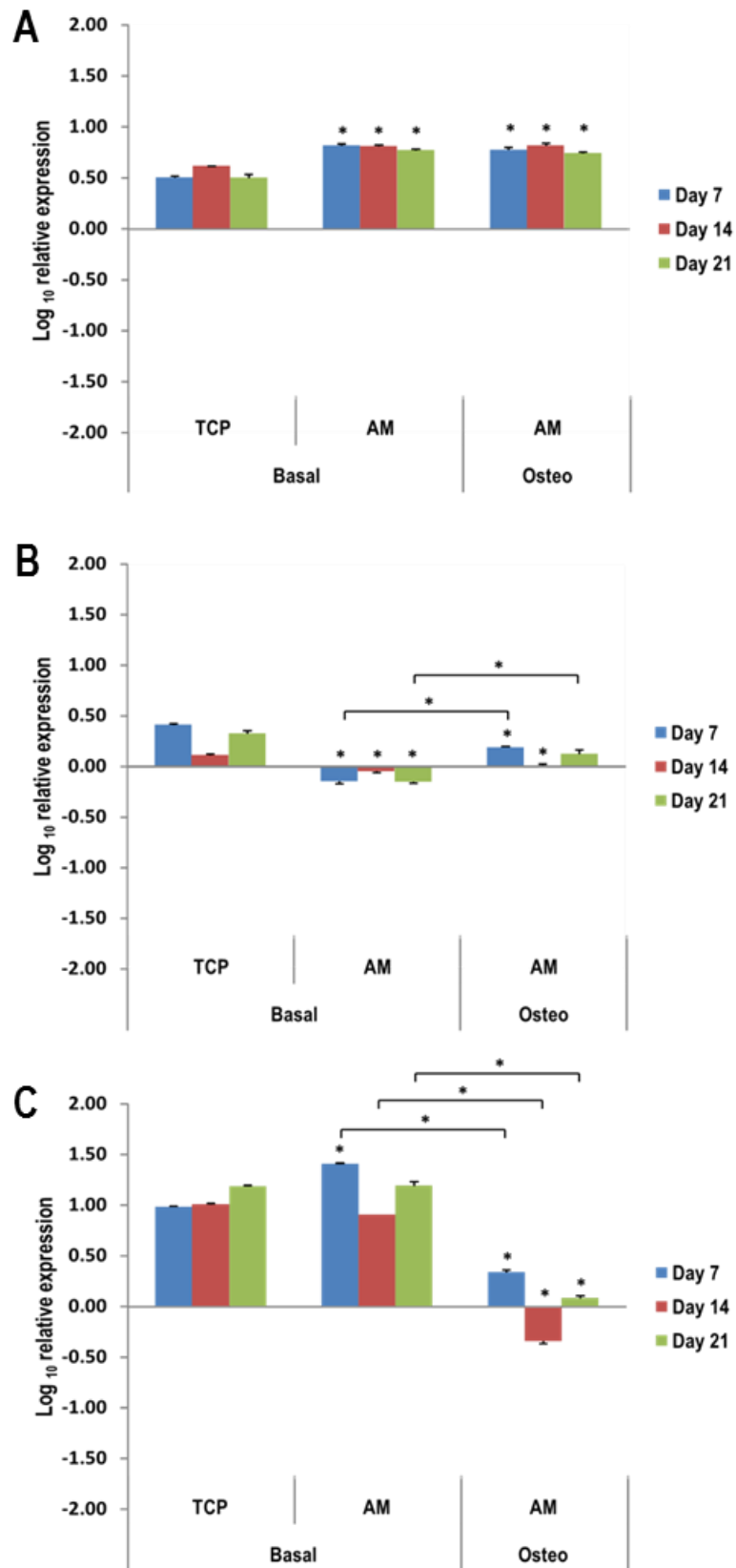
Figure 5.11: Real-time PCR analysis of Runx 2 gene expression on AM-GC substrates in both basal and osteogenic conditions and also for basal TCP control samples at 7, 14 and 21 days. Three independent donors were analysed A, B and C and expression level normalised to that at day 0. Mean data are shown + SEM (n=3) * p<0.05.
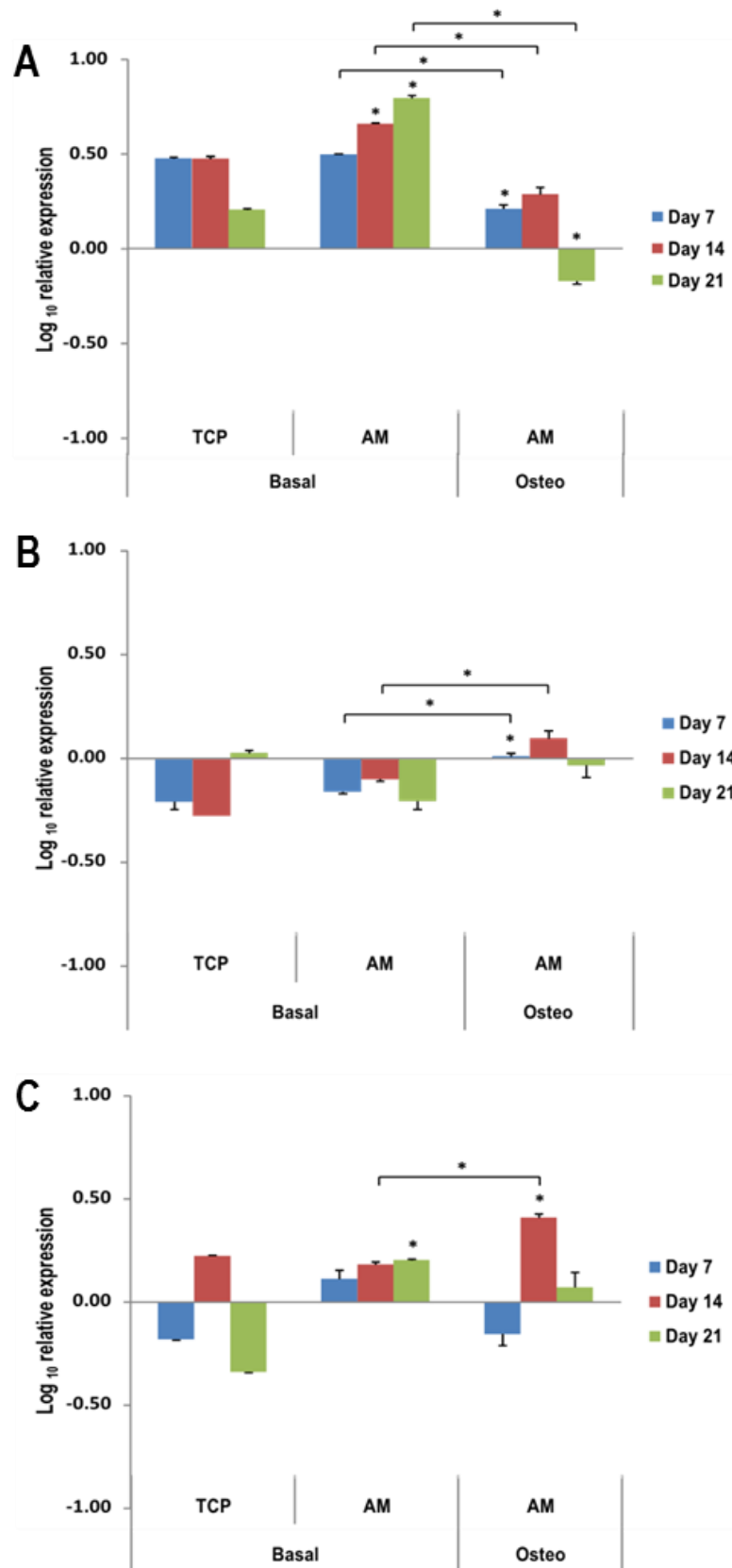
Figure 5.12: Real-time PCR analysis of collagen alpha 1 gene expression on AM-GC substrates in both basal and osteogenic conditions and also for basal TCP control samples at 7 14 and 21 days. Three independent donors were analysed A, B and C and expression level normalised to that at day 0. Mean data are shown + SEM (n=3) * p<0.05.

The expression of OC showed no significant increases on AM-GC substrates in either basal or osteogenic culture conditions when compared to TCP in basal media. However, there was a significant decrease in OC gene expression seen in two out of nine instances for AM-GC samples cultured in basal conditions and four out of nine instances when cultured in osteogenic conditions. With regard to OC expression donor C shows a notable difference in trend as in all but one instance gene expression with regard to TCP basal is significantly reduced on AM-GC substrates, however, between donors A and B there is only one instance of any significant difference (Figure 5.13).

In basal culture conditions ON gene expression was significantly greater on AM-GC scaffolds at six out of the nine time points and significantly lower at only three time points. The addition of OM to AM-GC culture reduced the number of significantly greater expression levels on AM-GC substrates to five instances while the number of reductions remained at three instances. With regard to ON expression there is a notable difference in trend seen in donor A as in all instances expression levels are significantly lower for all AM-GC substrate samples compared to TCP basal comparators. In both donors B and C the expression levels on AM-GC substrates are significantly greater in all but one instance (Figure 5.14).

OP shows a significant increase in gene expression at all nine time points when cultured on AM-GC scaffold substrates compared to TCP under basal conditions. The inclusion of OM for AM-GC culture reduces the instances of significantly greater gene expression to seven of the nine time points and induces one instance of significantly lower gene expression on AM-GC substrates (Figure 5.15).

Over the total 54 time points analysed, in 80% of those instances the gene expression level on the AM-GC in basal media was equal to or significantly greater than that observed on TCP. This observation may imply that the AM-GC substrate alone is acting in a osteoinductive manner under basal conditions. The addition of OM to AM-GC substrates only marginally reduces the total number of significantly greater gene expression instances but has a greater influence on the number of significantly lower expression levels observed taking it up seven instances to 18 in total (Table 5.1). Therefore, under OM the number of instances where the gene expression level is greater than or equal to that of TCP is reduced to 67%.
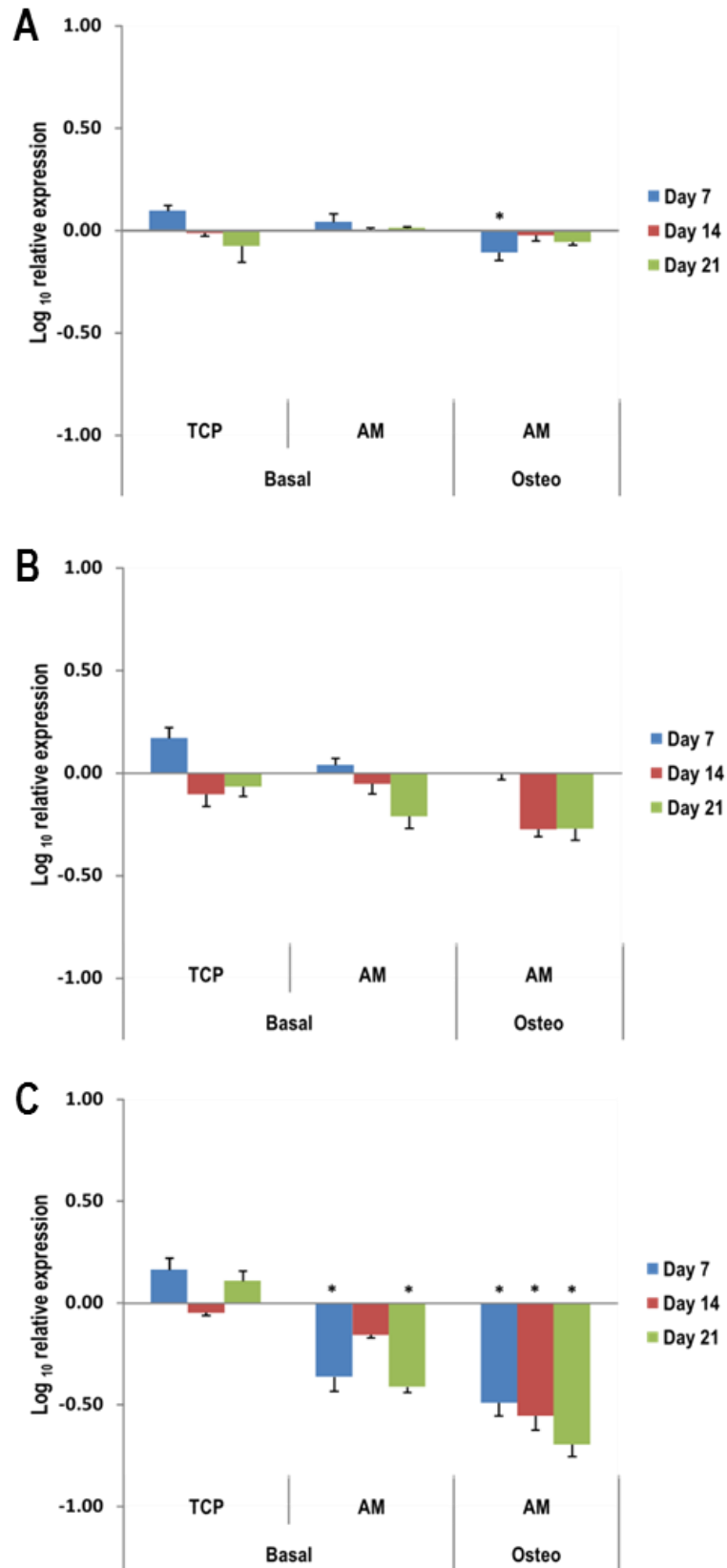
Figure 5.13: Real-time PCR analysis of osteocalcin gene expression on AM-GC substrates in both basal and osteogenic conditions and also for basal TCP control samples at 7 14 and 21 days. Three independent donors were analysed A, B and C and expression level normalised to that at day 0. Mean data are shown + SEM (n=3) * p<0.05.
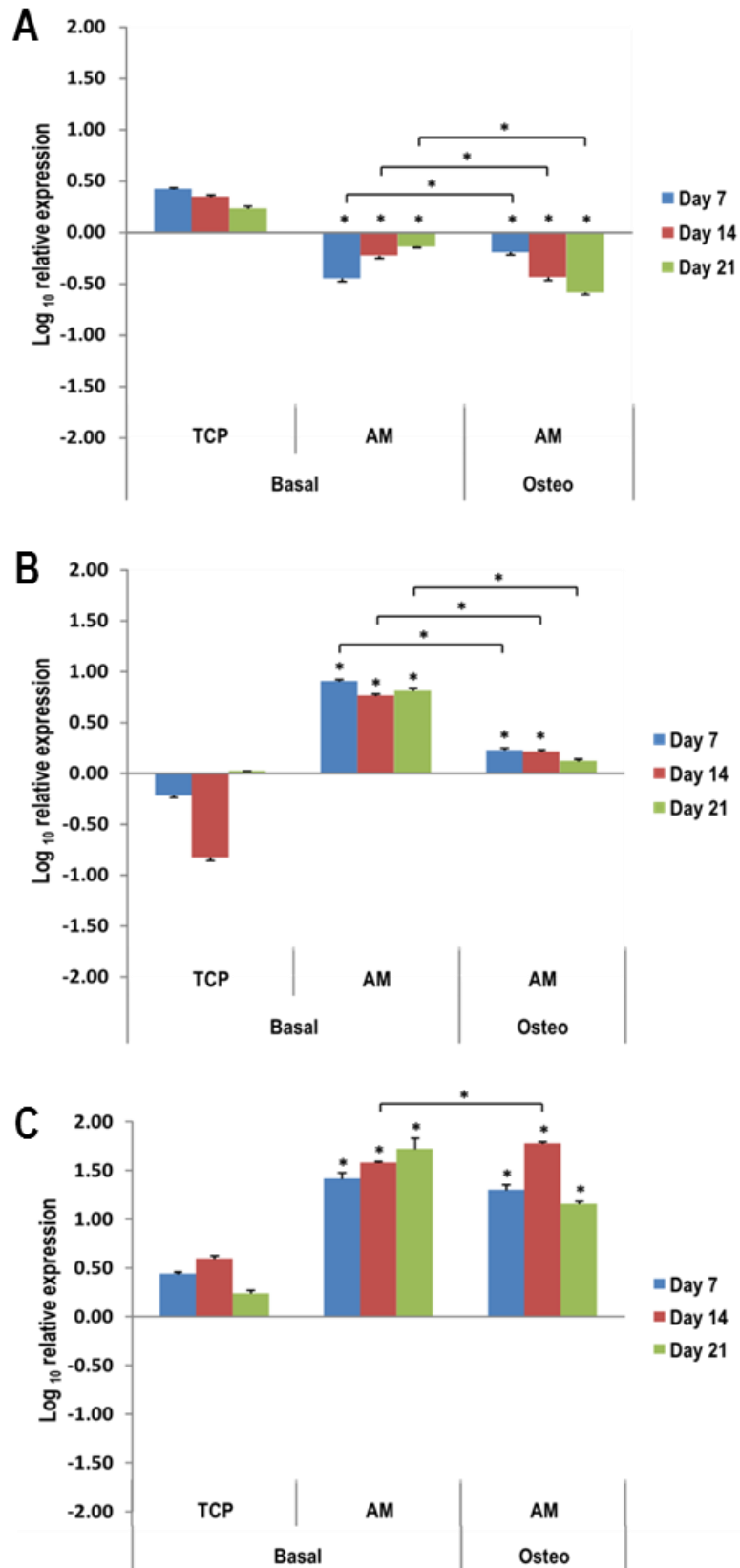
Figure 5.14: Real-time PCR analysis of osteonectin gene expression on AM-GC substrates in both basal and osteogenic conditions and also for basal TCP control samples at 7 14 and 21 days. Three independent donors were analysed A, B and C and expression level normalised to that at day 0. Mean data are shown + SEM (n=3) * p<0.05.
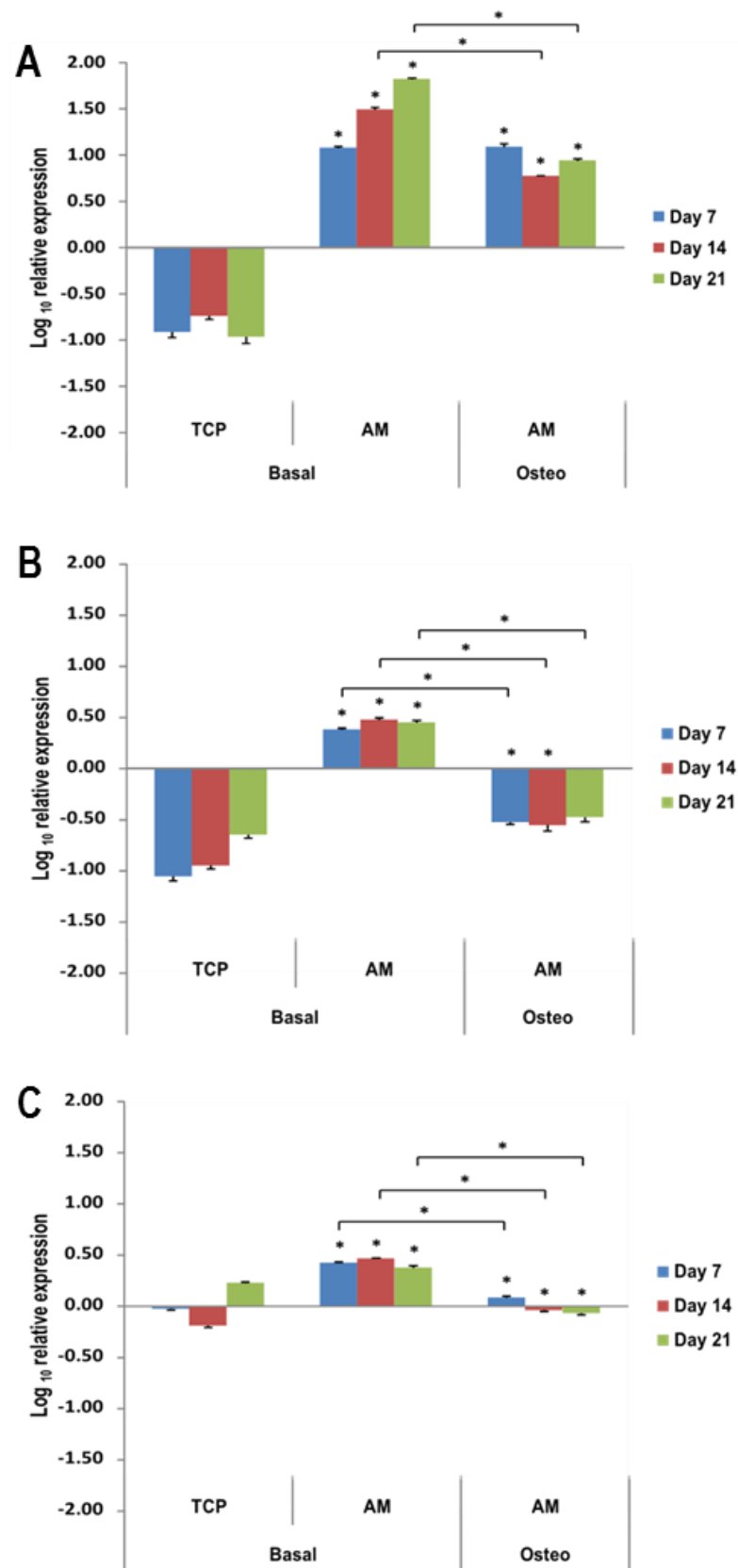
Figure 5.15: Real-time PCR analysis of osteopontin gene expression on AM-GC substrates in both basal and osteogenic conditions and also for basal TCP control samples at 7 14 and 21 days. Three independent donors were analysed A, B and C and expression level normalised to that at day 0. Mean data are shown + SEM (n=3) * p<0.05.

Gene	Medium	Time Point Instances		
		Greater expression on AM-GC	Lower expression on AM-GC	No difference between AM-GC and TCP
ALP	Basal	2	3	4
	Osteogenic	5	3	1
Runx 2	Basal	4	3	2
	Osteogenic	3	5	1
Col αl	Basal	3	0	6
	Osteogenic	2	2	5
Osteocalcin	Basal	0	2	7
	Osteogenic	0	4	5
Osteonectin	Basal	6	3	0
	Osteogenic	5	3	1
Osteopontin	Basal	9	0	0
	Osteogenic	7	1	1
Total	Basal	24	11	19
	Osteogenic	22	18	14

Table 5.1: Summary of real-time PCR results.

In summary, 44% and 41% of instances the culture on a AM-GC substrate significantly increases gene expression levels in basal and OM, respectively. Comparing the influence of basal and OM on the AM-GC substrate alone over the total data set, we find that there are 12 instances of significantly greater gene expression in osteogenic conditions compared to 22 instances of significantly lower expression. This data implies that in 41% of instances addition of OM to AM-GC substrate culture significantly lowers gene expression levels and significant up regulation is only seen 22% of the time. This data is summarised in Table 5.2.

Gene	Time Point Instances		
	greater expression in osteogenic media	greater expression in basal media	No difference between osteogenic and basal media
ALP	5	3	1
Runx 2	2	3	4
Col αl	3	3	3
Osteocalcin	0	0	9
Osteonectin	2	5	2
Osteopontin	0	8	1
Total	12	22	20

Table 5.2: Summary of real-time PCR results on AM-GC substrates alone.

5.3.3.2 Within Donor Gene Expression Analysis

The expression levels of the six target genes, ALP, Runx2, Col αl, OC. ON and OP were determined on AM-GC scaffold substrates in both basal and osteogenic culture conditions at 7, 14 and 21 day time points and compared to TCP basal controls. The repeated measures ANOVA technique was used to determine if substrate condition (e.g. TCP basal, AM-GC basal or AM-GC osteogenic culture) had a significant ($p < 0.05$) influence on the MSCs expression level of each of the six genes of interest. This analysis was therefore performed across the total data set independent of donor for each gene with data shown as estimated marginal means Log_{10} of $2^{-\Delta\Delta Ct}$ (Figure 5.16).

The data showed that the expression of both ALP and Runx 2 were not significantly influenced by the substrate conditions but all other genes were. The trends seen in the repeated measures analysis show that for all genes except ALP the AM-GC substrate in basal media seemed to outperformed the AM-GC substrate in OM. Both ON and OP displayed the most consistent influence of substrate on gene expression level, with OP giving the greatest range between culture conditions throughout (Figure 5.16). In cases where the substrate was deemed to have a significant influence TCP basal conditions were only observed to be greater than that on AM-GC substrates for OC expression at days 7 and 21. It may also be noted that in the case of ALP addition of OM is observed to increase expression on AM-GC substrates at 7 and 14 days.
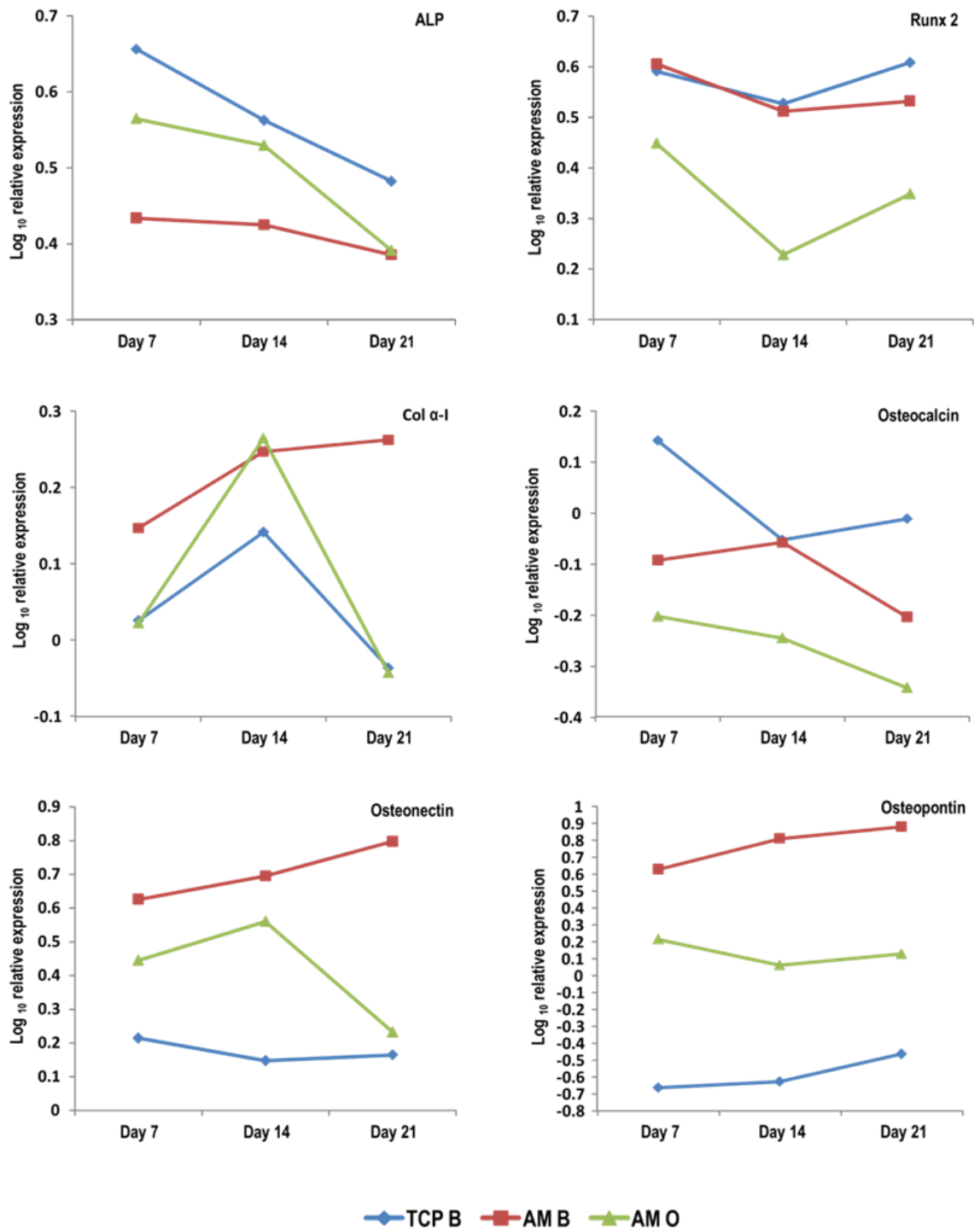
Figure 5.16: Within donor real-time PCR analysis of gene expression on AM-GC substrates in both basal and osteogenic conditions and also for basal TCP control samples at 7, 14 and 21 days. Three independent donors were analysed and expression level normalised to that at day 0. Estimated marginal means for repeated measures ANOVA (n=9).

5.4 *Discussion*

The ideal bioceramic should support a progenitor cell population whilst also being able to stimulate repair and regeneration of the natural bone tissue. The current chapter used *in vitro* cell culture techniques to evaluate attachment, proliferation, viability and the osteoconductive/osteoinductive capacity of MSCs on porous AM-GC scaffolds. Previous studies have demonstrated that the introduction of MSCs to porous glass-ceramics can improve the efficiency of *in vivo* bone formation, especially in the initial stages following implantation [163].

The initial seeding density can influence many factors, such as cellular attachment, proliferation and differentiation characteristics on mineralised scaffold substrates. Several studies have reported either no influence or significant reductions in cellular attachment as initial seeding densities increased [164-166]. Also, inverse relationships between seeding density and proliferation are observed, with lower seeding density equating to greater proliferation rates and prolonged culture generating similar cell numbers [165]. This is believed to be due to the saturation phenomenon, which has been demonstrated on a number of CaP based biomaterials previously using both osteoblastic and MSC populations [164, 167, 168]. However, in the case of cells undergoing OM induced differentiation this phenomenon is found not to occur. Instead an inverse relationship exists with lower seeding densities imparting higher specific ALP activity. This has led to the postulation by some that the increased proliferation rates observed at lower seeding densities may also translate to greater differentiation rates. In relation to mineralised tissue deposition, lower seeding density only delays its formation and following longer culture periods levels of mineralisation, do not differ in relation to seeding density [165].

The substantial influence that seeding density can have on the *in vitro* cellular functions of cell populations make it necessary to consider carefully the seeding density selected to evaluate the current AM-GC scaffold constructs. It was observed that a confluent cell layer was formed after 24 hours with an initial seeding density of $5X10^5$ cells. MSCs were also seen to surround individual scaffold particles and bridge gaps between them. This seeding density was chosen instead of $1X10^6$ cells as this level of over confluence could lead to reduced proliferation and differentiation rates [165]. Initial seeding at $5X10^5$ cells would also minimize the number of *in vitro* cell expansion steps required as over expansion can impair proliferation rates, differentiation potential and possibly cause senescence in MSC populations [169]. Hence, early confluence is desirable as reduced time in culture can result in higher bone formation [168]. Further to this reasoning the current study is concerned with the direct influence of the scaffold on the cell

population and any subsequent seeding after a confluent layer is formed may only act to inhibit the detection of cellular response at the cell/biomaterial interface.

It was observed that the initial seeding density on the AM-GC was considerably less efficient than that observed on TCP. This is perhaps expected as TCP is designed for optimal cell attachment and growth while many CaP and HA based scaffolds demonstrate low seeding efficiencies, especially with regard to the static seeding techniques [100, 170]. However, it was found that population doubling times were directly comparable irrespective of substrate or initial seeding efficiency with significant cell number increases seen at both 3 and 7 day time points on AM-GC. This data is supported by the observed EdU incorporation of a proliferating cell fraction at 24 hours, which was also in line with the reported population doubling times. In addition the fluorescent live/dead assay demonstrated a consistently viable cell population for up to 21 days on AM-GC with a scarcity of dead cells seen throughout. This considered, the material appears to exhibit excellent *in vitro* biocompatibility characteristics.

The level of variance seen in the proliferative cell fraction at 24 hours via EdU incorporation may be due to the presence of multiple material phases, specifically residual glass, at the biomaterial surface as was illustrated in a previous chapter (Figure 4.17). Composition and structure of bioceramics and glasses are well known to influence proliferation rates of MSCs, and for AM-GC in particular crystallisation can directly modify osteoconductivity with reduced bone integration attributed to the presence of amorphous surface regions [128, 170]. It is therefore possible to propose a local influence of the phases present on the cells in direct contact. Although, in the current study there is no concern regarding the viability of cells on the AM-GC, demonstrated via the live/dead assay, aspects such as proliferation rate and attachment, however, may differ between regions. Previous work demonstrated the osteointegrative capacity of AM-GC *in vivo*, a prime indication of bioactive material behaviour. However, the inability to identify any dissolution or HCA layer formation eludes to the inherent stability of any proposed phases either amorphous or crystalline. Therefore, FA is the only known bioactive phase present in the material and with fluorine noted to stimulate proliferation and differentiation of bone cells it is perhaps suitable to propose that cellular response may differ in regions of higher FA content when compared to those composed of either mullite or residual glass. This may help account for the presence of a reduced and/or variable proliferating cell fraction.

ALP, a biochemical marker of bone cells, is an early stage indicator of osteogenic differentiation with increased activity representing a shift towards a more differentiated state [171]. Hence, ALP activity is used to confirm the osteogenic differentiation of the progenitor MSC population. When compared to basal TCP controls the specific ALP activity indicated that in 75% of instances the MSCs cultured on AM-GC were in a more osteogenically differentiated state regardless of OM supplementation. However, addition of OM supplements did still in 67% of instances lead to a further increase in specific ALP activity. Reports have been made previously of the osteoinductive capacity of FA containing bioceramics, with ALP activity levels used as a positive indicator. The ability of dental pulp stem cells and MG-63 cells to differentiate and mineralise without osteogenic supplements has been demonstrated on enamel-like FA surfaces [172, 173]. Also, Yoon *et al*, showed that ALP activity was significantly increased at 10 days culture following substitution of FA into HA-collagen composite scaffolds [152]. However, to my knowledge a direct influence on the ALP activity of MSCs in the absence of supplementation has not been reported for AM-GC compositions *in vitro*, although, it has recently been demonstrated on biphasic calcium phosphate composites with additions of 10% to 30% mullite [171]. Investigations into the ALP activity of MSCs on porous AW glass ceramics found there to be no significant increase in activity over 21 days culture in basal conditions, but significant increases were seen in OM. This has also been observed for rat foetal osteoblasts cultured on AW discs [100, 174].

Although enzymatic ALP activity was seen to increase in the presence and absence of osteogenic supplements, stereo microscopy of ALP stained samples found there to be no discernible increase in ALP activity over the 21 day period in basal conditions, while there was a notable increase observed by day 14 on those cultured in OM. If we then consider the fact that there is still a positive influence of OM on ALP activity, then by definition the cells are in a more progressed osteogenic state which may account for the notable difference in surface characteristics, due to a more established matrix maturation phase. This is perhaps a more valid explanation than the possibility of increased cell proliferation, as this is reported to be inhibited on bioceramics when seeded at confluence, as in the current study, and by OM additions [165, 168]. Also, as the specific ALP activity is greater in OM supplemented scaffold culture this would represent a reduced proliferative capacity in conjunction with the more differentiated state [146].

In the current study mRNA expression levels for a range of established osteogenic markers (Runx 2, ALP, Col αI, OP, ON and OC) were used to assess the differentiation of MSCs on AM-GC substrates in the presence and absence of OM, with basal TCP controls, which has not been

performed previously. The closest biomaterial compositionally was studied by Kalmodia *et al*, who reported on the ability of HA-mullite particle eluates to induce up regulation in Runx 2, Col αl and OC mRNA expression in the absence of OM indicating a possible osteoinductive nature. The capacity of bioceramics to induce osteogenic differentiation is widely documented, specifically for the calcium phosphate based compositions, HA, *β*-tricalcium phosphate and the biphasic calcium phosphates. However, the majority of this work focuses on enzymatic ALP activity levels and *in vivo* animal models with relatively few *in vitro* studies of osteogenic marker expression. This large imbalance between *in vitro* and *in vivo* work stems from the apparent poor ability of *in vitro* studies to reliably *predict in vivo* performance [162]. However, Yuan *et al.* recently used MSCs to assess the expression levels of several osteogenic differentiation markers *in vitro* on a range of CaP/HA bioceramics. The expression levels of bone sailoprotein, OP, ON and Runx 2 mRNA were all seen to be up regulated on the substrates when compared to monolayer controls. Furthermore, the trends seen in the osteogenic marker expression levels between substrates correlated with the amount of bone formation observed in an *in vivo* sheep model [175].

Interestingly the aforementioned study found that ALP and Col αl expression did not increase or markedly vary either on or between any bioceramic substrate. The expression of Runx 2 was also noted to be less influenced between substrates. This is perhaps noteworthy as in the current study ALP and Runx 2 were found to be the only two genes analysed that showed no significant influence of the AM-GC substrate for the within donor analysis. In the between donor analysis ALP expression was only seen to be notably influenced by the addition of OM which gave a 33% increase in the number of instances ALP expression was higher on AM-GC substrates in respect to TCP controls, while Runx 2 expression did not show any discernible trends regarding either substrate or media conditions.

In the current study the most notable influence on MSC gene expression was seen for both the ON and OP differentiation markers. ON is a bone matrix protein that regulates mineralisation and extracellular remodelling with a high affinity for binding both HA and Col αl, hence, it is a nucleator necessary for bone mineralisation [176]. The ON expression levels in the current study were observed to be up regulated in 67% of instances on AM-GC in relation to TCP basal conditions. The addition of OM to AM-GC cultures, however, appeared to have a inhibitory influence on expression, causing significantly lower levels in 56% of instances. This is clearly illustrated by the within donor analysis means data plot (Figure 5.16). Dyson *et al*, also reported on the ON expression levels in AW glass ceramics and noted the same trend of increased

expression under basal culture with respect to TCP and a subsequent inhibitory influence of OM [100]. The extent of the influence, although, was not as prominent as that seen in the current AM-GC material.

OP is thought to function in both cell attachment and crystal formation due to its observed accumulation at the cement line in bone and ability to bind HA [177]. In the current study OP was the only marker to demonstrate greater expression when cultured on AM-GC in every instance with respect to TCP basal conditions. The addition of OM again lead to a reduction in OP levels for 89% of instances on AM-GC substrates. This trend was again noted by Dyson *et al*, for MSCs cultured on porous AW glass ceramics. The expression of OP has been shown previously to increase with extracellular calcium ion levels for human dental pulp cells. Calcium represents a significant component in both AM and AW glass ceramic compositions, therefore, it is possible that calcium dissolution may influence OP expression in these materials. Calcium ions have also been shown to decrease mRNA expression of ALP which may account for the observed reduction in base line ALP expression seen on AM-GC substrates, particularly in the between subject analysis (Figure 5.16) [178]. However, Goodridge *et al* found that extracellular calcium levels did not change for AM-GC during 14 days submersion in SBF [110]. One study has reported up regulation of OP in the presence of OM at 7 and 14 days on AW glass ceramic substrates [179]. However, these materials were composites that also included a bisphenol-a-glycidyldimethacrylate based resin and the primary cells were isolated from rat bone marrow which makes any direct comparison difficult.

Runx 2 is considered to be critical for the osteogenic differentiation of stem cells in response to growth factors, specifically the BMPs. However, in the current study Runx 2 expression was not found to be significantly influenced by substrate conditions but other late markers were, as was enzymatic ALP activity. This may be attributed to the fact that HA has previously been shown to induce osteoprogenitor cell differentiation without activation of Runx 2 in C3H10T1/2 cells [180]. Lin *et al*, also ruled out the possible influence of geometric factors by performing HA conditioned medium studies. Also ruled out where several possible inductive influences, such as, excessive calcium and phosphate or adsorption of BMP like factors from the serum. This was believed to imply the presence of an alternative pathway to that typically associated with osteogenesis. The authors postulated that HA/stem cell interactions lead to the synthesis of a potent factor that acts as an inducing cytokine and facilitates the commitment of the progenitor cells into the osteogenic lineage in a paracrine fashion, independent of Runx 2. This proposed difference may be

strengthened by the *in vivo* observation that osteoinduction by a biomaterial is always intramembranous while that induced by BMPs is almost always endochondral [162]. This theory could account for the more prominent influence of AM-GC on late stage markers in the apparent absence of pronounced Runx 2 expression increases. This is especially pertinent when we consider the close compositional relationship between HA and the FA phase found in the current material. Though it should be remembered that Runx 2 is still being expressed and cannot be ruled out as the key osteogenic regulator in the current research.

Although the current study did demonstrate the expression of OC its level was reduced on AM-GC substrates, though only marginally in basal conditions. The addition of osteogenic supplements lead to a reduction in 44% of instances in relation to TCP basal conditions. However, there was no significant difference in expression seen at any time between cells cultured in either basal or OM on the AM-GC. Dyson *et al* also found little positive influence of AW substrates on OC expression when compared to TCP controls [100]. The expression of OC during HA induced osteogenesis in C3H10T1/2 cells has previously been demonstrated to significantly decrease by day 4 of culture. Also, the OC expression of human MSCs cultured under osteogenic conditions on HA substrates has been observed not to differ significantly compared to TCP controls after 7 days culture [175, 180]. Therefore, although in the current study the OC expression levels show no pronounced up regulation, this may solely be an artefact of the time point chosen.

5.5 *Conclusion*

In the current analysis as well as showing excellent *in vitro* biocompatibility characteristics AM-GC also demonstrates an ability to up-regulate a number of mRNA markers of osteogenesis and specific enzymatic ALP activity in the absence or presence of OM supplements. This considered, it would suggest that AM-GC is clearly osteoconductive but may also possess elements of an osteoinductive nature. Decisive influence of the AM-GC substrate was observed on the later stage osteogenic markers ON and OP. This marked difference in the response from specific osteogenic markers may account for some of the difficulties encountered when comparing biomaterial and OM induced osteogenesis and supports the need for more detailed *in vitro* examination of the specific material factors and signalling pathways involved in regulating this response on the current AM-GC substrate.

After investigating in the present chapter the substrate, from the perspective of osteogenic differentiation capacity, to truly understand in the first instance the materials potential to act as a bone substitute biomaterial. These encouraging results considered, efforts must now turn to the proposed EP application. Although suitable strength characteristics and osteogenic potential have been established, it is yet to be determined as to whether or not the scaffold has the potential to act as a substrate for the development of the cartilage like tissues of the natural EP. Further still, the question remains, can these constructs then deliver the required nutrient transfer function of the natural tissue.

Chapter 6: Permeability Testing & Construct Development

6.1 *Introduction*

It is important to establish the key parameters in order to assess biological function. Although the osteogenic MSC response, mechanical behaviour and material structure have been previously characterised, a key remaining function of natural EP tissue is to permit the supply of nutrients to the tissue of the IVD. Permeability is a parameter that measures quantitatively the ability of a porous medium to conduct fluid flow and it depends on the combination of porosity, pores size, orientation and interconnectivity. Therefore, permeability is proposed as a representative measure of the AM-GC construct's ability to facilitate this nutrient supply function. The current chapter then strives to develop a suitable permeability measurement technique, allowing for the future comparative study of cell seeded constructs against the permeability levels of the natural EP tissues.

6.1.1 *Permeability of the Vertebral EP*

It is well established that the diurnal loading cycles of the human spine are a key contributor to the fluid flow characteristics between the IVD and adjacent vertebral bodies, and that the dominant flow path is through the EP region [181]. Therefore, the permeability at this interface could govern the convective nutrient exchange into the avascular regions of the IVD. This would infer that interference to mass transfer through the vertebral EP, via aspects such as calcification, will lead to a mechanobiologic imbalance of the spine and may promote IVD degeneration. Quantitative studies support this theory demonstrating positive correlation between EP thickness and degenerative state [182]. Furthermore, complex finite element analysis governed by non-linear coupling of cellular metabolism, pH and oxygen concentration along with the strain dependent properties of the IVD ECM, predicted maximum glucose concentration decreases of approximately 45% associated with EP permeability [183]. It was also reported that reduced permeability more strongly effected glucose concentration in the NP regions, which supports previous observations of increased capillary bed density in the central EP regions directly adjacent to the NP [139, 181, 183].

Though there have been a number of studies aimed at elucidating the permeability of both the NP and AF tissues of the IVD, there is unavoidably a large reporting range for this data, from approximately 7×10^{-16} m⁴/Ns to 1×10^{-15} m⁴/Ns [181]. This is owing to the large differences that

exist between factors such as sample species, age, and testing protocol. Historically there are relatively few studies that report quantitative data on the EP permeability, one study on baboon tissues used compressive creep properties analysed in accordance with poroviscoelastic constitutive model theory and reported a hydraulic permeability of 14.3×10^{-14} m^4/Ns [184]. However, it is the view of the author that in this instance the samples still maintained a considerable amount of NP tissue which may have influenced the result, as the NP would not be considered a component of the EP in the context of my study.

More recently a study on the macroscopic permeability of ovine EP tissue was carried out in such a manner as to mimic the *in vivo* conditions of mass transfer and eliminate any effect of flow induced matrix compaction. Hence, eliminating any false representation of EP permeability under conditions not representative of normal daily loads [139]. The hydrostatic pressure exerted on the IVD under normal conditions is between 0.6 MPa and 2 MPa, assuming that the osmotic swelling pressure due to the high fixed charge density of the PG content is in the range 0.15 MPa to 0.2 MPa [185]. Therefore, permeability was measured as a function of transient pressure relaxation at a level < 0.15 MPa. Mean permeability of the central EP region was reported to range between 1.66×10^{-14} m^4/Ns to 1×10^{-14} m^4/Ns for samples taken from 2 and 6 month old lambs respectively, indicating an age related decrease in sample permeability [58].

Therefore, it is believed that although the structural and mechanical parameters of tissue engineered cell/scaffold constructs for EP applications are valid research elements. The key to providing a functional tissue engineered solution lies with providing the correct interface permeability, as this is the sole element capable of facilitating nutrient mass transfer and preventing any further onset of IVD degeneration regardless of the underlying root cause. Hence, facilitating anything other than the correct permeability as a minimum requirement would lead to a construct not fit for purpose.

6.1.2 Study Aim

The aim of the current chapter is the development of test equipment and protocols able to measure permeability within natural EP samples and also cell-seeded AM-GC constructs. As a consequence it also falls within the remit of this study to determine a suitable cell seeding and culture methodology able to provide such constructs for future development and optimisation towards a true tissue engineered EP solution. Hence, part of the current chapter will focus on the ability to induce the chondrogenic differentiation of primary human MSC on the AM-GC substrate in such a manner as to be representative of the early stage development of osteochondral constructs. As the production of true osteochondral constructs would perhaps warrant a PhD project in its own right, the work here will only endeavour to provide the initial seeding and culture methods and to demonstrate their potential for further exploration in regard to the EP application.

In light of this challenge the chapter will rely heavily on both cell biology, materials science and engineering knowledge built up throughout the course of the current multidisciplinary PhD programme and hopefully represents a true tissue engineering approach to a subject at the interface of both the physical and biological scientific disciplines.

6.2 Materials & Methods

6.2.1 Permeability Testing Theoretical Considerations

In the first instance a proven methodology was identified from current literature that was believed in principal to be best suited to determining the permeability of vertebral EP tissues, but could also be adapted for use with scaffold constructs. The chosen method allowed for the determination of the macroscopic permeability based upon a transient fluid flow rate into the biological component [139, 181]. Due to the quasistatic nature of the flow, this method maintained minimum flow induced matrix compaction of the organic tissue component and the test fixture ensured control over boundary conditions. However, on closer examination of the proposed theoretical considerations underlining the test methodology a number of proposed errors were identified within the workings and are outlined below:

1. The initial theoretical considerations report flow rate due to fluid compressibility (B_f) as a function of $\dot{p}$, the relative pressure variation in time and V_0, the fluid mean velocity. This is reported as the conservation of mass. However, after examination and consultation with a mathematician, B_f was determined to in fact represent the Bulk modulus of the sample and not compressibility. Also, V_0 was representative of the sample volume and not mean velocity as previously stated. With this considered it is apparent that the governing equation represents the conservation of volume and not that of mass.

2. The previous report stated a solution to first order differential equation relating to the relative pressure at a given time (p_t). This solution differed significantly from that obtained using the integrating factor methodology whilst reviewing the work with an experienced applied mathematics professor. The key difference was observed in the positive sign given to the exponential term representative of p_t throughout the test duration which lead to further discrepancies in the equations relating to the second testing phase.

Due to the substantial discrepancies identified throughout the previously published literature and our own interpretation of the proposed testing methodology, in this chapter a corrected derivation of the theoretical considerations behind the permeability test methodology will be used.

6.2.1.1 Derivation of Theoretical Considerations

The fluid flow through the component was controlled by quasistatic piston displacement, this was to ensure the negligible influence of inertia as a function of fluid acceleration throughout testing. The conservation of volume flow during testing is presented in Equation 6.1 below:

$$\frac{V_o}{B_s}\dot{p} + q_1 + q_2 + q_s = S_p\dot{U}_p$$ **Equation 6.1**

Where:

V_o = sample volume

B_s = sample bulk modulus

$\dot{p}$ = relative pressure variation in time

q_1 = leak rate around the sample

q_2 = leak rate into the venting pipe

q_s = flow rate through the biological sample

S_p = piston cross sectional area

$\dot{U}_p$ = piston velocity

From this governing equation the flow rate into the biological sample / scaffold construct was characterised using Darcy's law (Equation 6.2), which is a constitutive equation describing the flow of fluid through a porous medium:

$$q_s = \frac{K_s S_s}{\mu l_s}p$$ **Equation 6.2**

Where:

K_s = intrinsic permeability of the sample

S_s = sample cross sectional area

μ = fluid viscosity

l_s = sample length

p = relative pressure

Using the same principal as that above to characterise flow rate through the sample, the fluid leak components were represented as a product of the relative pressure and coefficients γ_1 and γ_2 relating to leakage around the sample and through the venting pipe respectively.

$$q_1 = \gamma_1 p$$

Equation 6.3

$$q_2 = \gamma_2 p$$

Equation 6.4

In order to account for the global stiffness of the testing apparatus a liner elastic deformation was assumed and represented by Hooke's law. This is presented in Equation 6.5 which relates the piston displacement to that actually achieved for a given applied load.

$$pS_p = k(U - U_p)$$

Equation 6.5

Where:

k = liner stiffness coefficient
U = input displacement of actuator device
U_p = actual piston displacement achieved

On substitution of equations 6.2 through 6.5 into equation 6.1 we were able to determine the relative pressure variation in time in the form of an ordinary differential equation.

$$\dot{p} + \frac{1}{\tau}p = \frac{1}{B}\dot{U}$$

Equation 6.6

In which:

$$\frac{1}{\tau} = \frac{A}{B}$$

Equation 6.7

$$A = \frac{1}{S_p}\left(\gamma_1 + \gamma_2 + \frac{K_s S_s}{\mu l_s}\right)$$

Equation 6.8

$$B = \frac{1}{S_p}\left(\frac{V_o}{B_s} + \frac{S_p{}^2}{k}\right)$$

Equation 6.9

Where:

τ = time constant

A = constant proportional to the pressure loss due to both the sample and leak components

B = constant proportional to sample bulk modulus and the global system stiffness

Equation 6.6 shows that the pressure variation in time is a function of the input velocity of the actuator device, $\dot{U}$. Throughout the proposed testing methodology there are two key phases. In **phase 1** the actuator velocity remains constant up to a pre-determined pressure (p_1) over the respective time period (t_1). Solving equation 6.6 using the integrating factor method over the period between time 0 and t_1 generated the following solution to p_1.

$$p_1(t) = \frac{\dot{U}_1}{A}\left(1 - e^{-\frac{t_1}{\tau}}\right)$$

Equation 6.10

In Which: $\dot{U}_1 = \dot{U}, \quad \forall_t \in [0, t_1]$

In **phase 2** of the test methodology the actuator velocity was brought to a standstill and as such the displacement was held constant from t_1. The transient pressure relaxation starting from p_1 can then be expressed throughout the second phase up to a chosen point p_2 over the given time period (Equation 6.11).

$$p_2(t) = \frac{\dot{U}_1}{A}\left(e^{\frac{t_1}{\tau}} - 1\right)e^{-\frac{t}{\tau}}$$

Equation 6.11

In Which: $\dot{U}_1 = 0, \quad \forall_t \in [t_1, \infty]$

The time constant τ was derived from the exponential least square fitting technique applied to the phase two experimental results throughout the transient pressure relaxation, p_1 to p_2. The derived least square fit Equation 6.12 is displayed below:

$$\tau = \frac{(\sum_{i=1}^{n} t_i)^2 - n\sum_{i=1}^{n} t_i{}^2}{n\sum_{i=1}^{n} t_i \ln p_i - \sum_{i=1}^{n} t_i \sum_{i=1}^{n} \ln p_i}$$

Equation 6.12

Finally on substitution of equation 6.8 into 6.11 allowed for the determination of the samples permeability in Equation 6.13, expressed below:

$$\frac{K_s}{\mu} = \left[\frac{\dot{U}_1}{p}\left(e^{\frac{t_1}{\tau}} - 1\right)e^{-\frac{t}{\tau}} - \frac{(\gamma_1 + \gamma_2)}{S_p}\right] \times \frac{S_p l_s}{S_s}$$

Equation 6.13

6.2.2 Permeability Testing Equipment Design & Development

In the initial concept development stage the key design requirement of the testing equipment was to *hold the biological/scaffold sample consistently in such a manner that it allowed for continuous fluid flow throughout the two principal phases of the testing methodology identified within the theoretical considerations*. This requirement was met via the concept of applying a uniaxial confined compression to a rubber sealing tube, subsequently applying a circumferential strain to hold the component in position whilst simultaneously creating an adaptive seal around the sample periphery. An initial testing equipment design based upon this concept was created (Figure 6.1) and an illustrative schematic is also presented to aid interpretation (Figure 6.2).
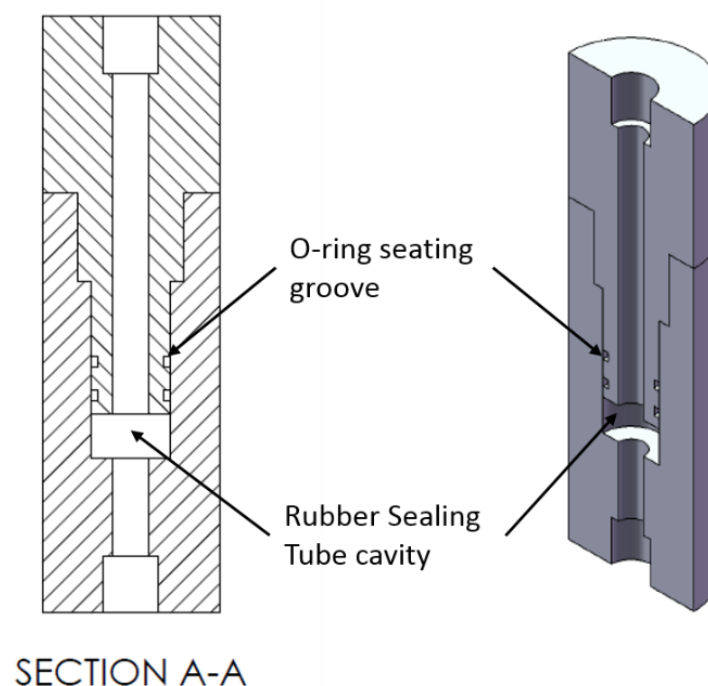
Figure 6.1: Permeability testing apparatus, sample holding component initial design. The sealing tube cavity is where the sample will be placed within a compressible rubber tube. Section A-A allows for the observation of the central fluid flow path through the equipment, with the o-ring seating groves positioned to facilitate the o-ring seals within the system to eliminate leakage from behind the sample when under pressure.
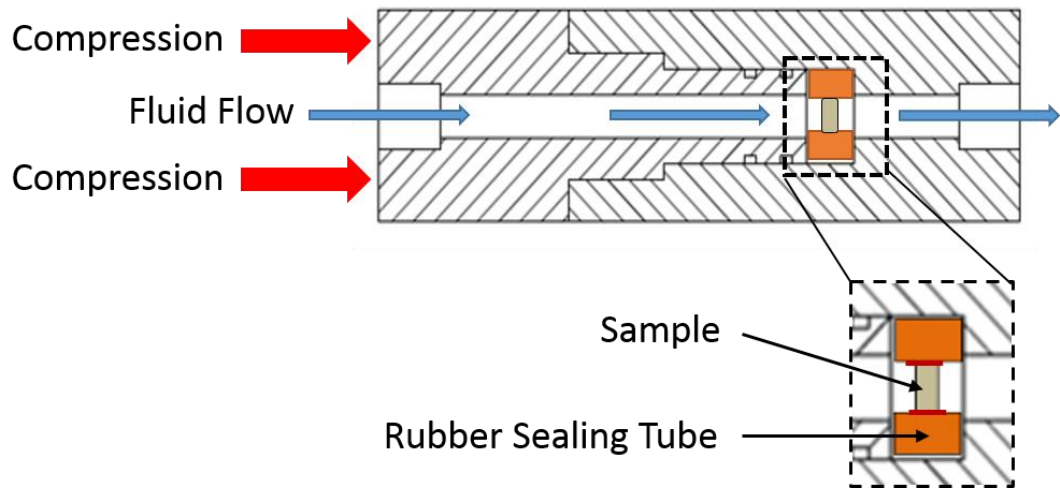
Figure 6.2: Schematic representation of sample holding principal during testing, an adaptive seal is created around the sample periphery as a function of the uniaxial compressive force (red arrows). This then allows for fluid flow path through the sample during testing (blue arrows).

This sample holding method then allowed for a fluid flow path through the sample during testing. The fluid displacement within the system was facilitated via a simple pistoning device, designed and manufactured from Perspex, again to allow for identification of any leaks or air within the system (Figure 6.3). Two o-ring seating groves were included on the piston to eliminate any leakage during testing. The piston component had a M20 stainless steel thread component which was glued into the Perspex body, this facilitated fixation to the hydraulic testing actuator load cell.
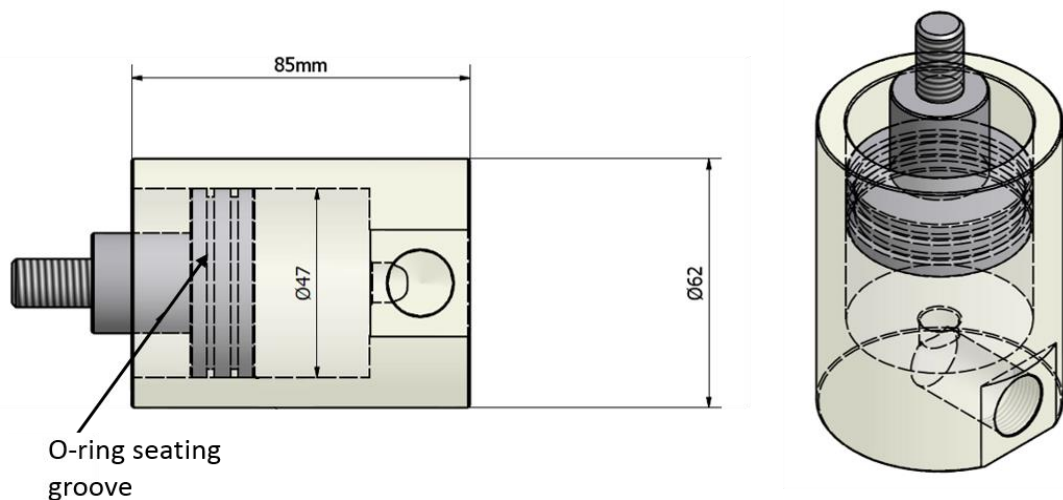
Figure 6.3: Piston and cylinder design assembly drawing, both components are Perspex while the threaded element is a stainless steel adaptor. O-ring seating groves allow for the system to be sealed to prevent leakage under testing pressures. Also, the cross flat on the cylinder body facilitates hose attachment to the sample holding assembly.

6.2.2.1 Design Iterations

Though the principal design concept for the sample holding equipment did not change to any significant degree from this early stage there were a few key design iterations made prior to the final test equipment production. These key iteration steps are presented below:

1. *The initial component was to be manufactured from stainless steel, however, this was later changed to Perspex. This design iteration allowed for the sample to be viewed in real time to maintain it was secure throughout testing. Also it allowed for the visualisation of die passing through the system/samples aiding in the identification of any potential leaks or trapped air within the system.*

2. *Initially the design included three grub screws positioned equidistantly around the female component, this was to allow for the uniaxial compression to be maintained on the sample throughout testing by tightening the screws whilst the sample was loaded (Figure 6.4).*
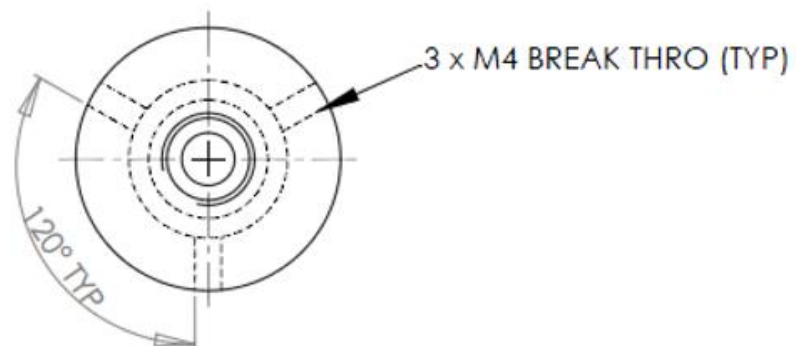
Figure 6.4: Initial design concept drawing showing proposed grub screw hole positioning on the female component.

On application of the grub screw concept it was found that tapping the polymer with such a low thread diameter (M4) made it hard to apply the required torque in order to maintain the position of the male component under loading. This lead to the development of a separate holding fixture onto which the assembled system could be positioned once the sample was in place (Figure 6.5)*. This mechanised fixture then allowed for the addition of uniaxial compression under the control of a lead screw. Therefore a repeatable displacement could be applied between individual permeability test runs for any given sample.*

Figure 6.5: Holding fixture to allow for the uniaxial compression to be applied to the sample under the control of the lead screw component. This allows for consistent displacement to be maintained between experiments.

3. *In the first design iteration the male component was to include tapped through holes into the fluid flow chamber. This was in order to accommodate a pressure transducer to allow the real time monitoring of pressure in the immediate vicinity of the sample component (Figure 6.6). However, there was insufficient funding to purchase the required transducer component.*
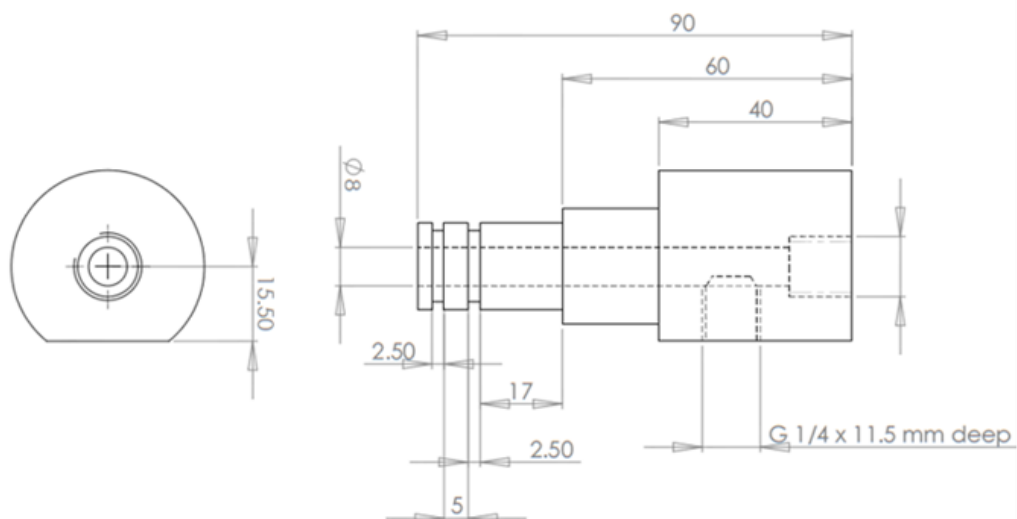
Figure 6.6: Initial design drawing showing the location of the tapped through hole to accommodate the pressure transducer in the male component, a cross flat would have also been required to facilitate this feature.

*Therefore, in order to determine the pressure in real time during testing values were obtained from the actuator load cell (Dynacell, Dynamic load cell, Cat No: 2527-102). This was achievable as the system required a third component, a simple pistoning devise to displace the fluid through the component at a constant velocity through **phase 1** of testing. Hence, the load cell was used to track the force during both phases of testing. This load trace data was subsequently divided by the cross sectional area of the piston (S_p) to provide the transient pressure (p) throughout the testing duration.*

4. *The final design iteration for the sample holding component was the addition of quick release 10mm (outer diameter) hose adaptors to the fluid inlet and outlet points. This allowed for the rapid assembly and disassembly of the test rig. These components also facilitated the inclusion of a t-section release valve to allow the rapid release of pressure from the system prior to and following subsequent testing runs (Figure 6.7).*
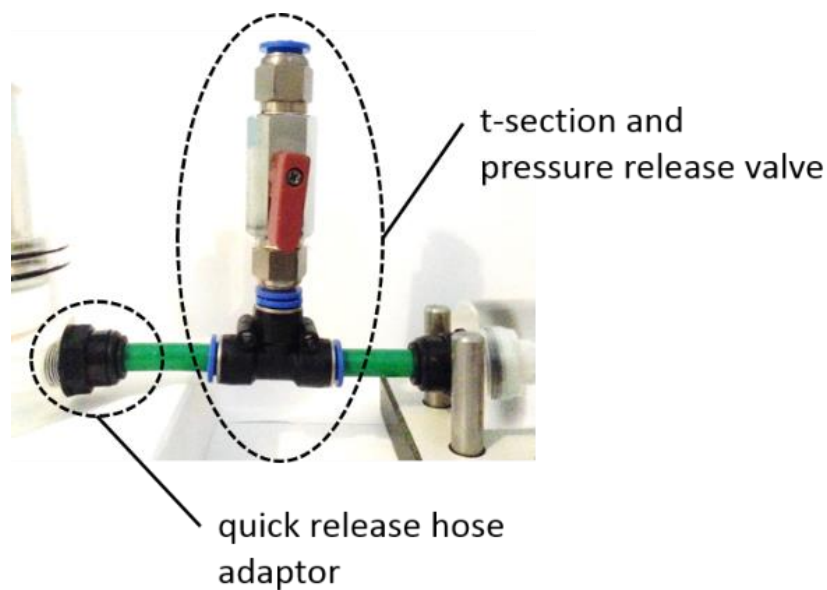
Figure 6.7: Quick release hose adaptors added to inlet and outlet of each system component to allow rapid assembly and disassembly of the system. Also, the t-section valve added to facilitate pressure release prior to and following experimental runs.

6.2.2.2 Construct Permeability Adaptor

In order to allow for cell seeded scaffold constructs to be tested for permeability within the same equipment a sample adaptor was designed to fit within the rubber sealing tube cavity of the system. The adaptor was designed to utilise two o-ring components which are compressed to

create an adaptive seal around the scaffold using the same principals as the standard system setup (Figure 6.8). This system approach maintains the ability to test natural EP samples over a larger area more representative of the central region permeability, but also smaller homogeneously structured cell seeded scaffold constructs can be tested at a smaller scale. This was an important design consideration due to the high cell number requirements to generate construct samples.
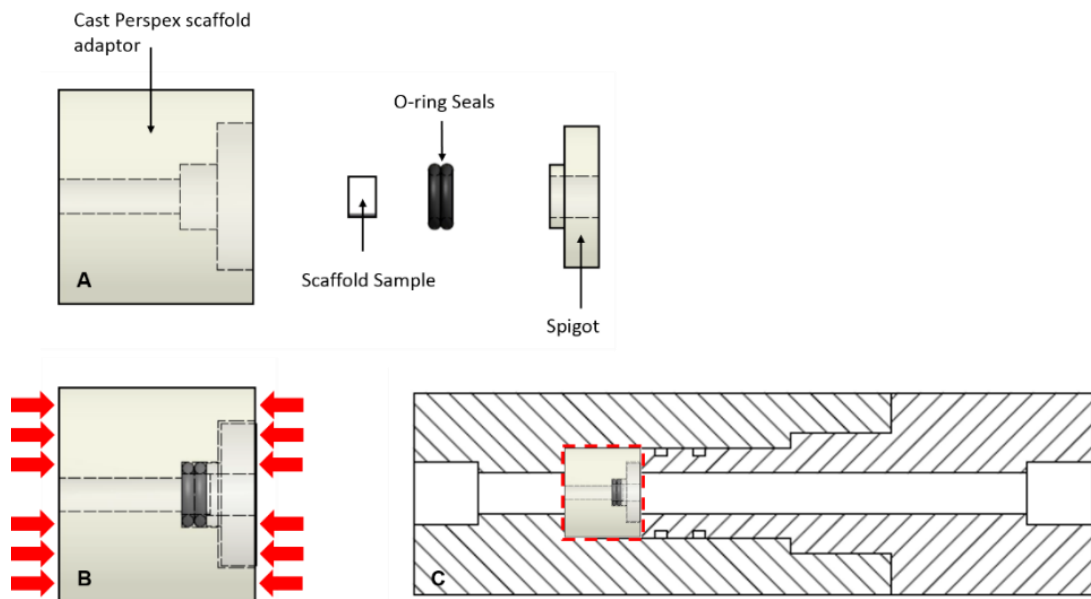
Figure 6.8: The construct adapter assembly allows for scaffolds to be sealed within the system via the uniaxial confined compression of two o-rings positioned around the scaffold body (A-B). This adaptor assembly is positioned within the standard system in place of the rubber sealing tube in order to facilitate testing (C).

6.2.3   Permeability Testing Protocol

In order to maintain that the system was fully saturated during testing the components were submerged in distilled water an placed under vacuum (Gallenkamp, Cat No: OVA0311.881.1) for 1 hour, after which the components were assembled whilst still submerged. The rig assembly was then taken from the water tank and positioned onto the base of a tensile testing machine (Instron, Electropulse E3000, Model No: 2527/102155) with the pistoning component attached. The piston cross head was then brought down into the cylinder with the pressure release valve in the open position, once the piston was within the cylinder to a depth below the o-ring seals the valve was closed and testing protocol could begin.

The piston surface had a cross sectional area of 1735 mm^2 (S_p) and was displaced throughout phase 1 of the testing at a constant velocity of 1.15X10^{-3} m/s ($\dot{U}_p$) to generate a volumetric flow rate of 2 mm^3/s within the system. The system was allowed to run until the pressure build up behind the sample reached 0.12 MPa ($p_1(t)$). Once this pressure target was reached phase 2 began and the piston cross head was stopped and the transient pressure relaxation monitored for a further 1080 s. The values for the sample permeability were then able to be determined using Equation 6.13. This two phase test methodology performed in line with the theoretical considerations is illustrated graphically below (Figure 6.9). In the case of both the standard system and the instance where the cell seeded scaffold adaptor was used, the value representative of possible leakage around the system ($\gamma_1 + \gamma_2$) were able to be determined using a solid steel plug of the same diameter as the bovine test samples.
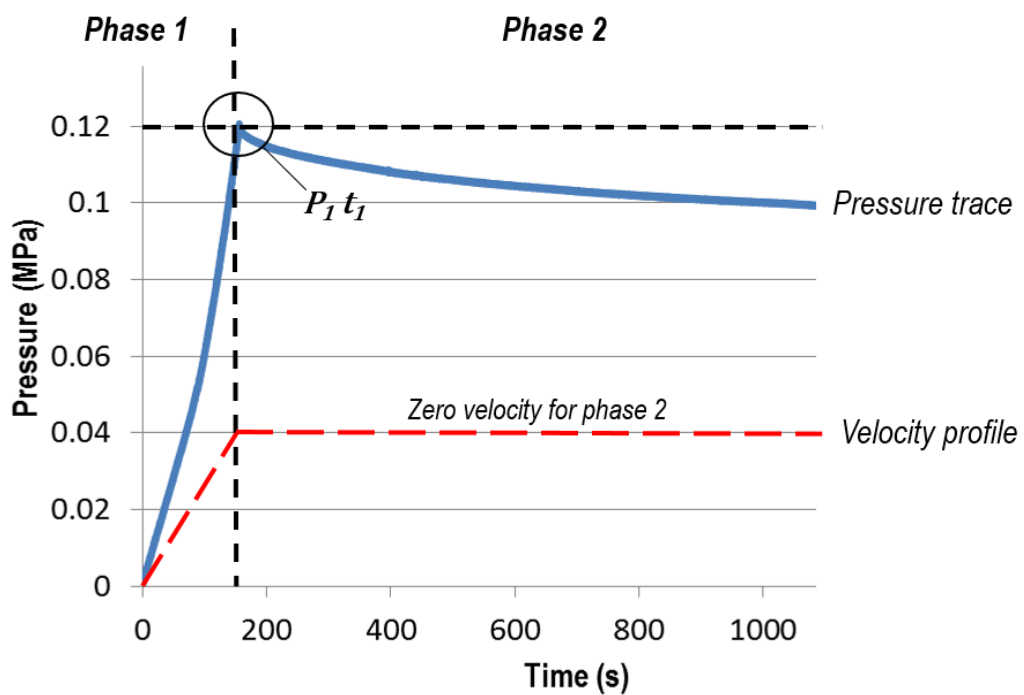
Figure 6.9: Graphical representation of the experimental phases within the permeability testing protocol.

6.2.4   Bovine Endplate Identification & Test Sample Preparation

Bovine tail bone samples were obtained from the abattoir on the day of slaughter and all surrounding tissues were removed from the vertebra and IVDs. The remaining spinal tissue was then sectioned into functional spinal units, consisting of one IVD and the two adjacent vertebra which were then sectioned transversely through A and B (Figure 6.10, A). Next a 10 mm core drill

was used to remove the central region of the IVD and adjacent residual bone fractions producing a core plug Figure 6.10, B-C). Finally this plug was sectioned sagittally along its centre to provide a greater surface area once embedded (Figure 6.10, D).
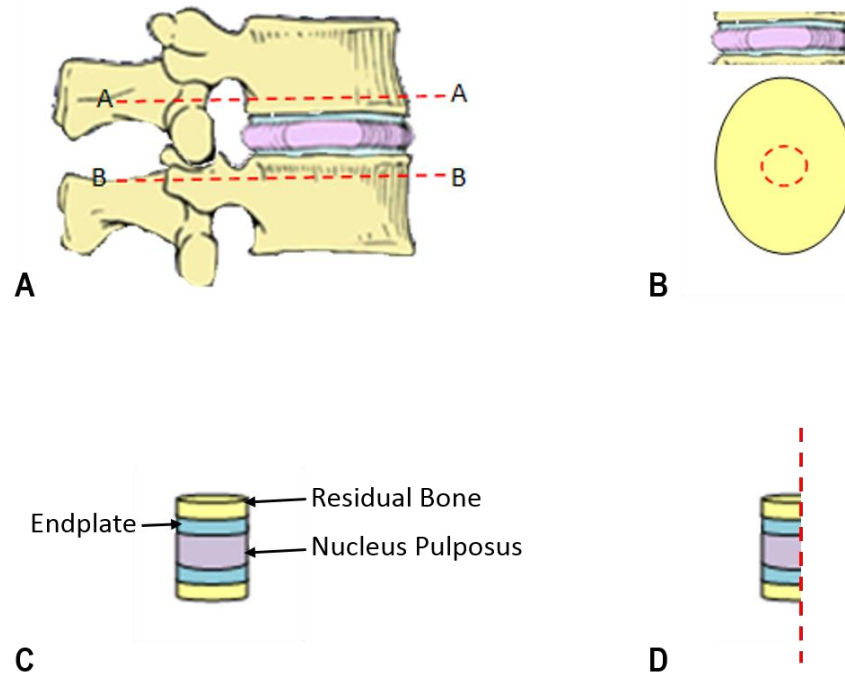
Figure 6.10: Schematic representation of bovine tissue sample preparation for paraffin embedding/OCT mounting. Samples were sectioned transversely through A and B (A), a core was then taken from the central region (B-C). This core was then sectioned sagittally to generate a surface to section from once embedded (D).

Following dissection the samples were fixed in 4% paraformaldehyde in phosphate buffered saline for 48 hours. Beyond this point two samples were prepared in each of the following manners:

1. *Surface decalcification;* samples were first embedded in paraffin wax in a two day automated processing unit (Shandon Citadel 2000, Thermo Electron Corporation, Waltham, MA), following which the samples were surface decalcified in nitric acid solution for 30 minutes prior to sectioning on a microtome.

2. *Cryosectioning;* samples were decalcified in EDTA for 14 days after which they were mounted in optimum cutting temperature (OCT Embedding Matrix, Fisher Scientific, Waltham, MA) mounting fluid and sectioned on the cryotome.

3. ***Standard microtome*** samples were decalcified in EDTA for 14 days and then placed into the automated paraffin embedding procedure for two days. Once embedded samples were sectioned on the microtome.

After sectioning all samples were mounted on slides and stained using Haematoxylin and Eosin according to the standard lab protocol and viewed under a light microscope (Leitz Laborlux 12).

In order to prepare natural EP samples for permeability testing, once all surrounding tissues were removed from the bovine tail bone, individual vertebrae were separated (Figure 6.11, A). Following this the vertebrae were sectioned sagittaly approximately 10mm below the endplate, measured from the outer most anterior edge. The IVD component was then carefully removed via micro-dissection using a binocular microscope (Figure 6.11, B). Finally, an 8mm core was taken from the centre of the sample, using a standard manual coring tool. Once removed the core sample was cleaned in a thorough manner using a dental pick water lavage (Oral B Professional Dental Care) to remove as much residual blood and soft tissue as possible from within the trabecular structure (Figure 6.11, C).
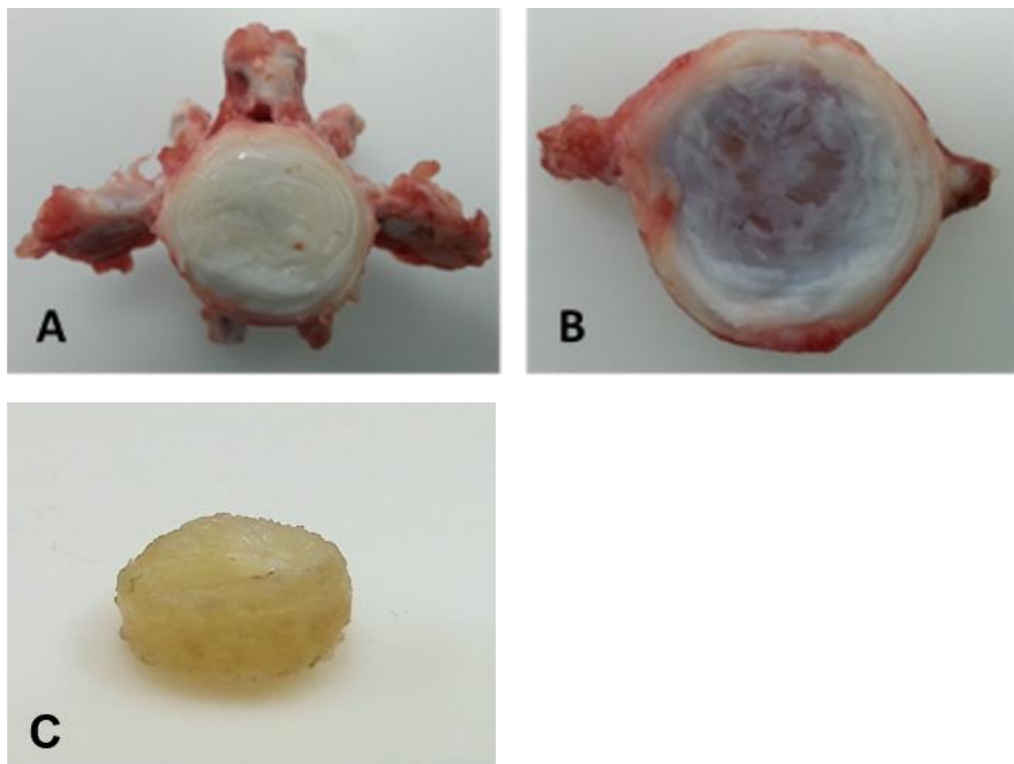
Figure 6.11: Individual bovine vertebra dissected from bovine tail bone (A). Micro-dissection was then carried out to remove the NP and AF tissues, following which the bovine endplate was sectioned approximately 10mm below the anterior endplate periphery (B). Finally, the 8mm core was removed using a standard manual coring tool and cleaned with a water pick device (C).

6.2.5 Mixed Particle Ratio Scaffold Production

For instances in which scaffold permeability was investigated in the absence of a cellular component, specific carbon moulds were manufactured to generate samples with an 8 mm diameter for use in the standard permeability testing equipment . In order to determine the potential influence of <45 μm and 45-90 μm particle mass fraction ratios on permeability a number of samples were prepared in 50g batches. The ratios investigated are given in Table 6.1 below:

%Wt Ratio of <45μm to 45 -90μm Particles			
20/80	40/60	60/40	80/20

Table 6.1: %Wt ratios of <45μm to 45 -90μm particle fractions prepaired for the manufacture of 8mm diameter scaffolds for permeability testing.

6.2.6 Cell Seeded Construct Production

In relation to the cell-seeded construct development activities within the current chapter the AM_{96} scaffolds geometries were used (Section 5.2.1). In all cases the 45-90 μm AM parent glass particles were used exclusively. These substrates are used to develop and analyse different seeding methodologies in regard to their potential to be used in future efforts to create osteochondral EP constructs. Two principal seeding methods were addressed, the micro-mass and pellet techniques outlined below:

6.2.6.1 Micro-Mass Constructs

In order to ensure that the MSC seeded as a micro-mass on the surface of AM-GC scaffolds were retained at the surface, a specialised seeding technique was developed. In the first instance 150 μl of sterile 3% agarose gel mixture was added to the well of a 96 well plate (Figure 6.12, A). This plate was then placed on ice and a sterile 3.4 mm diameter steel bar placed into the centre of the well and held for approximately 60 seconds until the agarose had set (Figure 6.12, B). Once set the steel bar was removed and an individual AM_{96} scaffolds placed within the void. The surface of the scaffold was then seeded with a $1x10^7$ cells/ml MSC suspension in basal medium, 10 μl of this suspension was added to each scaffold surface giving a total of $1x10^5$ cells/scaffold (Figure 6.12, C). The micro-mass suspension was then allowed to adhere for 2.5 hours at 37°C and 5% CO_2. Finally a further 200 μl of chondrogenic or basal media was carefully added to each well and the plate placed back in to culture (Figure 6.12, D). The media was changed every 3 days thereafter and cultured maintained at 37°C in a humidified atmosphere of 5% CO_2.
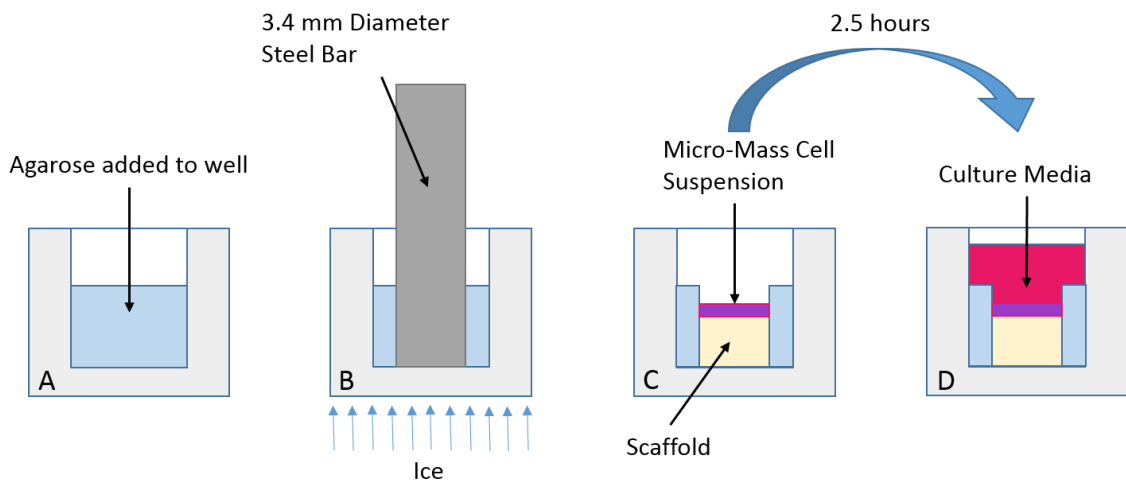
Figure 6.12: Schematic representing the micro-mass construct seeding methodology.

6.2.6.2 Pellet Constructs

Pellet cultures were prepared via the centrifugation of 96 well U-bottomed non TCP culture plates, in which each well contained $2X10^5$ MSCs suspended in 400 µl of basal media. Following centrifugation pellets were placed into culture at 37°C in a humidified atmosphere of 5% CO_2 for 24 hours, after which the basal media was carefully removed and 400 µl of chondrogenic media added to each pellet (Figure 6.13, B). The 96 well plate was then returned to culture for a further 14 days throughout which chondrogenic media was refreshed every 3 days. Once the 14 day chondrogenic pre-differentiation was complete, three pellets were carefully taken up into a pipette and deposited onto the surface of a single AM_{96} scaffold. The AM_{96} scaffolds had themselves been pre-seeded with $6X10^4$ MSCs and placed into osteogenic differentiation culture conditions for 14 days prior to the addition of the chondrogenic pellets (Figure 6.13, A). Finally 400 µl of osteochondral culture media (Section 2.3.4) was added to each well containing a cell scaffold construct (Figure 6.13, C) and the plate placed back into culture with the media refreshed every 3 days.
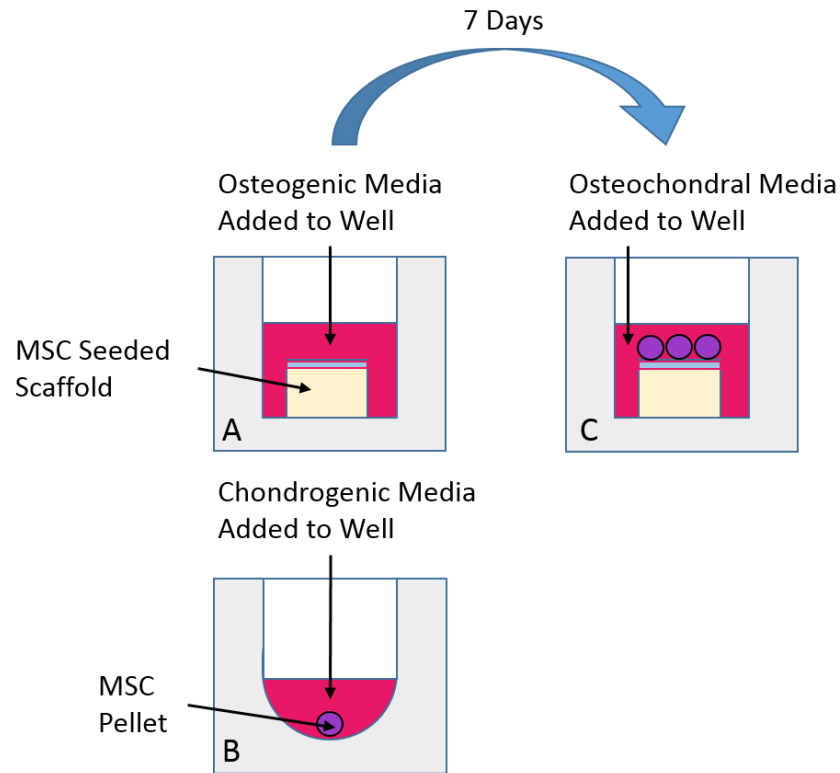
Figure 6.13: Schematic representing the pellet construct seeding methodology.

6.2.7   SEM Analysis of Seeded Constructs

Samples seeded via the pellet construct methodology were analysed via SEM in triplicate at both 7 and 21 day time points, while those seeded via the micro-mass construct methodology were imaged in triplicate at the 14 day time point following both basal and chondrogenic culture conditions.

6.2.8   Histological Analysis of Seeded Constructs

In the case of pellet seeded constructs histological slides were prepared in the manner described in the general methods (Section 2.5), in triplicate following both 7 and 21 days in osteochondral culture conditions. However, in the case of micro-mass seeded constructs histological slides were prepared in triplicate at the day 0 time point in basal conditions and for both basal and chondrogenic culture conditions at the 14 day time point.

6.2.8.1 McNeal's Tetrachrome Staining of Construct Sections

Sample slides were first agitated in 50% methanol in distilled water for 10 minutes, followed by immersion in distilled water for 3 minutes. Samples were then transferred to a 0.1% formic acid solution and agitated for a further 10 minutes and then underwent three separate immersions in distilled water each for a 3 minute period. Samples were then placed into a 10% McNeal's Stain (5 ml modified McNeal's Tetrachrome [500 ml methanol, 500 ml glycerol, 1 g methylene blue chloride (Cat No:M6900, Sigma-Aldrich), 1.6 g azure A eosinite (Cat No:190600250, Thermo Fisher Scientific) and 0.2 g methyl violet (Cat No:202090010, Thermo Fisher Scientific)] and 2.5 ml of 0.1% toluidine blue solution [20 mg toluidine blue, 20 ml distilled water] diluted in 42.5 ml of distilled water) for 5 minutes after which they were washed in running tap water for a further 5 minutes. Samples were next dipped into 70% ethanol and immersed in 0.1% basic fuchsin (0.5 g basic fuchsin in 500 ml distilled water) for 30 seconds, followed by a second 5 minute wash in running tap water. Finally samples were air dried in for a minimum of 2 hours and imaged under an inverted light microscope (Olympus IX71) under normal illumination. Images were captured using a digital camera attachment (Olympus U-CMAD3).

6.2.9   Alcian Blue Staining of Constructs

AM_{96} scaffolds seeded via the micro-mass seeding technique (Section 6.2.6) were investigated at 0 and 14 days culture under both basal and chondrogenic conditions. In order to elucidate the production of the chondrogenic ECM PG aggrecan an Alcian Blue stain was used. First micro-mass seeded constructs were washed twice with distilled water for 2 minutes in individual wells of a 96 well plate. Scaffold constructs were then covered with 200 μl of 1% Alcian Blue (Alcian Blue 8GX powder, Sigma A-5268) solution made up in distilled water with a pH less than 1, achieved via acetic acid buffering. The samples were then incubated for 30 minutes before the Alcian Blue solution was removed and the samples were washed in 1% acetic acid. Next samples were washed once more in distilled water to remove excess stain and transferred into 20% glycerol until imaging could be performed. The stained scaffolds were then imaged on a stereo microscope (Zeizz, AxioCam MRc5).

6.3 *Results*

6.3.1   *Bovine Endplate Identification*

From the three sample preparation methods utilised, it was easy to distinguish the bone cartilage interface (Figure 6.14, C-F). However, it was not possible to make out features characteristic of EP tissue in all samples regardless of the preparation method. Only in the case of surface decalcified samples at X15 magnification was a clear definition obtained (Figure 6.14, B). Using this method there is a clearly visible tide mark region and the cells have a larger vacuous space surrounding their nuclei, this is the chondron, a collagenous shell created around the cells characteristic of EP chondrocytes and those found in articular cartilage [14]. Digital magnification of the proposed bovine EP with the tide mark and chondron periphery indicated is provided (Figure 6.14, G)
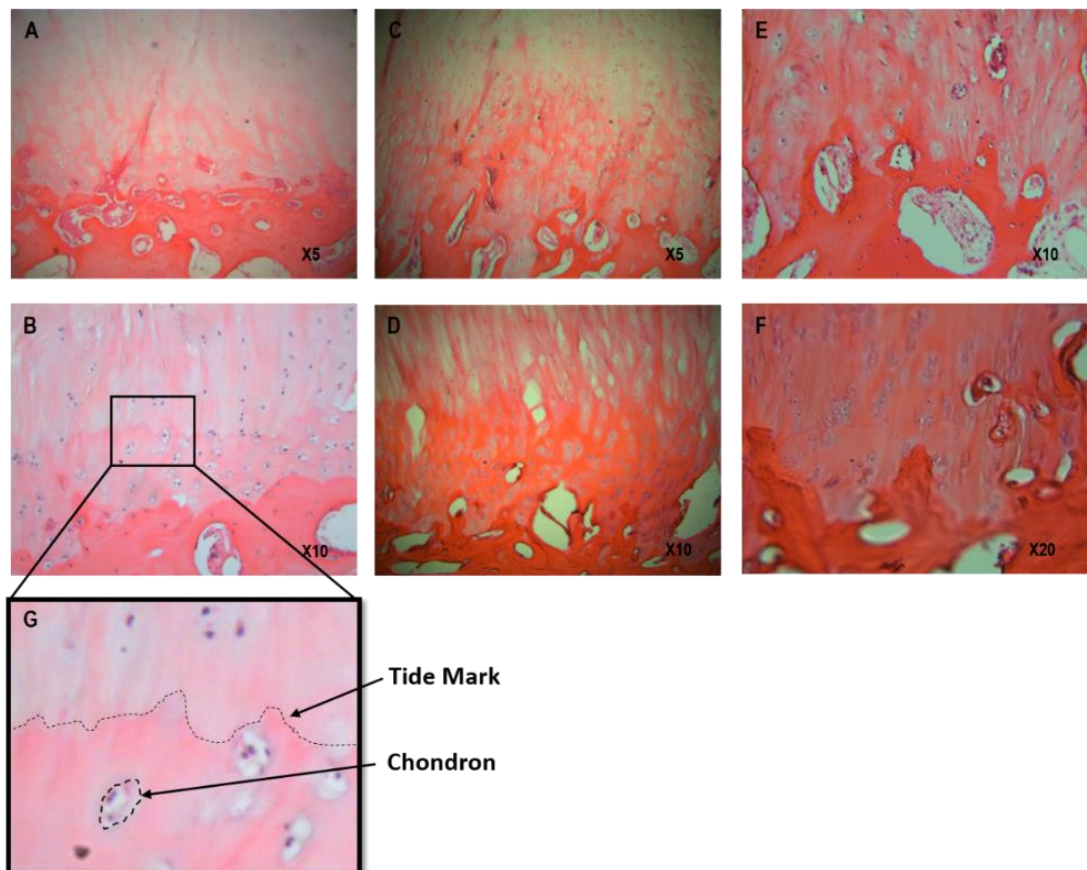
Figure 6.14: Histological sections of the bovine endplate region stained with Haematoxylin and Eosin. Samples were prepared by either surface decalcification prior to paraffin embedding (A-B) or 14 days decalcification in EDTA followed by either paraffin embedding and sectioning on a microtome (C-D) or OCT embedding and sectioning on a cryotome (E-F). The presence of a tide mark and the chondron is illustrated on a digital magnification of panel B giving clear indication of a present EP structure (G).

6.3.2 Pellet Seeding Analysis

SEM analysis of constructs seeded via the pellet seeding methodology outlined above (Section 6.2.6.2) identified that at 7 days post seeding and culture in osteochondral media, the spheroids maintained their rounded morphology (Figure 6.15, A). Higher magnification found there to be no obvious sign of fusion between the cell components of the individual spheroids with each other as there is still clear definition at spheroid junctions (Figure 6.15, B-C). Also, there appeared to be no obvious integration with the pre-existing cell monolayer that was present on the scaffold prior to addition of the spheroid components. However, there is a notable area of no cell coverage around the spheroid cluster on the scaffold substrate (Figure 6.15, B). This may be evidence of a degree of cell layer integration between the spheroids and substrate monolayer that has been broken during the dehydration of the samples, as shrinkage of the spheroids may be considerable given the cell number within each component.

By the 21 day time point the scaffolds displayed a confluent cell layer over its entire surface and evidence showing a degree of flattening within the spheroid components (Figure 6.15, D). Higher magnification imaging in this instance does show signs of a confluent layer covering the spheroid components (Figure 6.15, E), however, at this point it is still not possible to determine whether the confluence represents an interaction between the spheroid and monolayer constituents or if the monolayer has simply grown over the spheroid components. Again there is an area of rupture present on what appears a once confluent layer concentrated around the spheroid components (Figure 6.15, E-F). This points towards the degree of shrinkage within the spheroids during dehydration leading to this artefact as in this instance there are no signs of this rupturing anywhere else on the scaffold surface

Histological examination at 7 days showed there to be again a maintained spheroidal morphology, however, the region between the spheroids were observed to contain a build-up of cells creating a bridge between the monolayer and spheroid components while also demonstrating a build-up of cells in the space between spheroids (Figure 6.16, A-B). There is no clear evidence of mineral formation in the monolayer regions which were pre-differentiated for 7 days in osteogenic conditions, however, there is a clear difference in the coloration of the spheroid components and cells surrounding the spheroids and within the monolayer. The spheroids present a much darker blue/purple coloration indicative of a more PG-rich tissue structure (Figure 6.16, A-B). On closer magnification the interface between the spheroid and the

scaffold substrate showed no sign of integration with the spheroid effectively sitting over the AM-GC surface (Figure 6.16, C)

7 Days   21 Days
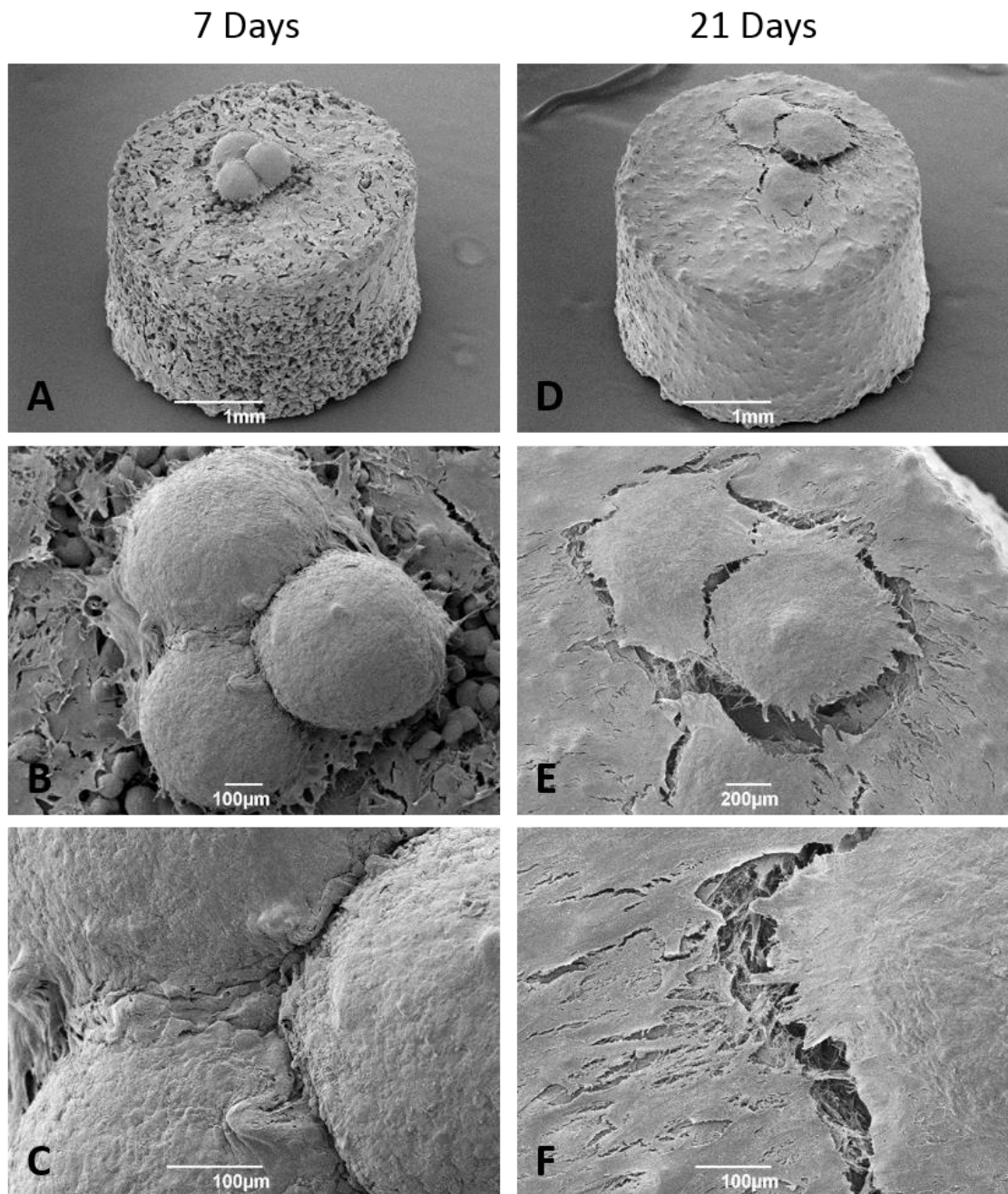
Figure 6.15: SEM imaging of cell pellet seeded scaffolds, images were taken at both 7 (A-C) and 21 (D-F) days post culture in osteo-chondral medial.
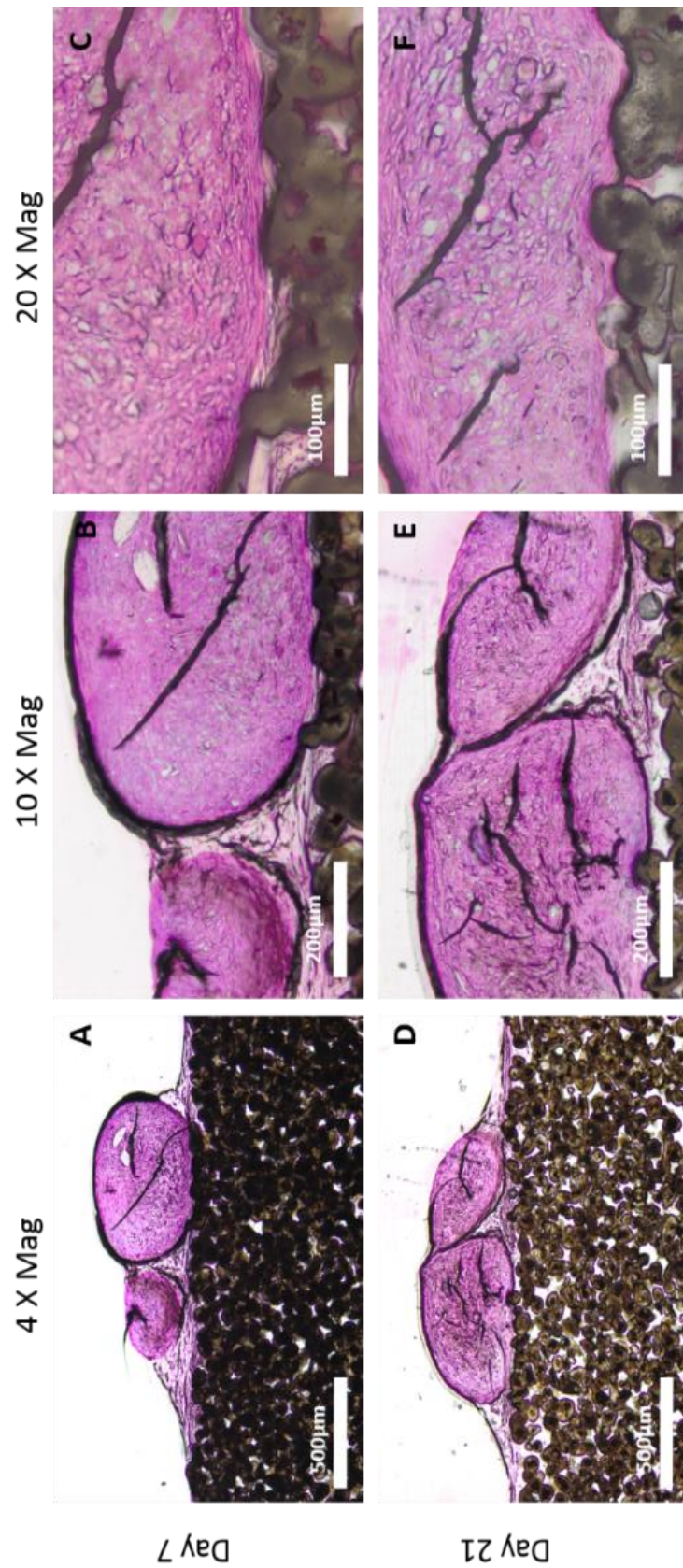
Figure 6.16: McNeal's Tetrachrome Staining of Resin Embedded pellet seeded constructs at 7 (A-C) and 21 (D-F) days post culture in osteo-chondral media.

At the 21 day time point, spheroids did appear to have a slightly less rounded morphology with cells still demonstrating a bridging nature between the monolayer and the spheroid. However, there was still a clear dividing line between the spheroid interfaces and no clear sign of integration with either other spheroids or the monolayer cells (Figure 6.16, D-E). Again the 21 days spheroids retain a much more significant staining perhaps indicating a more PG rich tissue nature. Higher magnification inspection of the spheroid interface with the AW-GC found there to be more conformance between the two components, though no true ingrowth of the spheroid into the scaffold (Figure 6.16, C and F). Also, on inspection there appeared to be no observable indication of ingrowth from the monolayer cells within the scaffolds at either 7 or 21 day time points, with both only showing cells present at the uppermost surface.

6.3.3 Micro-Mass Seeding Analysis

Following 14 days under chondrogenic culture conditions SEM imaging showed a less confluent cell layer when cultured in basal media than that observed for chondrogenic conditions (Figure 6.17, A-D). At higher magnification there is more evidence of cracking over the basal cell layer covering the surface, while there is no evidence of this in the chondrogenic samples (Figure 6.17, E-F). This could be attributed to the dehydration and subsequent cell shrinkage, however, both basal and chondrogenic samples were processed together an thus underwent the exact same dehydration conditions. Therefore, it is more likely the cellular and/or ECM composition that has led to this notable difference. In the case of basal culture the periphery of the scaffolds were noted to possess a sub-confluent region on the uppermost surface (Figure 6.17, G-H), however, This may be an artefact of the seeding methodology, as is the cell free periphery of the scaffolds in both basal and chondrogenic culture conditions (Figure 6.17, A-B).
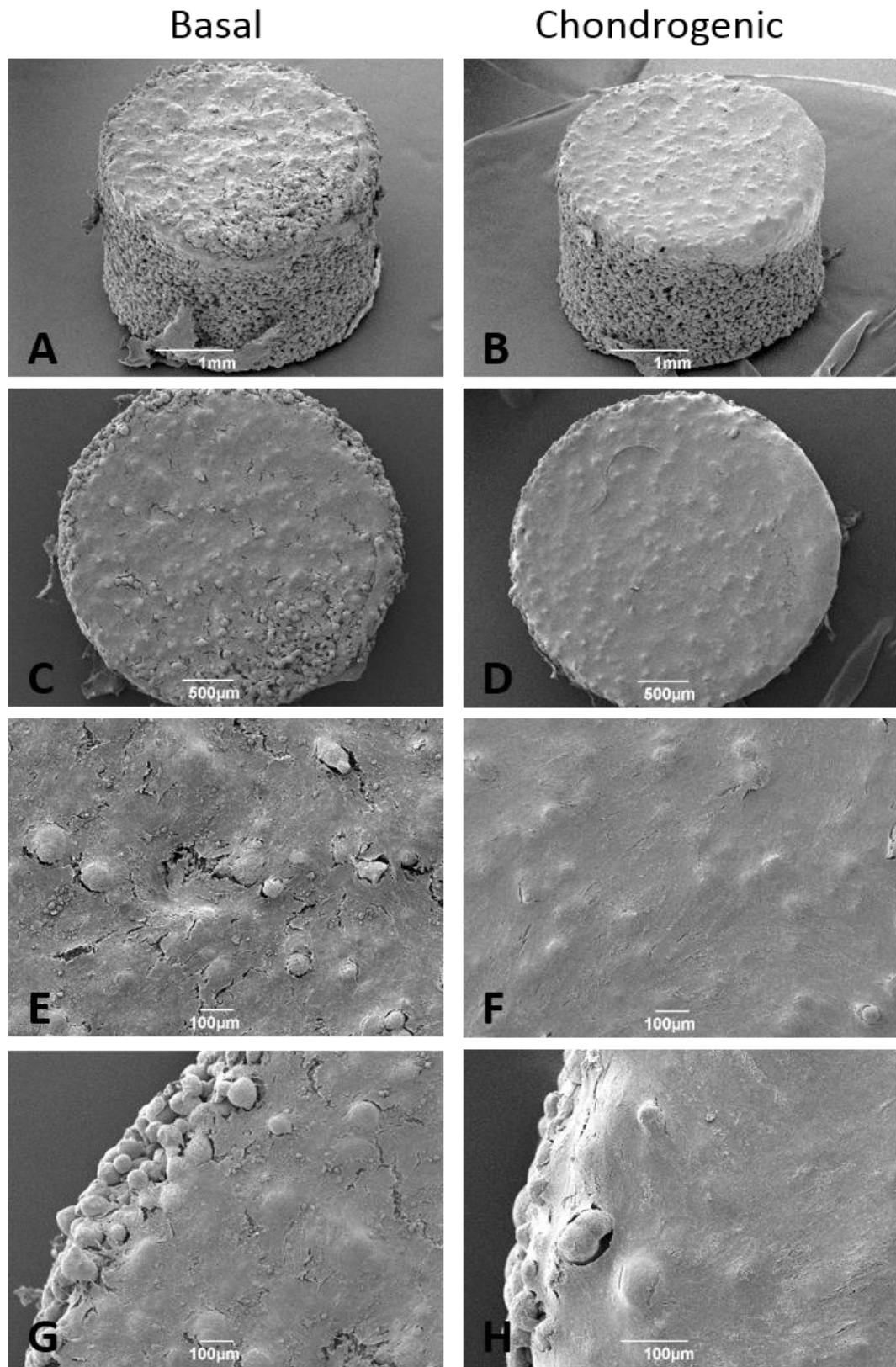
Figure 6.17: SEM imaging of micro-mass seeded scaffolds, images were taken following 14 days culture in both basal (A,C,E,F) and chondrogenic (B,D,F,H) media.

Alcian Blue staining of the micro-mass seeded scaffolds was carried out in order to determine if there was an increased indication from the staining under chondrogenic culture conditions, relating to higher levels of PG synthesis. When compared to the unseeded control sample there was an obvious difference in the degree of staining indicating that cell seeded scaffolds retained a greater amount of stain within their structure. There was no significant distinction between the day 0 and day 14 samples under basal culture conditions. Both showed patches of darker staining, however, most of the surface was much like that of the control, but with a higher degree of reflectivity indicative of a cell monolayer with the contours of the scaffold particles still visible. The day 14 chondrogenic sample, however, demonstrated the darker region of staining over a much greater degree of the surface. Also, at higher magnifications the natural scaffold contours were less visible, perhaps indicating a more established cell and/or ECM component (Figure 6.18). To better indicate the influence of the chondrogenic culture condition effect on cell layer component coverage a grey scale image was also prepared. This image makes it easier for the reader to observe the contrast difference between the basal and chondrogenic samples cell layers (Figure 6.19).
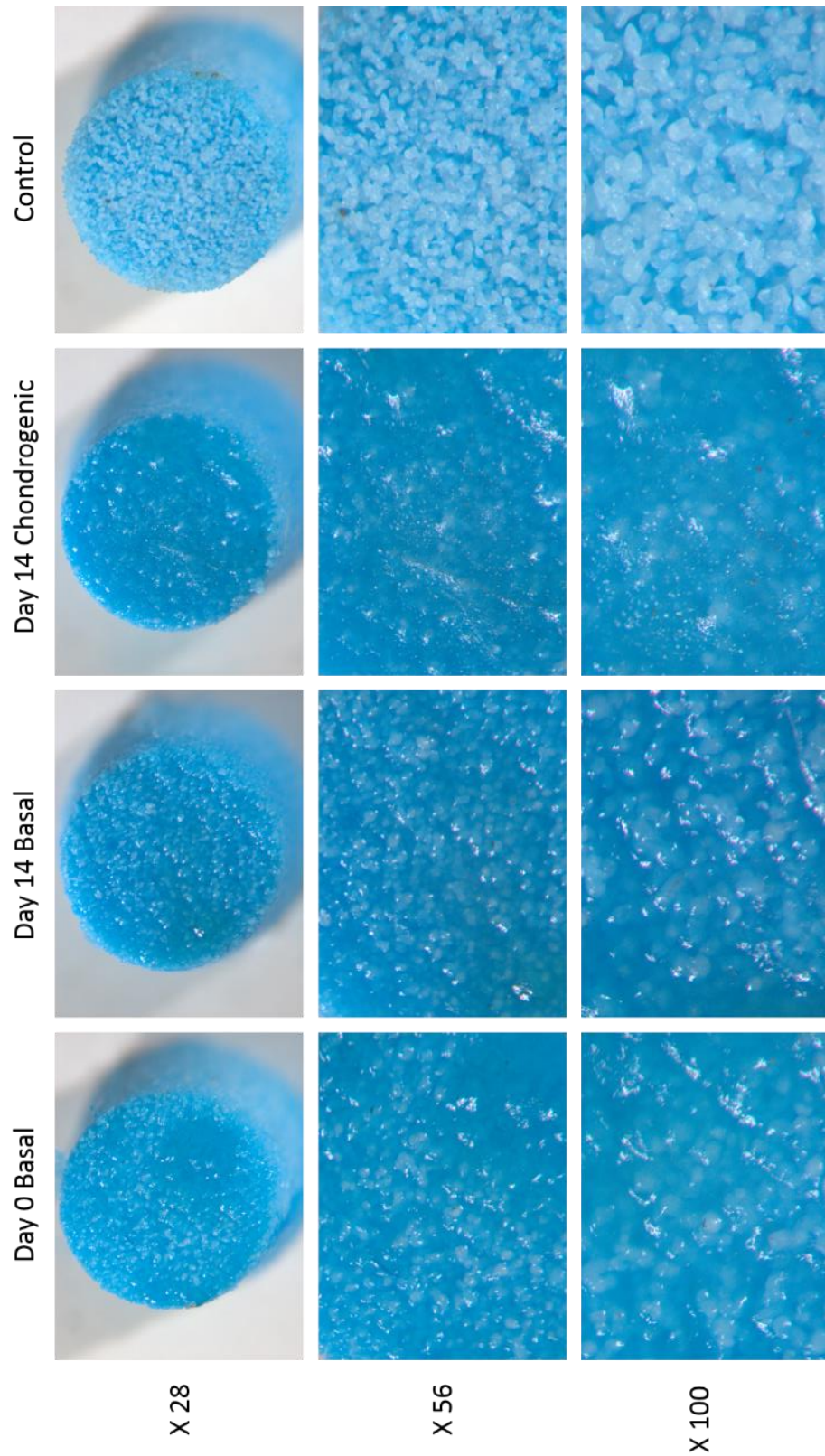
Figure 6.18: Alcian Blue staining of micro-mass seeded scaffolds at days 0 and 14 in basal conditions and day 14 in chondrogenic culture. A control sample is also included with no cells seeded.
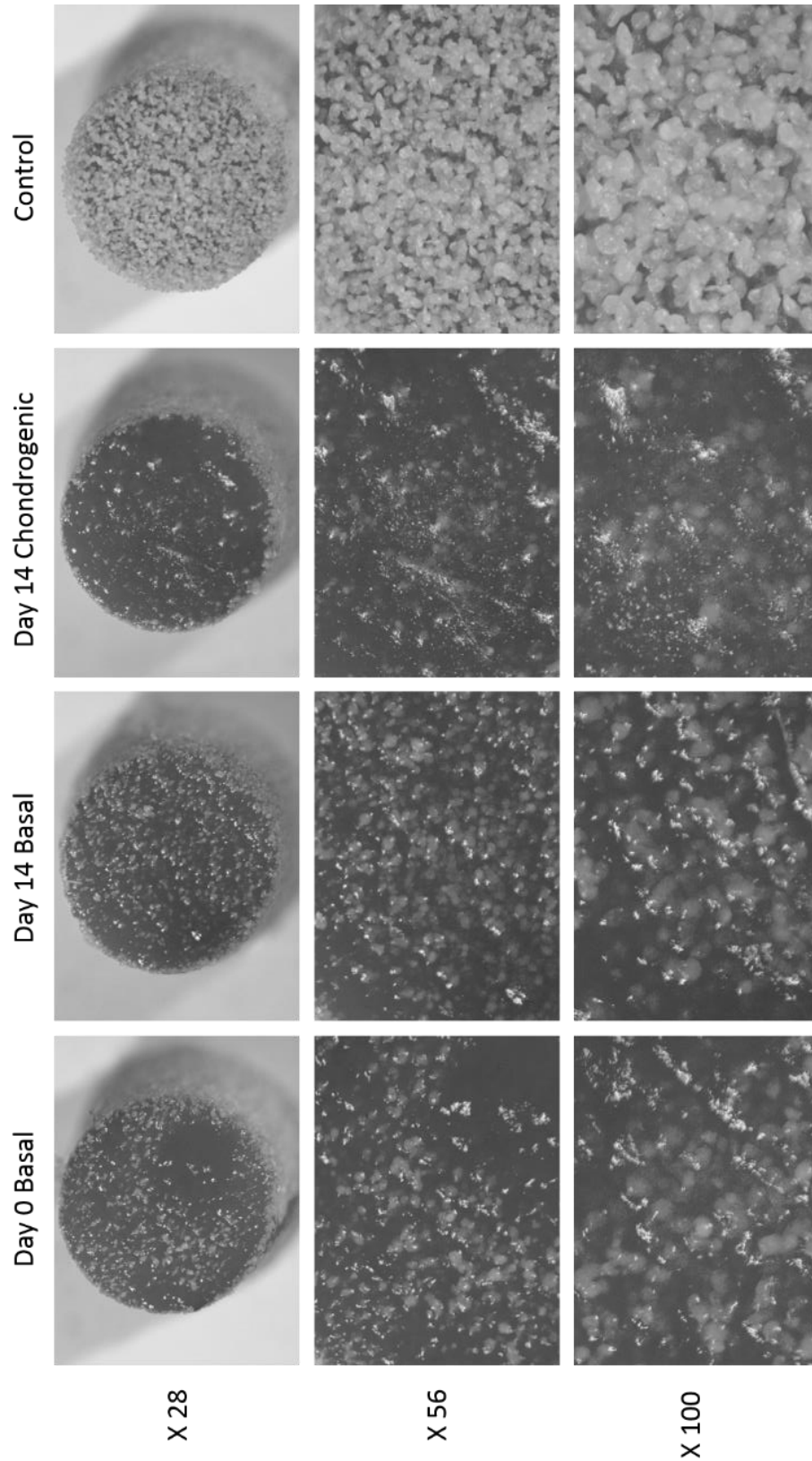
Figure 6.19: Grey scale copy of Figure 6.22, making it easier to see the difference in cell layer coverage between day 14 basal and day 14 chondrogenic samples.

Histological analysis of micro-mass seeded scaffolds showed that at day 0 in basal conditions the cell layer retained a significant degree of stain within a thin but notable layer at the scaffold surface (Figure 6.20, A-B). It was evident, however, that there was no notable cell migration into the scaffold at this time point (Figure 6.20, C). By day 14 of culture under basal conditions the cell layer thickness was notably less and the degree of staining appeared to have reduced (Figure 6.20, D-E). There was some notable indication of cell penetration into the scaffold though this was quite faint with regard to staining for cartilage like tissue compositions, identified by blue/purple staining (Figure 6.20, F). In contrast the 14 day samples cultured under chondrogenic conditions demonstrated a slightly more pronounced superior surface cell layer, which also showed a greater degree of staining (Figure 6.20, G-H). The samples cultured under these conditions also showed a much more significant degree of cell penetration and retained a greater amount of staining within the infiltrating cell fraction (Figure 6.20, I).
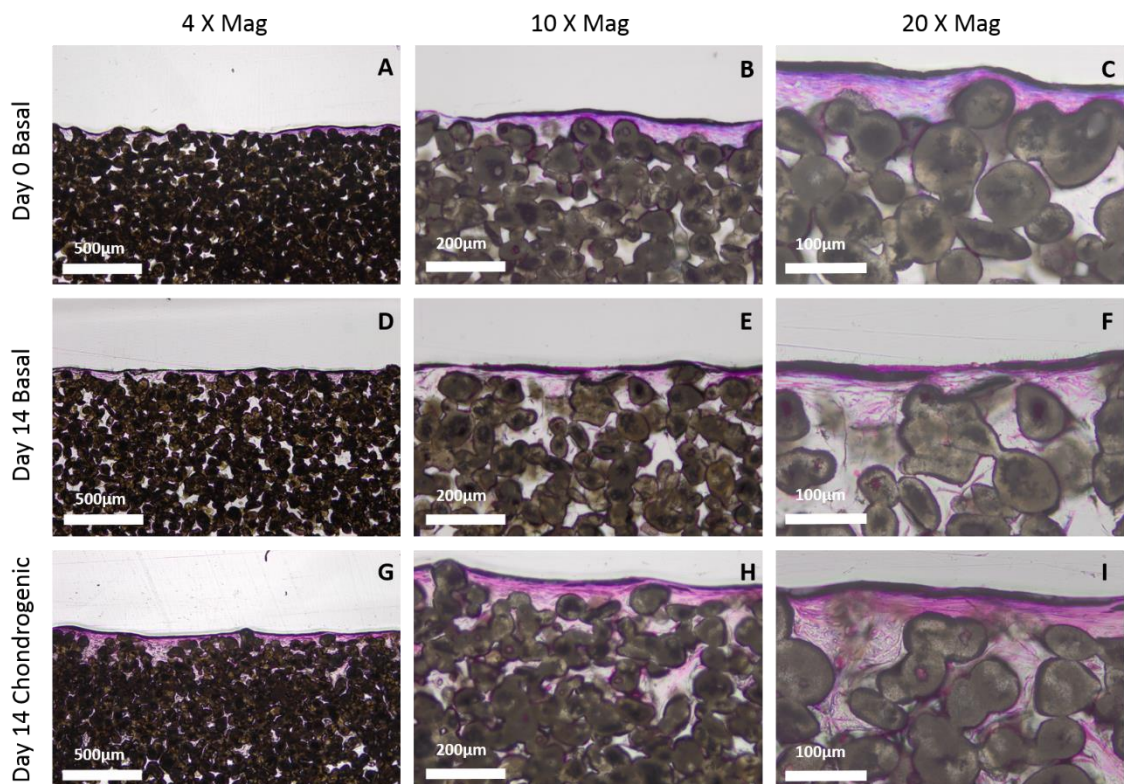
Figure 6.20: McNeal's Tetrachrome Staining of Resin Embedded Micro-Mass constructs at both day 0 (A-C) and day 14 (D-F) basal conditions and day 14 chondrogenic conditions (G-I).

6.3.4 Blocked System Permeability

With the solid steel plug positioned within the standard testing equipment the experimental procedure was carried out a total of four times back to back, termed Run 1 to Run 4. These sequential experimental runs were carried out under two conditions, firstly the testing was carried out such that the pressure remaining in the system following the end of test *phase 2* (Figure 6.9) was released prior to the next test. This four sequential test methodology was then repeated, only this time the pressure was not released from the sample between subsequent experimental runs. It was found that for tests in which pressure was released the permeability steadily decreased from 1.42×10^{-14} m^4/Ns to 8.49×10^{-15} m^4/Ns between Run 1 and Run 3, a slight increase to 9.31×10^{-15} m^4/Ns was then observed on run 4 (Figure 6.21). In the instances where the pressure was not released the permeability decreased sharply from 3.15×10^{-14} m^4/Ns on Run 1 to 1.09×10^{-15} m^4/Ns for Run 2, however, between run 2 and run 3 the permeability dropped further to 3.45×10^{-16} m^4/Ns after which a slight increase was observed to 4.62×10^{-16} m^4/Ns on Run 4 (Figure 6.21).
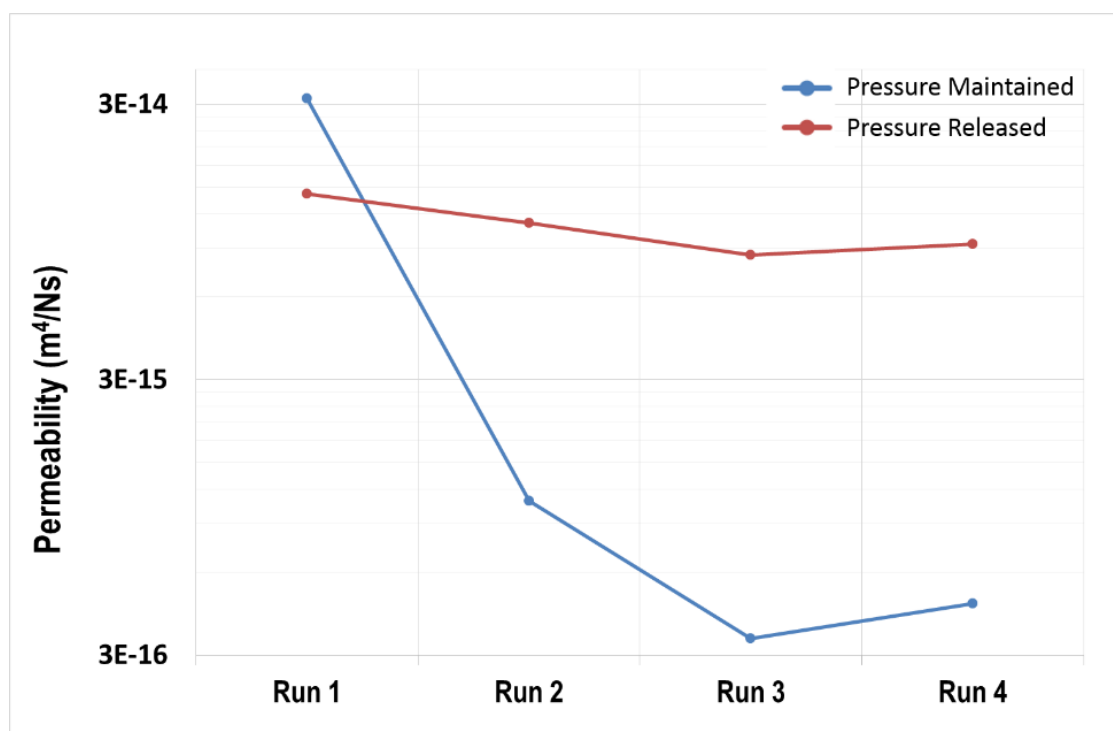
Figure 6.21: Permeability results determined from sequential experimental test runs on the blocked standard system. It can be observed that in instances where the pressure is released between experimental runs (red line) the system permeability is markedly higher than that observed when pressure is maintained between runs (blue line).

When the blocked system, fitted with the construct adaptor was tested, under the maintained pressure regime the permeability on Run 1 was 4.76×10^{-13} m^4/Ns, an order of magnitude more permeable than that of the standard blocked system (3.15×10^{-14} m^4/Ns). Throughout the following three runs the permeability drops to a level of 1.04×10^{-14} m^4/Ns by Run 4, following a conditioning cycle curve similar to that of the standard blocked system but maintaining a notably higher permeability throughout (Figure 6.22).
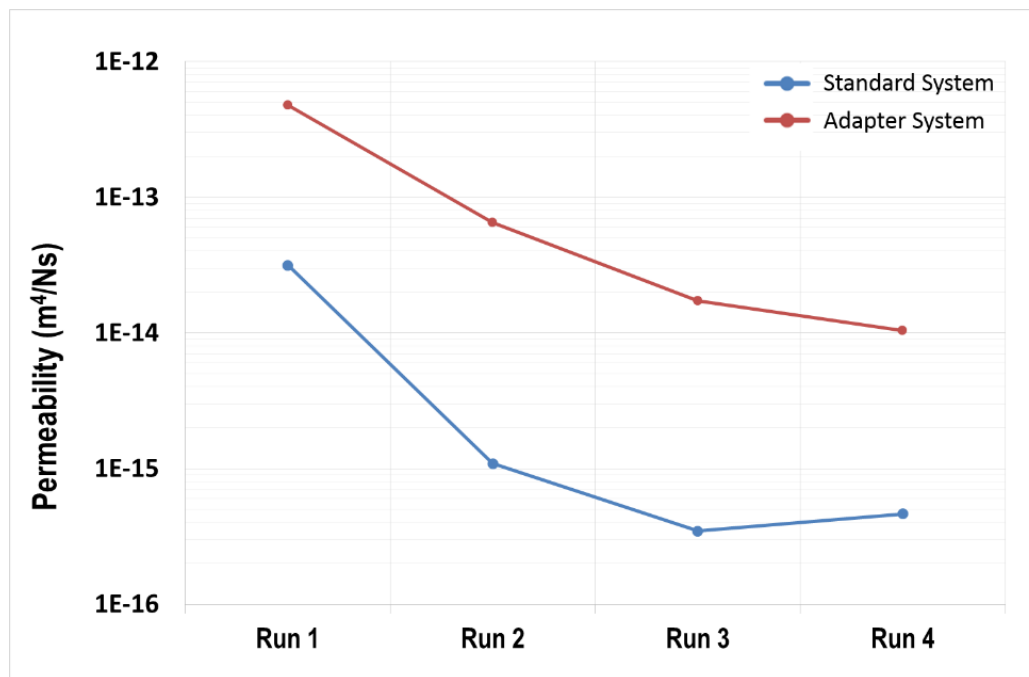
Figure 6.22: Permiability test results observed on blocked systems following suquential experimental runs between which pressure was maintained. It can be observed that both traces follow a simial path, however, the standard system (blue line) maintains a consistently lower permiability level throughout when compaired to the blocked adapter system (red line).

As both the standard and construct adapter systems were sealed with non-porous ($K_s = 0$) plugs, transposition of Equation 6.13 allows for the intrinsic head loss ($\gamma_1 + \gamma_2$) due to probable system leakages to be determined. It was observed that between Run 1 and Run 3 this head loss term in the standard system decreases from 3865×10^{-4} mm^3/MPa.s to 42×10^{-4} mm^3/MPa.s, there is then a slight increase on Run 4 to 57×10^{-4} mm^3/MPa.s. In comparison the head loss due to potential leakage in the construct adapter fitted system decreased from 17283×10^{-4} mm^3/MPa.s on Run 1 to 377×10^{-4} mm^3/MPa.s by Run 4, providing a consistently greater level than that observed in the standard system (Figure 6.23). This result infers that there is a

considerably greater leakage volume present in the adapter system as a function of unit pressure applied when compared to that in the standard system.

	Run 1	Run 2	Run 3	Run 4
■ Standard	3865	134	42	57
■ Adapter	17283	2348	629	377
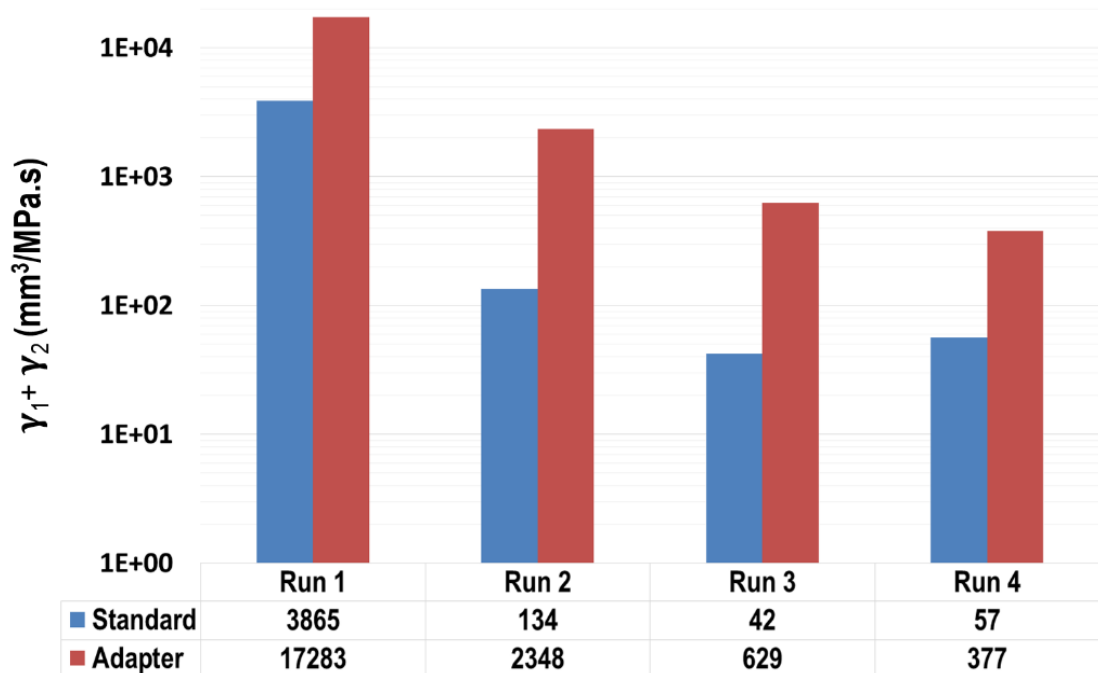
Figure 6.23: Intrinsic head loss within both the standard (blue) and adapter (red) systems. This result demonstrates the consistently greater head loss observed in sequential experimental runs within the construct adapter system.

6.3.5   Bovine EP Sample Permeability

In order to assess the effect of multiple experimental runs on the bovine EP a sample prepared as described previously (Section 6.2.4) was placed into the testing apparatus. Once positioned 7 sequential test runs were then carried out with no pressure release between experimental runs as this was deemed more suitable from the conditioning test carried out on the blocked system. Briefly, the results of the blocked system indicate that the system is not fully saturated in the first instance and a number of runs are required to generate a stable test result. Hence, maintaining the pressure between runs reduces any influence of this factor and provides a more stable and accurate result. Subsequent experimental runs on the bovine EP sample found there to be a substantial permeability decrease from 3.48×10^{-13} m^4/Ns to 1×10^{-13} m^4/Ns between Run 1 and 2 respectively, the permeability then continues to drop in a more consistent manner after Run 2 to 3.48×10^{-14} m^4/Ns by Run 7 (Figure 6.24).
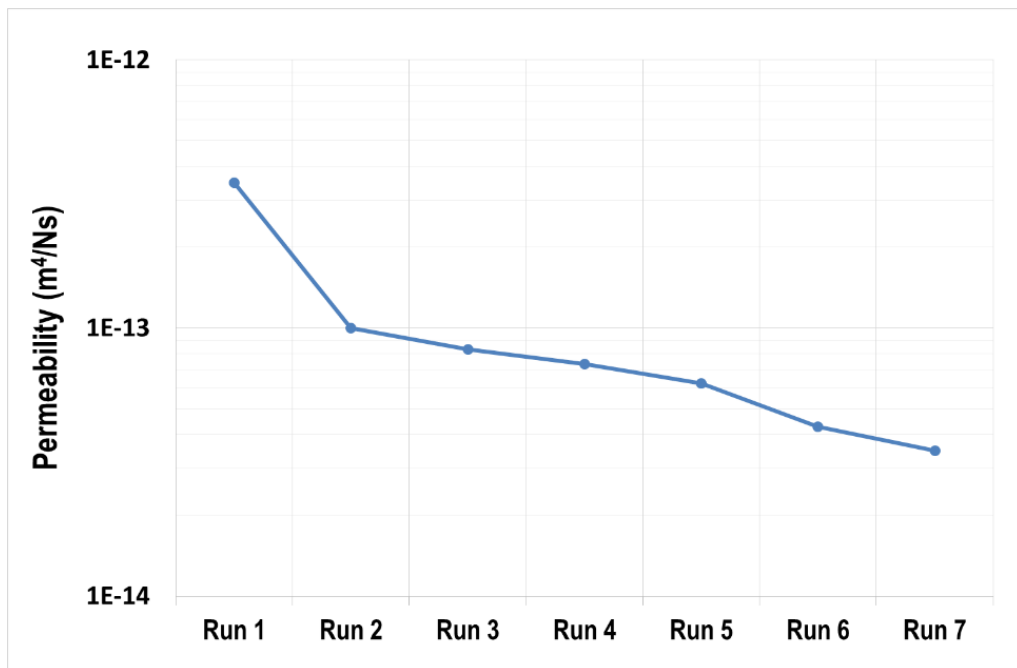
Figure 6.24: The permiability of the natural bovine EP sample measured with the pressure maintained between experimental runs. There is a more notable presessure reduction between run 1 and 2, following which the decrease becomes more consistent throughout.

This permeability on Run 7 (3.48×10^{-14} m^4/Ns) is two orders of magnitude greater than that measured in the fully blocked system by Run 4 (4.62×10^{-16} m^4/Ns), indicating that the EP is providing a much higher permeability in the system. However, the consistent reduction in the result up to and perhaps even following Run 7 indicates that there is still a system element contributing accumulatively to the detected permeability between experimental runs.

6.3.6 Scaffold and Construct Permeability

When permeability testing was carried out using the construct adapter system on cell seeded scaffold samples following 21 days culture in either basal or chondrogenic conditions, the results were unable to return a detectable level of permeability. In both cases the pressure was unable to build up within the system to a level suitable to generate a comparator result to evaluate against the natural EP. On initiating the construct permeability test the stereotypical linear region associated with pressure build up in relation to the constant velocity piston displacement of *phase 1* (Figure 6.9) is not observed. Instead there is a near immediate tail off followed by a slight positive gradient which then proceeds throughout the test. Therefore, the sample was unable to reach a pressure level of any practice significance, when compared to the natural

tissue, generating maximum pressures in the region of 0.02 MPa as opposed to the 0.12 MPa target (Figure 6.25).
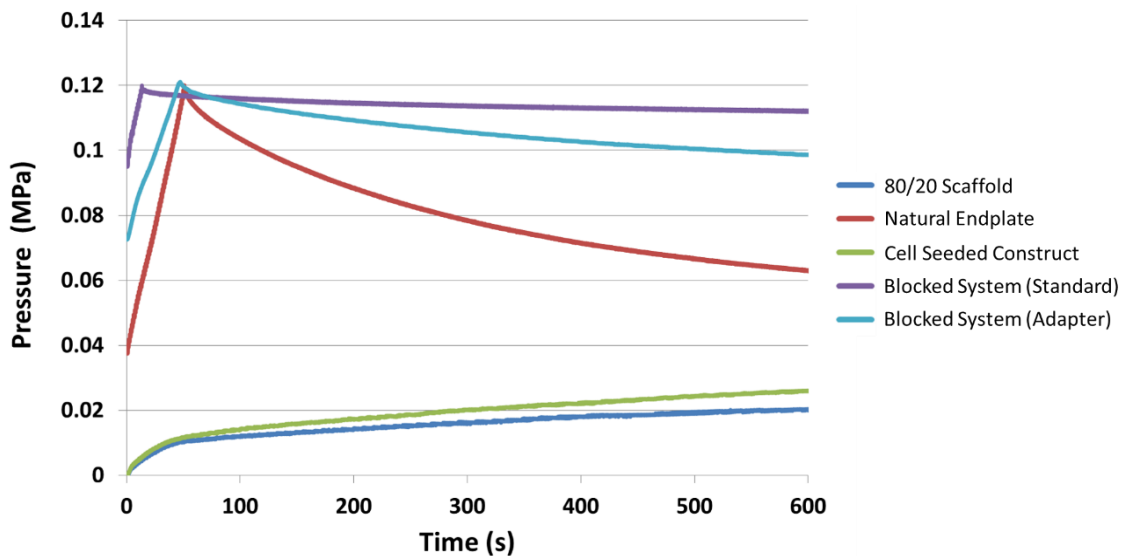
Figure 6.25: Typical experimental pressure vs time curves related to the components being tested in the system. It can be seen that the cell seeded construct and the 80/20 particle mass ratio scaffold provided no resistance to flow within the system. This infers that their permiability is too high for the resolution of the system under the current experimental conditions.

It was in response to this result that the effect of <45 μm to 45-90 μm %wt ratio scaffold components were investigated. However, the ratio compositions analysed again had no significant effect on the outcome with scaffold constructs composed of up to 80% <45 μm particles generating almost exactly the same result as the construct samples (Figure 6.25). Therefore, considering that the blocked adapter system was able to generate the pressure prior to *phase 2* of the test, as was the natural EP sample, this indicates that the scaffolds have extremely high permeability levels in relation to the natural EP tissue. This being outside the detectable range of the current experimental setup even in the presence of a micro mass seeded cell layer following 21 days culture. Hence, the extremely shallow gradient seen for all scaffold samples in *phase 1* of testing indicates that at pressure as 0.02 MPa the system fluid is able to flow almost unrestricted through the samples.

6.4 *Discussion*

Traditional *in vitro* methods of chondrogenic differentiation are based around mimicking the natural processes of mesenchymal condensation and the subsequent pre-chondrogenic tissue phase of endochondral ossification. This chondrogenic phase is principally indicated via the up regulation of SOX9, regarded as the master transcriptional regulator of chondrogenesis, along with L-SOX5 and SOX6 facilitating the production of cartilage ECM proteins such as collagen (type II, type IX, type XI) and aggrecan [186]. *In vitro* it has been shown that in order to enter the chondrogenic pathway a favourable 3D environment is required in addition to the chondrogenic media supplementation [187, 188]. This mesenchymal condensation like environment is conventionally achieved through centrifugation, as was carried out for the pellet culture in the present study. Following 24 hours culture cell-cell attachment should form and by 7 days up regulation of the cartilage ECM proteins and the wet mass of the tissue increase, indicating the deposition of a PG-rich tissue [189]. In the current study histological inspection of the pellets did illustrate dark purple staining indicative of PG expression (Figure 6.16). However, there was little evidence of fusion seen between pellets, this was further evidenced in the SEM analysis which shows clear definition at the pellet boundary's at day 7 (Figure 6.15, B & C). It was originally hoped that a significant fusion and flattening would occur in the pellets over this time frame. This lack of fusion is perhaps explained by the nature of the pellet culture, as the biomechanical forces on the tissue due to radial expansion have been shown to lead to a more fusiform flattened and un-differentiated cell layer at the surface. It is under this layer that traditionally, MSCs take a more rounded morphology and begin to produce PG and collagen rich ECM components [189]. Though there is perhaps some indication of a more fusiform layer evident in the current chondrogenic pellets it is not conclusive due to the nature of the current staining technique (Figure 6.16, C & F).

In the current analysis there was little indication of any interaction between the pellets and the pre-osteogenically treated monolayer, with the monolayer cells seeming to grow over the pellets by 21 days co-culture (Figure 6.15, D-F). Previously Tuli *et al*, produced osteochondral constructs using poly-D, L-lactic acid (PLA) scaffold substrates with common primary human MSCs used for both the chondrogenic and osteogenic elements [190]. In order to produce the constructs, a large number of MSCs ($1.5X10^6$) were press-seeded onto the substrate surface and cultured in chondrogenic supplementation for 2 to 5 weeks while concurrently, monolayer cultures from the same patient were osteogenically induced. Following this, the pre-differentiated osteogenic fraction was seeded onto the opposite side of the PLA scaffold and the construct cultured further

in an osteochondral supportive media. Under these conditions, Tuli *et al* identified a transitional zone between the two surfaces which displayed a large degree of calcification at the interface. In the current study there was no indication of calcification between the pellet and monolayer cell components after 21 days of co-culture. Other techniques developed for the osteochondral culture of MSCs have demonstrated clearly the fusion characteristics between co-cultured osteogenic and chondrogenic pre-differentiated cell populations as early as 24 hours [191]. Spheroid based MSC culture and differentiation techniques pioneered within the Genever lab allow for the formation of 3D MSC spheres achieved using a 20% methylcellulose containing cell suspension media in non-adherent U-shaped wells [192]. Under these conditions cells naturally adhere and fabricate towards an innate mesenchyme condensation, unaided by centrifugation over a 24 hour period forming spheroids. These cultures have then been demonstrated capable of both chondrogenic and osteogenic differentiation through the same media supplementation conditions used in the current study [191, 193]. It was demonstrated that following 6 days chondrogenic and osteogenic pre-differentiation respectively, that co-culture of the spheroids in osteochondral media lead to fusion occurring in as little as 24 hours. Cell tracker green and red labelling of the osteogenic and chondrogenic cell fraction respectively in combination with SEM analysis showed that following 6 days co-culture the spheroids integrated completely and that the chondrogenic cell fraction took up a position on the periphery to form a chondrogenic casing. This observation would perhaps strengthen the hope in the current application that the chondrogenic pellet would start to flatten and in principal encase the osteogenic monolayer of the substrate, but there was no sign of this interaction.

Though the difference in culture techniques associated with the spheroid MSC model environment and the centrifuged pellet are hugely significant factors prohibiting any direct comparison, the chondrogenic differentiation of spheroid cultures did present a change in the surface, becoming smoother over time up to 21 days, perhaps akin to the fusiform layer of the cell pellet. This considered, it is perhaps possible that the 14 days of chondrogenic pellet culture prior to co-culture on the monolayer substrate may have been a significant factor inhibiting any potential interactions allowing the more fusiform layer to form as a consequence of radial growth. This is more relevant when considering that in the cases where fusion between osteogenic and chondrogenic spheroids is observed, pre-differentiation took place over a considerably lower time frame, only 6 days [191]. Therefore, although in the current study 14 days of pre-differentiation was believed to be a better option to allow for a more established chondrogenic phenotype to develop it may actually be an inhibitory factor on potential interactions and any future efforts may

be best focused on the time at which co-culture is commenced. Also, the use of spheroid culture preparation techniques should be seriously considered as either a comparator or replacement methodology.

The micro mass seeding technique in the current chapter was developed based on observed methods in literature aimed at the development of osteochondral constructs, specifically those that focus on a scaffold free approach to the cartilage component. There are relatively few studies to this effect and the majority utilise mammalian articular chondrocytes as their cell source [85, 194-196]. The use of primary chondrocytes is a logical choice as they are the terminally differentiated cell type responsible for the production of collagen type II and PG ECM components. These cells are also easy to obtain through enzymatic digestion of the natural tissues [197]. However, the main limitation to this approach is that primary chondrocytes are known to de-differentiate when cultured *in vitro* and although approaches such as growth factor supplemented media [198] and/or 3D culture techniques, within a range of scaffold materials, have shown marked improvements in retaining phenotype [199]. It is still difficult to obtain sufficient amounts of chondrocytes under *in vitro* conditions [200]. Wang *et al* seeded primary porcine chondrocytes onto a range of common biomaterial substrates, PLA and collagen-HA and found significant amounts of collagen type II and GAG content within the ECM along with partial integration with the scaffold substrates. However, it was observed that the collagen-HA substrates were superior in terms of both cell viability and cellular integration [194]. Following this Kandel *et al* seeded a porous calcium phosphate substrate with sheep articular chondrocytes with biochemical and biomechanical testing following 3 and 9 months implantation into full thickness osteochondral defects in the trochlear grove of sheep, which showed promising results. Neither the cellularity nor PG content of the implanted constructs, when it remained *in vivo*, changed significantly between 3 and 9 months although the collagen content increased slightly [196]. Hence, given the previous success on CaP based substrates in the much harsher mechanical environment of articular cartilage the current approach may prove superior in terms of cell source availability provided chondrogenic differentiation of the MSC can be achieved on the AM-GC substrate.

MSCs are considered to be the cell type of choice for cell-based cartilage tissue engineering because of (1) the ease with which they can be isolated and expanded and (2) their multilineage differentiation capabilities [201]. The current study attempts to utilise MSC populations to the same effect as those previously focused on the primary chondrocyte. As with the pellet based

model of chondrogenesis, the principals of the micro-mass culture technique are based on replication of the condensing mesenchyme seen in endochondral ossification. This approach was first pioneered by Ahrens *et al*, who demonstrated that when cells of the developing wing buds in chick embryos are removed and cultured in cell layers greater than confluence, within a restricted surface area, that cartilage differentiation occurs. By three days the cells aggregate to form cartilage nodules easily recognised by their Alcian blue staining [202]. Later these micro-mass culture techniques were adopted using C3H10T1/2 cells, a murine cell line with multiple differentiation potential. The study focused on determining a stimulatory influence of BMP-2 on chondrogenesis. It was revealed that both BMP-2 concentration, cell plating density and culture time bore significant influence on the chondrogenic differentiation. It was in this study that 10^7 cells/ml seeding density, used in the current study, was identified as optimal for PG production [203]. It was hoped that in the current study we could develop a seeding methodology to facilitate the use of the micro-mass culture methods of primary MSCs on the AM-GC substrates.

The results of the current study weigh quite favourably towards this seeding methodology, albeit partially due to the lack of any significant results associated with the pellet seeding technique. The micro mass seeding method showed markedly better histological results under chondrogenic conditions than basal at 14 days. Demonstrating a much more prominent surface layer, which also showed better staining indicative of a greater degree of PG within the ECM. It was also observed through SEM that the cellular structure maintained a greater degree of confluence at 14 days in chondrogenic conditions when compared to the same time point in basal media. Bearing in mind that these samples were prepared together under the exact same conditions, this points towards the cellular/ECM composition being the chief influencing factor contributing to this difference. The cells under chondrogenic conditions on SEM display a smother structure over the surface, a characteristic also observed on chondrogenic spheroids and pellets previously at 21 day time points [189, 191]. Though Alcian blue staining was attempted, the nature of the scaffold substrate makes the differentiation between the degree of staining extremely difficult, however, there is again an indication that a greater wet tissue mass is present on the scaffold surface, better observed on the grey scale image indicative of greater PG content (Figure 6.19). Tulie *et al*, was the only noted study to utilise primary human MSC in the absence of a scaffold as is the case here. They subsequently reported a significant hyaline like cartilage structure, though this was not observed until 10 weeks and in fact by 4 weeks they reported considerably less ECM and more cellularity akin to the ingrowth observed at only 2 weeks in the present analysis [190]. This increased cellular ingrowth observed in the current 14 day scaffolds under chondrogenic

conditions is also believed beneficial as it may allow for better fixation between the scaffold and cartilage components, especially in the early stages of fixation should an EP construct ever be realised in the clinic.

It will be apparent to the reader that there is a wealth of chondrogenic characterisation that has not been performed in the current chapter, most notably standard histological approaches to defining chondrogenic differentiation such as, collagen II, aggrecan and sulphated GAG staining. This is due to the fact that this is purely a developmental chapter with the aim of providing a basis for future in-depth construct study, although here we do observe a greater capacity to develop an AM-GC/hMSC construct through micro-mass seeding methods, demonstrating a clear response to chondrogenic culture conditions. The major challenge which limits the histological characterisation within the remit of the current study is the nature of the AM-GC. Its hardness in contrast to the cellular component makes preparation extremely complex and time consuming. This being said a specialised approach to the histological preparation utilising resin embedding, diamond blade sectioning and subsequent sequential grinding is clearly defined in the current work (Section 2.5). This resin embedding presents a significant challenge to standard histological protocols requiring substantial re-optimisation of traditional paraffin or cryosectioning methods. The real aim here is to develop the construct alongside the permeability testing equipment so that any future in-depth development of the cell/scaffold constructs in relation to elements known to have effect on final ECM composition such as, seeding density, culture time, media supplementation, mechanical stimulus or any combination of the these factors [189, 197, 200] can all be done in line with a suitable permeability test methodology. This facilitates the determination of which combinations of these factors achieves the correct level of permeability to allow the construct to perform its *in vivo* function of providing nutrition to the IVD tissue regions. This then allows the emphasis to be taken away from whether or not the tissue has the exact same architecture and composition of the natural tissue but instead asks, "will it perform the same function", which is the true goal.

The permeability testing equipment and methodology proposed here for the partnered development of tissue engineered constructs for potential future EP applications, in this instance focusing on AM-GC scaffolds, has a number of key advantages. Not only does the technique mimic the *in vivo* conditions of mass transfer at the interface region of the IVD and adjacent vertebral body. But it does this in a quasistatic manner so as to eliminate any influence of dynamic effects due to fluid velocity and/or acceleration such as, turbulent flow or inertia. As a

consequence the fluid induced matrix compaction within the samples, either constructs or natural tissues, is minimised. The current testing generated resultant axial compression forces of 6 N and 1 N in the standard and construct adapter systems respectively. This is a key distinguishing factor to the technique in light of the proposed tissue engineering application, as many permeability test methodologies would impart greater pressures and, hence, loads over the soft tissue elements of the structure effectively increasing the permeability as a consequence of the matrix compaction. This would lead to differing levels of permeability when used in specific applications compared to those indicated during *in vivo* testing.

The current analysis of the standard system indicated that for instances in which pressure was maintained between experimental runs, much lower levels of permeability were determined following Run 1 (Figure 6.21). Given that the load trace was not torn between these runs and that the same pressure level was maintained as the initiation point for phase 2, it is proposed that this marked reduction in permeability is due to saturation of the system and sample components following sequential runs. Therefore, indicating that in instances where pressure is maintained the system permeability is no longer influenced by system saturation and is more able to accurately reflect the sample measurement without a system contribution. To further illustrate this point it was observed that when using the same system to analyse the natural EP, the permeability determined at Run 4 was two orders of magnitude greater than the blocked system at 7.33×10^{-14} m^4/Ns. Indicating a much greater permeability is attributed to the insertion of the EP sample, and given the magnitude of this increase it may be considered that the inherent permeability of the system would not contribute significantly to the result.

However, on investigation of the natural EP permeability within the standard system it was observed that the reported permeability level continued to drop following sequential runs up to Run 7 and would perhaps have carried on past this point. The data plotted in this regard has been provided in the current chapter on a log scale in order to emphasise this continual reduction to the reader as the scale of the initial permeability reduction following Run 1 can lessen the perceived impact when plotted on the standard scale (Figure 6.24). On first impressions it may be believed that this consistent reduction is a function of continued system conditioning via system saturation, as was proposed for the blocked system. However, on inspection of the consistent reduction associated with the intrinsic pressure head loss calculated for the fully blocked system up to Run 4, it was found that at this point the contribution of the leakage function was low (57 $\times 10^{-4}$ $mm^3/MPa.s$). Therefore, given that the experimental method is based around the

conservation of volume and that the proposed volume fluid loss through leakage was so low it is believed that creep within the piping element may be a key contributor to this persistent factor. This is particularly relevant when we consider the time frame over which the testing is taking place. One way to access this possibility would be to use a more rigid pipe component in the same experimental setup. This being said, it is not yet known whether this is a true limitation for the current system application as following the current preliminary system development and pilot test data analysis, further testing on large sample numbers would allow for clear definition of the acceptable limits of variability within the equipment.

Though this large data set analysis was not part of the current project scope, the pilot data shown in the current chapter determined based on the outlined theoretical considerations, appears capable of determining permeability within the range expected of the natural EP tissues. If we assume that this system is conditioned following run two and consider Run 3 as a representative reading from a fully saturated sample based on the initial blocked system analysis (Figure 6.22), assuming further reductions as a creep element. The permeability of the natural EP sample at Run 3 is reported as 8.33 $X10^{-14}$ m^4/MPa.s. This value as a first indication fits well with the values reported in literature for a range different species; 1.03 $X10^{-14}$ m^4/Ns ovine [181], 13.9 $X10^{-14}$ m^4/Ns porcine [139], 14.3$X10^{-14}$ m^4/Ns baboon [184]. Therefore, the permeability determined here for the bovine EP sample should be considered extremely encouraging as initial pilot data. Also, given the large standard deviations observed over sample sets due to the inherently large sample variability, for example 13.9 $\pm$ 13 $x10^{-14}$ m^4/Ns reported for porcine samples [204]. This standard deviation factor level will have an influence on the importance of the proposed creep element of the current system. However, it should be bore in mind that in the current analysis the aim is to develop a system to compare the EP samples against tissue engineered constructs and as a consequence it would only be the relative difference between the two samples that would be of importance, hence, the system should be fit for this purpose following further development of the constructs to reach the required permeability levels.

The only limiting factor on the ability to make direct comparisons between the natural EP and construct components is the consistently higher permeability observed in the blocked system when fitted with the construct adapter component as compared to the standard setup (Figure 6.22). The main issue being that the permeability of the blocked adapter system is measuring in the range representative of the actual EP tissues, 1.73 $X10^{-14}$ m^4/MPa.s at Run 3. This notable difference is most likely driven by the greater pressure head loss in the system determined via the

$(\boldsymbol{\gamma_1 + \gamma_2})$ leakage component (Figure 6.23). It is believed that in this instance leakage is perhaps occurring around the o-ring components as the uniaxial compression is limited by the size of the component, therefore, a redesign of the adapter component to allow a larger compression on the o-rigs and a tighter tolerance on the overall dimensions may bring the leakage component down to a suitable level. If this were not successful in reducing the leakage component then manual addition of sealant around the adaptor may be a suitable approach. Once the leakage component of the adapter has been addressed, bringing the blocked system permeability down below the natural EP level the system will function to allow direct comparison between samples.

Unfortunately when the micro-mass seeded constructs were tested following 21 days culture in either chondrogenic or basal conditions the system did not register a result. This indicates that the permeability of the component is much greater than is determinable under the current system settings. The limiting factor on determining a result in the construct is the resolution of the load cell, as in order to obtain a result the pressure achieved in phase 1 would have to be considerably reduced. As a consequence of this result, further investigation into the effect of <45 µm particle addition to the 45-90 µm composition, in regard to mass fraction was carried out. It was observed that even at a ratio of 80:20, there was no notable effect on the scaffold permeability in the current system, again indicating that the scaffold alone would not suit the intended function (Figure 6.25).

There have been a number of studies in literature in which permeability of ceramic and glass ceramic scaffolds has been investigated in relation to bone replacement applications, however, the permeability is measured as a surrogate indicator of the potential for bone regeneration. This was driven by apparent disagreements to the traditional concept that bigger pores give better bone regeneration been reported in literature [205, 206]. Hollister *et al* found no significant influence on bone volume between either 30%, 50% or 70% porous polypropylene / TCP scaffolds [207]. Other research into the relationship between both porosity and average pore size demonstrated that permeability itself is not solely dependent on one factor. Therefore, the advantage of using permeability as a scaffold design parameter is that it encompasses all the effects of porosity, pore size and interconnectivity on scaffold mass transport characteristics. Hence, scaffolds with equal porosity, even with the same geometry, can have different permeability values if the pore sizes differ [207]. This being said, almost all scaffolds analysed in the literature, in regards to bone applications report in terms of intrinsic permeability within the

range 1 X10^{-11} m^2 – 1 X10^{-9} m^2 [208-211]. This is also in a similar range for trabecular bone permeability levels reported for both bovine (2 X10^{-9} to 9.5 X10^{-9} m^2) and human (5.1 X10^{-9} to 7.2 X10^{-9} m^2) tissues [212, 213]. Given that the 45-90 μm scaffolds generate a mean pore size of ≈30 μm and an overall porosity < 30% it may be reasonable to expect an increase in permeability as the majority of scaffolds analysed in literature have porosity over 50% and all those referenced in the current study have a mean pore size in the range 250 to 900 μm. However, it is perhaps the case that the main contributor to the highly permeable nature of the current scaffolds is due to the highly interconnected structure partly formed as a consequence of the current particle sintering process.

6.5 *Conclusion*

The aim of the current chapter was twofold; firstly to develop a test methodology capable of measuring the intrinsic permeability of both natural EP tissues and *in vitro* tissue engineered constructs, allowing for future comparative studies of permeability to facilitate natural nutrient transfer to the IVD region. Secondly; this chapter strived to develop a preliminary method by which cell/scaffold constructs, utilising AM-GC, can be produced *in vitro* with enough potential to provide a basis for the future optimization and characterisation towards a natural EP substitute. The results of the permeability testing carried out are both disappointing, in that neither the micro-mass seeded constructs or the varied particle mass fraction scaffold compositions were able to provide permeability in a detectable range using the current system. However, it is encouraging that in the natural EP tissue sample permeability was able to be detected, and the level reported was close to those determined previously in literature. Also, the blocked system conditioning and calibration techniques demonstrated substantial promise, should the true permeability be generated within a construct. Hence, the test methodology is sound but the permeability of current constructs is not fit for application at this point in time.

Chapter 7: Summary Discussion

The current body of work presents a truly interdisciplinary approach to the development of AM-GC materials towards application in the region of the vertebral EP's. Focusing equally on the aspects of glass-ceramic production, theory and MSC biology that govern this materials use in the proposed application. Further to this, engineering knowledge is subsequently applied to develop a comparative analysis methodology truly representative of the *in vivo* nutrient transfer function of the natural tissue. This interdisciplinary experimental approach has successfully led to an increased understanding of the potential use of AM-GC's as both bone substitute biomaterials and tissue engineered EP construct substrates from multiple perspectives. These being, mechanical strength, composition, cellular response and *in vivo* biological function. In order to achieve this goal the project was split into four key objectives:-

1. Reproducibly manufacture a glass-ceramic material suitable for further development and characterisation towards providing a substrate scaffold for tissue engineering applications.

2. Characterise the glass-ceramic material further to demonstrate the full range of both compositional and mechanical properties obtainable in relation to proposed function.

3. Demonstrate the osteogenic differentiation capacity of primary human MSCs on the glass-ceramic substrate to determine potential for bone replacement application.

4. Develop a comparative test methodology to assess the biological function of natural EP tissue against that of *in vitro* tissue engineered constructs.

7.1 *Summary Discussion*

The first step in determining the potential of AM-GC for application as a tissue engineering scaffold was to gain an understanding of the variability within the parent glass production process and the subsequent influence on the final sintered components. Particularly with regard to mechanical strength as the principal requirement of a bone substitute biomaterial is to replace the load bearing structure of the natural skeletal tissues. Repeated batch production of the current AM-GC indicated a significant variability in sintered component flexural strength between individual batches in a number of cases, however, in some instances there was no significant difference observed. Following this a control chart approach was used to rationalise the exclusion of only one batch from the creation of a stock glass for the remainder of the study. This was necessary to allow for a consistent material source throughout the investigation and was not deemed a concern, as this in principal provides only one material with its own inherent characteristics. The variability seen between batch strength as a consequence of production only has implications were the material required in a mass production setting, hence process control parameters would need to be addressed in more detail to provide a consistent product to a commercial market. The key variability within the sintering process was observed to exist around the Tp of the FA phase component. This leads to the proposal that some degree of F loss occurs during the production process, evidenced by an number of factors, such as, the lower intensity and broader apatite peak with respect to that of mullite following DTA and the fact that F loss has been shown to influence the strength of similar compositions previously [94, 106, 117]. This would be expected due to the known effect of F on the glass network, increasing the number of non-bridging oxygens within the structure, also lending to the current observation of slightly greater Tp's when compared to previous studies [114, 115].

On defining the optimum heat treatment regime for the current glass composition it was found that the initial more unorthodox process of placing the scaffolds into the furnace at 1200°C provided greater mechanical strength in the final components. Initially believed due to a low crystalline fraction within in the material when introduced to the high temperature, allowing for more sintering to occur in the first instance. Although this may still be a contributing factor, later analysis of material bulk composition and EDX imaging of the internal fracture surfaces lead to the conclusion that the current internal structure was due to a greater degree of phase equilibrium occurring between prior CaP and Al-Si rich amorphous phase separated constituents. This generated a consistent apatite aspect ratio throughout the material and as the apatite phase

forms prior to that of mullite this then restricts the mullite phase from forming defined crystals within the dense apatite crystal network. Further evidenced by the clear definition of mullite crystals within internal pores and at the material surface. It is perhaps then this consistent dense interlocking apatite structure that provides a greater strength than that of the traditional two stage heating regime often considered optimum.

The initial flexural strength levels reported for hrA (31.8 ± 3.4 MPa) were determined to be more than suitable for further development based on consideration of tensile fracture strengths reported in literature for natural cancellous bone, and for those reported for similar AM-GC based materials [109, 118, 119]. Later analysis using the BFS testing methodology was carried out on a range of particle size fractions, this method was chosen to better represent the *in vivo* situation and comparisons were made to available EP strength data in literature. Though there was a large strength range reported in relation to particle fraction used (16.2 – 116.4 MPa) considering the over and under estimations of strength attributable to natural tissue and scaffold components respectively. All particle fractions may be considered suitable for application in the region of the vertebral EP, especially when we consider that the typical hydrostatic pressures in the EP region under normal daily loads are as low as 0.6 – 2 MPa [139, 140]. However, given the inherent but unavoidable differences in the strength determination methods used in the case of both scaffolds and natural tissue the 1000 – 2000 μm particle would not be deemed wise for *in vivo* application. This is perhaps further strengthened by the fact that Al_2O_3 was identified at the material surface for this particle fraction following sintering.

Though all other particle fractions would be deemed suitable from a mechanical perspective the differing requirements of the bone and disc interface regions in the current EP application would perhaps necessitate a regional structure within the scaffold component. Hence, it is proposed that at the bone interface the 125 - 1000 μm particle fraction is used to facilitate the osseointegration function. As this particle fraction is the only one with a mean pore size, as determined via μCT analysis, within the range able to facilitate vascular ingrowth (100 – 500 μm) and as a consequence bone ingrowth [142, 143]. One element for consideration in regard to particle fraction used is the presence of vastly differing surface compositions as a function of particle size, this again is thought to be due in part to F loss at the surface as the bulk composition did not differ in the same manner. Also, anorthite is observed at the surface and is known to occur in regions lacking F, this phase though was not observed in the bulk and only registered small percentage contributions to overall composition identified via Rietveld analysis. This recurring

issue of potential F loss is perhaps then not significant with respect to the bulk material composition but may have substantial impact at the surface. From the perspective of a bioactive material this regional surface response could have a definitive impact on the formation of a HCA layer. This possibly eludes to the reason why in the case of the current composition SBF studies fail to identify typical bioactive response characteristics [110, 129]. As the current study aims to develop an EP substrate and given the more cortical like nature of the natural bone tissue in this region, the 45 – 90 µm particle fraction was taken forward for characterisation with regard to MSC response. This material also presented the largest proportion of apatite phase at its surface which would be deemed a desirable trait for bone substitute materials. Further work into understanding and controlling this surface response would allow a more unrestricted application of varying particle size fractions. One aspect of the current composition that might have a substantial effect on this surface effect is the current Ca:P ratio of 1.56. This sits close to the boundary of 1.5, below which surface nucleation has been shown to dominate [113, 114]. Therefore, increasing the current Ca:P ratio may reduce this pronounced surface effect and provide a more uniform material structure at the surface.

Initial characterisation of MSC response to the AM-GC substrate under basal culture conditions was extremely encouraging. The material demonstrated excellent *in vitro* biocompatibility characteristics, with MSCs forming confluent monolayers following 24 hours culture post seeding. These cells were then demonstrated to proliferate, with significant increases in cell numbers observed at both 3 and 7 day time points. Also, the MSCs maintained viability for up to 21 days in culture with no notable dead cell fraction observed throughout. There was a noted low proliferating cell fraction, however, this was believed due to the regional variability in substrate composition which was noted in the prior EDX analysis. This again would be a considerable factor, were different particle size fractions to be used in the same application it would no doubt have some influence on proliferation as amorphous substrates have already been noted to affect cell responses [128, 170].

In relation to the osteogenic differentiation capacity of MSCs it was observed that the specific enzymatic ALP activity was greater in both basal and OM supplemented conditions when compared to TCP monolayer controls. Though little influence was observed for ALP in terms of mRNA expression levels, it is postulated that this may be attributable to probable calcium dissolution, demonstrated previously to decrease ALP mRNA expression levels [178]. Also, previous studies into a number of late stage osteogenic marker expression levels, including the

OP and ON genes covered in the present study, observed a positive trend between *in vitro* mRNA expression level and *in vivo* bone deposition. They too observed that both ALP and Col αI did not increase or markedly vary between a number of CaP/HA based substrates [175]. Interestingly the current AM-GC substrate had the most pronounced effect on both the ON and OP differentiation markers, both of which are believed to function specifically in the cellular attachment and mineralisation processes of bone. In the current analysis these markers demonstrated the most pronounced response to the substrate material under basal conditions, however, the addition of OM led to a reduced expression level, though this was still above that seen in TCP basal controls. This OM related down regulation response was also observed in previous *in vitro* studies on AW glass ceramic, a proven bioactive scaffold that already see clinical application [100]. Hence, this commonality is encouraging for the potential bone substitute application proposed for the current AM-GC.

This is the first time that AM-GC has been characterised based on the *in vitro* influence on primary human MSC populations. The scaffolds have demonstrated an ability to up regulate a number of mRNA markers of osteogenesis in both the absence or presence of OM supplements. This would suggest that AM-GC is osteoconductive but may also possess elements of an osteoinductive nature, clearly demonstrating the osteogenic differentiation capacity of MSCs on the glass-ceramic substrate, hence, their suitability for bone replacement application. Especially when considering the flexural strength levels achieved over the range or particle fraction sizes generated in the current study. Further characterisation of the MSC response to the changing surface compositions demonstrated through EDX analysis would perhaps be required to understand further the potential impact of this factor at the biological level. However, the 45 – 90 µm particle fraction scaffolds characterised in the current study may be deemed suitable enough to consider taking forward for *in vivo* based analysis techniques to generate an understanding of their bone forming capacity in the presence of a true biological system. This will allow factors such as protein adsorption, HCA layer formation and immune system influences that are not accounted for in the present study to be considered, as the bioactive response of Si based biomaterials is governed very much by the host environment.

In the final stages of the current PhD study a parallel development approach was taken to provide both a suitable *in vitro* seeding and culture methodology able to generate early stage osteochondral EP constructs for future refinement, and a permeability testing technique that allows comparative analysis between these constructs and the natural EP tissues. This will allow

for the aforementioned future refinement efforts to maintain that the construct is able to provide the principal nutrient transfer function of the natural tissue. In relation to the seeding and culture methods addressed the pellet based approach was deemed the least promising. Although there was an indication of increased PG staining within the pellet structure there was no evidence of fusion between either individual pellets or between the pellets and the pre-osteogenically cultured monolayer. Further to this there was little flattening of the pellets or evidence of cellular ingrowth following 21 days on the AM-GC substrates. It is believed that the main driver for the lack of any significant results in this approach is the time for which the pellets underwent pre-chondrogenic differentiation as similar approaches have provided encouraging results in the past, though co-culture took place as early as 6 days [191]. It is postulated that the formation of a fusiform cell layer on the outer regions of the pellets as a consequence of radial growth inhibit the interactions that might typically occur between the interfacing osteogenic and chondrogenic cell populations. Perhaps further evidenced by the lack of any calcified transitional zone at the interface of the pellets with the monolayer constituents, as this has been found to occur at the interface of osteogenic and chondrogenic pre-differentiated cell populations previously [190]. Hence, though this method did not return a satisfactory result in the current study, it is still worthy of further investigation into the timing at which co-culture is commenced. Also, perhaps the methods by which the pellets are produced would warrant review as MSCs prepared by spheroid culture techniques have seen more encouraging results in relation to interaction with the osteogenic counterparts [191].

In contrast to the pellet seeding methodology the micro-mass approach showed encouraging results. Cells seeded in this manner showed enhanced PG staining and a more prominent surface layer at only 14 days chondrogenic culture. This was further confirmed by both SEM analysis and Alcian Blue staining showing a marked difference in the surface layer confluence under chondrogenic conditions. Further to this the micro-mass seeded scaffolds demonstrated a substantially higher degree of cellular ingrowth into the scaffold under chondrogenic culture conditions at 14 days when compared to the basal control and the pellet seeded constructs following up to 21 days culture. This would be deemed very desirable in relation to the proposed application as it would no doubt aid in the interface resistance to shear loading, an element of EP constructs proven to be lacking in those developed using primary bovine chondrocytes previously [85]. Though these results are extremely encouraging for the potential use of micro-mass seeding methods on AM-GC substrates for the production of osteochondral constructs, the current permeability measurements were the limiting factor.

The proposed permeability test methodology mimics the *in vivo* conditions of mass transfer at the interface region of the IVD and adjacent vertebral body. It does this in a quasistatic manner so as to eliminate any influence of dynamic effects due to fluid velocity and/or acceleration such as, turbulent flow or inertia. As a consequence the fluid induced matrix compaction within the samples, either constructs or natural tissues, is minimised. Though it was found that the standard system setup was able to determine the permeability of the natural EP samples and that the leakage component was negligible in this instance, evidenced by both the blocked system test results and previously reported values in literature for mammalian EP tissue permeability [139, 181, 184, 204]. When it came to the construct adapter system the permeability level when blocked was within the range of the natural EP tissues, therefore, in order for the system to allow for comparative testing the inherent permeability of this system needs to be brought up to a level similar to that of the standard system to allow readings to be registered in the desirable range. However, this should be achievable by analysing some of the design parameters surrounding the tolerances around the sample fixation or the possible use of a system sealant approach. One element for consideration was the proposed effect of creep within the polymer piping components thought to be the cause of consistent incremental permeability reductions in the system given the maintained pressure levels and the time of the independent experimental runs. The degree to which this factor is a concern would require significant test numbers to be carried out in order to better understand the level of inter donor variability in the first instance. Either way the current system is for consideration as a comparative test method between the natural samples and the tissue engineered constructs so as long as the results are taken under the same experimental conditions then relative comparison should be considered suitable. This said the current system in principal would function to provide this direct comparator functionality should the adapter leakage component be suitably reduced.

The biggest disappointment from the current study was the inability of the system to register a reading for the permeability of either the micro-mass seeded constructs or the mixed composition scaffolds, given addition of up to 80 % of < 45 µm particles. This infers that the system fluid is able to pass through the scaffold samples almost unhindered in respect to the natural EP tissues, representing a considerably large permeability difference. However, this in itself is perhaps the most important finding as it emphasises the fact that although throughout the current body of work it has been shown that the AM-GC scaffolds demonstrate favourable mechanical characteristics, osteogenic differentiation capacity and the potential to support chondrogenic differentiation of micro-mass cultures, in order to provide an EP like structure. However, It is the

ability to provide this nutrient transfer function, represented here by permeability, that is the principal requirement at the IVD interface and this is currently lacking. It should be bore in mind that in all instances of osteochondral tissue engineering this key functionality has never before been addressed to any degree. Therefore, the fact that we have found such a high discrepancy between the constructs and scaffolds when compared to the natural tissues illustrates the need for more focus on this parameter in the field of tissue engineering as a whole. In relation to the current study and its findings it is perhaps worth considering further refinement of the micro-mass seeding methodology in relation to optimal cell number and investigating the effect of prolonged culture periods *in vitro* as this can have a marked influence on the ECM composition and may in turn reduce the permeability of the constructs. However, it is perhaps the scaffold manufacturing technique itself that promotes the high level of permeability, as evidenced by the micro CT analysis of the pore structure demonstrating a highly interconnected network. It may therefore be advisable to investigate other production methods utilising the same material that might aid in reducing this highly interconnected nature and reduce the level of permeability.

Definitions

ALP	Alkaline Phosphatase
APS	Amorphous Phase Separation
r_a	Anion Radius
AF	Annulus Fibrosus
AM-GC	Apatite Mullite Glass Ceramic
AW	Apatite Wollastonite
BFS	Biaxial Flexural Strength
BMP	Bone Morphogenic Protein
CPP	Calcium Polyphosphate
r_c	Cation Radius
Col αI	Collagen Alpha 1
cDNA	Complementary DNA
CT	Computated Tomography
CLD	Cross-Link Density
DNase	Deoxyribonuclease
DNA	Deoxyribonucleic Acid
DTA	Differential Thermal Analysis

DSC	Differential Scanning Calorimetry
DTT	DL-Dithiothreitol
DMEM	Dulbecco's modified Eagle's medium
EP	Endplate
EDX	Energy Dispersive X-ray Spectroscopy
EDTA	Ethlenediminetetraacetic Acid
ECM	Extra-cellular matrix
FGF	Fibroblast Growth Factor
FA	Fluorapatite
T_f	Freezing Point
Tg	Glass Transition Temperature
GAG	Glycosaminoglycan
HMDS	Hexamethyldisilazane
HA	Hydroxyapatite
HCA	Hydroxyl-carbonate Apatite
Ihh	Indian Hedgehog
ICDD	International Center For Diffraction Data
IVD	Intervertebral Disc

LBP	Lower Back Pain
MMP	Matrix Metalloproteinase
MTS	Maximum Tensile Strength
M-CSF	Monocyte/Macrophase Colony-Stimulating Factor
MSC	Mesenchymal Stem/Stromal Cells
NP	Nucleus Pulposus
NPR	Nucleus Pulposus Replacement
ONT	Optimum Nucleation Temperature
ONt	Optimum Nucleation Time
OC	Osteocalcin
OM	Osteogenic Media
ON	Osteonectin
OP	Osteopontin
Tp	Peak Crystallisation Temperature
PNPP	P-Nitrophenyl Phosphate
PLA	Poly-D, L-lactic Acid
PCR	Polymerase Chain Reaction
PG	Proteoglycan

RANKL	Receptor Activator of Nuclear Factor Ligand
RNase	Ribonuclease
RNA	Ribonucleic Acid
RPS27A	Ribosomal Protein subunit 27A
Runx2	Runt-related Transcription Factor 2
SEM	Scanning Electron Microscopy
SLS	Selective Laser Sintering
SBF	Simulated Body Fluid
SOX	Sry related HMG box
3D	Three-dimensional
TCP	Tissue Culture Plastic
TDR	Total Disc Replacement
TGF-β	Transforming Growth Factor Beta
Wnt	Wingless-related integration site
XRD	X-ray Diffraction

References

1. Middleditch, A. and J. Oliver, *Functional anatomy of the spine*. 2nd ed. ed. 2005, Edinburgh: Elsevier.

2. Mayfield Clinic. *anatomy of the spine section* 2013 [cited 2013 November 22]; Available from: http://www.mayfieldclinic.com/PE-AnatSpine.htm#.UpDVXdK-18H.

3. American Medical Association. *Pathophysiology of Bone Loss and Fractures*. 1995-2006 [cited 2013 November 22]; Available from: http://stg.centrax.com/ama/osteo/part4/module03/02path/02.htm.

4. LeGeros, R.Z., *Properties of osteoconductive biomaterials: calcium phosphates.* Clin Orthop Relat Res, 2002(395): p. 81-98.

5. Weiner, S. and W. Traub, *Crystal size and organization in bone.* Connect Tissue Res, 1989. **21**(1-4): p. 259-65.

6. Currey, J.D., *Bones : structure and mechanics*. 2002, Princeton, N.J. ; Oxford: Princeton University Press.

7. Hamilton, W.J., *Textbook of human anatomy*. 1956, London ; New York: Macmillan and Co.

8. Lees, S. and C.L. Davidson, *The role of collagen in the elastic properties of calcified tissues.* J Biomech, 1977. **10**(8): p. 473-86.

9. Dempster, D.W., *Anatomy and Function of the Adult Skeleton*, in *Primer on the Metabolic Bone Diseases and Disorders of Mineral Metabolism* 2006, Washington: ASBMR p. 7-11.

10. Young, B.P.D.W.s.f.h. and P.R.F.h. Wheater, *Wheater's functional histology : a text and colour atlas*. 5th ed. / Barbara Young ... [et al.] ; drawings by Philip J. Deakin. ed. 2006, [Edinburgh]: Churchill Livingstone Elsevier.

11. Huiskes, R., et al., *Effects of mechanical forces on maintenance and adaptation of form in trabecular bone.* Nature, 2000. **405**(6787): p. 704-6.

12. Bogduk, N., *Clinical anatomy of the lumbar spine and sacrum*. 4th ed. 2005, Edinburgh: Elsevier/Churchill Livingstone. xii, 250 p.

13. O'Halloran, D.M. and A.S. Pandit, *Tissue-engineering approach to regenerating the intervertebral disc.* Tissue Eng, 2007. **13**(8): p. 1927-54.

14. Roberts, S., et al., *1991 Volvo Award in basic sciences. Collagen types around the cells of the intervertebral disc and cartilage end plate: an immunolocalization study.* Spine (Phila Pa 1976), 1991. **16**(9): p. 1030-8.

15. Richardson, S.M., et al., *Intervertebral disc biology, degeneration and novel tissue engineering and regenerative medicine therapies.* Histol Histopathol, 2007. **22**(9): p. 1033-41.

16. Yu, J., *Elastic tissues of the intervertebral disc.* Biochem Soc Trans, 2002. **30**(Pt 6): p. 848-52.

17. Marchand, F. and A.M. Ahmed, *Investigation of the laminate structure of lumbar disc anulus fibrosus.* Spine (Phila Pa 1976), 1990. **15**(5): p. 402-10.

18. Hickey, D.S. and D.W.L. Hukins, *Relation between the Structure of the Annulus Fibrosus and the Function and Failure of the Intervertebral-Disk.* Spine, 1980. **5**(2): p. 106-116.

19. Schollmeier, G., R. Lahr-Eigen, and K.U. Lewandrowski, *Observations on fiber-forming collagens in the anulus fibrosus.* Spine (Phila Pa 1976), 2000. **25**(21): p. 2736-41.

20. Beard, H.K., S. Roberts, and J.P. O'Brien, *Immunofluorescent staining for collagen and proteoglycan in normal and scoliotic intervertebral discs.* J Bone Joint Surg Br, 1981. **63B**(4): p. 529-34.

21. Yu, J., et al., *The elastic fiber network of the anulus fibrosus of the normal and scoliotic human intervertebral disc.* Spine (Phila Pa 1976), 2005. **30**(16): p. 1815-20.

22. Inoue, H., *Three-dimensional architecture of lumbar intervertebral discs.* Spine (Phila Pa 1976), 1981. **6**(2): p. 139-46.

23. Roberts, S., J. Menage, and J.P. Urban, *Biochemical and structural properties of the cartilage end-plate and its relation to the intervertebral disc.* Spine, 1989. **14**(2): p. 166-74.

24. Coventry, M.B., R.K. Ghormley, and J.W. Kernohan, *The Intervertebral Disc - Its Microscopic Anatomy and Pathology .1. Anatomy, Development, and Physiology.* Journal of Bone and Joint Surgery, 1945. **27**(1): p. 105-112.

25. Moore, R.J., *The vertebral end-plate: what do we know?* Eur Spine J, 2000. **9**(2): p. 92-6.

26. Antoniou, J., et al., *The human lumbar endplate. Evidence of changes in biosynthesis and denaturation of the extracellular matrix with growth, maturation, aging, and degeneration.* Spine (Phila Pa 1976), 1996. **21**(10): p. 1153-61.

27. Aigner, T., et al., *Variation with age in the pattern of type X collagen expression in normal and scoliotic human intervertebral discs.* Calcif Tissue Int, 1998. **63**(3): p. 263-8.

28. Johnstone, B., et al., *Identification and characterization of glycanated and non-glycanated forms of biglycan and decorin in the human intervertebral disc.* Biochem J, 1993. **292 (Pt 3)**: p. 661-6.

29. Roberts, S., et al., *Proteoglycan components of the intervertebral disc and cartilage endplate: an immunolocalization study of animal and human tissues.* Histochem J, 1994. **26**(5): p. 402-11.

30. Yang, Y. and Asbmr, *Chapter 1. Skeletal Morphogenesis and Embryonic Development*, in *Primer on the Metabolic Bone Diseases and Disorders of Mineral Metabolism*. 2009, John Wiley & Sons, Inc. p. 1-10.

31.   Olsen, B.R., *Bone Embryology*, in *Primer on the metabolic bone diseases and disorders of mineral metabolism*. 2006, ASBMR. p. 2-6.

32.   Shapiro, F., *Bone development and its relation to fracture repair. The role of mesenchymal osteoblasts and surface osteoblasts.* Eur Cell Mater, 2008. **15**: p. 53-76.

33.   Komori, T., et al., *Targeted disruption of Cbfa1 results in a complete lack of bone formation owing to maturational arrest of osteoblasts.* Cell, 1997. **89**(5): p. 755-64.

34.   Bi, W., et al., *Sox9 is required for cartilage formation.* Nat Genet, 1999. **22**(1): p. 85-9.

35.   Day, T.F., et al., *Wnt/beta-catenin signaling in mesenchymal progenitors controls osteoblast and chondrocyte differentiation during vertebrate skeletogenesis.* Dev Cell, 2005. **8**(5): p. 739-50.

36.   Cook, D. and P. Genever, *Regulation of mesenchymal stem cell differentiation.* Adv Exp Med Biol, 2013. **786**: p. 213-29.

37.   Hu, H., et al., *Sequential roles of Hedgehog and Wnt signaling in osteoblast development.* Development, 2005. **132**(1): p. 49-60.

38.   Akiyama, H., et al., *The transcription factor Sox9 has essential roles in successive steps of the chondrocyte differentiation pathway and is required for expression of Sox5 and Sox6.* Genes Dev, 2002. **16**(21): p. 2813-28.

39.   Dyson, J.A., *Development of Patient Specific Bioceramic Scaffolds for Bone Tissue Engineering*, in *Leeds Dental Institute*2008, The University of Leeds.

40.   Mak, K.K., et al., *Wnt/beta-catenin signaling interacts differentially with Ihh signaling in controlling endochondral bone and synovial joint formation.* Development, 2006. **133**(18): p. 3695-707.

41.   Rodda, S.J. and A.P. McMahon, *Distinct roles for Hedgehog and canonical Wnt signaling in specification, differentiation and maintenance of osteoblast progenitors.* Development, 2006. **133**(16): p. 3231-44.

42.   Hadjidakis, D.J. and Androulakis, II, *Bone remodeling.* Ann N Y Acad Sci, 2006. **1092**: p. 385-96.

43.   Boyle, W.J., W.S. Simonet, and D.L. Lacey, *Osteoclast differentiation and activation.* Nature, 2003. **423**(6937): p. 337-42.

44.   Parfitt, A.M., *Targeted and nontargeted bone remodeling: relationship to basic multicellular unit origination and progression.* Bone, 2002. **30**(1): p. 5-7.

45.   Silver, I.A., R.J. Murrills, and D.J. Etherington, *Microelectrode studies on the acid microenvironment beneath adherent macrophages and osteoclasts.* Exp Cell Res, 1988. **175**(2): p. 266-76.

46.   Delaisse, J.M., et al., *Matrix metalloproteinases (MMP) and cathepsin K contribute differently to osteoclastic activities.* Microsc Res Tech, 2003. **61**(6): p. 504-13.

47. Frost, H.M.e., *Bone biodynamics*. 1964, Boston: Little Brown.

48. Anderson, H.C., *Matrix vesicles and calcification.* Curr Rheumatol Rep, 2003. **5**(3): p. 222-6.

49. Heino, T.J., et al., *Evidence for the role of osteocytes in the initiation of targeted remodeling.* Technol Health Care, 2009. **17**(1): p. 49-56.

50. Biomedical Tissue Research Group. *Image Library*. 2013 [cited 2013 November 23,]; Available from: http://www.york.ac.uk/res/btr/Image%20Library/Bone%20remodelling.jpg.

51. Ehrlich, G.E., *Low back pain.* Bulletin of the World Health Organization, 2003. **81**(9): p. 671-676.

52. Ehrlich, G.E., *Back pain.* Journal of Rheumatology, 2003. **30**: p. 26-31.

53. Maniadakis, N. and A. Gray, *The economic burden of back pain in the UK.* Pain, 2000. **84**(1): p. 95-103.

54. Freemont, A.J., et al., *Current understanding of cellular and molecular events in intervertebral disc degeneration: implications for therapy.* J Pathol, 2002. **196**(4): p. 374-9.

55. Luoma, K., et al., *Low back pain in relation to lumbar disc degeneration.* Spine, 2000. **25**(4): p. 487-92.

56. Boos, N., et al., *Classification of age-related changes in lumbar intervertebral discs: 2002 Volvo Award in basic science.* Spine, 2002. **27**(23): p. 2631-44.

57. Urban, J.P., et al., *Nutrition of the intervertebral disk. An in vivo study of solute transport.* Clin Orthop Relat Res, 1977(129): p. 101-14.

58. Bibby, S.R. and J.P. Urban, *Effect of nutrient deprivation on the viability of intervertebral disc cells.* Eur Spine J, 2004. **13**(8): p. 695-701.

59. Boyling, J.D., G.A. Jull, and G.P. Grieve, *Grieve's modern manual therapy : the vertebral column*. 3rd ed. 2004, Edinburgh: Churchill Livingstone. xvi, 643 p.

60. Holm, S., et al., *Nutrition of the intervertebral disc: solute transport and metabolism.* Connect Tissue Res, 1981. **8**(2): p. 101-19.

61. Roberts, S., et al., *Transport properties of the human cartilage endplate in relation to its composition and calcification.* Spine, 1996. **21**(4): p. 415-20.

62. Crock, H.V. and H. Yoshizawa, *The blood supply of the lumbar vertebral column.* Clin Orthop Relat Res, 1976(115): p. 6-21.

63. Urban, J.P., S. Smith, and J.C. Fairbank, *Nutrition of the intervertebral disc.* Spine (Phila Pa 1976), 2004. **29**(23): p. 2700-9.

64. Shirazi-Adl, A., M. Taheri, and J.P.G. Urban, *Analysis of cell viability in intervertebral disc: Effect of endplate permeability on cell population.* Journal of Biomechanics, 2010. **43**(7): p. 1330-1336.

65.   Bernick, S. and R. Cailliet, *Vertebral end-plate changes with aging of human vertebrae.* Spine (Phila Pa 1976), 1982. **7**(2): p. 97-102.

66.   Nachemso.A, et al., *In-Vitro Diffusion of Dye through End-Plates and Annulus Fibrosus Ofhuman Lumbar Inter-Vertebral Discs.* Acta Orthopaedica Scandinavica, 1970. **41**(6): p. 589-&.

67.   Horner, H.A. and J.P. Urban, *2001 Volvo Award Winner in Basic Science Studies: Effect of nutrient supply on the viability of cells from the nucleus pulposus of the intervertebral disc.* Spine, 2001. **26**(23): p. 2543-9.

68.   Nerlich, A.G., E.D. Schleicher, and N. Boos, *1997 Volvo Award winner in basic science studies. Immunohistologic markers for age-related changes of human lumbar intervertebral discs.* Spine (Phila Pa 1976), 1997. **22**(24): p. 2781-95.

69.   Urban, J.P.G. and S. Roberts, *Degeneration of the intervertebral disc.* Arthritis Research & Therapy, 2003. **5**(3): p. 120-130.

70.   Peng, B.G., et al., *The relationship between cartilage end-plate calcification and disc degeneration: an experimental study.* Chinese Medical Journal, 2001. **114**(3): p. 308-312.

71.   Lupparelli, S., S. Cecconi, *Advances in technology and spinal fusion: A clinician's perspective*, in *Advances in spinal fusion*, D.L.W. K. Lewandrowski, D.J. Trantolo , M.J. Yaszemski , A.A. White III Editor. 2004, M. Dekker: New York.

72.   Harrop, J.S., et al., *Lumbar adjacent segment degeneration and disease after arthrodesis and total disc arthroplasty.* Spine (Phila Pa 1976), 2008. **33**(15): p. 1701-7.

73.   Beutler, W.J. and W.C. Peppelman, Jr., *Anterior lumbar fusion with paired BAK standard and paired BAK Proximity cages: subsidence incidence, subsidence factors, and clinical outcome.* Spine J, 2003. **3**(4): p. 289-93.

74.   Shim, C.S., et al., *Partial disc replacement with the PDN prosthetic disc nucleus device: early clinical results.* J Spinal Disord Tech, 2003. **16**(4): p. 324-30.

75.   Luk, K.D. and D.K. Ruan, *Intervertebral disc transplantation: a biological approach to motion preservation.* Eur Spine J, 2008. **17 Suppl 4**: p. 504-10.

76.   Luk, K.D., et al., *Intervertebral disc autografting in a bipedal animal model.* Clin Orthop Relat Res, 1997(337): p. 13-26.

77.   Seguin, C.A., et al., *Tissue engineered nucleus pulposus tissue formed on a porous calcium polyphosphate substrate.* Spine (Phila Pa 1976), 2004. **29**(12): p. 1299-306; discussion 1306-7.

78.   Gruber, H.E., A.A. Stasky, and E.N. Hanley, Jr., *Characterization and phenotypic stability of human disc cells in vitro.* Matrix Biol, 1997. **16**(5): p. 285-8.

79.   Ganey, T.M. and H.J. Meisel, *A potential role for cell-based therapeutics in the treatment of intervertebral disc herniation.* Eur Spine J, 2002. **11 Suppl 2**: p. S206-14.

80.   Watanabe, K., et al., *Effect of reinsertion of activated nucleus pulposus on disc degeneration: an experimental study on various types of collagen in degenerative discs.* Connect Tissue Res, 2003. **44**(2): p. 104-8.

81.   Okuma, M., et al., *Reinsertion of stimulated nucleus pulposus cells retards intervertebral disc degeneration: an in vitro and in vivo experimental study.* J Orthop Res, 2000. **18**(6): p. 988-97.

82.   Ganey, T., et al., *Disc chondrocyte transplantation in a canine model: a treatment for degenerated or damaged intervertebral disc.* Spine (Phila Pa 1976), 2003. **28**(23): p. 2609-20.

83.   Yamamoto, Y., Mochida, J., Sakai, D., Nomura, T., *Reinsertion of nucleus pulpopus cells activated by mesenchymal stem cells using coculture methods decelerated intervertebral disc degeneration.* The Spine Journal, 2003. **3**: p. 67S.

84.   Kim, S., Le Visage, C., Tateno, K., Sieber, A., Kostuik, J., Leong, K., *Interaction of human mesenchimal stem cells with disc cells: changes in biosynthesis of extrcellular matrix.* The Spine Journal, 2002. **2**: p. 107S.

85.   Hamilton, D.J., et al., *Formation of a nucleus pulposus-cartilage endplate construct in vitro.* Biomaterials, 2006. **27**(3): p. 397-405.

86.   Zarzycki, J., *Glasses and the vitreous state*. 1991: Cambridge University Press.

87.   Shand, E.B., *Glass engineering handbook*. 2nd ed. ed. 1958, New York ; London: McGraw-Hill.

88.   Walker, P.M.B., *Larousse dictionary of science and technology*. 1995, Edinburgh: Larousse.

89.   Vogel, W. and N.J. Kreidl, *Chemistry of glass*. 1985, Columbus, Ohio: American Ceramic Society.

90.   Jones, G.O. and S. Parke, *Glass*. 2nd ed. / revised by S. Parke. ed. 1971, London: Chapman and Hall.

91.   Wood, D. and R. Hill, *Glass ceramic approach to controlling the properties of a glass-ionomer bone cement.* Biomaterials, 1991. **12**(2): p. 164-70.

92.   Zachariasen, W.H., *THE ATOMIC ARRANGEMENT IN GLASS.* Journal of the American Chemical Society, 1932. **54**(10): p. 3841-3851.

93.   McMillan, P.W., *Glass-ceramics*. 2nd ed. ed. 1979, London: Academic Press.

94.   Stanton, K.T., *The Effect of Fluorine on Microstructural Development in Apatite-mullite Glass-ceramics*. 2000: University of Limerick.

95.   Wange, P., Carl, G., Naumann, K., Vogel, J., Vogel, W,. Gotz, V., Holand, W., *Development of glass ceramics and ceramic reinforced glass ceramics*. Vol. 56. 1991, Mons, BELGIQUE: Silicates industriels. 7.

96. Grossman, D., *Glass-ceramic applications.* Advances in Ceramics., 1981. **4**: p. 249.

97. Kokubo, T., *Bioactive glass ceramics: properties and applications.* Biomaterials, 1991. **12**(2): p. 155-163.

98. Mullin, J.W., *Crystallisation.* 2nd ed. ed. 1972, London: Butterworths.

99. Chalmers, B., *Principles of Solidification. [With illustrations.].* 1964, New York: John Wiley & Sons.

100. Dyson, J.A., et al., *Development of custom-built bone scaffolds using mesenchymal stem cells and apatite-wollastonite glass-ceramics.* Tissue Eng, 2007. **13**(12): p. 2891-901.

101. Hench, L.L., *Bioceramics.* Journal of the American Ceramic Society, 1998. **81**(7): p. 1705-1728.

102. Remes, A. and D.F. Williams, *Immune response in biocompatibility.* Biomaterials, 1992. **13**(11): p. 731-743.

103. Hench, L.L., et al., *Bonding mechanisms at the interface of ceramic prosthetic materials.* Journal of Biomedical Materials Research, 1971. **5**(6): p. 117-141.

104. Kokubo, T.S., M.; Nagashima,Y.; Tashiro, M.; Nakamura, T.; Yamamuro, T.; Higashi, S. , *Apatite- and wollastonite-containing glass-ceramic for prosthetic application.* Bull. Inst. Chem. Res., Kyoto Univ, 1982(60): p. 260-268.

105. Wood, D.H., R, *Structure-Property Relationships in Ionomer Glasses* Clinical Materials, 1991. **7**: p. 301-312.

106. Hill, R.W., D., *Apatite-Mullite Glass-Ceramics.* Journal of materials science: materials in medicine, 1995. **6**: p. 311-318.

107. Stanton, K.T., *The Effect of Fluorine on Microstructural Development in Apatite-Mullite Glass-Ceramics*, 2000, university of limerick: limerick. p. 77.

108. Rafferty, A.C., A. Hill, R., *Influence of Fluorine Content in Apatite-Mullite Glass-Ceramics.* J. Am. Ceram. Soc 2000. **83**(11): p. 2833-38.

109. Goodridge, R.D., K.W. Dalgarno, and D.J. Wood, *Indirect selective laser sintering of an apatite-mullite glass-ceramic for potential use in bone replacement applications.* Proc Inst Mech Eng H, 2006. **220**(1): p. 57-68.

110. Goodridge, R.D., et al., *Biological evaluation of an apatite-mullite glass-ceramic produced via selective laser sintering.* Acta Biomater, 2007. **3**(2): p. 221-31.

111. Marotta, A., A. Buri, and F. Branda, *Nucleation in glass and differential thermal analysis.* Journal of Materials Science, 1981. **16**(2): p. 341-344.

112. Clifford, A. and R. Hill, *Apatite-mullite glass-ceramics.* Journal of Non-Crystalline Solids, 1996. **196**: p. 346-351.

113. Hill, R. and D. Wood, *Apatite Mullite Glass-Ceramics.* Journal of Materials Science-Materials in Medicine, 1995. **6**(6): p. 311-318.

114. Rafferty, A., et al., *Influence of Fluorine Content in Apatite–Mullite Glass-Ceramics.* Journal of the American Ceramic Society, 2000. **83**(11): p. 2833-2838.

115. Rafferty, A., R.G. Hill, and D. Wood, *An investigation into the amorphous phase separation characteristics of an ionomer glass series and a sodium-boro-silicate glass system.* Journal of Materials Science, 2003. **38**(11): p. 2311-2319.

116. Moisescu, C., C. Jana, and C. Rüssel, *Crystallization of rod-shaped fluoroapatite from glass melts in the system SiO2–Al2O3–CaO–P2O5–Na2O–K2O–F−.* Journal of Non-Crystalline Solids, 1999. **248**(2–3): p. 169-175.

117. Fathi, H., et al., *The influence of calcium fluoride (CaF2) on biaxial flexural strength of apatite-mullite glass-ceramic materials.* Dent Mater, 2005. **21**(9): p. 846-51.

118. Wirtz, D.C., et al., *Critical evaluation of known bone material properties to realize anisotropic FE-simulation of the proximal femur.* Journal of biomechanics, 2000. **33**(10): p. 1325-1330.

119. Goldstein, S.A., *The mechanical properties of trabecular bone: Dependence on anatomic location and function.* Journal of biomechanics, 1987. **20**(11–12): p. 1055-1061.

120. Callister, W.D., *Fundamentals of materials science and engineering : an integrated approach*. 2nd ed. ed. 2005, Hoboken, NJ: John Wiley & Sons.

121. Xiao, K., et al., *Indirect selective laser sintering of apatite-wollostonite glass-ceramic.* Proc Inst Mech Eng H, 2008. **222**(7): p. 1107-14.

122. Silva, M.J., et al., *Direct and computed tomography thickness measurements of the human, lumbar vertebral shell and endplate.* Bone, 1994. **15**(4): p. 409-414.

123. Jones, J.R. and L.L. Hench, *Biomedical materials for new millennium: perspective on the future.* Materials Science and Technology, 2001. **17**(8): p. 891-900.

124. Cao, W. and L.L. Hench, *Bioactive materials.* Ceramics International, 1996. **22**(6): p. 493-507.

125. Myeroff, C. and M. Archdeacon, *Autogenous bone graft: donor sites and techniques.* J Bone Joint Surg Am, 2011. **93**(23): p. 2227-36.

126. Charbord, P., *Bone marrow mesenchymal stem cells: historical overview and concepts.* Hum Gene Ther, 2010. **21**(9): p. 1045-56.

127. Holand, W., et al., *Interface reactions between machinable bioactive glass-ceramics and bone.* J Biomed Mater Res, 1985. **19**(3): p. 303-12.

128. Freeman, C.O., et al., *Crystallization modifies osteoconductivity in an apatite–mullite glass–ceramic.* Journal of Materials Science: Materials in Medicine, 2003. **14**(11): p. 985-990.

129. Agathopoulos, S., et al., *The fluorapatite-anorthite system in biomedicine.* Biomaterials, 2003. **24**(7): p. 1317-31.

130.   Kalmodia, S., B. Basu, and T.J. Webster, *Gene expression in osteoblast cells treated with submicron to nanometer hydroxyapatite-mullite eluate particles.* J Biomater Appl, 2013. **27**(7): p. 891-908.

131.   Johnson, A., et al., *The effect of casting conditions on the biaxial flexural strength of glass-ceramic materials.* Dent Mater, 1998. **14**(6): p. 412-6.

132.   Yilmaz, H., C. Aydin, and B.E. Gul, *Flexural strength and fracture toughness of dental core ceramics.* J Prosthet Dent, 2007. **98**(2): p. 120-8.

133.   Oxland, T.R., et al., *Effects of endplate removal on the structural properties of the lower lumbar vertebral bodies.* Spine (Phila Pa 1976), 2003. **28**(8): p. 771-7.

134.   Grant, J.P., T.R. Oxland, and M.F. Dvorak, *Mapping the structural properties of the lumbosacral vertebral endplates.* Spine (Phila Pa 1976), 2001. **26**(8): p. 889-96.

135.   Hou, Y. and Z. Luo, *A study on the structural properties of the lumbar endplate: histological structure, the effect of bone density, and spinal level.* Spine (Phila Pa 1976), 2009. **34**(12): p. E427-33.

136.   Rockoff, S.D., E. Sweet, and J. Bleustein, *The relative contribution of trabecular and cortical bone to the strength of human lumbar vertebrae.* Calcif Tissue Res, 1969. **3**(2): p. 163-75.

137.   Tan, J.S., et al., *Interbody device shape and size are important to strengthen the vertebra-implant interface.* Spine (Phila Pa 1976), 2005. **30**(6): p. 638-44.

138.   Zhao, F.D., et al., *Vertebral fractures usually affect the cranial endplate because it is thinner and supported by less-dense trabecular bone.* Bone, 2009. **44**(2): p. 372-9.

139.   Accadbled, F., et al., *A measurement technique to evaluate the macroscopic permeability of the vertebral end-plate.* Med Eng Phys, 2008. **30**(1): p. 116-22.

140.   Wilke, H.J., et al., *New in vivo measurements of pressures in the intervertebral disc in daily life.* Spine (Phila Pa 1976), 1999. **24**(8): p. 755-62.

141.   Black, J. and G.W. Hastings, *Handbook of biomaterial properties*. 1998, London: Chapman & Hall.

142.   LeGeros, R.Z., *Calcium phosphate-based osteoinductive materials.* Chem Rev, 2008. **108**(11): p. 4742-53.

143.   Baino, F. and C. Vitale-Brovarone, *Three-dimensional glass-derived scaffolds for bone tissue engineering: current trends and forecasts for the future.* J Biomed Mater Res A, 2011. **97**(4): p. 514-35.

144.   O'Flynn, K.P. and K.T. Stanton, *Nucleation and Early Stage Crystallization of Fluorapatite in Apatite-Mullite Glass-Ceramics.* Crystal Growth & Design, 2010. **10**(3): p. 1111-1117.

145.   Augello, A. and C. De Bari, *The regulation of differentiation in mesenchymal stem cells.* Hum Gene Ther, 2010. **21**(10): p. 1226-38.

146. Stein, G.S. and J.B. Lian, *Molecular mechanisms mediating proliferation/differentiation interrelationships during progressive development of the osteoblast phenotype.* Endocr Rev, 1993. **14**(4): p. 424-42.

147. Ducy, P., et al., *Osf2/Cbfa1: a transcriptional activator of osteoblast differentiation.* Cell, 1997. **89**(5): p. 747-54.

148. Krause, C., et al., *Chapter 2. Signal Transduction Cascades Controlling Osteoblast Differentiation*, in *Primer on the Metabolic Bone Diseases and Disorders of Mineral Metabolism.* 2009, John Wiley & Sons, Inc. p. 10-16.

149. Aubin, J.E., et al., *Osteoblast and chondroblast differentiation.* Bone, 1995. **17**(2, Supplement 1): p. S77-S83.

150. Marom, R., et al., *Characterization of adhesion and differentiation markers of osteogenic marrow stromal cells.* J Cell Physiol, 2005. **202**(1): p. 41-8.

151. Salgado, A.J., O.P. Coutinho, and R.L. Reis, *Bone tissue engineering: state of the art and future trends.* Macromol Biosci, 2004. **4**(8): p. 743-65.

152. Yoon, B.H., et al., *Stability and cellular responses to fluorapatite-collagen composites.* Biomaterials, 2005. **26**(16): p. 2957-63.

153. Farley, J. Wergedal, and D. Baylink, *Fluoride directly stimulates proliferation and alkaline phosphatase activity of bone-forming cells.* Science, 1983. **222**(4621): p. 330-332.

154. Bhadang, K.A., et al., *Biological responses of human osteoblasts and osteoclasts to flame-sprayed coatings of hydroxyapatite and fluorapatite blends.* Acta Biomater, 2010. **6**(4): p. 1575-83.

155. Inoue, M., et al., *Effect of fluoride-substituted apatite on in vivo bone formation.* J Biomater Appl, 2011. **25**(8): p. 811-24.

156. Huggins, C.B., *The phosphatase activity of transplants of the epithelium of the urinary bladder to the abdominal wall producing heterotopic ossification.* Biochem J, 1931. **25**(3): p. 728-32.

157. Urist, M.R., *Bone: formation by autoinduction.* Science, 1965. **150**(3698): p. 893-9.

158. Urist, M.R. and B.S. Strates, *Bone morphogenetic protein.* J Dent Res, 1971. **50**(6): p. 1392-406.

159. Urist, M.R., et al., *The bone induction principle.* Clin Orthop Relat Res, 1967. **53**: p. 243-83.

160. Dimitriou, R., et al., *Bone regeneration: current concepts and future directions.* BMC Med, 2011. **9**: p. 66.

161. Yao, J., et al., *Ectopic bone formation in adipose-derived stromal cell-seeded osteoinductive calcium phosphate scaffolds.* J Biomater Appl, 2010. **24**(7): p. 607-24.

162.   Barradas, A.M., et al., *Osteoinductive biomaterials: current knowledge of properties, experimental models and biological mechanisms.* Eur Cell Mater, 2011. **21**: p. 407-29; discussion 429.

163.   Zhang, H., X.J. Ye, and J.S. Li, *Preparation and biocompatibility evaluation of apatite/wollastonite-derived porous bioactive glass ceramic scaffolds.* Biomed Mater, 2009. **4**(4): p. 045007.

164.   Zhou, Y.F., et al., *Does seeding density affect in vitro mineral nodules formation in novel composite scaffolds?* Journal of Biomedical Materials Research Part A, 2006. **78A**(1): p. 183-193.

165.   Lode, A., A. Bernhardt, and M. Gelinsky, *Cultivation of human bone marrow stromal cells on three-dimensional scaffolds of mineralized collagen: influence of seeding density on colonization, proliferation and osteogenic differentiation.* J Tissue Eng Regen Med, 2008. **2**(7): p. 400-7.

166.   Holy, C.E., M.S. Shoichet, and J.E. Davies, *Engineering three-dimensional bone tissue in vitro using biodegradable scaffolds: investigating initial cell-seeding density and culture period.* J Biomed Mater Res, 2000. **51**(3): p. 376-82.

167.   Ishaug-Riley, S.L., et al., *Three-dimensional culture of rat calvarial osteoblasts in porous biodegradable polymers.* Biomaterials, 1998. **19**(15): p. 1405-12.

168.   Wilson, C.E., et al., *Evaluating 3D bone tissue engineered constructs with different seeding densities using the alamarBlue assay and the effect on in vivo bone formation.* J Mater Sci Mater Med, 2002. **13**(12): p. 1265-9.

169.   Derubeis, A.R. and R. Cancedda, *Bone marrow stromal cells (BMSCs) in bone engineering: limitations and recent advances.* Ann Biomed Eng, 2004. **32**(1): p. 160-5.

170.   Seebach, C., et al., *Comparison of six bone-graft substitutes regarding to cell seeding efficiency, metabolism and growth behaviour of human mesenchymal stem cells (MSC) in vitro.* Injury, 2010. **41**(7): p. 731-8.

171.   Nath, S., S. Kalmodia, and B. Basu, *In vitro biocompatibility of novel biphasic calcium phosphate-mullite composites.* J Biomater Appl, 2013. **27**(5): p. 497-509.

172.   Wang, X., et al., *In vitro differentiation and mineralization of dental pulp stem cells on enamel-like fluorapatite surfaces.* Tissue Eng Part C Methods, 2012. **18**(11): p. 821-30.

173.   Liu, J., et al., *The effect of novel fluorapatite surfaces on osteoblast-like cell adhesion, growth, and mineralization.* Tissue Eng Part A, 2010. **16**(9): p. 2977-86.

174.   Loty, C., et al., *In vitro bone formation on a bone-like apatite layer prepared by a biomimetic process on a bioactive glass-ceramic.* J Biomed Mater Res, 2000. **49**(4): p. 423-34.

175.   Yuan, H., et al., *Osteoinductive ceramics as a synthetic alternative to autologous bone grafting.* Proc Natl Acad Sci U S A, 2010. **107**(31): p. 13614-9.

176. Abou Neel, E.A., et al., *In vitro bioactivity and gene expression by cells cultured on titanium dioxide doped phosphate-based glasses.* Biomaterials, 2007. **28**(19): p. 2967-77.

177. Ozawa, S. and S. Kasugai, *Evaluation of implant materials (hydroxyapatite, glass-ceramics, titanium) in rat bone marrow stromal cell culture.* Biomaterials, 1996. **17**(1): p. 23-9.

178. Rashid, F., et al., *The effect of extracellular calcium ion on gene expression of bone-related proteins in human pulp cells.* J Endod, 2003. **29**(2): p. 104-7.

179. Nishio, K., et al., *Effects of apatite and wollastonite containing glass-ceramic powder and two types of alumina powder in composites on osteoblastic differentiation of bone marrow cells.* J Biomed Mater Res, 2001. **55**(2): p. 164-76.

180. Lin, L., K.L. Chow, and Y. Leng, *Study of hydroxyapatite osteoinductivity with an osteogenic differentiation of mesenchymal stem cells.* J Biomed Mater Res A, 2009. **89**(2): p. 326-35.

181. Accadbled, F., et al., *Influence of location, fluid flow direction, and tissue maturity on the macroscopic permeability of vertebral end plates.* Spine (Phila Pa 1976), 2008. **33**(6): p. 612-9.

182. Wang, Y., et al., *The osseous endplates in lumbar vertebrae: thickness, bone mineral density and their associations with age and disk degeneration.* Bone, 2011. **48**(4): p. 804-9.

183. Jackson, A.R., C.Y. Huang, and W.Y. Gu, *Effect of endplate calcification and mechanical deformation on the distribution of glucose in intervertebral disc: a 3D finite element study.* Comput Methods Biomech Biomed Engin, 2011. **14**(2): p. 195-204.

184. Setton, L.A., et al., *Compressive properties of the cartilaginous end-plate of the baboon lumbar spine.* J Orthop Res, 1993. **11**(2): p. 228-39.

185. Ayotte, D.C., et al., *Direction-dependent constriction flow in a poroelastic solid: the intervertebral disc valve.* J Biomech Eng, 2000. **122**(6): p. 587-93.

186. DeLise, A.M., L. Fischer, and R.S. Tuan, *Cellular interactions and signaling in cartilage development.* Osteoarthritis Cartilage, 2000. **8**(5): p. 309-34.

187. Johnstone, B., et al., *In vitro chondrogenesis of bone marrow-derived mesenchymal progenitor cells.* Exp Cell Res, 1998. **238**(1): p. 265-72.

188. Mackay, A.M., et al., *Chondrogenic differentiation of cultured human mesenchymal stem cells from marrow.* Tissue Eng, 1998. **4**(4): p. 415-28.

189. Oldershaw, R.A., *Cell sources for the regeneration of articular cartilage: the past, the horizon and the future.* Int J Exp Pathol, 2012. **93**(6): p. 389-400.

190. Tuli, R., et al., *Human mesenchymal progenitor cell-based tissue engineering of a single-unit osteochondral construct.* Tissue Eng, 2004. **10**(7-8): p. 1169-79.

191.   Palmer, S.B.L., *Tissue engineering osteochondral composites using mesenchymal stem cells*, 2009, s.n.]: York.

192.   Saleh, F.A., et al., *Three-dimensional in vitro culture techniques for mesenchymal stem cells.* Methods Mol Biol, 2012. **916**: p. 31-45.

193.   Saleh, F.A. and P.G. Genever, *Turning round: multipotent stromal cells, a three-dimensional revolution?* Cytotherapy, 2011. **13**(8): p. 903-12.

194.   Wang, X., et al., *Tissue engineering of biphasic cartilage constructs using various biodegradable scaffolds: an in vitro study.* Biomaterials, 2004. **25**(17): p. 3681-8.

195.   Waldman, S.D., et al., *Effect of biomechanical conditioning on cartilaginous tissue formation in vitro.* J Bone Joint Surg Am, 2003. **85-A Suppl 2**: p. 101-5.

196.   Kandel, R.A., et al., *Repair of osteochondral defects with biphasic cartilage-calcium polyphosphate constructs in a sheep model.* Biomaterials, 2006. **27**(22): p. 4120-31.

197.   Danisovic, L., et al., *The tissue engineering of articular cartilage: cells, scaffolds and stimulating factors.* Exp Biol Med (Maywood), 2012. **237**(1): p. 10-7.

198.   Schulze-Tanzil, G., *Activation and dedifferentiation of chondrocytes: implications in cartilage injury and repair.* Ann Anat, 2009. **191**(4): p. 325-38.

199.   Chung, C. and J.A. Burdick, *Engineering cartilage tissue.* Adv Drug Deliv Rev, 2008. **60**(2): p. 243-62.

200.   Tuan, R.S., G. Boland, and R. Tuli, *Adult mesenchymal stem cells and cell-based tissue engineering.* Arthritis Res Ther, 2003. **5**(1): p. 32-45.

201.   Seo, S. and K. Na, *Mesenchymal stem cell-based tissue engineering for chondrogenesis.* J Biomed Biotechnol, 2011. **2011**: p. 806891.

202.   Ahrens, P.B., M. Solursh, and R.S. Reiter, *Stage-related capacity for limb chondrogenesis in cell culture.* Dev Biol, 1977. **60**(1): p. 69-82.

203.   Denker, A.E., et al., *Chondrogenic differentiation of murine C3H10T1/2 multipotential mesenchymal cells: I. Stimulation by bone morphogenetic protein-2 in high-density micromass cultures.* Differentiation, 1999. **64**(2): p. 67-76.

204.   Laffosse, J.M., et al., *Correlations between effective permeability and marrow contact channels surface of vertebral endplates.* J Orthop Res, 2010. **28**(9): p. 1229-34.

205.   Kuboki, Y., Q. Jin, and H. Takita, *Geometry of carriers controlling phenotypic expression in BMP-induced osteogenesis and chondrogenesis.* J Bone Joint Surg Am, 2001. **83-A Suppl 1**(Pt 2): p. S105-15.

206.   Otsuki, B., et al., *Pore throat size and connectivity determine bone and tissue ingrowth into porous implants: three-dimensional micro-CT based structural analyses of porous bioactive titanium implants.* Biomaterials, 2006. **27**(35): p. 5892-900.

207. Dias, M.R., et al., *Permeability analysis of scaffolds for bone tissue engineering.* J Biomech, 2012. **45**(6): p. 938-44.

208. Ochoa, I., et al., *Permeability evaluation of 45S5 Bioglass-based scaffolds for bone tissue engineering.* J Biomech, 2009. **42**(3): p. 257-60.

209. Li, S., et al., *Macroporous biphasic calcium phosphate scaffold with high permeability/porosity ratio.* Tissue Eng, 2003. **9**(3): p. 535-48.

210. Lee, K.W., et al., *Fabrication and characterization of poly(propylene fumarate) scaffolds with controlled pore structures using 3-dimensional printing and injection molding.* Tissue Eng, 2006. **12**(10): p. 2801-11.

211. Jeong, C.G., H. Zhang, and S.J. Hollister, *Three-dimensional poly(1,8-octanediol-co-citrate) scaffold pore shape and permeability effects on sub-cutaneous in vivo chondrogenesis using primary chondrocytes.* Acta Biomater, 2011. **7**(2): p. 505-14.

212. Kohles, S.S., et al., *Direct perfusion measurements of cancellous bone anisotropic permeability.* J Biomech, 2001. **34**(9): p. 1197-202.

213. Nauman, E.A., K.E. Fong, and T.M. Keaveny, *Dependence of intertrabecular permeability on flow direction and anatomic site.* Ann Biomed Eng, 1999. **27**(4): p. 517-24.